DETECTING DAMAGE IN BEAMS AND STRUCTURES THROUGH MODAL ANALYSIS

LEE DOWNER

DETECTING DAMAGE IN BEAMS AND STRUCTURES THROUGH MODAL ANALYSIS

by

© Lee Downer

A Thesis Submitted to the

School of Graduate Studies

in Partial Fulfillment of the Requirements for the Degree of

Master of Engineering

Faculty of Engineering and Applied Science

Memorial University of Newfoundland

December 2010

St. John's Newfoundland Canada

Abstract

Based on a review of previous literature on the subject of modal testing, it was determined that modal parameters such as frequency, damping ratio and mode shape change with the introduction of damage to a beam or structure. However, relating those changes back to the exact nature and location of the damage is a subject of ongoing study. In the current work, a method has been proposed for quantifying and localizing defects in structures using multiple regression models and response surfaces obtained through design of experiments (DOE) techniques, which are initially developed to relate modal frequencies to parameters such as defect location and defect depth. Once the models are developed, multiple models can subsequently be inverted and solved for the multiple defect parameters required to characterize a defect by using modal frequency measurements of a test specimen. The method was also successfully employed in many scenarios involving theoretical, finite element and physical models. In addition to the development of this method, a series of full-scale utility poles were tested in order to investigate whether modal impact testing could be used to assess their condition. Static destructive tests were used to determine material properties as well as failure stress at the ground line and break location for each pole. It was found that each modal damping ratio correlated to some degree with these maximum stress values. Moreover, it was found that the average of damping ratio across multiple modes correlated with maximum stress better than either individual damping ratio, and that correlation progressively improved as a greater number of modes were considered in the averaging process. Regression models were developed to relate average damping ratio to maximum stress and proved to provide better predictions of maximum stress for the specimens involved in the study than did commercial ultrasonic NDT equipment.

Acknowledgements

I would like to acknowledge and thank the following people, without whom this study would not have been possible: Dr. Geoff Rideout for providing guidance, supervision and insight, Asim Haldar, Paul Dillon and the rest of NL Hydro for providing funding, materials and practical suggestions, Matthew Curtis for providing help with laboratory work during full-scale pole testing and throughout the period of study, Oliver Whelan and Andrew Lawlor for helping to prepare and run the full scale pole tests, technical Services staff for fabrication assistance, laboratory technicians Craig Mitchell, Tom Pike, Caroline Koenig, Don Taylor and Shawn Organ as well as fellow graduate students, colleagues and many others for assistance of various forms, and especially Melanie and my family for patience and support.

Table of Contents

List of Tables

List of Figures

List of Abbreviations

ANOVA - 'analysis of variance'. A statistical technique, within the design of experiments framework, that allows factors to be assessed for their respective level of effect on the studied response.

CM - 'center of mass'. Used in full-scale pole test results to specify the distance of the center of mass from the each poles butt end.

DOE - 'design of experiments'. Used throughout the current study and refers to the process of determining the effect of factors on a measured response though experimental procedures.

FFT - 'fast Fourier transforms'. Used by modal testing software to transform measured data from the time domain to the frequency domain.

FRF - 'frequency response function'. Used to display the amplitude of vibration across a certain band of frequencies.

GL - 'ground line' of a full-scale utility pole. With respect to laboratory testing, it refers to the section of pole immediately adjacent the clamp on the cantilever side.

LVDT – 'linear variable differential transformer'. Sensors used to measure displacement on either side of the clamp when testing full-scale poles. These measurements were used to calculate the rigid body effect of clamp flexure on measured pole deflection during static tests.

POL - 'point of load'. The point of load is the location where full-scale utility poles are loaded during static testing. It was normally taken as two feet from the tip (or the free end) of the pole.

SYP - 'Southern Yellow Pine' species of wood.

WRC - 'Western Red Cedar' species of wood.

List of Appendices

Chapter 1

Introduction

Wooden poles are widely used by utility companies to support transmission lines. In Newfoundland and Labrador alone there are approximately 26000 wooden poles in service ranging in age up to 38 years with about 34% over 30 years of age (Haldar, 2003). Ensuring their structural integrity is important to the people who work around them as well as those who rely on them for uninterrupted power transmission. Defects due to rot, ant and woodpecker damage can be serious threats to the bending strength and load carrying capacity of a pole. These types of defects can be hidden from view and can occur in relatively new poles that would otherwise have a long service life. Treatment using fluoride and boron based preservatives as well as creosote coverings can slow the formation of these types of defects. However, there is still a need for non-destructive test methods to detect hidden defects and estimate pole strength. Various non-destructive test methods are already being used and include sonic and ultrasonic devices, x-ray and nuclear magnetic resonance, decay detecting drills and electrical resistance instruments (Wareing, 2005). Many of these methods are used locally but do not provide a definite indication of a pole's condition, especially when in the intermediate stages of deterioration. The author and research collaborators have proposed the use of modal impact testing as a new non-destructive test method for detecting hidden internal defects in wooden poles.

A somewhat novel approach will be suggested by the author for detecting and quantifying defects in beams using their modal frequency. The method involves first using design of experiments theory to create regression models of multiple modal frequencies of the beam. Each regression model expresses a particular natural frequency in terms of a number of factors that have a significant effect on that natural frequency. The factors could include easily measurable parameters of the beam as well as parameters that are desired to be predicted. If defects are desired to be detected, then their parameters (such as dimensions and location) should be included as factors in the regression models. Once the regression models are acquired, they can be used to detect defects by first measuring the natural frequencies of the beam using some experimental technique (such as modal impact testing). The natural frequencies are then used as inputs for the regression models. Any other easily measurable parameters are also collected and input into the regression models. The regression models are then rearranged and solved for the appropriate defect parameters. The regression models can only be solved if there are at least as many equations as unknowns. Therefore, the number of defect parameters that can be predicted is limited to the number of modal frequencies that can be accurately measured. It is also important that the regression models be an accurate fit to the beams actual modal behaviour in order for them to provide good predictions of defect parameters. Since the modal frequencies of a beam are affected by its length, cross sectional area, second moment of area of the cross section, modulus of elasticity and density then any easily measurable parameters that affect the above parameters should be included in the regression models. For example, a wood beams density is affected by its moisture content. Therefore, if moisture content can be measured easily in practice then it should be included in the models in order to increase their accuracy. The benefit to using this of approach is that it could be used for complex structures that are difficult to determine theoretical natural frequencies for in order to compare to experimental values. The regression models simply have to be developed first by experimental measurements on the desired structure type. It may be useful for quality control purposes as well where products are produced in mass quantities and dedicating a number of specimens from an assembly line may not be significant if they allow for the development of regression models that can be used for future inspection.

The goal of this study is to confirm or deny the validity of the above method by applying it to controlled theoretical, finite element and small scale experimental models. Models for frequency will be developed according to the above approach, and then used to predict the defect condition of validation specimens. The predictions made by this method will be compared to the actual known (and controlled) defect parameters in validation specimens for accuracy assessment. Some preliminary work will also be done to determine if this method, or a similar approach, is practical for testing full scale in service utility poles. Full-scale utility poles will be tested in the lab using existing non-destructive test (NDT) methods as well as modal impact testing. The poles will then be tested to destruction in the lab to determine strength. The existing NDT as well as the modal impact results will then be compared to strength measurements in order to assess the relative value of modal testing.

Chapter 2

Literature Review

For any structure, there exist an infinite number of vibration modes. Each of these modes has a unique shape by which deformation occurs during vibration and a corresponding natural frequency at which that vibration takes place. Generally vibration is damped in non-ideal situations and each vibration mode has a certain (but not necessarily unique) degree of damping which is expressed as a modal damping ratio. Any state of vibration can generally be expressed as the superposition of an infinite number of these modes. The amplitude of each mode's vibration response, due to the addition of energy to the structure via an input force or initial condition, will be dependent upon the degree to which that mode's natural frequency is excited. These three parameters; mode shape, frequency and damping ratio; are often measured through experimental modal analysis and are typically the focus of attempts to perform vibration based damage assessment.

Modal testing has already been used in various applications to detect material defects. For example, it has been used to detect cracks in a wheel end spindles of US Army vehicles (Ackers, et al., 2006). It has also been used to characterize the properties of fiber-reinforced composite materials for quality control purposes (Gibson, 2000). In addition, it has been used to determine modal parameters that helped to design more dynamically wind resistant steel, aluminum and fibreglass light poles (Caracoglia & Velazquez, 2008). However, current applications are mostly limited to materials that are manufactured to be homogeneous and isotropic in nature. Wooden poles are normally non-homogeneous and usually contain naturally occurring defects such as knots and spiral grain. In addition, wood is an orthotropic material with independent material properties in three mutually perpendicular directions relative to the direction of grain growth (Green, Winandy, & Kretschmann, 1999). This means that material properties can vary between specimens depending on their individual patterns of grain formation. For these reasons, any modal impact-test method that is developed for use on wooden poles must be based heavily on experimental data (with some validation of experimental results by finite element and theoretical means).

The current research initiative stems from a preliminary study by Budipriyanto et al. In their study, three rectangular cross section cantilevered beams were analyzed under random excitation to determine modal frequencies and damping ratios for the first two transverse modes. The beams were tested intact and with rectangular slotted defects at the clamped end. Input force was measured with a load cell and response was measured with two strain gauges (near the clamped end) and two accelerometers (one near the clamped end and one near the tip). With slots introduced it was found that natural frequency decreased and damping ratios changed but with no definite trend. Finite element analysis validation achieved different frequency values but did show a similar percentage change with slot introduction when compared to experimental results. The numerical study also included results for the first ten modes (including torsion and axial modes as well as transverse modes along two planes) with three different sized slots. It was found that all modal frequencies decreased with increased slot size. In addition, a damage index was proposed as a function of the modal frequency, the modal damping ratio, and the response. It was claimed to increase for defected beams. The damage index increased with slot introduction when determined based on response from the accelerometer mounted near the clamped end but showed no definite trend when determined using response from the accelerometer mounted near the tip. The authors suggested that the damage index increased using the base mounted accelerometer because that accelerometer was located near the defect. This result was said to confirm that the damage index could quantify as well as localize damage (Budipriyanto, Swamidas, Adluri, & Haldar, 2007). However, even though the damage index did increase for the accelerometer mounted near the base for all specimens, the magnitude of the increase was not consistent between specimens. In addition, the ratio of damage index increase between the first and second modes was not consistent between specimens. While some of the results of this study are promising and show that defects can cause some change in modal characteristic of beams, more work has to be done in order to accurately quantify these changes. Prediction models have yet to be derived that relate vibration response directly to defect size or to bending strength reduction. Since the goal is to ultimately use this method for field evaluation of in-service poles, expanding this work to include full-scale pole testing will need to be done. In addition, modal impact testing should be investigated since random excitation is impractical for field use.

Chui et al. suggest that a pole's modulus of elasticity is an important quality control parameter since it correlates well with strength. They present a method to dynamically determine a tapered pole's modulus of elasticity based on its first transverse modal frequency. Ten poles were tested using this method and the dynamically determined modulus was compared to a statically determined modulus based on ASTM standard procedures. The relationship between them was good except for one outlier that was determined to be weakened by ring shake. When comparing the statically determined modulus of elasticity to bending strength there was a good correlation. However, when comparing the dynamically determined modulus of elasticity to bending strength the damaged pole did not correlate well. The authors feel that this result means vibration testing may not be able to accurately identify defected poles due to the low stress levels involved (Chui, Barclay, & Cooper, 1999).

In a review of studies that used modal frequency as an indicator of structural damage, Salawu pointed out that frequency can be a useful parameter but has some downfalls. Many researchers have confirmed that the existence of a defect is comparable to the local reduction of cross sectional moment of inertia which in turn reduces local bending stiffness (defected beams have been modelled in previous studies as two sections joined by a torsion spring). This loss of stiffness results in a lowered natural frequency and the frequency reduction is most severe when a defect is located at a point of high curvature for any particular mode. There are some exceptions, but at modal nodes, the stress in a structure is often low and therefore damage occurring near those areas may not have a significant effect on the frequency of that particular vibration mode. This means that changes in the frequency of multiple modes may need to be considered together in order to provide an accurate picture of whether or not damage is present. There also is some debate about whether low order modes or high order modes should be used to detect damage. It has been shown that high order modes are the most sensitive to damage but at the same time are much harder to accurately measure in practice. In addition, high order modes obviously have a greater number of nodes that could potentially hide the presence of defects (Salawu, 1997).

It has been shown that changes in the stiffness of the connection between a structure and its supports can change the measured natural frequency of the structure. This may be of some concern to pole testing since varying soil conditions (i.e. drying, freezing etc.) could change the stiffness of a pole's support and influence modal test results. In addition, many researchers have had difficulty quantifying the effects of environmental conditions (such as temperature and humidity) and have not been able to accurately incorporate these factors into their test methods. Testing on-site wood poles would likely mean dealing with this same problem. In order to avoid having to account for environmental factors it has sometimes been found useful to define a threshold value beyond which damage can be assumed as present. Others have simply ensured that measurements are made at the same time of year to minimize the change in environmental conditions (Salawu, 1997).

Like modal frequency, modal damping ratio (or loss factor) has also been shown to change with the presence of defects. One study involved drilling an increasingly large number of holes into a wooden beam and tracking how the modulus of elasticity and loss factor changed. It was found that as a general trend the loss factor increased as the number of holes increased. The trend however was erratic suggesting that loss factor is difficult to measure experimentally. It was also found that the modulus of elasticity decreased as the number of defects increased (Ouis, 2003). This is significant since the modulus of elasticity has been found to correlate well with strength (Chui, Barclay, & Cooper, 1999). In a follow up study, a similar experiment was conducted using sand filled holes instead of void holes and a similar trend was found for modulus of elasticity. However, In this case damping increased at a greater rate with defect introduction. The sand filled holes were intended to better simulate rot pockets and seemed to amplify the effect of defects on loss factor (Ouis & Zerizer, 2006).

Most of the previously mentioned works have limited their study to changes in modal frequencies and damping in order to detect damage in structures. While these methods seem promising for examining overall specimen properties, they are less useful for localizing defects. The use of changes in mode shapes to localize defects is another possibility. However, using the change in displacement mode shapes between intact and damaged specimens has shown little success. The change in a parameter called the curvature mode shape had been proposed as a better indicator of damage location. This parameter can be calculated using central difference approximation from a displacement mode shape or can be determined directly by measuring localized strains. In a numerical study, Pandey et al. demonstrated that, for the first five modes, the absolute difference in curvature mode shape between intact and defected specimens were useful in localizing the defect. The defect was introduced as a local reduction in the modulus of elasticity (E). As the modulus of elasticity was incrementally lowered, the magnitude of absolute difference in curvature mode shape at that location was shown to proportionally increase for all five modes (Pandey, Biswas, & Samman, 1991).

Lestari et al. used the difference in curvature mode shapes to identify defects in laminated carbon/epoxy composite beams. In a study involving six beams they found that curvature mode shapes gave a reasonable estimate of damage location for three distinct types of defect. The defect types studied include de-lamination, impact damage and saw cut damage. In their analytical study, the curvature mode shapes for each of the first four modes localized damage very well except when the damage occurred near a node. In their experimental study, beams were tested using impact excitation as well as actuator induced sine sweep excitation. For impact testing, the response of the beam was measured at sixteen nodes and the frequency response function from twenty different data sets were averaged for each node. The curvature mode shapes were measured directly using PVDF film sensors to avoid loss of accuracy that may occur when converting displacement mode shapes to curvature mode shapes. The authors found that impact testing was better at localizing damage despite sine sweep excitation giving smoother mode shapes (Lestari, Qiao, & Hanagud, 2007). This work shows that curvature mode shapes can be used to experimentally localize defects in beams. However, the beams used in this study were manufactured and could be assumed to have constant material properties along their entire length. In addition, the authors focused on comparing experimentally determined curvature mode shapes for defected beams to analytically determined curvature mode shapes for intact beams. This method may be less useful for indentifying defects in wooden beams given that naturally occurring defects such as knots could make curvature mode shape of intact beams different from their theoretically expected shapes. A more useful method of localizing introduced defects in wood may be to compare experimentally determined curvature mode shapes of each individual beam for both the intact and the damaged condition.

One other noteworthy area of study is the use of added mass as an indicator of damage in beams. Al-Said suggested that the change ratio of the first natural frequency reaches a maximum algebraic value as an added mass is moved near the location of a crack. The same can be said for the second frequency, except that the change ratio now reaches a minimum near the crack. He also showed that as the added mass was moved past the crack, the trend in the change ratio for each of the first two modes showed a discontinuity. Plots showed that the first modal frequency generally decreases while the second modal frequency oscillates as a mass traverses towards the tip of a clamped-free beam (Al-Said M. S., 2008). This oscillating behaviour of higher modal frequencies, occurring as added masses traverse along beams, has been shown in many studies. Frequency generally drops by a greater amount as an added mass traverses away from a modal node. Its effect diminishes as it approaches the next modal node resulting in an oscillating behaviour (Al-Said & Al-Qaisia, 2008)(Fung & Yau, 2001)(Zhong & Oyadiji, 2008). As was noted earlier damage can be hidden if it is located near a modal node. The use of change in frequency due to an added mass shares this downfall since its effect is reduced when the mass is located near a node.

Despite its weaknesses, modal analysis continues to be a widely studied topic in the area of damage assessment and non-destructive testing. It shows promise when applied to controlled and familiar structures such as cracked beams with ideal end conditions. With further work, it could be developed into a staple method for condition monitoring which is applicable to a wide range of practical situations.

Chapter 3

Theory and Background Information

Some theory and background information will be presented in the following sections. Knowledge of these topics is essential for following the work presented in later chapters. Some of the results presented here will also be directly referred to in later chapters. Note that the terms 'frequencies', 'modal frequencies' and 'natural frequencies' will be used interchangeably in this and subsequent chapters and unless otherwise stated they will refer to transverse modal vibration frequencies (as opposed to axial modes, torsion modes etc).

3.1 Modal Frequencies of an Undamped Clamped-Free Beam

Here we will derive the theoretical modal frequencies for a general un-damped cantilever beam. This theory is useful for understanding what parameters affect modal frequencies and thus what parameters should be considered when trying to use modal frequency as an indicator of defect presence. It will also be used as a baseline when solving for frequencies of intact beams for comparative purposes in later chapters. The theory used here models the beam as a distributed parameter system and is covered in Inman's text (Inman, 2001).

For a cantilever, the boundary conditions are clamped–free. We will define an origin at the center of the cross section on the clamped end and the positive x-axis extending along the length of the beam for a beam of length l.

Figure 3.1 - Clamped-Free Beam Schematic

For free vibration the beams is governed by the wave equation:

$$\frac{\partial^2 w(x,t)}{\partial t^2} + c^2 \frac{\partial^4 w(x,t)}{\partial x^4} = 0$$

Where:

$$c = \sqrt{\frac{EI}{\rho A}}$$

The beam's motion $w(x,t)$ can be expressed as a function of a spatial equation $X(x)$ and a frequency equation $T(t)$ as follows:

$$w(x,t) = X(x)T(t)$$

Through separation of variables, we solve the wave equation for the spatial function $X(x)$:

$$X(x) = a_1 sin\beta x + a_2 cos\beta x + a_3 sinh\beta x + a_4 cosh\beta x$$

The coefficients $a_1$through a_4 can be found by applying the boundary conditions for a clamped-free beam. The spatial function has an infinite number of solutions for β corresponding to different mode shapes. Each solution represents a mode with the natural frequency (in rad/s):

$$\omega_n = \beta_n{}^2 \sqrt{\frac{EI}{\rho A}}$$

Where ρ = density, I = moment of inertia, E = modulus of elasticity and A = cross sectional area. The derivation of the values of β for a fixed-pinned beam is presented in Inman. However, we want the natural frequencies for a fixed-free beam so we can continue to derive them ourselves. From the boundary conditions at each end, we get four equations:

At the clamped end, $(x = 0)$we know the deflection is zero:

$$Deflection = w = 0 \; at \; x = 0$$

$$w(x,t) = X(x)T(t) = 0 \; at \; x = 0$$

Since $T(t) \neq 0$:

$$X(x) = a_1 sin\beta x + a_2 cos\beta x + a_3 sinh\beta x + a_4 cosh\beta x$$

$$X(0) = a_2 + a_4 = 0$$

At the clamped end $(x = 0)$, we also know that the slope is zero:

$$Slope = \frac{\partial w}{\partial x} = 0 \; at \; x = 0$$

$$X'(x) = a_1 \beta cos\beta x - a_2 \beta sin\beta x + a_3 \beta cosh\beta x + a_4 \beta sinh\beta x$$

$$X'(0) = a_1 \beta + a_3 \beta = 0$$

At the free end $(x = l)$, we know that the bending moment is zero:

$$Bending\ Moment = M = EI\frac{\partial^2\omega}{\partial x^2} = 0\ at\ x = l$$

Assuming $EI \neq 0$:

$$\frac{\partial^2 X}{\partial x^2} = 0\ at\ x = l$$

$$X''(x) = -a_1\beta^2 sin\beta x - a_2\beta^2 cos\beta x + a_3\beta^2 sinh\beta x + a_4\beta^2 cosh\beta x$$

$$X''(l) = -a_1\beta^2 sin\beta l - a_2\beta^2 cos\beta l + a_3\beta^2 sinh\beta l + a_4\beta^2 cosh\beta l = 0$$

At the free end ($x = l$), we also know that the shear force is zero:

$$Shear\ Force = v = \frac{\partial}{\partial x}\left[EI\frac{\partial^2\omega}{\partial x^2}\right] = 0\ at\ x = l$$

$$X'''(x) = -a_1\beta^3 cos\beta x + a_2\beta^3 sin\beta x + a_3\beta^3 cosh\beta x + a_4\beta^3 sinh\beta x$$

$$X'''(l) = -a_1\beta^3 cos\beta l + a_2\beta^3 sin\beta l + a_3\beta^3 cosh\beta l + a_4\beta^3 sinh\beta l = 0$$

We now have four equations (one for each boundary condition) and four unknowns ($a_1, a_2, a_3\ and\ a_4$). These give us the following matrix:

$$\begin{bmatrix} 0 & 1 & 0 & 1 \\ \beta & 0 & \beta & 0 \\ -\beta^2 sin\beta l & -\beta^2 cos\beta l & \beta^2 sinh\beta l & \beta^2 cosh\beta l \\ -\beta^3 cos\beta l & \beta^3 sin\beta l & \beta^3 cosh\beta l & \beta^3 sinh\beta l \end{bmatrix}\begin{bmatrix} a_1 \\ a_2 \\ a_3 \\ a_4 \end{bmatrix} = \begin{bmatrix} 0 \\ 0 \\ 0 \\ 0 \end{bmatrix}$$

A non-zero solution exists only if the determinant of this matrix is zero:

$$
-\begin{vmatrix} \beta & \beta & 0 \\ -\beta^2 sin\beta l & \beta^2 sinh\beta l & \beta^2 cosh\beta l \\ -\beta^3 cos\beta l & \beta^3 cosh\beta l & \beta^3 sinh\beta l \end{vmatrix} - \begin{vmatrix} \beta & 0 & \beta \\ -\beta^2 sin\beta l & -\beta^2 cos\beta l & \beta^2 sinh\beta l \\ -\beta^3 cos\beta l & \beta^3 sin\beta l & \beta^3 cosh\beta l \end{vmatrix} = 0
$$

$$
\begin{aligned}
-\beta[\beta^2 sinh\beta l \cdot \beta^3 sinh\beta l - \beta^2 cosh\beta l \cdot \beta^3 cosh\beta l] \\
+ \beta[-\beta^2 sin\beta l \cdot \beta^3 sinh\beta l + \beta^2 cosh\beta l \cdot \beta^3 cos\beta l] \\
- \beta[-\beta^2 cos\beta l \cdot \beta^3 cosh\beta l - \beta^2 sinh\beta l \cdot \beta^3 sin\beta l] \\
- \beta[-\beta^2 sin\beta l \cdot \beta^3 sin\beta l - \beta^2 cos\beta l \cdot \beta^3 cos\beta l] = 0
\end{aligned}
$$

$$
\begin{aligned}
-\beta^6 sinh^2\beta l + \beta^6 cosh^2\beta l - \beta^6 sin\beta l \cdot sinh\beta l + \beta^6 cos\beta l \cdot cosh\beta l + \beta^6 cos\beta l \cdot cosh\beta l \\
+ \beta^6 sin\beta l \cdot sinh\beta l + \beta^6 sin^2\beta l + \beta^6 cos^2\beta l = 0
\end{aligned}
$$

$$
\beta^6[-sinh^2\beta l + cosh^2\beta l + 2cos\beta l \cdot cosh\beta l + 1] = 0
$$

$$
2\beta^6[1 + cos\beta l \cdot cosh\beta l] = 0
$$

Since $2\beta^6 \neq 0$:

$$
1 + cos\beta l \cdot cosh\beta l = 0
$$

Solving this equation numerically we can get the value of βl that corresponds to each mode (the first five values are approximately βl = 1.87, 4.70, 7.85, 11.00 and 14.13).

3.2 Modal Frequencies of an Undamped Single-Stepped Clamped-Free Beam

We will refer to the following theory in later chapters. For now, the theory is presented for reference purposes.

In order to derive the exact solution of a stepped Euler-Bernoulli beam we can represent the beam as two separate spans each with its own unique parameters and wave equation. Theoretical guidance for this approach comes from Inman's derivation of natural frequencies for constant cross section beams (Inman, 2001) as well as Koplow's description of the basic steps involved in deriving the natural frequencies of a 'stepped' free-free beam with applied force excitation (Koplow, Bhattacharyya, & Mann, 2006).

We begin by representing the beam as two spans (span a, and span b) as shown in Figure 3.2, with each span having its own unique length, density, elastic modulus, cross sectional area and second moment of area (i.e. span 'a' has parameters $L_a, \rho_a, E_a, A_a, I_a$ and span 'b' has parameters $L_b, \rho_b, E_b, A_b, I_b$). For our application, the elastic modulus and density of both sections will be the same but we will keep them as separate parameters in order to derive a more general beam.

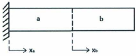

Figure 3.2 - Clamped-Free Single-Stepped Beam Schematic

Each spans motion is governed by the wave equation so that:

$$E_a I_a \frac{\partial^4 w_a(x_a, t)}{\partial {x_a}^4} + \rho_a A_a \frac{\partial^2 w_a(x_a, t)}{\partial t^2} = 0$$

$$E_b I_b \frac{\partial^4 w_b(x_b, t)}{\partial {x_b}^4} + \rho_b A_b \frac{\partial^2 w_b(x_b, t)}{\partial t^2} = 0$$

We first need to recognize that the transverse motion of each section of the beam, $w_a(x_a, t)$ and $w_b(x_b, t)$, are functions of space and time such that:

$$w_a(x_a, t) = Y_a(x_a)T(t)$$

$$w_b(x_b, t) = Y_b(x_b)T(t)$$

Through separation of variables, we can then solve each wave equation for the spatial functions

$$Y_a(x_a) = Asin\beta_a x_a + Bcos\beta_a x_a + Csinh\beta_a x_a + Dcosh\beta_a x_a$$

$$Y_b(x_b) = Esin\beta_b x_b + Fcos\beta_b x_b + Gsinh\beta_b x_b + Hcosh\beta_b x_b$$

In a similar fashion to the continuous cross section beam, we need to use boundary conditions to set up a system of equations that are reduced to a frequency equation. The roots of the frequency equation determine the natural frequencies of the beam. Here our boundary conditions are (recognizing that we only need the spatial portions of $w_a(x_a, t)$ and $w_b(x_b, t)$):

At the clamped end, we have no displacement and no slope:

$$Y_a(0) = 0$$

$$Y'_a(0) = 0$$

At the interface between the two sections displacement, slope, bending moment and shear are all equal:

$$Y_a(L_a) = Y_b(0)$$

$$Y_a'(L_a) = Y_b'(0)$$

$$E_a I_a Y_a''(L_a) = E_b I_b Y_b''(0)$$

$$E_a I_a Y_a'''(L_a) = E_b I_b Y_b'''(0)$$

At the free end, we have no bending moment and no shear:

$$E_b I_b Y_b''(L_b) = 0$$

$$E_b I_b Y_b'''(L_b) = 0$$

By solving the spatial functions $Y_a(x_a)$ and $Y_b(x_b)$ for their first three derivatives (with respect to x_a and x_b respectively) and then applying the above boundary conditions we can solve for a characteristic equation in terms of β_a and β_b. In order to solve this characteristic equation for its roots, we need a second equation that relates β_a and β_b. This equation comes from the two beam sections making up a single beam, with a single set of modal frequencies expressed as:

$$\omega_n = {\beta_{a_n}}^2 \sqrt{\frac{E_a I_a}{\rho_a A_a}} = {\beta_{b_n}}^2 \sqrt{\frac{E_b I_b}{\rho_b A_b}}$$

Therefore for each mode:

$$\beta_b = \beta_a \left(\frac{E_a I_a}{\rho_a A_a} \frac{\rho_b A_b}{E_b I_b}\right)^{0.25}$$

Jang has performed this type of derivation and presents a reduced version of the characteristic equation as follows (Jang & Bert, 1989) (note that variable syntax in Jang's solution has been modified slightly here to be consistent with the syntax above):

$$\begin{vmatrix} S1 - SH1 & C1 - CH1 & -S2 - SH2 & -C2 - CH2 \\ C1 - CH1 & -S1 - SH1 & K(C2 + CH2) & K(-S2 + SH2) \\ -S1 - SH1 & -C1 - CH1 & K^2I(S2 - SH2) & K^2I(C2 - CH2) \\ -C1 - CH1 & S1 - SH1 & -K^3I(C2 - CH2) & K^3I(S2 + CH2) \end{vmatrix} = 0$$

Where:

$$S1 = \sin \beta_a L_a$$

$$S2 = \sin \beta_b L_b$$

$$C1 = \cos \beta_a L_a$$

$$C2 = \cos \beta_b L_b$$

$$SH1 = \sinh \beta_a L_a$$

$$SH2 = \sinh \beta_b L_b$$

$$CH1 = \cosh \beta_a L_a$$

$$CH2 = \cosh \beta_b L_b$$

$$K = \frac{\beta_b}{\beta_a}$$

$$I = \frac{I_b}{I_a}$$

We can solve this characteristic equation for its roots and subsequently solve for the corresponding modal frequencies of various stepped beams with unique parameters. Appendix A contains a Maple worksheet that was used for solving for these roots when they were required for the current work.

3.3 Modal Impact Testing

Experimental modal analysis involves exciting a structure and using a transducer to measure its response. The response is then analyzed to estimate modal parameters. Excitation can be provided by a modal hammer (modal impact testing) that excites a wide band of frequencies at the same time or by a shaker that progressively sweeps through a range of frequencies. Typical transducers include accelerometers, strain gauges or LVDT's (Inman, 2001). Modal impact testing and the specific arrangement that was used in the current study are discussed in more detail below.

Modal impact testing uses a modal hammer to supply an impulse force to a specimen. A force transducer on its impact head relays the measured force to a signal conditioner. An accelerometer mounted on the specimen measures its response due to the impact and relays this response back to the signal conditioner as well. The signal conditioner provides a supply voltage to each of the transducers and measures the response voltage. This measurement is amplified and sent to computer software through a data acquisition card, which is connected to a computer. Computer software samples a time series of data from each of the transducers. It then converts the time series data into a frequency response function (FRF) using Fast Fourier Transforms (FFT). It also estimates modal frequencies, modal damping ratios and mode shapes by applying curve-fitting techniques to the FRF. Many texts, including Inman's, go into further detail about modal testing methods and how modal parameters are calculated from measured data (Inman, 2001). Table 3-1 lists the specific equipment used for modal testing in the current study and the schematic in Figure 3.3 shows the equipments arrangement.

Item	Description	Model	Manufacturer
Impact Hammer	2.204 mV/N (Actual) Used for Small Scale Specimens	8206-002	Bruel & Kjaer
Impact Hammer	0.24 mV/N (Actual) Used for Full Scale Utility Poles	086D50	PCB
Accelerometers	100 mV/g (Nominal)	4507-B-004	Bruel & Kjaer
Accelerometer Calibrator	1.0g RMS @ 79.6 Hz	HP 394B05	Agilent
Signal Conditioner	Scadas III (with PQA II Input Module)	SC302VB	LMS
Software	Test.LAB (Spectral Testing with PolyMAX)	Rev. 9A	LMS

Table 3-1 - Modal Testing Equipment Used in Current Study

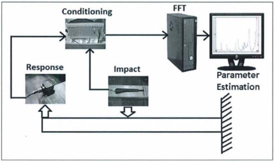

Figure 3.3 - Modal Impact Testing Schematic

Best practices were kept in mind throughout each series of modal tests performed in the current study. There are also many specific technique related notes to be made about how the modal tests were performed. Not all will be discussed in detail, but some of the following are worth mentioning:

- All equipment shown in Table 3-1 (except for the accelerometer calibrator) was newly purchased, and this was the first study undertaken using that particular set of equipment. The sensitivities of the modal hammers were determined through factory calibration prior to purchase. The sensitivity of each accelerometer was determined using the accelerometer calibrator. Those determined values for the accelerometers were double-checked against factory calibration values and were found to be in good agreement. The values determined by the on-site calibrator were used in the current study.
- The modal hammer was always kept as close to vertical as possible during impacts. Double hits, hits that produced a noisy autopower, and hits that did not produce an autopower that maintained at least 80% of its initial value across the band of interest were rejected. An attempt was made to maintain consistent force between impacts as well.
- Voltage ranges were adjusted appropriately so that a reasonable percentage of full scale output was realized for the accelerometers and the modal hammer during each test.
- In general, coherence was monitored and maintained as close to unity as possible, especially near the frequency bands of prospective modes.
- The bandwidth for each test was set at an appropriate level to allow for the desired measurement band to occupy no more than 80% of the entire band. This was done to avoid modes in the high portion of the band to be influenced by the bandwidth filter.
- Sampling rate was automatically set by the software in order to adequately provide a specified frequency resolution. Frequency resolution was set an appropriate level by the user prior to each test and was chosen depending upon the nature of the test.

- Frequency response was averaged over at least five impacts (but usually six) before being analyzed to determine modal parameters. When obtaining mode shapes by impacting multiple locations along a specimen, at least five impacts at each location were averaged.
- Speculation about the nature of a mode was avoided, unless there was sufficient information to identify the mode. For example, if frequency alone was desired for a particular mode, and upon analyzing the frequency response function multiple stable modes appeared within the frequency band of the anticipated mode, then further testing was performed to obtain the mode shape for each of those stable modes in order for the desired mode could be properly identified.
- For cantilevered specimens, torque was controlled using a torque wrench each time the fixed end was secured in its clamp. A level was also used to ensure that round specimens were clamped in the appropriate plane.

In order to enforce some of the above techniques, a display such as the one shown in Figure 3.4 was produced and inspected after each measurement run. Time domain plots for the modal hammer and accelerometer are shown on the top left and right respectively. An overlaid plot of autopower of the hammer and accelerometer is shown on the bottom left. In addition, an overlaid plot of frequency response and coherence is shown of the bottom right. Modal hammer and accelerometer output levels, as well as measurement run data were also provided to the user (but are not displayed in the figure).

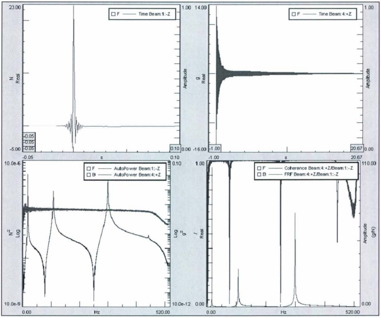

Figure 3.4 - Software Output for Each Modal Impact Run

3.4 Response Surfaces, Regression Models and Design of Experiments

Throughout this study there will be references made to response surfaces regression models and design of experiments (DOE). A very brief introduction to these concepts will be presented here. Further discussion of these topics can be found in many texts including Montgomery's (Montgomery, 2009).

Design of experiments theory lays out an approach for determining the effects of various factors on a response. It was traditionally used to increase agriculture yields. For example if we wished to determine how factors such as amount of water and amount of fertilizer had on a crop yield we could segment our field and apply different fertilizer and water treatments to each segment. Design of experiments theory tells us exactly how many segments are needed and what treatments are required on each segment. By measuring the response (crop yield) for each field segment, we can then use statistical techniques to develop an equation that expressed yield as a function of the factors investigated. This is usually referred to as a regression equation. Shown below is a generic regression equation:

$$Response = f(factor\ A\ , factor\ B\ , FactorC\ \ldots)$$

The design of experiments approach gives us a structured framework for designing the experiment runs, and often the minimum number of runs, required to develop accurate regression equations. It also lets us determine which factors have a statistically significant effect on the responses studied. However, the most important aspect of this approach may be that it allows us to determine how factors interact with one another. For example, if we revisit the crop yield scenario, we may find that water has some moderate effect on yield and fertilizer has its own moderate effect as well. By varying water and fertilizer levels independently, we may be able to estimate the effect that each has on yield. However, if they are used in combination the yield may increase to a level much higher than we would expect based on their summated individual effects. This is referred to as an interaction effect. These interactions show up naturally as interaction terms in the regression equations when using a design of experiment approach. If we express the effect of water as factor A, the effect of fertilizer as factor B, the level of water as X_1, the amount of fertilizer as X_2 and the response (crop yield) as Y we get the equation below (assuming a first order model) where C is the interaction effect:

$$Y = Const + AX_1 + BX_2 + CX_1X_2$$

This type of linear equation is easily obtained by using a factorial (2^k) design. A factorial design allows us to fit a linear regression equation and normally consists of us performing experiment runs where the factors are at all possible combinations of their high and low levels. Fractional factorial designs are also possible, where some subset of the runs required in the factorial design are performed and important factor effects can still be estimated with adequate accuracy.

By plotting the regression equation of a response in terms of two factors, it is easy to imagine that we get a surface. The x and y axes would be reserved for the two factors and the z axis for the response. We could obtain a surface of any imaginable shape depending on how the factors affected the response. However, complex surfaces are harder to develop, require more experiment runs and are not commonly found in most physical systems. One of the most common types of response surfaces is a second order surface that can be obtained using a central composite design consisting of nine experiment runs. The term 'response surface' is often used to refer to a second order surface even though response surfaces can technically be of higher order. A second order regression equation could be of the following form for two factors (X_1 and X_2):

$$Y = Const + AX_1 + BX_2 + CX_1^2 + DX_2^2 + DX_1X_2$$

A generic second order response surface based on the above equation could look like the one shown below:

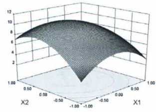

Figure 3.5 - Generic Second Order Response Surface

It is also very plausible to have responses that are affected by more than two factors. This type of response cannot completely be represented by a three dimensional response surface. However, we could fix all but two of the factors and then plot a response surface to show how the response is affected by those two factors alone. In this case changing the values of the other fixed factors would likely results in different response surfaces for the two factors in question.

Note that the commercial package predominantly used in this study to handle DOE calculations and response surface modeling was Design Expert 8. JMP 8 was also used in some instances but to a lesser extent.

Chapter 4

Proposing a Method for Detecting Defects

A somewhat novel approach will be presented here for detecting, quantifying and localizing defects using modal frequency. The method will be presented with the target application being inspection of beams. With a little more development, the method is hoped to be applicable to testing in-service wooden utility poles. However, as will be discussed later, one of its benefits is that it could easily be applied to other applications. As mentioned in Chapter 3 the terms 'frequencies', 'modal frequencies' and 'natural frequencies' will be used interchangeably in this and subsequent chapters and unless otherwise stated they will refer to transverse modal vibration frequencies (as opposed to axial modes, torsion modes etc). This is worth mentioning again because even though the method will be presented here with transverse modes in mind it could very well be applied using any type of vibration mode.

4.1 Introducing the Proposed Method

The method involves first using design of experiments theory to create regression models of multiple modal frequencies of a beam. Each regression model expresses a particular natural frequency in terms of a number of factors that have a significant effect on that natural frequency. The factors could include easily measurable parameters of the beam as well as parameters that are desired to be predicted. If defects are desired to be detected, then their parameters (such as dimensions and location) should be included as factors in the regression models.

Once the regression models are acquired, they can be used to detect defects in other specimens. This involves first measuring the natural frequencies using some experimental technique (such as modal impact testing). The natural frequencies are then used as inputs for the pre-acquired regression models. Any other required parameters (such as overall geometry measurements) are also collected and input into the regression models. The regression models are then rearranged and solved for the appropriate defect parameters. The regression models can only be solved if there are at least as many equations as unknowns. Therefore, the number of defect parameters that can be predicted is limited to the number of modal frequencies that can be accurately measured and the amount of data that is available for fitting regression models. Note that the goal of our defect detection method is normally to identify whether a defect is present, and if so then characterize it in terms of its severity and location. If this is done then the load carrying capacity of the specimen can be obtained by simply applying mechanics of solids methods for the appropriate loading type.

It is important that regression models be an accurate fit to the beam's actual modal behaviour in order to provide good predictions of defect parameters. Since the modal frequencies of a beam are affected by its length, cross sectional area, second moment of area of the cross section, modulus of elasticity and density then any easily measurable parameters that affect the above parameters should be included in the regression models. Note that a significant benefit comes naturally from the design of experiments approach here. We can include any derivative of the factors that are known to have an effect on natural frequency instead of actually having to include the specific factors themselves. For example, a wood beam's density affects its natural frequency but density may be difficult or impractical to measure in the field. However, we know that the density of a beam is affected by its moisture content. Therefore, if moisture content is the main contributor to density variations, and it can be measured easily in practice, then it should be included in the regression models in order to increase their accuracy.

Another benefit to using the design of experiments approach is that it could be applied to complex structures with natural frequencies that are difficult to determine theoretically. The regression models simply have to be developed first by experimental measurements on the desired structure type. It may be useful for quality control purposes as well where products are produced in mass quantities and therefore sacrificing a number of specimens from an assembly line may not be significant if they allow for the development of regression models that can be used for future inspection.

4.2 Illustrating the Proposed Method

To add to the above description we can progress though a couple of general cases in order to illustrate how the proposed defect detection method works.

4.2.1 Manipulating the Regression Equations

Generally, a simple linear regression model with two factors could be of the following form:

$$\omega_n = a_n + b_n A + c_n B + d_n AB$$

Where in this case ω_n is the natural frequency of mode n, a_n is a constant for mode n, A and B are defect parameters (such as defect location and depth for example) and b_n, c_n and d_n are constants corresponding to the effect of these defect parameters on mode n.

We would normally solve for the constants a_n, b_n, c_n and d_n when building the regression models from experimental data. Using the proposed method described earlier to we would take our established regression models and solve them for the defect parameters we wish to predict in other specimens. In this case, we have two defect parameters (A and B) and therefore need at least two equations in order to solve for them. The equations required in this case are:

$$\omega_1 = a_1 + b_1 A + c_1 B + d_1 AB$$

$$\omega_2 = a_2 + b_2 A + c_2 B + d_2 AB$$

Here we have chosen $n = 1$ and $n = 2$ for our two equations. This refers to us choosing to use regression models that reflect the behaviour of modes 1 and 2. Note that we could have chosen a combination of (nearly) any two modes as long as their modal frequencies were measureable and we were initially able to develop their corresponding regression models. Mode number, along with model order, will be discussed further in the next section. For now, we can solve the two equations above for A and B to get the following:

$$A = \frac{c_1 a_2 - a_1 c_2}{b_1 c_2 - c_1 b_2} + \frac{c_2}{b_1 c_2 - c_1 b_2}\omega_1 - \frac{c_1}{b_1 c_2 - c_1 b_2}\omega_2$$

$$B = \frac{a_1 b_2 - b_1 a_2}{b_1 c_2 - c_1 b_2} + \frac{b_2}{b_1 c_2 - c_1 b_2}\omega_1 - \frac{b_1}{b_1 c_2 - c_1 b_2}\omega_2$$

We are now left with explicit equations for the defect parameters A and B in terms of regression model constants and the first and second modal frequencies. In practice, we could now take a specimen, measure its first and second modal frequencies experimentally and solve for its defect parameters according to the above equations.

Note that this is a very simple case and is only intended to help demonstrate the suggested procedure for detecting defects. The linear models, as we will see later, are not actually indicative of typical modal behaviour. In addition, it may be very difficult to find explicit equations for defect parameters if the regression models are of higher order. Numerical solvers would likely have to be employed for most practical cases.

4.2.2 Visualizing the Solution

In order to provide a visual demonstration of how the method works we can plot two simple regression models as response surfaces. The two regression equations obtained from experimental data could be as follows:

$$\omega_1 = 4 + 0.1A + 0.3B$$

$$\omega_2 = 7 - 0.6A + 0.2B$$

The response surfaces corresponding to the above equations would look like the ones shown in Figure 4.1.

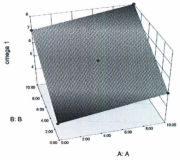

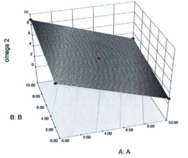

Figure 4.1 - Simple Planar Response Surfaces

Note again that planar surfaces are not indicative of actual modal behaviour and are only used here out of convenience in order to demonstrate the procedure.

Say, for example, that we experimentally measured two modal frequencies $\omega_1 = 6$ and $\omega_2 = 8$. It may not be immediately intuitive but for this case there is only one combination of factors A and B that can accommodate those (or any two) frequency measurements. To demonstrate that this is indeed the case let's first find all the values of A and B that satisfy the condition $\omega_1 = 6$. This can be done by simply intersecting a horizontal surface at $\omega_1 = 6$ with the 'omega 1' response surface in Figure 4.1. The line that lies along the intersection of these planes is therefore made up of all A and B combinations that satisfy $\omega_1 = 6$. The projection of the resulting line on the A-B plane is shown below in Figure 4.2. This can also be thought of as a contour line of the 'omega 1' response surface at $\omega_1 = 6$.

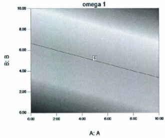

Figure 4.2 - Contour Line of 'omega 1' Response Surface

The line above has been projected onto the A-B plane to show the A and B combinations that satisfy $\omega_1 = 6$. Since the A-B plane is common between both response surfaces we can take the above line and apply it to the A-B plane of the 'omega 2' response surface in Figure 4.1. From the 'omega 2' response surface we now have to find out which of the A and B combinations from this contour line satisfies $\omega_2 = 8$. To do this we can simply project this line up onto the 'omega 2' response surface. We can imagine that this projection creates a new line in the three dimensional 'A-B-Omega 2' space. We can also imagine that this new line will pierce a horizontal $\omega_2 = 8$ plane at only one point (assuming that this new line is not parallel to the $\omega_2 = 8$ plane). The [A,B] coordinates of this point of this piercing corresponds to the A and B combination for our solution.

A slightly easier way to visualize the solution may be to make contour lines on the A-B plane for each of the two response surfaces at their respective measured frequencies. Since the A-B plane is common between the two response surfaces, we can plot the contour lines together on the same axis. The [A,B] coordinate where the contour lines intersect represents the solution to the regression equations. In addition to demonstrating how the method works this approach is suggested as a graphical method for solving the regression models in practice and is shown in Figure 4.3 for the above problem.

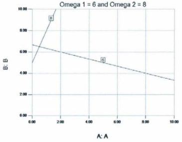

Figure 4.3 - Graphical Method of Intersecting Contour Lines

4.3 Sensitivity and Errors

Consider again the example and explanation from section 4.2.2. The existence of a unique combination of A and B that meets the requirements of the two measured natural frequencies seems to have an exception, to which we have already alluded. This exception occurs if the new projected line in three-dimensional 'A-B-Omega 2' space (that was said to pierce the ω_2 response surface at one point) were parallel to the $\omega_2 = 8$ surface (i.e. if it were horizontal). In this case, there would either be no solution (if the projected line were offset from the $\omega_2 = 8$ surface), or an infinite number of solutions (if the projected line was coincident with the $\omega_2 = 8$ surface). We can also think of this as the two contour lines in the graphical solution being parallel or coincident. However, if for a moment we think back to what the 'omega 2' response means we can determine that this exception would never be an issue. The projected line would only be horizontal if the response surface itself was horizontal, and if the response surface itself was horizontal then it would not have been created in the first place since the response (i.e. ω_2 in this case) was not significantly affected by either of the factors (i.e. A and B in this case). Note also that by the same logic if a response surface is horizontal with respect to one of its factors (and not the other), then that factor's effect is not significantly affecting the response and can therefore be eliminated from the model. The problem then becomes one-dimensional and the remaining significant factor can still be predicted using one regression model and a single measured frequency.

The above rebuttal against the potential exception to the existence of a unique solution may seem unnecessary; however, it does serve as a prelude to some actual concerns. If a planar response surface is angled only slightly away from horizontal then its factors have very weak effects on the response. Considering the example of section 4.2.2 again this would mean that A and/or B have only a weak effect on ω_1 and/or ω_2. In this case, even if the data used to obtain the regression model was obtained very carefully allowing for an accurate portrait of actual modal behaviour and a very high R^2 value, small errors in measuring the frequencies of a test specimen could be projected into large errors in prediction due to the shallow response surface. This illustrates that strong factor effects are desired in order to obtain accurate predictions.

4.4 Independence of Responses

Since we plan to use a system of equations to solve for unknown defect parameters, it follows naturally that those equations should be independent. Because we are obtaining our equations by fitting regression models to experimental data there will naturally be some error involved in the coefficients of each equation. If an insufficient number of runs are used to fit systems that have a large amount of variability, we may even get an inconsistent set of individual terms showing up as significant in the models depending on the data that is obtained. Choosing a different model order and significance threshold for use in regression may even result in slightly different models from the same data set. Because of this, physical responses that are actually dependant may actually result in algebraically independent equations. This should be taken into consideration when attempting to use a set of equations for prediction. Two equations that appear 'nearly dependant' (or conversely 'loosely independent') should be approached with caution. If two equations have common terms, and the ratio of coefficients are nearly the same between terms, then the equations could actually be representing dependant responses in the physical system. In this case, a graphical approach of overlaying contour lines may result in two (or more) lines that are nearly the same shape and run almost parallel to each other. Even though they may intersect at a certain point that represents a legitimate algebraic solution to the system it should be understood that this solution is illegitimate due to the responses involved being dependant in the actual physical system. This is one of the reasons why the numerical and graphical approaches should be used in conjunction while making predictions.

4.5 Issues with Higher Order Linear Regression Models

Up until now, we have considered only first order linear models for purposes of illustrating the suggested defect detection method. Other issues arise if we have higher order models. An example of a higher order linear regression model could be the following second order model:

$$\omega_n = a_n + b_n A + c_n B + d_n AB + e_n A^2 + f_n B^2 + g_n A^2 B + h_n AB^2$$

Where again in this case ω_n is the frequency of mode n, A and B are defect parameters and a_n... h_n are constants obtained in developing the regression models from experimental data.

4.5.1 Extrema Considerations

Higher order models are likely to contain a number of extrema and any extremum point becomes horizontal by its nature. Areas close to these points are also nearly horizontal. Therefore, an issue similar to the one described in section 4.3 for weak factor effects arises; near each extremum point, exists an area with potential for higher error in prediction. In general, as mentioned in section 4.3, if any response surface has areas that are nearly horizontal (i.e. where factor effects are weak) then prediction is expected to be less accurate in those areas due to the significance of errors in measurement becoming relatively higher. For higher order models, these horizontal areas will be present at various locations depending on where extrema exist in the models themselves. This will be discussed further in section 4.6.4 as it relates to actual vibration modes.

4.5.2 Dealing with Multiple Solutions

By extending our scope to models of higher order, we also introduce the possibility of multiple solutions emerging from the proposed defect detection technique. Determining which solution relates back to the actual defect conditions of a test specimen is of great importance and will be addressed here.

First it will be noted that when developing regression models we specify upper and lower limits for each factor level and within this range lie all of the design points from which our models are derived. Therefore, as with any curve-fitting scenario, we should be cautious of problems that may arise when making predictions outside the range of our data set. Obviously, our regression model may not be accurate if we are extrapolating solutions outside of this range. The actual behaviour of the physical system may be inconsistent with the behaviour of our model outside of the considered design space, and therefore making predictions outside of the design space is somewhat reckless, and should be avoided whenever possible. However, the main focus of this argument as it relates to the current section is that extra solutions may exist outside of the design space and these extra solutions should be the first omitted from consideration when attempting to make predictions of defect parameters from a potential set of multiple solutions. Solutions outside the design space should be considered suspect for multiple reasons. First, consider the graphical approach of overlaying contour lines. Extrapolation may cause errors large enough that contour lines redirect and intersect at solutions outside of the design space where solutions would not otherwise exist. Even if the models were accurate for some portion of space outside of our design space we may get solutions that do not even physically make sense. For example, predicted defect sizes could be larger than the specimens themselves, or defect location could be past the limits of the specimen's geometry. By being aware of these issues, we may be able to filter out some obvious incorrect solutions.

In order to actually solve our regression equations for a finite number of defect parameter solutions, we need as many regression equations as we have defect parameters to predict. If one or more of these regression equations is nonlinear, we may end up with multiple solutions that do lie within our design space. In this case considering extra regression models (that define the behaviour of other vibration modes) will aid in narrowing in on the correct solution. This can be done in many ways:

- The defect parameters from each predicted solution can be fed into the extra regression model and then that regression model can be solved for its corresponding response (the response being modal frequency in our case). This calculated response can then be compared to the actual measured frequency of the extra mode being considered and the agreement should be substantially better for the correct solution. Note that this agreement will not generally be exact due to errors involved in experimentally measuring the modal frequencies that were used in fitting the regression models themselves as well as measuring those used for prediction. The regression models will also have extra error related to its goodness of fit.
- Numerical optimization built into some design of experiments software will not only allow us to automatically solve for the original solutions based on the minimum number of responses but also allows us to add extra responses that we can use to eliminate multiple solutions. The software will numerically solve for the solutions that best satisfy each of the specified responses (including the extra, added response). Each response can even be weighted so that we can better maintain the initial solution values by adding higher weight to the responses that were used to get the original set of multiple solutions. Each solution can be returned with a desirability value associated to it. The correct solution will have a distinctively higher desirability. It is even possible to plot solution desirability over the entire design space to visually show where the most desirable solutions lie.
- The graphical approach from section 4.2.2 can also be employed to distinguish between multiple solutions. By simply adding the extra contour line (from the added response) to the plot and observing which of the solutions it intersects, we can determine which of the

solutions is correct. Note again that the errors involved will make this approach non-exact. The extra contour line will not generally intersect exactly at the correct solution, but it should be noticeably closer to the correct solution than any other solutions.

This process of adding extra regression models to eliminate multiple solutions will be demonstrated in Chapter 5 as we progress through various validation examples. It is expected that in most practical cases we will need to consider $n + 1$ regression models if we wish to predict n defect parameters. In this case, we may still get multiple remaining solutions, but by continuing to add extra responses, we should eventually arrive at a definitive solution. Note that in anticipation of having to deal with multiple solutions in this manner we should consider $n + 1$ as the minimum number of regression models that are required for prediction prior to developing the models. We can then ensure that an appropriate number of design points and responses are considered upfront.

Multiple solutions can sometimes arise when a single defect condition can actually be defined in a number of different ways. For example, consider a beam with two defect parameters. 'A' defines the location to the center of a defect and 'B' defines the length of the defect. It is easy to imagine that if the defect happens to occur at either end of the beam there may be multiple [A,B] combinations that are valid for defining the defect. Actually, there will be an infinite number of valid solutions. This is shown in Figure 4.4. The [A1,B1] combination on the left of the figure can be considered as the simplest form. However, there are an infinite number of equally valid [A2,B2] solutions as well. We will have to deal with a similar scenario in section 5.3.

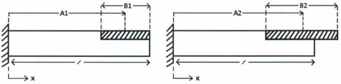

Figure 4.4 - Defining a Single Defect in Multiple Ways

Note that this type of multiple-solution scenario is distinct from the earlier case where we discussed omitting solutions that occurred outside of our design space. In this scenario we may consider the dimension A to be anywhere along the length of the beam. The [A2,B2] solution above demonstrates that a defect can extend past the limits of the physical system even though the defect parameters are within the limits of the design space.

One approach to dealing with this type of situation may be to use a design space with non-constant factor ranges. This type of design space is depicted in Figure 4.5. Here the range of possible A values would be dependent upon the value of B. Note that if we considered defects so large that they extended the entire length of the beam (so that B=l) this design space would actually become triangular. This approach involves actually modeling our response surface to fill only the necessary design space despite it being somewhat irregular. However, this approach may not be possible in some commercial DOE software packages. An alternate approach would be to simply recognize by inspection whether or not a particular solution creates a defect that extends beyond the physical limits of the system and then manually deduce the simplest possible form of the solution. This calculation would be straightforward.

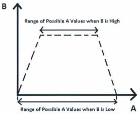

Figure 4.5 - Design Space with Non-Constant Factor Ranges

4.6 The Behaviour of Actual Vibration Modes

Up until this point, we have considered the approach in very general terms and assumed that we have no prior knowledge of how actual vibration modes behave. This assumption is not strictly true. Here we will discuss some issues that arise when applying the method using actual vibration modes as our responses.

4.6.1 Independence of Modal Frequencies

In section 4.4, we discussed that all responses should be independent in order to be used in the suggested method of defect detection. Therefore, it is required that regression models for our actual modal frequencies be independent. Note that a distinction should be made between modal frequencies being independent and the independence of regression models where modal frequencies are considered as the response. For a given physical system (with fixed parameters), the theoretical modal frequencies are obviously linked to each other though a common characteristic equation from which they are all derived. With respect to our defect detection method, each modal frequency should respond to changes in the varied defect parameters in an independent manner. This is a fundamentally different matter.

It will be demonstrated in Chapter 5 through validation examples that modal frequencies are actually independent in this sense. For now, we will simply give justification for why this should be the case. Take, for example, a beam with a single defect parameter: the location of a crack. Though various works that have been cited in the literature review of Chapter 2 we know that as a defect nears a modal node its effect on frequency is diminished. This is due to lower stress occurring near modal nodes of a vibrating specimen. As discussed, many authors view this occurrence as a downfall of using frequency as a defect detection parameter; it essentially masks the effect of defects that occur near a node for any particular mode in question. However, for our case it insures that the response of each mode is independent with respect to our defect parameter (change in crack location) because each mode shape is unique and has a different number of nodes at varying locations.

4.6.2 Required Regression Model Order and Number of Design Points

In order to accurately capture the trend of each mode as it relates to the factors being considered we must ensure that an adequately high model order is used. Different defect parameters may require different model orders in order for their effects to be accurately modelled. The model order required for some parameters may also be dependent upon the vibration mode considered. As we discussed in section 4.6.1 the effect of defect location on a particular modal frequency is dependent upon the mode shape and number of nodes associated with that mode. Therefore, we expect that the profile of a response surface will show oscillation with respect to the effect of defect location. Required model order will increase for higher modes in this case. The model order required to capture the effects of defect severity may be dependent upon the geometry of the defect being considered. For example modelling the effect of changing the radius of a circular defect will be different from modelling the effect of changing the length of a rectangular defect. This is expected simply because the area of a circle changes with the square of the radius (as opposed to the first power of length for the rectangular defect). The second moment of area will also change in a different manner for each defect type. For each case, these differences will simply be reflected in regression models by following the standard procedure and will not have to be directly attended to by the user.

Traditional two-level factorial and second-order response surface designs, as we will see, are often inadequate for capturing the behaviour of modal frequencies as they relate to defect parameters. Therefore, some rough guidelines for a space filling approach will be suggested here for determining the model order and number of design points required to create our regression models. The aspects of this approach will be demonstrated through various validation examples in Chapter 5. Before presenting the approach, note that the focus of the current body of work is simply to demonstrate and validate the proposed method of defect detection using modal frequency measurements. This work does not attempt to derive design of experiments theory and these rough guidelines will likely not dictate the most efficient method for fitting the complex regression models that are involved. These guidelines are suggested only because they have been found by the author to work well in practice. Future work may significantly reduce the required number of design points by using some subset of the overall set of design points suggested here and perhaps by better positioning them within the design space.

4.6.2.1 The Order of Individual Effects

Before attempting to develop our regression models, we first need to determine the model order required to capture the effect of each individual response. This is done by simulating closely spaced design points in a finite element environment and meshing them together to create single response plots or response surface plots. These plots can then be examined to determine the typical number of inflection points that occur with respect to each factor. Considering the cross section at various locations of response surface plots can be useful for this purpose. Once we know the number of inflection points that are typical for each factor considered, two design points are required for each section of the curve between those inflection points. If there are no inflection points, we can consider a first or second order model (requiring two or three points respectively). This suggested method for choosing the number of design points to use in modelling is demonstrated in Figure 4.6. Note again that these are only suggested guidelines.

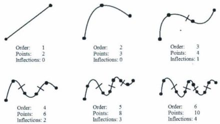

Figure 4.6 - Number of Design Points Suggested to Fit Models of Different Order

It is common knowledge, however, that in polynomial interpolation we can use n points to fit a polynomial of order $n - 1$ (Chapra, 2005). This is shown up to order 4 in Figure 4.7.

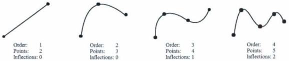

Figure 4.7 - Fitting Polynomials to Minimum Number of Points

The number of design points suggested for fitting curves up to third order is the same as the minimum number required. For every increase in required order, above third order, the suggested number of design points is increased by two (instead of the minimum of one). Note that including extra design points does not necessarily mean that we will use the extra points to allow fitting of a higher order model than is required to capture the effects of the physical system. It is widely known that fitting models of higher order than required, at least in the case of single factor polynomials, can result in oscillation and large errors through Runge's phenomenon (Chapra, 2005). The curve fit will be a best fit to the extra data and will not generally pass directly through each design point in this case. The extra points are suggested in part because we will not know the ideal positions at which to locate a minimum set of points. Because we will not generally know the optimum location for a minimum set of design points, and to avoid uneven weighting of points throughout the design space that may favor one region over another in terms of predictive power, design points will be positioned in an even distribution throughout the space.

The shape of a response with respect to any single factor may change as the values of other factors change. This will happen when interaction effects are significant. Therefore even if an ideal set of design point locations was established for modeling each factor that set would only be valid while all other factor levels are constant.

In addition we may end up with a situation similar to the one shown in Figure 4.8. The figure shows the same curve attempting to be fit to a minimum number of design points and an evenly distributed set of design points.

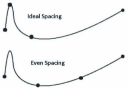

Figure 4.8 - Demonstrating the Merit of Extra Design Points

It's easy to imagine that the minimum number of points would be adequate for fitting the curve if the points were ideally spaced. However, if we use an even distribution of the same number of points we would likely not get an accurate curve fit. The suggested number of design points is only modestly above the minimum number required and will not allow for an ideal fit of any possible curve, but it should help to mitigate the demonstrated problem when it occurs with moderate severity. Using extra design points also helps to mitigate the effect of experimental random error on the accuracy of the fitted regression models. The suggested number of design points essentially represents a balance or appropriate middle ground between accuracy and resource expenditure when developing the regression modals.

4.6.2.2 The Overall Model Order

Once we know the number of design points required to accurately fit each individual factor effect we can simply take their product as the overall required number of points to fit the regression models. In other words for n factors each with N_i required design points (where

$i = 1 \dots n$ and refers to the mode number) we can find the overall number of required design points N_{total} as follows:

$$N_{total} = N_1 * N_2 * N_3 \dots * N_n$$

For example if we are investigating two factors with the first factor (factor A) requiring six design points and the second factor (factor B) requiring four design points. Our two dimensional design space would then be made up of twenty-four evenly spaced design points in a six point by four point mesh. This is demonstrated in Figure 4.9. By even spacing here we mean that points are evenly spaced with respect to other points in the dimension of each individual factor. Obviously each factor in the space may be scaled individually resulting in a space that appears uneven between dimensions (in other words a point may not appear equidistant from the next closest point in either direction but all points lying on any linear path will have equal spacing). Note again that in the figure each point represents an [A,B] combination that would be used when performing an experiment run. Each experiment run is done to determine the response at that particular set of factor levels. In the figure the response would be measured along the z-axis which would be coming out of the page. By measuring the response at all these points we can fit a surface. This procedure, while not as easy to visualize, remains valid when considering more than two factors.

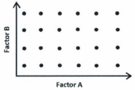

Figure 4.9 - Example Six by Four Design Space

4.6.3 Splitting the Design Space

Some commercial design of experiments software packages, including the one predominantly used in this study, have an upper limit to the model order that can be used when developing regression models. If this maximum available model order is insufficient for the particular system being considered then we have the option of splitting the design space into sections. It will be suggested that an extra design point be granted to each factor that is split by this method. The extra point can be thought of as added at the interface between the new design space segments where the design space has been split. For example consider the six by four point design space considered in section 4.6.2.2. If the factor that required six design points cannot be accurately modeled due to software constraints then we can add an extra point to that factor and split the design space into two separate four by four segments. The extra point is added at the interface between segments and is therefore shared by each segment so that the overall space remains continuous. Each segment should then be modeled individually and will require a lower model order than the original design space. The locations of the design points can be adjusted so that they remain evenly distributed after the addition of the extra point. This splitting process is demonstrated in Figure 4.10.

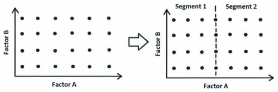

Figure 4.10 - Splitting a Design Space to Accommodate Software Constraints

Multiple splits may be required for complex problems that consist of a variety of high order factors. When using this splitting method all individual design space segments will have to be analyzed for each response whenever the models are being used for prediction of defect parameters. When using the graphical method of overlaying contour lines these segments can simply be positioned next to each other in order to show the entire design space.

4.6.4 Choosing Which Modes to Use for Prediction

As was discussed in the literature review of Chapter 2 higher modes are more sensitive to defects. Therefore, in the spirit of trying to use factors with strong effects we may be inclined to choose higher modes to use for defect detection. However also mentioned in the literature review was that higher modes are harder to measure accurately through experimental means. This would affect the accuracy of developed regression models as well as the accuracy of experimental measurements made for prediction purposes. In addition, factor effects become progressively more complex and therefore the number of design points required to develop regression models becomes increasingly prohibitive for higher modes. These issues tend to lead us towards choosing the lowest ranked set of modes possible that would allow us to make accurate predictions.

A fact also mentioned in the literature review is that modal nodes seem to hide the effect of defects located near them. Higher modes would obviously contain more of these problem areas. However, our modelling process accommodates for this problem by considering the combined effect of multiple modes simultaneously. One issue remains though relating to the sensitivity issues raised in sections 4.3 and 4.5.1. We must be aware of where extrema and other regions of weak factor effects are located within the design space of each response.

With these issues in mind, a somewhat algorithmic approach can be suggested here for choosing which modes to use for prediction. Generally, we would only develop regression models for the minimum number of responses necessary to make definitive predictions. It was suggested in section 4.5.2 that $n + 1$ regression models are required if we wish to predict n defect parameters. Several ways were also suggested for how the extra model could be used for making predictions. Keeping those methods in mind it will be suggested here that to make the best use of our $n + 1$ models we would first make a prediction for the defect parameters using all of our available models without giving precedence to either individual mode. This means that we would use equal weighting in our numerical optimization. When using the graphical technique we would also estimate an equally weighted solution since we will not typically get the contour lines of all of our $n + 1$ modes to intersect at exactly the same location. However, as mentioned earlier, it should be obvious that they are close to an intersection point and their deviation from true intersection will be dependent upon experimental error and the goodness of fit of the regression models. In this case, we would pick a point based on inspection, which is close to where a true intersection point is thought to be, as demonstrated in Figure 4.11 for some hypothetical system.

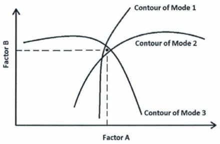

Figure 4.11 - Choosing an Estimated Intersection Point Using Graphical Method

Once we have an estimate of our solution we can then inspect each of our regression models to determine if this solution lies near any maxima or other areas that are expected to have low accuracy. If we find that the solution does lie in an area of concern for one of the modes used then we can re-evaluate our solution with that in mind. For numerical optimization we can apply custom weighting so that the modes with the best expected sensitivity, in the general region of design space near the solution, are more heavily favored. Using the graphical approach we can also adjust our estimate of factor levels accordingly. We can shift our estimated intersection point towards, or even so far as to be at, the actual intersection of the contour lines of the best modes. In this case the extra mode is still required to isolate the correct solution from multiple solutions that may lie within the entire design space. However, it does not necessarily have to be considered with respect to estimating the actual numerical values of predicted factor levels at any particular solution.

The accuracy of each regression modal will vary within different regions of the design space depending on how strong the factor effects are in each region. Each model's accuracy will be higher in certain regions and those specific regions will vary between models. Naturally weak factor effects as well as poor model fit may both contribute to design space regions where we get poor predictions. The overall accuracy of different regions of the design space, when considering all modes used for prediction, may vary depending on the nature of the structure being studied. It would be of interest to identify the accuracy of each design space region, and we will attempt to do this for one of our validation studies in section 5.2.3. We will see that defects occurring in different design space regions will result in the contour lines of some modes being visibly better. Thus the act of choosing which modes to use for prediction, at least when using the graphical method, will become somewhat straightforward.

4.6.5 Supplementary Factors and Developing Accurate Regression Models

So far, we have focused on including the defect parameters that we wish to predict, such as defect location and severity, as factors in our regression models. However, in many applications it may not be valid to assume that all specimens are identical on all measures other than the parameters required to characterize a defect. Regression models with modal frequency as their response need to be an accurate fit to the modal behaviour of the actual specimens considered. As demonstrated in sections 3.1 and 3.2 modal frequencies are functions of geometry as well as density and elastic modulus. Defects in this study have primarily been associated with localized changes in geometry alone with the assumption all other factors including overall geometry are otherwise constant between specimens. However, if the overall physical dimensions of a specimen are subject to change then the parameters that characterize those dimensions should also be included as factors in the regression models since they will have some significant effect on the response. In addition, if any other factors such as density or stiffness are variable then they should be included as well. As mentioned earlier the method is somewhat flexible and parameters that are more easily measurable can be used in place of density and stiffness as long as they are the underlying cause of the density or stiffness variation. The example that was used earlier for wood specimens is that if moisture content is the cause of variation in density then it can be included in regression models instead of density. This makes the procedure more practical since moisture content is far more easily measured than density for large and secured structures. We can assign the label 'supplementary factors' to those factors which are required for obtaining accurate regression models but do not characterize defects. The regression models would assume the following general form when supplementary factors are included (where ω_n is the natural frequency of mode n):

$$\omega_n = f(Defect\ Parameters, Supplementary\ Factors)$$

Supplementary factors would typically be easily measured and supplied as inputs to the regression models prior to any predictions being made. By measuring supplementary factors first, the regression models can be reduced to a form where only modal frequencies and desired defect parameters are the unknowns. Defect parameters would then be estimated in the usual way using experimental modal frequency measurements to solve the system of regression equations.

4.7 Choosing and Controlling Factors

The choice of which factors and how many modes to include when developing a set of regression models is very much dependent upon the specific application. It may not be necessary to include a comprehensive set of factors that affect frequency response if in the desired application some of those factors are known to be controlled. In most cases, a minimum set of factors is desired because of the time and resource savings that accompany a reduction in experiment runs.

In some situations the actual development of regression models may also be complicated somewhat because one or more factors that need to be included in the models are not easily controllable. In this case only experiment runs at random factor levels may be available. This may make the design space uneven resulting in some areas having better prediction power than others. In general, if naturally occurring defects are not easily introduced in a controlled manner, such as with closed or internal cracks for example, then only the data that is obtained from specimens with naturally developed defects may be available for fitting regression models. On one hand the behaviour of these specimens, on an individual basis, would likely better represent the behaviour of in service specimens because their defects are naturally developed, as opposed to artificially introduced in an idealized manner in the lab. However, depending on the available distribution of naturally occurring defects the resulting regression models may be biased in favour of certain regions. Predictive power may be better for small, intermediate or extreme defects. For example, if only severely defected specimens are identified and removed from service for assessment, and subsequently used in developing regression models, then those regression models would likely turn out to be very well fit in the regions of design space corresponding to severe defects (assuming that random error and random variation is consistent throughout the space). Other regions may conversely have a less than ideal fit. However, it may be desired that the method ultimately be used to identify specimens early in their deterioration phase when defects are smaller and less obvious. In this case, the resulting regression models may not be best suited to the desired application because of the restriction of not being able to control defect parameters during their development.

We will not attempt to dictate here the best statistical practices for developing regression models with non-controlled design points. That is an issue somewhat outside the scope of the current study. However, we should keep in mind that in some practical applications data may come from production line rejects or specimens removed from service and therefore in order for the proposed defect detection method to be applied we may need to compromise on best model development practices and use whatever data that may be available.

4.8 Potential Applications

As mentioned earlier the above defect detection method has been developed with the end goal in mind of assessing the condition of in-service wooden utility poles. However, an effort has also been made to present the method in a very general way so that it is be applicable to a broad range of applications beyond pole testing. Here we will consider some of those other potential applications.

Identifying cracks in beams or structures is an obvious and widely studied application. The proposed approach could be applied to many different structure geometries. Geometry parameters that vary between specimens would simply have to be included as supplementary factors in the regression models. Since the models are obtained from experimental runs and designed for the each specific application, they can easily handle geometries where calculating theoretical modal frequencies may be difficult. Even non-ideal end conditions are automatically accounted for in the models, and do not have to be considered on a theoretical level.

Quality control on a production line would be an ideal candidate for modal testing. Since the goal is often to make every unit identical (or at least within manufacturing tolerances) they should all have the same material properties and geometry. Therefore, they should all theoretically have the same modal frequencies. For a simple approach, we could gather modal data from a number of random samples. Random samples are regularly pulled from production lines for quality control anyway and gathering the modal data would just be one extra step in the process. We could develop mean and standard deviation values for one or more modal frequencies from those test specimens. We could also determine frequency thresholds for what constitutes an acceptable specimen (since each specimen removed from a production line would also be subjected to other tests that asses condition). Once we obtain these thresholds, automated non-destructive modal tests could be carried out on each specimen that passes through the production line. Note that some existing software already automates the process of choosing modes and estimating parameters from frequency response functions. Therefore, the technical challenges involved in developing completely automated modal testing equipment seem somewhat modest. Specimens with either modal frequency outside of its established threshold could be automatically ejected from the line. In order to determine specifically whether the problem was inappropriate density, geometry or material stiffness we would have to develop models reflecting how those parameters affect multiple modal frequencies (as per this chapter's proposed method). Using this simple approach, the actual problem with each specimen would not necessarily be known. However, a greater quantity of defected specimens should be ejected from the production line, and those ejected specimens could subsequently be subjected to existing or alternate quality control tests in order to determine the specific nature of each defect. In this case, modal testing would initially be installed in parallel with existing quality control techniques. Upstream and downstream random samples could be removed from production and tested using existing techniques in order to assess the effectiveness of modal testing. If a significant improvement in the quality of samples downstream of modal testing was realized, then some quality control efforts could potentially be shifted away from testing only a truly random sample of specimens (which normally involves destructive testing of many intact specimens and is inherently wasteful in terms of labour and lost merchandise). More effort could be allotted to testing known defective samples that were ejected by modal testing. By testing more known defective samples, we would get a better idea about which types of defects occur most often. Focus could then potentially be shifted towards making appropriate changes in the manufacturing process in order to mitigate the occurrence of specific regularly occurring defect types. This has the potential to improve overall product quality and better streamline quality control efforts.

Some manufacturing processes may be inherently prone to certain defect types. If so regression models could be used to capture the behaviour of those specific defect types. For example, if we are attempting to make castings, the overall dimensions may be fairly consistent (allowing them to be omitted from the regression modals), and we may be able to easily inspect the surface for defects. However, the interior of castings may be prone to voids or inclusions. In this case, the location and extent of voids could be included as factors in our regression models and predicted using the proposed method. It is possible that simply weighing a specimen in order to determine its mass will give some indication about whether voids are present in a casting. This has its own merit but it also means that we could characterise a defect as a localized loss of mass. The specimens could then be weighed and their corresponding mass could be input into the regression models in the regular way. This would allow us to obtain models that are more accurate. It could also allow us to use fewer regression models and simplify our approach if mass alone is considered adequate for characterising defect severity. Material from specimens with inappropriate mass may normally be melted down and reintroduced in future castings without actually determining where the void existed. However if, in addition to severity, the location of a void could be determined through modal testing then it may be possible to identify areas in the part that are prone to voids. This could lead to ideas about how to change the casting process or mould design in order to avoid future problems. One downfall with this approach is that regression model development may be difficult depending on the scale and material of parts. Defect extent and location would have to be determined for defective parts through dissection or some other means in order to obtain data that could be used for model development.

The factors predicted using the proposed method do not necessarily have to be related to a defect such as a void, crack or other compromise of structural integrity. With a little imagination, we could expand this method to fit many other applications. For example, if we had a pipe that was prone to clogging we could potentially use this method to locate a blockage. Since the blockage would add a somewhat localized mass to the pipe, it would affect the pipes modal frequencies, since they are dependent upon density. In this case, we could develop regression models to predict two factors: blockage location and extent. If the pipe were drained this would simply be a matter of localizing the added mass of the blockage in the above manner. However, if the pipe were not drained this method could still be applicable. The density would be somewhat constant along the section of pipe upstream of the blockage (since it would still be full of fluid), and after the blockage the density would abruptly decrease by an amount dependent upon the extent of the blockage. Models could still be developed in this case for blockage location and extent because of this change in density. The regression models would be distinct, and not interchangeable between the two cases (drained and un-drained), but the general procedure could likely still be applied in either case.

The above examples represent a small number of applications that may be appropriate for applying the proposed defect detection method. It is easy to imagine that there are still further applications that would be well suited, if a little creativity was employed in choosing factors.

4.9 Distributed Damage and Real World Concerns

The proposed method should be well suited to applications where continuous numerical factors are able to adequately define a specific irregular geometry such as the location (in one, two or three dimensions) and extent (diameter, width, length etc.) of one or more cracks or material voids. It could even be applied to locating localized reductions in density or stiffness. Models and factors would just have to be tailored to meet the needs of the specific application. However, if damage is not localized but rather a continuously varying level of deterioration over the entire specimen then the problem is somewhat more complex. We raise this issue here to bring into light that while the proposed method so far has been very accommodating to a wide spectrum of applications it does have some limitations. Real world applications are continuous and do not always include defects that can be defined using step changes in parameters.

As mentioned earlier this method has been developed with an end goal in mind of testing in-service wooden utility poles even though that particular application is perhaps a less than ideal fit to the existing form of the method. With wooden utility poles, many complications and practical challenges arise. Individual poles are of varying length, diameter and taper making supplementary factors necessary in the regression models. In addition, the state of deterioration is not likely to be a step change in one or more parameters. It is more likely to be a continuously variable level of deterioration along the pole. Other factors such as density may also be variable along the poles length. This issue of continuously variable (or distributed) factors lies on the boundary between current and future work. It will be discussed further in Chapter 6 (as it relates to pole testing) and section 7.2 (as it relates to future work). Some suggestions will also be made for how this issue may be handled with further development of the proposed defect detection method.

Admittedly, there are limitations to assessing damage condition using the current form of the proposed method, and further work is required to expand its scope before it can be used in many real world applications. We will nonetheless first focus on validating it for simple cases. In Chapter 5 we will use the proposed technique to determine the location and severity of various controlled defects in beams.

Chapter 5

Validating the Proposed Method for Detecting Defects

In order to validate the defect detection method that was suggested in Chapter 4, we will first present some example scenarios involving unique geometry and defect parameters. Each scenario will then be investigated further by applying the proposed method to theoretical, finite element and/or experimental models. Since the method has already been well explained in Chapter 4, only somewhat modest explanations of method and technique will be provided throughout these examples. For each example, the method will be employed as it was presented in Chapter 4 unless otherwise stated. Since the goal here is simply to assess whether the proposed method is useful for predicting the presence of defects in controlled conditions, supplementary factors will not generally be considered in the following examples. However, the importance of accounting for supplementary factors in many practical situations is nonetheless recognized.

5.1 The Two-Factor Beam

Part of our focus is to investigate how modal testing could be used to detect hidden defects in utility poles. The first example, which we will refer to as the 'two-factor beam', will therefore include a simplified version of a typical type of hidden defect found in utility poles. As can be seen in Figure 5.1, ants (in addition to rot) can penetrate poles and deteriorate the center of their cross section. This can start at the ground line and extend to various heights up the pole.

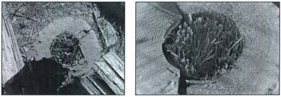

Figure 5.1 - Utility Poles with Ant Damage (Haldar, 2003) (Haldar & Tucker, 2006)

The first example will therefore be a cantilevered beam with defects appearing as holes of varying diameter and depth. The holes will start at the clamped end and penetrate lengthwise along the centerline. Since we will later try to validate this example experimentally, we will choose the beam's cross sectional geometry to be the standard lumber size of 3.5 in x 3.5 in for convenience (a nominal 4x4 post). The defect factors to be predicted are defect diameter and defect length.

Note that modal frequencies and strength in bending are each directly related to the second moment of area of a pole's cross section. Note also that defects located near the center of a pole's cross section will have a less significant effect on these properties than defects located near the surface, since they are closer to the neutral axis. The reason for choosing to investigate this internal type of defect, as opposed to more severe surface defects, is that it is not easily detected by visual inspection. In addition, internal defects can often appear in a pole before surface defects, due to the surface being better protected by higher preservative levels.

5.1.1 The Two-Factor Beam Scenario

Figure 5.2 presents a schematic and the appropriate parameters for the 'two-factor beam'.

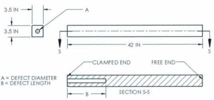

Figure 5.2 - Schematic of Two-Factor Beam

Here the two defect parameters are diameter and length of the defect. The diameter will have a low level of 0.75 in and a high level of 1.75 in. The length will have a low level of 6 in and a high level of 12 in.

5.1.2 Experimental Two-Factor Beam

In the early stages of developing an understanding about what factors affect modal frequency, and how those factors interact, the 'two-factor beam' scenario was chosen for a series of experimental tests. This series of tests was done before the method in Chapter 4 was developed. It was as much an exercise in learning to use the modal impact testing equipment and run a series of experiments, as it was an attempt to characterise defects using modal parameters. Therefore, the method of Chapter 4 will not be strictly adhered to in this section and some of the procedures and choices made seem inefficient in hindsight. However, the results do apply standard design of experiments techniques, and are still worthwhile to present as an intermediate step towards validating the proposed method of defect detection. Here two series of experiments were performed on the same set of western red cedar specimens. Western red cedar was chosen for the material since it is a common species used for full-scale utility poles. The experiment setup and specimens are shown in Figure 5.3.

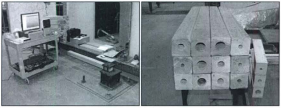

Figure 5.3 - Two-Factor Beam Experiment Setup and Specimens

5.1.2.1 First Series of Experiments

The first series of experiments for the two-factor beam scenario followed a traditional 2^4 factorial design with one replicate and four center points. The factors studied were defect diameter and location as well as moisture content and accelerometer location. Since no humidity-controlled room was available for conditioning the specimens, controlled moisture content was only obtained by purchasing specimens with two distinct initial moisture content levels. The experiments were then performed as quickly as possible in order to avoid progressive drying throughout the series of experiments. By following a random run order, the effect of drying should only show up as random error if it occurs. This is obviously not standard practice for controlling moisture content but there were no other options at the time of this series of experiments. Note that since only two factor levels were available for moisture content, it could not be incorporated into center points and was therefore considered as a categoric variable. The measured responses included the first two transverse modes and the first two torsion modes. For each mode, the frequency and damping ratio were obtained. Mode shapes were also obtained for each test in order to help identify each appropriate mode.

Since wood is an orthotropic material, having properties that vary depending on grain direction, then grain orientation should have been controlled unless it was chosen as one of the studied factors. However, since the specimens were pre-cut before purchase, there was no way to control grain direction. Therefore, some lack of fit is expected to show up in the resulting regression models due to the random error caused by variations in grain direction.

Data for the initial two-factor beam experiment, including factor levels and measured responses can be found in Table 5-1.

Specimen		Factor Levels for Initial Two Factor Beam Experiment				Defected Modal Frequencies (Hz)				Defected Damping Ratios (%)			
Std	Run	Defect	Defect	Accelerometer	Moisture	Transverse		Torsion		Transverse		Torsion	
Order	Order	Diameter [in]	Length [in]	Position [in]	Content [%]	1st	2nd	1st	2nd	1st	2nd	1st	2nd
1	17	0.75	6	0	12	45.55	297.07	307.32	947.86	1.08	0.76	1.15	0.51
2	11	1.75	6	0	12	41.98	281.35	279.19	876.00	3.12	0.67	0.65	0.63
3	13	0.75	18	0	12	42.42	287.76	245.74	785.11	4.48	1.30	1.37	0.81
4	10	1.75	18	0	12	41.41	276.53	246.63	895.05	4.58	1.08	3.78	0.64
5	2	0.75	6	42	12	44.25	283.07	305.30	947.38	3.76	1.25	1.28	0.97
6	8	1.75	6	42	12	41.69	285.72	262.26	878.38	3.06	1.01	3.91	1.77
7	1	0.75	18	42	12	42.54	291.29	242.32	780.70	3.27	1.62	1.95	0.95
8	20	1.75	18	42	12	42.65	288.19	297.56	904.19	2.35	1.01	1.56	1.19
9	14	0.75	6	0	18	42.56	269.58	249.83	779.75	2.91	1.69	1.59	0.95
10	16	1.75	6	0	18	38.42	255.48	314.15	1008.81	3.98	0.83	1.02	0.60
11	12	0.75	18	0	18	42.46	279.02	262.99	855.05	2.64	0.81	2.50	0.74
12	6	1.75	18	0	18	39.66	266.12	244.64	832.61	2.00	0.82	2.79	0.80
13	19	0.75	6	42	18	42.05	276.09	247.77	782.14	1.99	1.09	1.60	0.30
14	15	1.75	6	42	18	37.08	254.16	311.13	1016.24	3.09	1.00	0.31	0.46
15	7	0.75	18	42	18	42.38	269.55	256.35	840.67	2.26	0.77	2.25	0.87
16	4	1.75	18	42	18	39.57	264.67	243.71	829.94	2.27	0.75	2.82	0.88
17	5	1.25	12	21	12	43.28	293.06	262.18	864.89	3.36	0.80	2.51	0.90
18	3	1.25	12	21	18	39.67	265.80	309.45	971.44	3.52	0.93	1.59	0.74
19	18	1.25	12	21	12	42.84	273.55	245.27	777.75	2.80	1.08	1.58	1.43
20	9	1.25	12	21	18	41.09	272.55	250.14	851.33	4.97	1.34	2.44	0.93

Table 5-1 - Factor Levels and Measured Data for Initial 2-Factor Beam Experiment

Data was collected and analyzed following design of experiments procedures. Half-normal plots were employed to help indentify significant factors, and factors were deemed significant by using a 0.95% confidence level. Residuals were also analyzed in order to assure that the assumptions of normality, constant variance and independence of runs were justified. Once analysis was complete, only the first and second transverse modal frequencies resulted in decent regression models for this set of experiments.

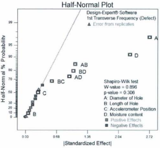

ANOVA for selected factorial model

Analysis of variance table [Partial sum of squares - Type III]

Source	Sum of Squares	df	Mean Square	F Value	p-value Prob > F	
Model	72.05	8	9.01	34.70	< 0.0001	significant
A-Diameter o	29.50	1	29.50	113.65	< 0.0001	
B-Length of h	0.015	1	0.015	0.059	0.8140	
C-Accelerom	0.31	1	0.31	1.21	0.3004	
D-Moisture c	20.93	1	20.93	80.64	< 0.0001	
AB	4.74	1	4.74	18.28	0.0021	
AD	3.71	1	3.71	14.28	0.0044	
BC	1.34	1	1.34	5.16	0.0493	
BD	4.42	1	4.42	17.05	0.0026	
Curvature	0.14	2	0.068	0.26	0.7757	not significant
Residual	2.34	9	0.26			
Lack of Fit	1.23	7	0.18	0.32	0.8941	*not significant*
Pure Error	1.11	2	0.55			
Cor Total	74.52	19				

Figure 5.4 - 1st Trans. Freq. Half-Normal and ANOVA for Initial 2-Factor Beam Experiment

Figure 5.4 shows the half-normal plot and analysis of variance (ANOVA) results for the first transverse modal frequency. We can see that diameter of the defect and moisture content were the two most dominant factors. There were some significant second order interaction effects as well. One interaction that involved accelerometer position was just inside the target significance level. It was kept in the model for that reason; however in reality it should not have affected the results. Modal parameters are a property of the specimen and accelerometer position should have no significant effect on them. The added mass of the accelerometer and the accelerometers lead wire could theoretically have some effect on modal response, although this effect would not likely be noticeable given the scale and accuracy level of the experiment. However, if the accelerometer was mounted near the node of any particular mode (although it was not in this case), that would have the effect of making measurement of the mode more difficult. The main effect of accelerometer position was included in the model as well, but only to maintain hierarchy, and it was not significant as a standalone factor. The resulting regression model for the first transverse frequency in terms of actual factors, as opposed to coded factors, is presented below:

$$1st\ Transverse\ Frequency\ [Hz]$$
$$= 41.67 - 1.36A - 0.031B - 0.14D + 0.54AB - 0.48AD + 0.29BC + 0.53BD$$

Where A, B, C and D represent the coded factors of defect diameter, defect length, accelerometer position, and moisture content respectively. 'Coded factors' refers to the studied factors being scaled to range between -1 and 1 (for example, defect diameter = 1.75 in would be expressed as A = 1 in coded units since it is the maximum defect diameter factor level used in the design space). If desired, coded equations can easily be transformed into equations that accept actual factor levels. However, using coded units does allow all categoric and numeric factors to be represented in a single equation. This equation actual resulted in a respectable R^2 value of 0.9686 (with an adjusted R^2 value of 0.9407).

The second transverse frequency did produce a model with some significant effects, but the overall model was not as strong as the model for first natural frequency. Again, moisture content and defect diameter strongly affected the response. However, in this case they were the only two significant factors. A half-normal plot and ANOVA results can be found in Figure 5.5 for the second transverse frequency. The resulting model, which had an R^2 value of 0.7729 (adjusted R^2

of 0.7426), is presented below in terms of coded factors. Again, A and D represent the coded factors of defect diameter and moisture content respectively:

$$2nd\ Transverse\ Frequensy\ [Hz] = 276.60 - 5.08A - 9.77D$$

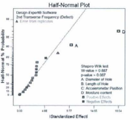

ANOVA for selected factorial model

Analysis of variance table [Partial sum of squares - Type III]

Source	Sum of Squares	df	Mean Square	F Value	p-value Prob > F	
Model	2115.41	2	1057.70	25.52	< 0.0001	significant
A-Diameter o	*412.10*	*1*	*412.10*	*9.94*	*0.0066*	
D-Moisture c	*1526.97*	*1*	*1526.97*	*36.84*	*< 0.0001*	
Curvature	23.80	2	11.90	0.29	0.7545	not significant
Residual	621.65	15	41.44			
Lack of Fit	*408.66*	*13*	*31.44*	*0.30*	*0.9346*	*not significant*
Pure Error	*212.99*	*2*	*106.50*			
Cor Total	2760.85	19				

Figure 5.5 - 2nd Trans. Freq. Half-Normal and ANOVA (Initial 2-Factor Beam Experiment)

For second transverse frequency, the pure error is found to have a more significant effect than lack of fit in the model. Some of the error in measuring the second transverse frequency may have arisen naturally from sources such variation in material properties between specimens. However, one likely source is related to the measurement of torsion modes at the same time as transverse modes. It can be seen in Table 5-1 that the frequencies of the second transverse mode and the first torsion mode are very close. This resulted in some difficulty analyzing the FRF in the band near those two modes. Extracting both modal frequencies from essentially a single peak on the FRF was at times ambiguous and made the measurement procedure for this series of experiments very tedious. High resolution three dimensional mode shapes often had to be obtained in order to positively identify each mode. This may have been a major contributing factor to the first torsion mode not yielding a viable regression model. On one hand, this interference between modes could be considered as an oversight in choosing what specimen geometry to use. However, it is important that modal testing be robust enough to handle any given specimen, and this interference inadvertently brings to light at least one concern that must be addressed when employing modal testing as a quality control technique. Despite being somewhat concerning, this interference could easily been avoided in future tests by choosing appropriate impact and measurement locations that excite and capture only the transverse modes.

If nothing else, these models at least indicate that a defect parameter (diameter in this case) can have some effect on multiple modal frequencies. As expected, moisture content has a significant effect on modal frequency as well. This is likely a reflection of moisture content's effect on stiffness and density, which are important factor affecting theoretical modal frequencies.

We could have used the two regression equations derived above to predict the diameter and length of defects in further validation specimens. This could have been done by inverting them according to the proposed method in Chapter 4. However, due to the weak presence of defect length in these equations (only significant with respect to one response and even then only showing up as part of an interaction effect), and the weak overall model for second transverse frequency, the predictions may not have been very accurate. At this point in the study, effort was thought to be best directed towards improving the models and developing a further understanding of the underlying theory behind modal vibration. These results are nonetheless a relevant first step in validating the proposed method of defect detection using modal frequency.

We will eventually attempt to calculate how the specimens in this experiment would have behaved using theoretical predictions of frequency, but first a second set of experiments using the same specimens will be discussed. This set of experiments was performed after the specimens had been left to dry for a sufficient amount of time.

5.1.2.2 Second Series of Experiments

After the series of experiments in section 5.1.2.1, the specimens used were set aside for a period of about three months to allow for drying to occur. The goal was for each specimen to arrive at common equilibrium moisture content. This was done by storing the specimens within common environmental conditions. They were stored in the same lab in which they were to be tested during the second series of experiments. Humidity and temperature in that lab were fairly well controlled. Moisture content was periodically checked at the surface with a hand held moisture meter and was found to be consistent at the end of the drying phase. However, internal moisture content could not be accurately determined without cutting into the specimens (to access the center with a moisture meter) or baking them (to determine the mass change when moisture is expelled). Either of these methods would have compromised the structure of the specimens.

Once the specimens were conditioned to common moisture content, they were subjected to a second series of experiments. In this series of experiments, defect diameter and defect length were the only factors considered. This time it was assumed that all specimens were identical except for the nature of their imposed defects. Therefore, we will essentially determine if the effects of defects are strong enough to outweigh random error due to variations in geometry and material properties between specimens. The measured responses included the first three transverse modal frequencies.

'Dried' Specimen		Defect	Defect	Transverse Modal Frequencies [Hz]		
Std Order	Run	Diameter [in]	Length [in]	1st Mode	2nd Mode	3rd Mode
1	3	0.75	6	46.268	297.057	879.539
2	9	0.75	6	46.102	299.531	872.793
3	7	1.75	6	43.076	291.072	846.894
4	11	1.75	6	39.515	267.727	795.771
5	8	0.75	18	44.228	296.352	850.996
6	12	0.75	18	45.337	293.667	880.283
7	2	1.75	18	44.314	291.935	869.999
8	6	1.75	18	42.110	292.249	829.640
9	1	1.25	12	44.907	303.550	912.010
10	4	1.25	12	42.681	287.353	862.354
11	5	1.25	12	44.054	292.856	839.704
12	10	1.25	12	42.954	305.444	867.578

Table 5-2 - Factor Levels and Measured Data for 'Dried' 2-Factor Beam Experiment

This time only the first transverse frequency produced a model of any interest. Even for that response, the model was quite poor, with a R^2 value of 0.676. However, the defect diameter, and an interaction effect between the defect diameter and defect length, were found to be significant. A half-normal plot and ANOVA results are found in Figure 5.6. Note that defect length was only included to maintain model hierarchy again. The corresponding regression model, in terms of coded factors, can be found below (where A and B are the coded factor levels of defect diameter and defect length respectively):

$$1st\ Transverse\ Frequency\ [Hz] = 43.80 - 1.61A + 0.13B + 0.83AB$$

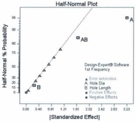

ANOVA for selected factorial model

Analysis of variance table [Partial sum of squares - Type III]

Source	Sum of Squares	df	Mean Square	F Value	p-value Prob > F	
Model	26.50	3	8.83	5.57	0.0233	significant
A-Hole Dia	*20.86*	*1*	*20.86*	*13.15*	*0.0067*	
B-Hole Lengt	*0.13*	*1*	*0.13*	*0.083*	*0.7801*	
AB	*5.51*	*1*	*5.51*	*3.47*	*0.0994*	
Residual	12.69	8	1.59			
Lack of Fit	*0.13*	*1*	*0.13*	*0.072*	*0.7966*	*not significant*
Pure Error	*12.56*	*7*	*1.79*			
Cor Total	39.19	11				

Figure 5.6 - 1st Trans. Freq. Half-Normal and ANOVA ('Dried' 2-Factor Beam Experiment)

The poor models resulting from this series of experiments indicate that other supplementary factors, such as grain direction, density and geometry variations, are likely significant in affecting the modal behavior of the specimens. All supplementary factors were assumed to be constant in this series of tests, and therefore none were considered. However, despite efforts to ensure that supplementary factors were adequately controlled, according to the results that seems not to have been a valid assumption.

Despite the poor models, all is not lost in these results. Defect parameters were again proven to have some significant effect on frequency, at least for the first mode. It can be imagined that with greater care in accounting for supplementary factors, models with suitable accuracy for making predictions could be obtained. In upcoming examples, focus will shift away from physical wooden tests towards theoretical and numerical modeling of defected beams. This will at least confirm that the method proposed in Chapter 4 can be used to predict defects under ideal conditions. Once this is confirmed for the ideal case, a shift can be made back to laboratory testing. In future laboratory tests, greater care for controlling (or accounting for) supplementary factors and variation between specimens will have to be ensured as well.

5.1.3 Theoretical Representation of the Two-Factor Beam

As a first attempt to validate the proposed defect detection method under ideal conditions, we will resort to a theoretical representation of the two-factor beam scenario presented in section 5.1.1. We will perform and analyze a series of experiments on this theoretical model, instead of a physical model. Thus, supplementary factors will be well controlled.

We can solve for theoretical natural frequencies of the two-factor beam using theory presented in section 3.2. To do this we can simply consider the 'two factor beam' to be a stepped beam with two distinct spans. The defected section near the clamped end of the beam can be labelled as span 'a' in the theoretical representation (with parameters $L_a, \rho_a, E_a, A_a, I_a$). Span 'b' can represent the un-defected section towards the free end (with parameters $L_b, \rho_b, E_b, A_b, I_b$).

Using the theory and method presented in section 3.2 and Appendix A respectively, we can solve for the natural frequencies of a stepped beam at the various required factor levels, and develop regression models in the usual way. Factor levels will be chosen here to allow each natural frequency to be modelled as a second-order, face-centered, central-composite response-surface. Since each experimental run will now be carried out using a theoretical model, instead of a physical specimen, we can easily add extra points and expand our model from the simple two-level factorial models used in section 5.1.2 to a second order response surface. The material properties were taken here as average values published for western red cedar. The elastic modulus was taken as 8.47 GPa (value corrected for shear effects and assuming 12% moisture content) and the density was taken as 320 kg/m^3 (Green, Winandy, & Kretschmann, 1999). The specific runs completed in this experiment are outlined below in Figure 5.7.

Standard Order	Defect Diameter [in]	Defect Length [in]	Theoretical Transverse Modal Frequency [Hz]		
			1st Mode	2nd Mode	3rd Mode
1	0.75	6	65.005	409.075	1144.357
2	1.75	6	65.797	415.173	1162.681
3	0.75	18	62.882	415.008	1145.953
4	1.75	18	65.914	431.096	1176.229
5	0.75	12	64.447	411.867	1145.296
6	1.75	12	66.289	424.964	1172.088
7	1.25	6	65.441	412.002	1152.629
8	1.25	18	64.336	421.761	1158.534
9	1.25	12	65.380	417.606	1156.426

Figure 5.7 - Factor Levels and Results for Theoretical Two-Factor Beam Experiment

We can see that the absolute values of the first three modal frequencies are somewhat different from the frequencies obtained in section 5.1.2. However, this is not alarming since material properties of wood can vary greatly between specimens. This is even true when specimens are of the same species. In fact, the source from which published material properties were obtained for this example actually published two very different values of elastic modulus (6.5 Gpa and 7.7 Gpa respectively, before correction is made for shear effects) depending upon whether the wood was 'green' or at 12% moisture content. Published elastic modulus values for some other wood species even double between these two moisture contents. In addition to stiffness, moisture content is also shown to affect density. The region where specimens are grown is also said to contribute to material properties (Green, Winandy, & Kretschmann, 1999). Therefore, since modal frequency of wood depends heavily upon these variable properties, it is expected for there to be some difference between measured frequencies and theoretical predictions of frequencies made using published properties. Clamping conditions not being ideal and mass loading from the accelerometers, among other factors, could also account for some of the difference between measured and theoretical frequencies.

Using stepwise regression and techniques similar to those used in section 5.1.2 to develop second order models with this data, we get the three prediction equations presented below in terms of coded factors (note that A and B refer to coded factor levels of defect diameter and defect length respectively):

$$1st\ Transverse\ Frequency\ [Hz] = 65.37 + 0.94A - 0.52B + 0.56AB - 0.48B^2$$

$$2nd\ Transverse\ Frequency\ [Hz] = 417.62 + 5.88A + 0.27B + 2.5AB$$

$$3rd\ Transverse\ Frequency\ [Hz] = 1155.86 + 12.57A + 3.51B + 2.99AB + 1.90A^2$$

Note that the three equations above have R^2 values of 0.9994, 0.9897 and 0.9944 respectively. Also, note that some second order effects did show up as significant in the models, which suggests that expanding to the second order response surface design was justified. Here we seem to have obtained three acceptable regression equations, with each indicating that both defect parameters significantly affect frequency. We also have very good R^2 values, which indicate that the regression models adequately represent the behaviour of the theoretical model (which is obviously somewhat more complex). This portrays the essence of using the design of experiments approach for this application; it allows us to represent the behaviour of complex systems by using simple statistical models. Because of this, the proposed method of predicting defects should be able to adapt to complex systems where finding theoretical modal frequencies would be difficult. Only experiment runs on physical specimens would be required for developing the regression models.

Since for this set of experiments we seem to have obtained adequate regression models, we can now use those models to make predictions of defect parameters for other validation runs. To do this we will simply choose arbitrary defect parameters, use the theoretical model to solve for modal frequencies of a beam with those parameters and input the resulting modal frequencies into our regression equations. We can then rearrange and solve the regression equations for predictions of defect parameters, and compare the predicted defect parameters to the actual parameters that were initially chosen. This exercise is useful for determining whether the regression models do indeed reflect the actual behaviour of the theoretical model in areas of design space away from the design points. It also allows us to assess whether defect parameters can practically, and definitively, be predicted from modal frequency measurements in the manner described in Chapter 4.

After performing four validations runs, and using numerical optimization with the first two modal frequencies to predict defect parameters for each run, we get the results shown in Table 5-3. As we can see, the predicted values are very close to the values of the actual defect parameters, indicating that the regression models do accurately reflect the behaviour of the theoretical model. Note that the third mode did not need to be employed since multiple solutions were not obtained for either prediction. There were nonlinear terms in the models; however, the nonlinear terms were not strong enough to create multiple solutions within the design space for either of our validation runs.

Validation Run	Actual Defect Parameters		Theoretical Transverse Modal Frequency [Hz]			Predicted Defect Parameters	
	Defect Diameter [in]	Defect Length [in]	1st Mode	2nd Mode	3rd Mode	Defect Diameter [in]	Defect Length [in]
1	0.90	15.00	64.135	415.060	1147.612	0.89	14.90
2	1.40	8.00	65.682	415.318	1159.391	1.41	7.87
3	1.20	10.00	65.409	415.257	1155.435	1.19	9.95
4	1.60	16.00	65.804	426.667	1166.750	1.62	15.93

Table 5-3 - Validation Runs for Theoretical Two-Factor Beam Experiment

If we plot these numerical optimization predictions against the actual defect parameters within our overall design space, we can see that the predictions are actually quite good.

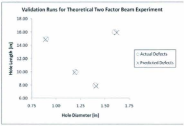

Figure 5.8 - Validation Runs for Theoretical Two-Factor Beam Experiment

If we pursue the graphical approach that was suggested in section 4.2.2, we get the results shown in Figure 5.9. The left plot in the figure shows our prediction using the first two modes and the right plot shows the result when the third mode is added. The predicted solution is where the contour lines for each modal frequency intersect within the two-dimensional design space.

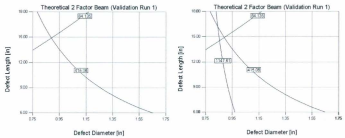

Figure 5.9 - Graphical Solution to Validation Run 1 of Theoretical Two-Factor Beam

In the left plot of the figure it can be seen that when using the first two modes, the graphical solution agrees well with the actual defect parameters. It also agrees well with the parameters predicted using numerical optimization. However, if we add the third modal frequency to the plot, as shown on the right of the figure, it does not quite intersect that solution. We anticipate a small amount of deviation between the third frequency and the intersection of the first two frequencies simply based on the regression models not being a perfect fit to the theoretical model. However, since the predicted defect parameters found using the first two frequencies alone were so close to the actual defect parameters, this seems to indicate that the regression model for third frequency is not such a good fit to the actual behavior of the third frequency within the theoretical model. Here we simply selected a textbook second order response surface design and attempted to capture the behavior of all three modes with it. However, as we have mentioned in Chapter 4, and will witness in upcoming examples, it is not easy to capture the behavior of higher modes and more complex regression models are actually required. Since higher order modes require higher order regression models, determining the minimum number of modes required to make definitive predictions is paramount. We have suggested a guideline in Chapter 4 of obtaining $n + 1$ regression equations if we desire to predict n defect parameters. However, as we have seen in this example, as long as no multiple solutions exist, then n equations are adequate. Knowing when n parameters are adequate requires experience and an in-depth understanding of how each modal frequency generally behaves with regard to specific defect parameters. It also depends upon the ranges of those parameters. In this example we considered only limited ranges for defect diameter and defect length. The ranges chosen here were meant to match the ranges used in the physical experiments of section 5.1.2, and they were initially chosen in that section to allow for defects to be practically introduced into the test specimens. In this case the limited ranges are at least partially responsible for the second order models providing an adequate fit to the theoretical behavior, and definitive solutions for two defect parameters being obtained using only two regression equations. We will see in future examples that the extra regression model is indeed often required to eliminate multiple solutions. However, before moving on to another example scenario, we will revisit this example using a finite element model, in place of the theoretical model, for simulating the behavior of the stepped beam.

5.1.4 Finite Element Representation of the Two-Factor Beam

In order to confirm the results that we obtained using the theoretical model in section 5.1.3, and to continue our attempts to validate the method proposed in Chapter 4, we will revisit the two-factor beam scenario and use a finite element model to simulate the behavior of the stepped beam. Ansys 12 was used to run the finite element simulations and the same published material properties were used here for western red cedar. The procedure here is very similar to the procedure in section 5.1.3, and therefore we will quickly progress to the results. A sample finite element analysis output for this series of experiments, which shows the first three modes, can be found in Figure 5.10.

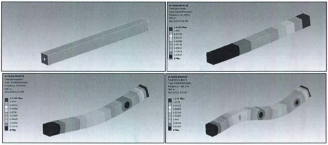

Figure 5.10 - Example Three Mode Finite Element Result for Two-Factor Beam

Table 5-4 summarizes the results of the experiment. Notice that a central composite, face-centered response surface design was again used. The actual frequency values obtained from the finite element model seem to correspond fairly well with the frequency values obtained using the theoretical model in section 5.1.3. The two models produce values within about five to ten percent of each other. However, note that the actual values of frequency are not as important as the behaviour of frequency when defect parameters are changed. This behaviour is what we must capture when developing regression models for prediction. In physical systems, the actual frequency values will always vary depending upon the structure being tested. However, since regression models are tailored to each situation, they should still perform well in identifying defects and the actual frequency values are not of high importance.

Standard Order	Defect Diameter [in]	Defect Length [in]	FEA Transverse Modal Frequency [Hz]		
			1st Mode	2nd Mode	3rd Mode
1	0.75	6	62.159	376.837	1006.725
2	1.75	6	61.543	372.737	992.532
3	0.75	18	62.153	378.230	1013.755
4	1.75	18	61.130	380.105	1033.082
5	0.75	12	62.141	376.900	1009.912
6	1.75	12	61.207	373.309	1010.698
7	1.25	6	62.002	375.478	1001.467
8	1.25	18	61.912	379.353	1021.548
9	1.25	12	61.910	375.761	1010.658

Table 5-4 - Factor Levels and Results for Finite Element Two Factor Beam Experiment

Once we use the data from Table 5-4 to develop regression models, and then perform validation runs to tests the predictive ability of those models, we get the predicted defect parameters shown in Table 5-5. These predictions are also plotted against the actual defects in Figure 5.11. The two dimensional area within the plot represents the considered design space. We can see that the predictions are again quite good, indicating that the regression models adequately capture the behaviour of the finite element model and are able to be definitively solved for defect parameters when provided with a measured set of modal frequencies.

Validation Run	Actual Defect Parameters		FEA Transverse Modal Frequency [Hz]			Predicted Defect Parameters	
	Defect Diameter [in]	Defect Length [in]	1st Mode	2nd Mode	3rd Mode	Defect Diameter [in]	Defect Length [in]
1	0.90	15.00	62.101	377.393	1013.977	0.96	15.03
2	1.40	8.00	61.854	374.593	1000.604	1.37	8.18
3	1.20	10.00	61.968	375.519	1006.045	1.19	10.32
4	1.60	16.00	61.437	377.539	1026.126	1.59	16.10

Table 5-5 - Validation Runs for Finite Element Two-Factor Beam Experiment

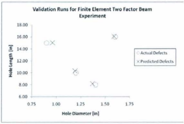

Figure 5.11 - Validation Runs for Finite Element Two-Factor Beam Experiment

Overall, early results based on investigating the 'two-factor beam' scenario indicate that the proposed method of defect detection is promising. We found that defect parameters do actually affect frequency response, and that regression models can be developed to capture the behavior of that response. We also found that those regression models can be solved to give accurate predictions of defect parameters in validation specimens. Next, we will further investigate the proposed technique by investigating a slightly more complex scenario, the 'two-factor rod'.

5.2 The Two-Factor Rod

The second example for validating the proposed regression model technique will involve a circular cross section rod. The defect will be a localized reduction in diameter of the cross section, which could be considered as an open crack. The factors will thus be the defect's diameter and its location. The motivation for choosing this arrangement is that it will provide insight into how well the method can localize a defect in addition to quantifying its severity.

For the two-factor beam, we started with a physical experiment essentially to become familiar with the modal testing equipment and to begin looking into the problem of detecting defects. Here we will attempt to characterize the behaviour of the two-factor rod within the finite element environment before attempting a physical experiment. This will allow us to gain an understanding of how the specimen behaves when localized defects are added, and will allow us to be better prepared when we do attempt a laboratory experiment. In this section, we will investigate a finite element as well as a physical model of the two-factor rod scenario. We will also examine whether the defect detection method is able to perform well in each case.

5.2.1 The Two-Factor Rod Scenario

The two-factor rod will generally be a circular cross section length of aluminum and is depicted in Figure 5.12. In this case, the only two factors to be studied are the location and diameter of the defect. Overall length and overall diameter have not been specified here, since they will be different for each implementation of this scenario in the coming sections, however, they will remain fixed within each specific implementation and will not be studied as factors.

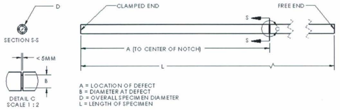

Figure 5.12 - Schematic of Two-Factor Rod

5.2.2 Finite Element Representation of the Two Factor Rod

Here we will consider the two-factor rod scenario within a finite element environment. We will use an overall length of 500mm and an overall diameter of 25mm for our specimens. A general 'non-linear aluminum alloy', built into the database of the finite element package, was chosen as the material. However, the actual material properties are again irrelevant since we only wish to validate the proposed defect detection method.

When examining the two-factor beam scenario, we continued to use simple and established experiment designs, such as the factorial and central composite response surfaces, to investigate which factors had significant effects on frequency response. However, we found that the third frequency might not have been adequately modelled by even the second order response surface. For the two-factor rod, instead of blindly applying an established design structure to investigate effects, we will follow the procedure that was presented in sections 4.6.2 and 4.6.3. This procedure dictates that we should use closely spaced finite element runs to determine what the actual behaviour is in advance, and then determine an appropriate number of design points that would be required to capture that behaviour in a regression model. If this approach is followed prior to attempting a physical experiment, then we can be somewhat assured that only one series of experiments will be required to adequately model the behaviour of a system.

If we create the two-factor rod within a FEA setting and gradually increment each of the two factors (defect location and diameter at the defect), we get response surfaces for the first five modes as shown in Figure 5.13. Note that these response surfaces were obtained by meshing these closely spaced FEA runs and are not fitted regression models. Therefore, they should give a true representation of the actual behaviour of the system. Note that the location is measured from the clamped end and diameter refers to the diameter at the defect, not the reduction in diameter at the defect. Therefore, lower diameter here corresponds to a more severe defect.

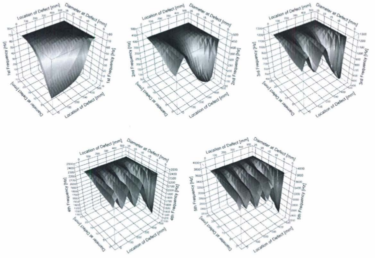

Figure 5.13 - FEA Meshed Response Surfaces (First Five Modes of the Two-Factor Rod)

We can see that frequency of each mode is generally reduced (relative to the intact case) by the introduction of a defect, as long as the defect is not near a location of low curvature (or the node of a curvature mode shape). As the defect nears a node, its effect becomes progressively less severe. In addition, more severe defects generally result in higher frequency reduction. If we plot two-dimensional cross sections of these response surfaces, we can get a better idea of exactly how each factor affects the frequency response of each mode. These two-dimensional sections are found in Figure 5.14 and Figure 5.15.

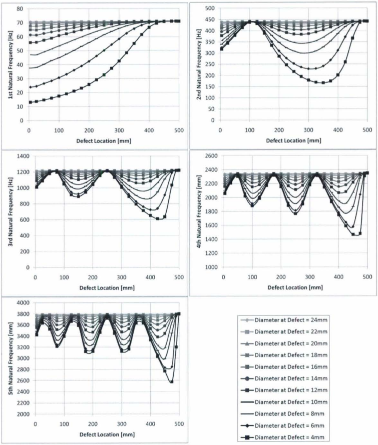

Figure 5.14 - Effect of Defect Location on FEA Meshed Surfaces (Two-Factor Rod)

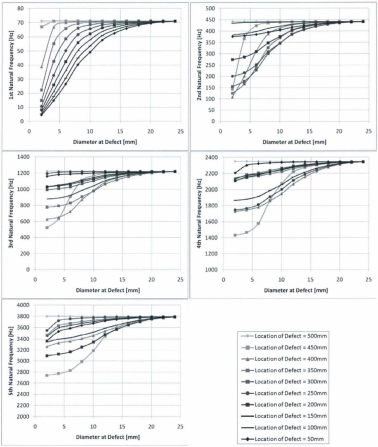

Figure 5.15 - Effect of Diameter at Defect on FEA Meshed Surfaces (Two-Factor Rod)

Following the general procedure described in section 4.6.2, we will first use the above plots as a guide so we can determine the minimum model order required to adequately capture the effects of each factor on each mode. We will then determine the minimum number of design points needed to fit our regression models to that model order.

Since we wish to predict the values of two defect parameters here (defect location and diameter at the defect) we need to model surfaces for at least two frequencies. Two frequencies would give us the same number of regression equations as unknowns and therefore allow us to find solutions for our unknowns. However, as we will see later, the regression equations that result from the first two modal frequencies are nonlinear and therefore will have multiple solutions. In anticipation of this problem, and to avoid having to determine a new model order and run the required experiments again later, we will adhere to the guidelines presented in Chapter 4 and assume that models of three frequencies are required to predict for two defect parameters.

If we wish to obtain response surface models and regression equations for a number of frequencies, we need to include enough design points in our experiment runs to model the highest order frequency of interest. Since we wish to model modes one through three, the frequency with the highest required model order is the third frequency in our case (as can be seen in Figure 5.13 through Figure 5.15).

Keeping with the guidelines presented in section 4.6.2, we determine that in order to accurately model the third frequency across our entire design space, we require four design points in the defect diameter dimension and ten design points in the defect location direction. This is determined by following the rough guideline that for every span between inflection points we require two design points. The defect diameter plots had one inflection point and the defect location plot had four inflection points. Note again that this is only a rough guideline and future work may dictate more efficient methods for modeling these complex surfaces.

Using the method described above we should be able to model our highest order mode using a four by ten point design space. However, due to model order limitations of the commercial design of experiments software used in this study, we are forced to split the design space into two segments. Each segment will be analyzed separately for modeling and prediction purposes. Splitting the design space was discussed in section 4.6.3, and following the guidelines presented in that section we add an extra point in the defect location dimension at the interface between the two segments. This point is also shared by each segment in order to maintain continuity in the space. Hence, we finally arrive at a procedure for developing regression models for the two factor rod scenario. We will consider two symmetric design space segments, each consisting of an evenly spaced four by six design point mesh. The total number of unique design points will be forty-four in this case.

We will consider the defect diameter values to range between 6 mm and 24 mm for each design space segment (note that the overall diameter was chosen as 25mm). For defect location we will choose a design space that ranges between 25 mm and 475 mm (note that our overall length is 500 mm). Since we have two separate design-space segments, with respect to defect location, our first segment will range between 25 mm and 250 mm and our second segment will range between 250 mm and 475 mm. Therefore, this design space considers nearly every physically possible defect of the form considered. We cut off our design space slightly before the physical limits in order to avoid anomalies at those limits (such as a beam with a defect diameter of zero).

Using the design structure established above, we can now develop our finite element model and perform the required simulation runs. A summary of the specific factor levels for each design point, and results obtained from each finite element simulation, are presented in Table 5-6 and Table 5-7 respectively for the two design space segments. Note again that four points at the interface between the two segments are common and appear in both tables.

Run	Defect Location [mm]	Defect Diameter [mm]	First Design Space Segment FEA Modal Frequencies		
			1st Mode [Hz]	2nd Mode [Hz]	3rd Mode [Hz]
1	25	6	24.648	350.082	1097.842
2	25	12	56.112	395.015	1149.664
3	25	18	67.552	427.928	1196.920
4	25	24	70.834	440.411	1217.519
5	70	6	28.114	411.371	1212.174
6	70	12	58.900	429.572	1217.759
7	70	18	68.362	438.357	1218.966
8	70	24	70.865	440.874	1218.635
9	115	6	32.143	439.486	988.510
10	115	12	61.625	440.705	1141.977
11	115	18	69.051	441.029	1202.338
12	115	24	70.887	440.977	1218.228
13	160	6	37.168	379.595	936.102
14	160	12	64.087	423.860	1104.647
15	160	18	69.654	437.694	1192.645
16	160	24	70.915	440.887	1217.896
17	205	6	43.055	301.936	1082.108
18	205	12	66.391	399.628	1167.720
19	205	18	70.137	432.508	1207.467
20	205	24	70.920	440.738	1218.289
21	250	6	50.223	252.281	1214.614
22	250	12	68.276	384.993	1217.736
23	250	18	70.502	429.160	1218.582
24	250	24	70.941	440.654	1218.576

Table 5-6 - Design Points and Results for First Design Space Segment of FEA 2-Factor Rod

Run	Defect Location [mm]	Defect Diameter [mm]	Second Design Space Segment FEA Modal Frequencies		
			1st Mode [Hz]	2nd Mode [Hz]	3rd Mode [Hz]
21	250	6	50.223	252.281	1214.614
22	250	12	68.276	384.993	1217.736
23	250	18	70.502	429.160	1218.582
24	250	24	70.941	440.654	1218.576
25	295	6	57.682	229.446	1051.677
26	295	12	69.590	384.561	1153.770
27	295	18	70.762	429.606	1203.997
28	295	24	70.952	440.653	1218.165
29	340	6	64.669	236.235	864.143
30	340	12	70.445	398.746	1071.567
31	340	18	70.921	433.235	1184.795
32	340	24	70.960	440.758	1217.639
33	385	6	69.043	281.702	742.713
34	385	12	70.893	421.063	1067.803
35	385	18	70.999	437.481	1187.416
36	385	24	70.966	440.867	1217.742
37	430	6	70.834	384.354	757.245
38	430	12	71.077	436.795	1156.075
39	430	18	71.033	440.268	1207.610
40	430	24	70.969	440.970	1218.300
41	475	6	71.197	440.769	1189.497
42	475	12	71.149	441.667	1217.948
43	475	18	71.085	441.557	1219.467
44	475	24	70.974	441.050	1218.735

Table 5-7 - Design Points and Results for 2nd Design Space Segment of FEA 2-Factor Rod

After we analyze this data in the normal way using stepwise regression, we obtain six individual regression models; two models for each frequency, using three frequencies. The models are somewhat complex and consist of various high order terms. R^2 values are quite good and range between 0.9936 and 1.0000. We can use these models to predict defect parameters of additional validation runs, as we have done in previous sections. However, validating the models in this case is a little more complex. We need to insure that splitting the design space did not inhibit the ability of the models to give accurate predictions of defect parameters. To do this we need to ensure that an accurate solution is returned when using the correct design space segment, and that the other segment does not falsely return extra solutions. The results from a number of validation runs are summarized in Table 5-8.

Validation Run	Actual Defect Parameters		FEA Transverse Modal Frequencies [Hz]			Predicted Defects (1st Half Model)		Predicted Defects (2nd Half Model)	
	Location of Defect [mm]	Diameter at Defect [mm]	1st Mode	2nd Mode	3rd Mode	Location of Defect [mm]	Diameter at Defect [mm]	Location of Defect [mm]	Diameter at Defect [mm]
1	175	14	67.418	425.466	1153.482	180.99	13.95	(No Desireable Solution)	
2	400	9	70.791	402.367	930.692	(3rd Freq out of Range)		380.91	8.89
3	425	22	71.014	440.951	1216.689	(1st Freq out of Range)		451.15	23.32
4	75	10	51.260	427.219	1211.975	76.04	9.33	(No Desireable Solution)	
5	275	7	60.533	271.148	1154.181	275.00	7.00	287.14	7.22
6	250	20	70.758	435.526	1218.974	259.44	18.79	282.82	22.84
7	100	21	70.297	441.011	1216.011	140.32	22.05	(460.11)*	(22.13)*
8	300	14	70.771	424.362	1167.937	(184.51)*	(14.72)*	296.20	13.93

* Indicates that solution was obtained using numerical optimization but later rejected using the graphical approach

Table 5-8 - Validation Runs for FEA Two-Factor Rod

We can see that each of the validation runs resulted in fairly good predictions of defect parameters using our models. The predictions were made here largely from numerical optimization across all three responses. However to obtain those predictions we had to use both design space segment models.

For validation runs one through four, we can see that only one solution was obtained in each case. For the segmented model that was supposed to return a solution, a fairly good solution was returned with a high desirability in each case. For the segmented model that was not supposed to return a solution, either at least one of the frequency inputs were outside the range of frequencies that were obtained when developing that model, or no solution with an adequately high desirability was found. In each case desirability of solutions was compared between models and one was clearly higher than the other.

For validation runs five and six, two high desirability solutions were obtained using numerical optimization. However, in this case both solutions are somewhat acceptable, since they both lie near the interface between the two design space segments (which is at a location of 250 mm). It would not necessarily be clear which solution was best if we were employing the method in practice. The one with the slightly higher desirability could be chosen, or recognizing that they are both relevant predictions, the solutions could be averaged to obtain a single solution. In any event, these results at least verify that solutions near the interface between design space segments do not pose a serious problem when using the technique.

For validation runs seven and eight, obtaining a definitive solution was a little more difficult. Numerical optimization returned a solution with high desirability from each design space segment. Using the graphical approach was also a little ambiguous, but when the better graphical solution was chosen (knowing in this case that there should only be one unique solution) we were able to correctly eliminate the incorrect prediction. However, based on this difficulty, it is not clear whether we could choose the correct solution for all potential defect conditions. The difficulty experienced here with identifying certain defects will be discussed further in section 5.2.3 as we investigate which areas of the design space are more sensitive.

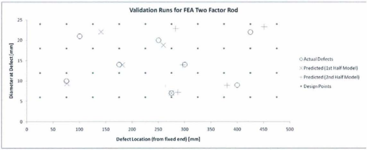

Figure 5.16 - Validation Runs for FEA Two-Factor Rod

We can gain a better perspective for how accurate the predictions were by again plotting actual defects and predicted defects together in the two dimensional design space, as shown in Figure

5.16. From the figure, we can see that more severe defects better predicted in general. This relates to the discussions in Chapter 4 relating to sensitivity. Design space regions in which the factor effects are stronger (or they have a high slope) are generally prone to better predictions than regions with weak effects (where the response surface is more horizontal). In this case, smaller defects result in weaker effects, correspond to more horizontal regions of each response surface, and thus are prone to higher error in their predictions.

The prediction process for the two factor rod experiment scenario is proving to generally be more complex than the two factor beam scenario presented in section 5.1. The graphical technique in particular provides a more interesting result. Shown in Figure 5.17 are the response surfaces for the first design space segments of modes one through three (left to right top), and their corresponding contour lines for the first validation run in Table 5-8 (left to right bottom).

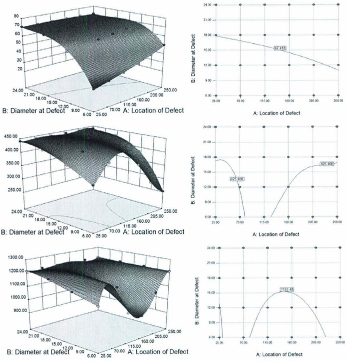

Figure 5.17 - Validation Run 1 Response Surfaces and Contour Lines for FEA 2-Factor Rod

If we use only the first two modes in our numerical optimization procedure for the first validation run, we get two solutions, each having a high desirability. They occur at location = 173.55, diameter = 14.03 and at diameter location = 36.33, diameter = 17.47. If we overlay the contour lines of the first two modes for this particular validation run, we get the plot shown in Figure 5.18. Those two solutions are clearly visible when using the graphical technique as well.

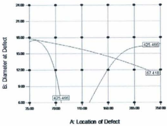

Figure 5.18 - Two-Mode Graphical Solution for Validation Run 1 of FEA 2-Factor Rod

Whereas when we were examining the two-factor beam we only required the first two modes to predict two defect parameters, it is obvious here that the extra mode is indeed required to isolate the correct solution. Because of the nonlinearity of the models in the current case, we have obtained multiple solutions when using the minimum required number of modes. If we now overlay the contour line of the third mode, we get the plot shown in Figure 5.19. The correct solution is now clearly visible using the graphical method. Employing a combination of numerical optimization and the graphical approach shown here can often be useful for identifying and fully understanding predictions.

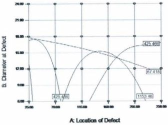

Figure 5.19 - Three-Mode Graphical Solution for Validation Run 1 of FEA 2-Factor Rod

We have examined the behavior of the two factor rod, obtained a suitable design structure and determined that the method of defect detection that was proposed in Chapter 4 can be successfully applied to this particular scenario. Therefore, it seems feasible that we can now pursue a set of laboratory experiments to continue exploring the two-factor rod scenario, and to validate the proposed defect detection method on a physical system.

5.2.3 Experimental Representation of the Two-Factor Rod

Here we will attempt to produce two factor rod results similar to those found in section 5.2.2 by performing a series of experiments on physical specimens. The overall length will be taken here as 1000 mm. This length was chosen, instead of the 500mm length used in the finite element model of section 5.2.2, since it produced frequencies that were more practical to quickly and accurately measure using our modal testing equipment. The overall diameter of the specimens was taken as 25.4 mm (1 in), instead of the 25 mm used in the finite element model, since that standard size of aluminum rod was readily available. TL 6160 grade aluminum was chosen as the material.

The previously used FEA models could be updated to match the material and dimensions of the specimens used in the upcoming experimental trials. However, this is not strictly necessary since we are only interested in validating the defect detection method, and not the agreement between actual values of the FEA and experimental runs. We expect that there would be some disagreement in these actual values anyway due to non-ideal clamping conditions for the physical experiments, mass loading from the accelerometer, variations in properties and dimensions between specimens, temperature variations and many other factors. Repeating all work done in section 5.2.2 using updated specimens properties simply to try and match actual values does not add a significant level of weight to the study and does not seem to be justified. If we expected to obtain similar values in our experimental model development runs, we could simply have skipped the model development process and used the FEA generated regression models for prediction of experimental validation runs. This would likely result in disappointing results. In later sections, we will discuss the possibility of eventually scaling regression models developed from FEA runs in order to allow them to be used for predicting defects in physical specimens. However, for now we will develop application specific regression models in the usual way using the indicated specimens.

Apart from the overall dimensions being slightly different, the design structure, modelling procedure and prediction method are much the same as those applied in section 5.2.2. Therefore, we will avoid many repetitive comments concerning method choices and directly discuss results. First, note that the setup for this series of experiments is shown in Figure 5.20.

Figure 5.20 - Experiment Setup for Two-Factor Rod

Using a similar forty-four point split design space, with each half containing a four by six mesh of evenly spaced design points, we get the data shown in Table 5-9.

	Run	Location of Defect [mm]	Diameter at Defect [mm]	Transverse Modal Frequencies [Hz]		
				1st Mode	2nd Mode	3rd Mode
1st Notch	1	300	24	17.1751	106.9219	300.5865
	2	0	24	17.0740	106.3026	299.1241
	3	400	24	17.1281	106.5321	299.9414
	4	100	24	17.0303	106.1066	298.8555
	5	500	24	17.1198	106.3745	299.7926
	6	199	24	17.1589	106.8916	300.8903
2nd Notch	7	100	18	16.5388	105.6059	299.2653
	8	199	18	16.7351	106.8528	298.3230
	9	400	18	16.9385	105.3331	297.6608
	10	500	18	17.0322	104.8062	300.3137
	11	0	18	16.3093	102.8208	289.8252
	12	300	18	16.8871	106.4710	295.8170
3rd Notch	13	500	12	16.7294	95.8033	301.6946
	14	300	12	15.8956	105.0604	277.9919
	15	199	12	15.2787	107.3561	290.4770
	16	400	12	16.3412	99.4471	289.3290
	17	0	12	13.7472	92.8933	270.2954
	18	100	12	14.4705	102.2533	297.7720
4th Notch	19	300	6	9.6188	96.2986	230.9971
	20	0	6	6.2418	79.6814	252.0857
	21	400	6	11.1189	75.8337	264.4200
	22	100	6	7.8159	95.3913	295.8050
	23	199	6	8.3167	107.2077	262.1869
	24	500	6	12.8485	63.2092	300.3192

Table 5-9 - Factor Levels and Measured Data for the Experimental 2-Factor Rod

As shown in the Table 5-9 we only obtained enough data to model one half of the overall design space. This was due to concerns over budget, time investment and material consumption. However, one segment is enough to validate the method. This one segment had defects that ranged from a location of 0 mm, to a location of 500 mm, from the clamped end (note again that the overall length was 1000 mm in this case).

One notable sacrifice that was made in this series of experiments, which would not be considered to follow best design of experiments practices, is that all of the experiment runs that were used to develop our half design space model were performed using only three specimens. The specimens were simply designed in such a way that they could be notched at one location and then tested twice, once while clamped from each end, to create two unique design points. The notches were also cut progressively deeper after each pair of tests so that all defect diameters could be obtained from each specimen. This decision to perform the experiment in this way was again made in light of budgetary and material consumption concerns. This method obviously raises some concerns about obtaining appropriate random error, as well as other effects leeching into our studied effects, especially for the case of defect diameter. However, attempts were made to mitigate these concerns. The angle at which each specimen was clamped (about its centerline) was purposefully chosen to be random for each experiment run so that it reinstated some random error. This variation in angle meant the modal frequencies were always measured in different planes. This is not quite as good as using separate specimens for each run, in terms of accounting for random variation between specimens, but it does help in capturing a similar type of variation. In addition, each specimen had to be remounted before each run, which meant that clamping force and clamping location (along the specimen's length) had some slight variation, and thus resulted in random error as well. Since defects had to be cut progressively deeper, runs were placed under some restriction and could not truly be random. However, random run order was chosen with respect to defect location between each successive round of notching. Accelerometers were always dismounted and remounted between tests and thus may have been positioned slightly different each time. In addition, random error always results because the hammer hits are manually imparted, and are therefore somewhat imperfect. It is the hope that all these sources of random error outweigh the random error that was lost by not using separate specimens for each run. In the end, the accuracy of predictions should show whether or not the models were obtained adequately. In any event, this set of experiments is simply meant to validate the proposed method of detecting defects. As long as we get somewhat decent models that agree with our finite element results, and can make adequate predictions from those models, then that task will have been accomplished. A small amount of bias in our results in this case is acceptable and worth the material savings.

Using the data obtained from the experiment runs we again obtain regression models in the usual way. Response surface models for the first half of the design space are shown in Figure 5.21 for each of the three modal frequencies measured in this set of experiments. These three models had R^2 values that were again quite good at 0.9974, 0.9967 and 0.9781, for modes one, two and three respectively. If we compare these response surfaces to the ones generated for the first half of the design space using the finite element model of the two-factor rod (shown in Figure 5.17), we can see that there is very good agreement in the behavior of both mediums. Note again, that the overall dimensions of the specimens in the finite element model were different from the dimensions used in the physical experiments, and therefore the actual values shown in each response surface will obviously be somewhat different. However, the agreement in behavior is most important.

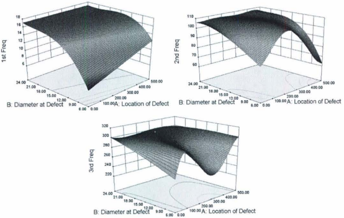

Figure 5.21 - Response Surfaces for the 1st 3 Frequencies of the Experimental 2-Factor Rod

If we again perform validation runs using these models we get the results shown in Table 5-10. A visual depiction of the results is also presented in Figure 5.22. We can see that for defects that fall within the upper portion of the defect diameter range, no definitive prediction could be obtained for defect parameters. Therefore, less severe defects here resulted in poor predictions. The results are somewhat worse in this particular case for small defects; however, this result is consistent with what was suggested in Chapter 4, and what was obtained in section 5.2.2. The poor predictions are again due to less severe defects being more prone to error because they create weak factor effects.

Validation Run	Actual Defect Parameters		Validation Transverse Freuencies [Hz]			Predicted Defect Parameters	
	Location of Defect [mm]	Diameter at Defect [mm]	1st Mode	2nd Mode	3rd Mode	Location of Defect [mm]	Diameter at Defect [mm]
1	251.50	20.00	17.0785	107.2110	299.7924	(No definitive Solution)	
2	460.00	21.00	17.1083	106.0463	300.2065	(No definitive Solution)	
3	39.50	21.00	16.8666	105.4630	297.4538	(No definitive Solution)	
4	354.50	17.00	16.9551	105.8164	295.3651	330.36	17.58
5	151.50	17.00	16.6176	107.0219	300.9382	164.88	15.55
6	460.00	9.00	15.5630	85.6377	297.0657	473.47	9.35
7	39.50	9.00	11.3044	91.4023	277.0929	16.74	9.15
8	251.50	8.00	12.4892	106.1885	254.0000	272.60	8.12

Table 5-10 - Validation Runs for Experimental Two-Factor Rod

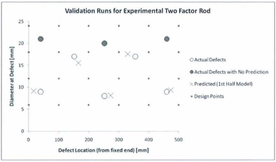

Figure 5.22 - Validation Runs for Experimental Two-Factor Rod

While these results have been somewhat consistent with previous results obtained from the finite element model, the fit of the actual regression models in this case is a contributing factor towards poor predictions. It should be noted that the determination of ‘no solution’ was arrived at using the graphical approach for each of the three points above. The numerical optimization approach did actually return a solution in each of those cases. To understand how the graphical technique was employed to reject the numerical optimization solution, we can refer to Figure 5.23.

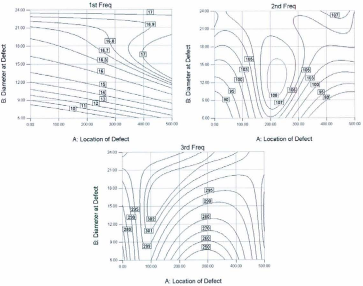

Figure 5.23 - General Contour Plots for Experimental Two Factor Rod

Figure 5.23 shows general contour plots for the first three modal frequency models of the current two-factor rod. As frequency rises for each, we initially see a smooth set of curves that have generally the same shape and progress towards the upper part of the design space. However, for each model we can see that at a certain point those smooth curves become unstable and local oscillation in the response surface occurs. This seems to occur between 16.8 Hz and 16.9 Hz for the first frequency model, between 105 Hz and 106 Hz for the second frequency model and between 299 Hz and 301 Hz for the third frequency model. This limit, at which the models become unstable, occurs when the contour lines are no longer able to be expressed as a function with respect to defect location (a 'function' meaning that only one value of defect diameter is possible for any given defect location). We know that the true behavior should be such that these contour lines are always functions of defect location. This is because we know that for any given local defect, a reduction in defect diameter should always reduce frequency (as seen in Figure 5.15). If these contour lines can no longer be represented by a function, then for a defect at any given location, there can be two or more distinct diameter reductions that produce the same frequency. If the frequency were to always decrease, as expected for any defect diameter reduction, then these multiple frequencies of this type would never exist.

If we plot one of our failed prediction points, we can see that each of the three frequency models produce contour lines that are above the stability limit which we have set. The resulting plot can be found in Figure 5.24 for the first validation run. It is obvious that the contours are above their suggested stability levels and there is no definite solution in this case. Compare this to the successful prediction of a two factor rod defect in Figure 5.19 and we can clearly see the difference.

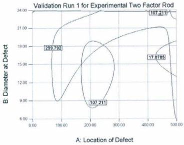

Figure 5.24 - Failed Graphical Approach for Validation Run 1 of the Two-Factor Rod

The regression models for each of the three modal frequencies are generally more stable for more severe defects. More severe in this case refers to a greater reduction in diameter. However, each of the three modal frequencies are stable in a slightly different portion of the design space. Variation in stability between the models is especially sensitive to defect location. Therefore, given a certain set of measured frequencies, we may find that some models are more stable than others. The nature of the defect in a test specimen will dictate which models are most stable. Hence, a guideline can be set that the two most stable models should generally be chosen when making predictions for this scenario. In this case, if the third mode's model (which is normally reserved for distinguishing between multiple solutions) is nearly stable, then we can at least use it to speculate about which solution is correct, given multiple solutions that were found using the first two modes. By simply speculating about what the shape of this extra contour line would look like at the given measured frequency, if the model were still stable and continued to hold the same general shape as lower frequency contour lines, then we may in some cases be able to use it to isolate the correct solution. This will depend upon the degree of stability of that extra model. As the frequencies get higher, this method may no longer be appropriate, and the true solution may become progressively more ambiguous.

We know that different regions of the design space are more stable than others for each model. Therefore, it would be of interest to find the limits of stability of each model. To take that idea one step further, we can find the limits of stability of each model and plot them within our design space in order to get a better idea about which regions will produce better prediction results. Figure 5.25 has the approximate stability limits of each model plotted within the design space. It also has the number of stable models that should result within each region of the design space.

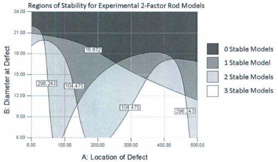

Figure 5.25 - Design Space Stability Variations for the Experimental 2-Factor Rod

Figure 5.25 gives us some idea about how accurate a prediction should be for each region of the design space. For example, if we obtain three stable models and make a prediction within a white region of the design space we would likely obtain a much more accurate prediction than if we obtained one stable model and had to make a prediction within one of the regions corresponding to 'one stable model', while using two slightly unstable models. This plot does not indicate that we cannot make predictions outside of the regions labeled to result in three stable models. There is generally a continuous degradation of stability of each model towards the upper part of the space and the limits here merely represent where the original shapes of the contours are no longer preserved. Within these limits the models are definitely still stable, and likely to result in good predictions. However, if we have a defect that is slightly outside the region corresponding to one of the stability limits, then the resulting contour line would likely still be fairly stable. It may continue to somewhat resemble the shape of more stable contour lines, and may still help in making decent predictions. This plot merely suggests regions where the best predictions will likely result from each model. When using the graphical approach, the most stable modes should generally be most heavily weighted in the prediction process. Therefore, the modes that should be most heavily weighted will depend on the nature of the defect, and will be determined on a case by case basis. Note the three failed predictions from Table 5-10 and Figure 5.22 occurred for defects that were within, or at least very near to, the region of Figure 5.25 that corresponds to '0 stable modes'. Also, this region of general instability is likely due to weak factor effects within the region, which result in slight oscillations in the goodness of fit of the models. In any case, when the correct prediction is not obvious, the experience of the user will likely dictate how graphical results are interpreted.

The experimental and finite element results presented in this section indicate that the defect detection method proposed in Chapter 4 is promising for applications under somewhat controlled conditions. Further work could likely be directed towards streamlining the regression model development process. The effects involved are fairly complex, and would definitely not be captured well using simple factorial or central composite design structures. For now, setting specific modeling concerns aside, we have at least accomplished our goal of validating the method. Next we will begin to investigate applying the method to predict more than two defect parameters.

5.3 The Three-Factor Rod

In this section, we will investigate how complexity increases when we apply the proposed defect detection method to predicting more than two defect parameters. The three-factor rod will extend upon the two-factor rod and include length of defect as its third factor. It will allow us to investigate the feasibility of using this method to predict three factors using three or more measured modal frequencies.

5.3.1 The Three-Factor Rod Scenario

A schematic and the appropriate parameters for the 'three factor rod' are presented in Figure 5.26. It essentially has the same geometry as the finite element representation of the two-factor rod in section 5.2.2. The only obvious difference is the addition of 'length of defect' as a third factor.

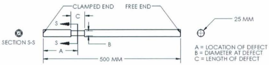

Figure 5.26 - Schematic of the Three-Factor Rod Scenario

5.3.2 Finite Element Representation of the Three-Factor Rod

In this scenario, we will use a finite element model of the three-factor rod to produce data, which can then be used to develop regression models in the usual way. We will then predict defect parameters for extra validation runs using those regression models. This will be done in order to verify that the regression models accurately capture the behaviour of the finite element model. By doing so we will also determine whether the proposed defect detection method can actually be employed to definitively solve for three defect parameters simultaneously.

Defect Factor	Min Level	Max Level	Design Points in Range
Location	5	500	27
Diameter	4	24	11
Length	1	200	9

Table 5-11 - Summary of Factor Ranges and Design Points for FEA 3-Factor Rod

Here we will consider the overall set of factor ranges and design points shown in Table 5-11. The number of design points shown here for each factor is slightly more than the minimum number that we would expect to be required according to section 4.6.2. However, in light of the concerns with model fit and instability of certain design space regions that was highlighted in section 5.2.3, we will fit the regression models in this section to a set of design points that we are certain will be adequate for capturing the specimen's behaviour. By doing this we can commit to validating the essence of the defect detection method for the case when three factors are to be predicted simultaneously. Thus, the method can be validated without concerning ourselves with the details of choosing an appropriate design structure, consisting of a minimum set of design points. In addition, since we are attempting to predict three defect parameters here we need to develop models for the first four modes, so that we have one extra model to be used for eliminating multiple solutions. Since higher modes require a higher model order and a larger number of design points, the number that we have chosen in Table 5-11 is essentially only slightly higher than what was suggested as a minimum set. In addition, we are somewhat unsure at this point about how defect length will affect modal frequencies, and thus including a few extra design points in our models is good practice. One the behaviour of this scenario is better understood, efforts can be taken to reduce the design points used. We are using an automated finite element model to produce the data that will be used for developing regression models as well, and therefore adding extra design points is not of great concern. However, if we were planning to subsequently investigate this scenario using a set of laboratory tests on physical specimens, as we did for the two-factor rod, then investigating a more efficient design structure would be of higher importance. Again, further work is required for developing more efficient design structures that are well suited to fitting the complex regression models involved here.

Hence, concerning ourselves only with examining the nature of the behaviour of the defect detection method in this scenario will suffice for the current study.

In this case, we again need to split our design space according to the method presented in section 4.6.3, due to software restrictions on model order. We already employed this splitting procedure when investigating the two-factor rod scenario so we will not discuss the process in detain here. However, in this case we have two factors that will likely require splitting. We will assume that defect length interacts with modal frequency according to the shape of each mode's curvature, and the relativity of the defect to areas of low curvature, in a manner similar to the way defect location did for the two-factor beam. Therefore, we will need to split both defect location and defect length in this case. In addition, we are trying to predict three defect parameters and so, adhering to the suggestions of Chapter 4, we assume that we need to develop models for four modal frequencies. Since the fourth mode will require a higher model order, we will split defect location into three segments. Since the range of defect length does not span the entire specimen, we will split that factor into two segments. Defect diameter has been shown to be adequately modeled using one segment in the two-factor rod scenario; therefore, we will not split the design space in terms of defect diameter here. We end up with a three dimensional, six-segment design space.

Since obtaining data and modelling six separate design space segments would be time consuming and tedious, we will only model and investigate one of the six segments in this study. Investigating one segment should be adequate since we have already demonstrated that the splitting process works well. This was done when we considered the two-factor rod scenario earlier. The segment we will investigate ranges from 5 mm to 180 mm in terms of defect location and between 1 mm and 100 mm in terms of defect length. In the usual manner, we can now proceed to run the finite element simulations necessary for model development. Due to the large number of design points involved we will not reproduce all of the modal frequency data from the finite element runs here. Instead, we will only reproduce the data for our single design space segment of interest. The amount of modal frequency data required to model this single design space segment is still extensive on its own, and can therefore be found in Appendix B along with the individual factor levels used for each design point. Once we obtain the data, and develop our single segment regression models for each of the first four transverse modal frequencies, we can proceed to validate the models by using them for prediction.

Run	Actual Validation Points [mm]			Transverse Modal Frequency [Hz]			
	Location	Diameter	Length	1st Mode	2nd Mode	3rd Mode	4th Mode
1*	120	16	50	50.94	445.10	1161.20	2245.10
2*	340	18	150	74.36	346.53	1040.16	1962.94
3*	480	12	1	71.19	442.07	1220.66	2343.92
4*	40	10	75	15.92	295.59	810.97	1774.08
5	90	7	40	12.53	350.68	925.47	2063.27
6	370	23	95	72.67	430.21	1169.00	2288.79
7	150	13	70	37.24	408.96	1125.08	2035.86
8	50	9	20	23.88	379.95	1154.63	2218.45
9	250	17	140	58.44	361.17	1030.95	2244.71
10	170	15	170	36.31	351.77	1244.80	1982.30

* Used regression models to predict a design point

Table 5-12 - FEA Measurements for 3-Factor Rod Validation Runs

The modal frequency data for a number of validation runs is presented in Table 5-12. Note that the first four validation runs were actually design points used in model development. Attempting to predict design points is a good first step, since it will allow us to employ the prediction process for validation runs where we expect to obtain somewhat decent predictions. As shown in the table of validation runs, we will perform predictions for a number defects removed from our original set of design points as well.

It should be noted that for some predictions of three-factor rod parameters, we may be required to transform our set of predicted defect parameters back to an equivalent set that does not result in defects extending outside of the geometric limits of the specimen. This technique, as well as the motivation behind it, was described in detail in section 4.5.2. In general, without restricting our models to a certain irregularly shaped design space, we may get defects that can be accurately characterized by multiple sets of defect parameters. Only one solution, out of the multiple solution set, is such that the defect fits within the specimen's geometry, and thus we should always transform back to that solution. For now we will simply note that the transformation is straightforward, and that we did have to perform the transformation for validation run number four in our current set of validation runs.

During the prediction process here, we simply wished to determine whether the single design space segment that we considered would perform as it was supposed to. Proper performance would mean that we obtain accurate predictions when a defect is actually within the factor limits of the segment. It also means that when a defect is not actually within (or at least not close to) the factor limits of the design space segment, then no solution is returned. Thus, if this design space segment behaves in the proper way on its own, then it's easy to imagine that we would get proper predictions over the entire design space using a complete set of design space segments. They would simply have to be considered simultaneously as was done in section 5.2 for the two-factor rod.

Keeping the considerations that were discussed above in mind, we carry out predictions by employing numerical optimization. Numerical optimization was done by considering all four of our modal frequencies in each case. For our series of validation runs, we get the prediction results shown in Table 5-13.

Run	Actual Validation Points [mm]			Should get	Predicted by First Model Segment [mm]			Require	Acceptable
	Location	Diameter	Length	a Prediction?	Location	Diameter	Length	Transformation?	Prediction?
1*	120	16	50	Yes	132.87	15.88	53.88	No	Yes
2*	340	18	150	No	(1st Freq Out of Range)			N/A	Yes
3*	480	12	1	No	(1st Freq Out of Range)			N/A	Yes
4*	40	10	75	Yes	24.83	10	87.76	Yes	N/A
4* (Transformed)	40	10	75	Yes	34.355	10	68.71	N/A	Yes
5	90	7	40	Yes	64.7	7.8	46.46	No	Yes
6	370	23	95	No	(1st Freq Out of Range)			N/A	Yes
7	150	13	70	Yes	150	12.82	66.39	No	Yes
8	50	9	20	Yes	44.54	5.58	1.68	No	Ok
9	250	17	140	No	(No soln./ Below 0.9 Desireability)			N/A	Yes
10	170	15	170	No	(No soln./ Below 0.9 Desireability)			N/A	Yes

* Used regression models to predict a design point

Table 5-13 - Defect Predictions for the 3-Factor Rod Validation Runs

We can see that the predictions were quite good and the model behaved exactly as it should have for each validation run. The model returned an accurate prediction when the defect was within its factor range limits and it returned no solution when the defect was outside of those limits. Since the design space is three-dimensional in this case, it would be difficult to produce a visual comparison of the actual and predicted defects within the design space, as we did for the previous two-dimensional problems. Therefore in order to gain a little further insight into how accurate our predictions were, we can determine the percentage error of each defect parameter for each prediction. Percentage error here is considered as the difference between the actual and predicted values divided by the range of the entire design space for the particular defect parameter in question. These calculated errors are presented in Table 5-14. The errors seem reasonably low for most predicted parameters.

Run	Actual Validation Points [mm]			Predicted by First Model Segment [mm]			Error (as percentage of full factor range)			Average Error
	Location	Diameter	Length	Location	Diameter	Length	Location	Diameter	Length	
1*	120	16	50	132.87	15.88	53.88	2.60%	0.60%	1.95%	1.72%
4* (Transformed)	40	10	75	34.355	10	68.71	1.14%	0.00%	3.16%	1.43%
5	90	7	40	64.7	7.8	46.46	5.11%	4.00%	3.25%	4.12%
7	150	13	70	150	12.82	66.39	0.00%	0.90%	1.81%	0.90%
8	50	9	20	44.54	5.58	1.68	1.10%	17.10%	9.21%	9.14%

* Used regression models to predict a design point

Table 5-14 - Error Involved in Predicting 3-Factor Rod Defects

By spending time to properly weight some modes more than others, and check each prediction using the graphical method, it may be possible to further refine these predictions. However, for now we will consider them to be adequate validation of the method, and we can say that it performs reasonably well when predicting three factors. However, the extra complexity and design points needed to develop regression models do begin to make it somewhat impractical.

Before concluding our validation process, we will look at how the graphical approach works for these three-parameter predictions. Figure 5.27 shows the solution for validation run number seven. We can see that when we use contour lines from one two or three models there is still some ambiguity in the solution. When using three contour lines, they still intersect at two locations. The fourth contour line is indeed required to isolate the correct solution, and when it is added the correct solution becomes obvious. This figure obviously shows only a cross section of our three dimensional design space. The value of defect length in this case is the value returned in the numerical optimization solution for run number seven.

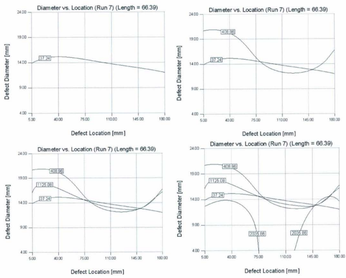

Figure 5.27 - Adding Sufficient Contour Lines in Graphical Method for the 3-Factor Rod

The graphical solution in Figure 5.27 was produced for visualization purposes after we already knew our solution based on numerical optimization. Therefore, we knew the value at which defect length should be set in order to see our solution. However, if we wished to employ the graphical approach to obtain a prediction without any prior knowledge of the solution, then we could still produce two-dimensional cross sections of our design space but sweep through the third dimension until we saw a solution emerge. This process is depicted in Figure 5.28 for validation run seven.

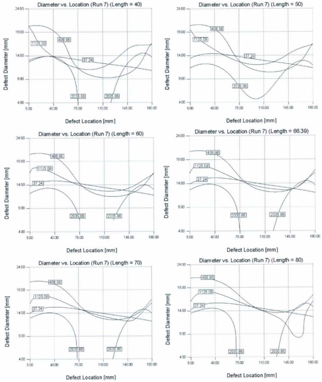

Figure 5.28 - Sweeping through Third Factor with Graphical Method (3-Factor Rod)

As we produce various contour plots using a gradually increasing defect length, we can see that a solution takes shape at the appropriate defect length. When we find the defect length that produces a contour plot with a solution, we simply read the defect diameter and defect location from that two-dimensional plot. In our case, producing these plots was somewhat time-consuming since contour lines were manually superimposed for each plot. However, this process could be easily automated and incorporated into future commercial design of experiments software packages. A superimposed display could be automatically produced for a given set of response measurements and then the user could scroll through a continuous series of plots, which would essentially animate how the contour lines change as the third response changes.

Since this problem is essentially four dimensional for each individual contour line (one frequency response and defect three factors), the solution becomes somewhat more difficult to visualize. The graphical approach also becomes somewhat more complicated. However, as we have shown, it is still possible to employ a graphical approach when predicting three factors and the resulting predictions can generally be good.

In this chapter, we have proven that the defect detection approach suggested in Chapter 4 can be successfully applied in a broad range of scenarios. Further work is still required to expand the method and allow it to handle multiple defects. Further validation also has to be done to see whether three or more factors can accurately be predicted in physical specimens. In addition, refining the design structure is important for reducing the number of design points required in developing regression models. It is also essential for improving the fit of those models to the behaviour of the physical systems that they represent. Nonetheless, the results obtained so far are in favour of using regression models of modal frequency as a basis for detecting damage in structures though the use of modal testing. In the next chapter, we will depart from this method and look at a more practical application of modal testing. We will begin to investigate whether it can be used as a successful non-destructive technique for assessing the condition of full-scale wooden utility poles.

Chapter 6

Full-Scale Utility Pole Testing

As a step aside from the purely academic problems that were addressed in Chapter 4 and Chapter 5, we will now undergo a preliminary investigation to determine whether modal impact testing is feasible for assessing the condition of in-service wooden utility poles.

As was alluded to earlier, wooden poles do not generally contain simple ideal defects in the form of notches and holes. The condition of a utility pole can be such that various forms of deterioration, including rot, ant and woodpecker damage, can be randomly dispersed throughout the specimen. Cracks, knots and grain defects are also likely to be present in most specimens. This, combined with the orthotropic behaviour of wood, makes for a specimen that is very difficult to assess structurally. In this case, localized defects cannot be considered on an individual basis and material condition measured at a single location is not sufficient to make a judgement call on structural integrity. Some method that considers the specimen as a continuum must be pursued.

In this chapter, we will discuss the difficulties involved with applying the method suggested in Chapter 4 and Chapter 5 to full scale pole testing. We will also focus on a separate technique that uses measured modal damping ratios for assessing the maximum stress that a pole can withstand before failure occurs. The difference between this concept and determining a pole's ultimate material strength will be clarified as well. Note that Appendix C and Appendix D contain supplementary data relevant to this chapter. Appendix C contains measurements from the full-scale pole tests. Appendix D contains plots and other material related to the use of damping ratio for assessing the condition of poles.

6.1 Static Testing of Full Scale Poles

Since we eventually plan to relate modal parameters to the condition of full-scale poles, a series of destructive laboratory tests were performed on fourteen full-scale poles in order to determine their material properties. Three of the fourteen poles were five years old, but never used in service (labelled BF1, BF2 and BF3). The others were removed from service after an appropriate service life (which was not necessarily consistent between specimens). As much as possible ASTM standards were followed during the series of static tests, as well as for calculation of material properties from the test data (ASTM, 1999). The equipment used in the static tests is presented in Table 6-1 and a test in progress is shown in Figure 6.1.

Item	Description	Model	Manufacturer
LVDT's	+- 2in Range, 40 VDC, 2.5V/in, Used to Measure Clamp Flexure	JEC-AG	Honeywell
Draw Wire Potentiometer	1000mm Range, Used to Measure Deflection 12' from GL	WPS-1000-MK46	Micro Epsilon
Draw Wire Potentiometer	3000mm Range, Used to Measure Deflection 24' from GL	WPS-3000-MK120	Micro Epsilon
Photoelectronic Time Transit Sensor	10000mm Range, Used to Measure Dflection 24' from GL (Relplacement)	X 1TA100MHT88	Wengler
Draw Wire Potentiometer	7500mm Range, Used to Measure Deflection 36' from GL	WPS-7500-MK120	Micro Epsilon
Draw Wire Potentiometer	7500mm Range, Used to Measure Deflection 36' from GL (Replacement)	WDC-7500-P115	Micro Epsilon
Draw Wire Potentiometer	10000mm Range, Used to Measure Deflection at POL	WDS-10000-P115	Micro Epsilon
Draw Wire Potentiometer	1250mm Range, Used to Measure Longitudinal POL Displacement	WPS-1250-MK46	Micro Epsilon
Strain Gauge Force Cell	11000 lb Limit, Used to Measure Applied Load at POL	5373	Sensotec
Software	Labview / Measurement and Automation Explorer	----	National Instruments

Table 6-1 - Equipment used in Static Tests of Full Scale Poles

Figure 6.1 - Full Scale Utility Pole Test Bed (Testing Specimen BF3)

6.1.1 Static Test Procedure and Results

Each destructive test was performed by first weighing the specimen using a load cell attached to the laboratory's overhead crane, so that density could later be determined. The specimen was then clamped at an appropriate ground line position near the butt end. The location of ground line for each specimen was measured from the butt end as ten percent of the specimens overall length plus two feet. This is typical of an in-service pole. The clamp was secured to the lab's concrete floor.

Next, appropriate non-destructive tests (NDT) were performed on the pole including modal impact testing (which will be discussed further in section 6.2), ultrasonic testing (which will be discussed in section 6.2.4) and resistograph drill testing (performed using a RESIF300-S resistograph manufactured by IML). Geometry such as length and circumferences (taken at five foot intervals) were also measured and recorded.

Once all non-destructive tests were complete, the static test was performed by applying a vertical load until failure occurred. The load was applied at a position of two feet from each poles tip using a hydraulic winch mounted above the point of load. A load cell attached in-line with the winch measured applied load. The hydraulic winch was positioned on a carriage which was held in place using the laboratory's overhead crane. The winch was mounted on a trolley, and was free to move in the longitudinal direction (along the poles length) as the pole deflected (as shown in Figure 6.2). This longitudinal displacement was measured during each test, and was taken into account for stress calculations. Controlled flow in the winch's hydraulic lines ensured that a proper strain rate was maintained during tests. Vertical deflection of the pole was also measured at four locations (at the point of load as well as twelve, twenty-four and thirty-six feet from the ground line) as each pole was stressed. LVDT's were positioned on either side of the clamp and measured the angle of flexure in the clamp. This flexure was also taken into consideration when performing calculations. All measurements were sampled at a rate of two Hertz and recorded to a computer file.

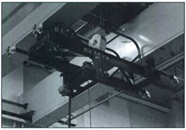

Figure 6.2 - Winch and Trolley System used to Apply Loading to Poles during Static Tests

Appropriate calculations were later performed for each pole in order to determine elastic modulus, density, maximum stress at the break location, maximum stress at the ground line, yield stress at the break location and yield stress at the ground line. A summary of the results for all fourteen poles is presented in Table 6-2.

Run	Pole	Species	Elastic Modulus [Mpa]	Density [Kg/m^3]	Max Stress at GL [Mpa]	Max Stress at Break [Mpa]	Yield Stress at GL [Mpa]	Yield Stress at Break [Mpa]	Break Location from GL as fraction of Clamped Length	Max Applied Load at POL [N]	Yield Applied Load at POL [N]
1	BF1	SYP	10446	614.4	41.10	29.20	27.84	20.23	0.44	14245	9348
2	BF2	SYP	11734	597.2	50.92	39.30	22.31	17.40	0.26	15692	6677
3	BF3	SYP	11004	684.4	59.08	59.08	39.91	39.91	0.00	21367	14000
4	1st Old	SYP	9401	715.5	22.35	17.69	13.87	11.07	0.33	5253	3205
5	2nd Old	SYP	7549	697.6	21.86	22.10	14.78	14.97	0.10	5431	3606
6	3rd Old	WRC	5907	419.0	21.05	15.59	15.79	12.18	0.81	6143	4496
7	4th Old	WRC	4809	434.5	12.65	20.78	12.65	20.78	0.62	6677	6677
8	5th Old	SYP	13050	649.9	32.30	32.31	18.79	18.81	0.02	6989	4006
9	6th Old	SYP	5348	430.4	17.07	10.32	9.98	6.14	0.83	9704	5609
10	7th Old	SYP	13039	750.1	46.79	51.40	33.86	37.65	0.32	10795	7612
11	8th Old	SYP	3703	525.1	13.30	10.83	13.30	10.83	0.65	6201	6201
12	9th Old	SYP	9339	617.7	29.02	20.61	19.85	14.27	0.47	6254	4207
13	10th Old	SYP	6223	712.3	16.99	11.31	12.30	8.21	0.62	4296	3098
14	11th Old	SYP	7920	767.3	25.84	11.30	17.56	7.98	0.72	5150	3405

Table 6-2 - Static Test Results for Full Scale Poles

As was mentioned in the literature review of Chapter 2, strength has been found to correlate to some degree with elastic modulus in other applications. In order to determine if this is the case for our full scale poles as well, we can plot maximum ground line stress against elastic modulus. This is shown in Figure 6.3. Note that we do not know the ultimate material strength at ground line, since the poles did not always fail at the ground line. This point will be emphasized in further sections.

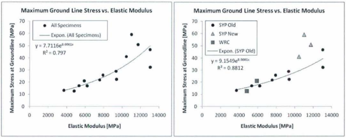

Figure 6.3 - Max. GL Stress vs. Elastic Modulus for Full Scale Poles

The left plot in the figure shows that when considering all specimens there is a significant correlation of R^2=0.797. We can also see in the right plot that the goodness of fit improves to R^2=0.8812 when only 'old' southern yellow pine specimens are considered in the regression process. An exponential regression model was employed in each case because it yielded slightly better results than other common models. The western red cedar specimens, as well as the 'new' southern yellow pine specimens were also plotted on the right for comparative purposes. We can see that the new pine specimens fell significantly above the trend line of old specimens. The old cedar specimens fell reasonably close to the trend line. Some upcoming sections will focus heavily on creating models for only the pine specimens (new and old together). Grouping all pine specimens together is done because of the limited amount of data that has been collected in the current study. However, the results shown here for maximum stress vs. elastic modulus indicate that there are distinct differences in the behavior of certain parameters between age groups, and age should likely be taken into consideration in future work if sufficient data is available.

6.1.2 Some Sources of Error in the Static Tests

Some sources of error were noticed in this series of tests and should be attended to for future tests. First, the trolley was noticed to stick and move in sudden incremental steps throughout each test. The rollers or tracks may require modification so that the trolley rolls more smoothly. The hydraulic lines were oversized for the application as well, and added unnecessary weight. The lines had to be pulled along as the trolley moved, which likely contributed to some of the sticking. In addition, the trolley did not start from a position that was perfectly level. This made it difficult to correctly position the trolley before each test. It also affected 'trolley displacement vs. point of load' curves. Three different 'trolley vs. POL' deflection curves are shown in Figure 6.4. The first curve shows an instance where the trolley was positioned well ahead of the POL, resulting in the trolley not moving until a significant POL deflection was realized. The second curve depicts the actual anticipated behavior, where the trolley moves in a smooth curve, which is essentially tangential to the x-axis. It should be tangential if the trolley starts applying a vertical load near the tip of a horizontal pole, so that the point of load initially deflects directly upwards and then progressively more towards the butt end of the pole. The third curve shows an instance when the trolley likely started behind the POL. The trolley initially moves quickly to catch up with the POL once the load is applied and the winch line is drawn tight. Discontinuities in the curves also show that the trolleys motion was abrupt. A curve fit was used in most cases to estimate trolley deflection due to the discontinuous nature of the curves. These curves were used to estimate the trolley displacement at yield and failure deflections, so that the longitudinal displacement of the point of load could be taken into account during stress calculations.

Therefore, error in estimating trolley displacement likely resulted in some error in our measured properties.

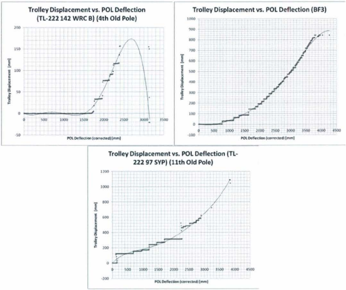

Figure 6.4 - Trolley vs. POL Displacement Curves Depicting Error in Results

Other error sources could include the LVDT's, which were used to measure clamp flexure, being initially positioned on the pole at some distance away from the clamp. Since the section of pole between the LVDT and the clamp on the poles cantilever side was under stress during the static tests, there was likely some pole deflection in this section that showed up as clamp deflection. Error in the measurement of clamp deflection may have also introduced error in the calculated properties. This was noticed to be the case for at least one pole that failed at the ground line.

Significant deflection in the section of pole between the LVDT and the clamp was witnessed after the pole began to yield. Bulging of surface fibers in this region during yielding added to the error from pure pole deflection. The cantilever side LVDT was positioned as close as possible to the clamp for subsequent pole tests.

One other notable source of error is that poles were not loaded from a purely unstressed condition. Since they were all cantilevered, they were subjected to some initial loading under their own weight. The weight loading applied to each pole would have affected the material property calculations due to initial displacement errors from sagging, as well as applied load errors as poles had to be lifted up to their unstressed position before 'positive' stress started to be applied. In addition, poles were of varying density and geometry (including taper) which meant that each pole was affected differently due to mass loading. Attempts to correct for this error, by determining the load and displacement required to align the tip directly with the butt (at the same height above the floor), were abandoned since misalignments due to irregularities in the shape of the poles often outweighed by far misalignments due to mass loading.

6.2 Modal Impact Testing of Full Scale Poles

The procedure for the modal impact tests of full-scale poles followed the general guidelines presented in section 3.3. For the tests on full-scale poles, bandwidth was always taken so that all frequencies of interest occurred within the first eighty percent in order to mitigate errors due to bandwidth filtering. This resulted in a chosen bandwidth of either 64 or 80 Hz, depending on the specimen. 4096 spectral lines were taken within the band, resulting in a resolution of at least 0.01953 Hz for each specimen, sometimes better depending on the chosen bandwidth. Accelerometers were positioned in the vertical plane (the same plane as loading during the static tests) at twelve and thirty feet. Another accelerometer was positioned at the position of impact for each pole, which was always near the tip. Impacts were performed near the tip in order to avoid modal nodes (for all reasonably low order modes), and to adequately excite the pole with modest impact forces. A hammer tip with appropriately low stiffness was chosen so that the frequency band of interest could be excited reasonably well. Six impacts were performed at a single impact location in each test. The six runs were then averaged, and software determined modal parameters in each case.

Impacts near the tip would not be feasible for upright, in-service poles. Therefore, to determine the feasibility of performing the impacts within reach from the ground line in the field, two specimens were tested with impacts at five, seven, ten and fourteen feet. Indeed, modal data was adequately obtained in each case. The first mode, however, was somewhat more difficult to excite with impacts closer to the ground line. Higher impact forces were required when testing near the ground line as well, although the impacts were still physically manageable.

For each pole, attempts were made to measure frequency and damping for six modes. The tests were only performed once in most cases and therefore modal parameters for each of the six modes were not definitively obtained for each specimen. Results from modal impact tests on the full-scale poles are summarized in Table 6-3.

Run	Pole	Species	Frequency [Hz]						Damping Ratio					
			Mode 1	Mode 2	Mode 3	Mode 4	Mode 5	Mode 6	Mode 1	Mode 2	Mode 3	Mode 4	Mode 5	Mode 6
1	BF1	SYP	0.9630	4.6810	11.9080	22.5580	35.7990	51.6800	0.0076	0.0081	0.0090	0.0126	0.0097	0.0093
2	BF2	SYP	1.1680	5.6090	14.3360	27.4750	44.2430	63.4950	0.0059	0.0058	0.0065	0.0131	0.0110	0.0095
3	BF3	SYP	1.1293	5.5001	14.0853	26.9304	43.0057	63.1326	0.0062	0.0066	0.0075	0.0091	0.0112	0.0089
4	1st Old	SYP	0.8402	3.9448	9.8480	18.0077	29.9616	44.0971	0.0125	0.0114	0.0184	0.0181	0.0185	0.0234
5	2nd Old	SYP	0.9390	4.8180	12.0460	23.0500	36.1540	N/A	0.0145	0.0110	0.0190	0.0144	0.0214	N/A
6	3rd Old	WRC	0.8930	3.7550	9.2350	16.7380	N/A	N/A	0.0070	0.0055	0.0062	0.0240	N/A	N/A
7	4th Old	WRC	1.2067	4.3712	10.3949	19.2092	31.1546	45.2459	0.0066	0.0062	0.0047	0.0082	0.0095	0.0140
8	5th Old	SYP	1.0219	4.3579	10.5789	19.7115	31.5294	45.8768	0.0060	0.0066	0.0077	0.0114	0.0177	0.0128
9	6th Old	SYP	1.3942	6.3544	15.4209	29.3003	N/A	N/A	0.0081	0.0085	0.0078	0.0254	N/A	N/A
10	7th Old	SYP	0.8456	3.6932	9.0678	16.4740	27.4990	39.1310	0.0053	0.0066	0.0064	0.0098	0.0130	0.0093
11	8th Old	SYP	0.9240	3.7960	9.2490	16.6640	24.4030	N/A	0.0054	0.0141	0.0211	0.0312	0.0359	N/A
12	9th Old	SYP	1.5042	6.5706	15.1822	28.9535	45.5076	66.5031	0.0092	0.0088	0.0119	0.0205	0.0337	0.0267
13	10th Old	SYP	1.8101	6.8287	17.1540	32.0770	48.8970	N/A	0.0054	0.0139	0.0156	0.0254	0.0159	N/A
14	11th Old	SYP	0.8977	3.9430	9.5590	17.6660	27.2200	39.4620	0.0231	0.0113	0.0255	0.0243	0.0120	0.0355

Table 6-3 - Modal Impact Test Results for Full Scale Poles

6.1 Modal Frequency as an Indicator of Pole Condition

Chapter 4 and Chapter 5 dealt exclusively with modal frequency, and used the combined effect of multiple modal frequencies to define the location and extent of individual defects. The method presented in those chapters, as least at its current stage of development and with the limited amount of data available in the current study, is not suited to defining the condition of wooden utility poles. As previously mentioned, damage in a utility pole is not likely to be localized, and is not likely to be characterized by some modest number of numeric factors, such as depth and width. It is more likely that some nonlinear distribution of deterioration exists throughout the pole. This topic will be discussed further towards the end of the chapter. In addition, material properties and geometry, which also have an effect on frequency, are likely to be unevenly distributed throughout the pole. Chapter 5 showed that the regression model method of using frequency was well suited to specimens with known and consistent properties. However, if properties change throughout the specimen, then the effect of those changes on frequency must be included in the regression models somehow. That would make the regression models very complex, and the amount of data required to characterize all distributed factors would be prohibitive. With the already limited dataset for full scale poles in this study, developing regression models to characterize all the necessary factors that affect frequency is simply not an option.

The predicted modal frequency, based on finite element analysis, is presented in Appendix C along with the experimentally measured modal frequency for each pole. The finite element frequencies are found using models with geometry based on the measured lengths and circumferences of individual poles. They are found in two ways for each specimen, first using the measured density and elastic modulus of each pole, found from the laboratory static test measurements, and second using published material properties for the appropriate wood species. These frequencies are presented in a table similar to Table 6-4 for each pole.

Modal Test (TL-222 108 SYP A) (1st Old Pole)				
Transverse Mode	Measured Frequency [Hz]	Measured Damping ratio	FEA Undamped Frequency (Measured Properties)	FEA Undamped Frequency (Published Properties)
1st	0.840	0.0125	0.827	1.107
2nd	3.945	0.0114	4.092	5.478
3rd	9.848	0.0184	10.486	14.038
4th	18.008	0.0181	20.098	26.905
5th	29.962	0.0185	32.726	43.810
6th	44.097	0.0234	48.392	64.782

Table 6-4 - Modal Test Data for '1st Old Pole'

By determining the ratio of measured frequency to frequency found using finite element analysis with published properties, we essentially arrive at a parameter that is normalized with respect to the varying geometry of each pole. If we were attempting to develop regression models to express this ratio as a function of factors that affect frequency, we could possibly neglect geometry as a significant factor. Essentially, geometry should be accounted for by determining the ratio. This has not been confirmed yet and is only a suggestion. If regression models of frequency are to be obtained for future pole assessment, then this type of normalization may be needed in order to create decent models from limited data. Other factors would definitely have to be considered as well, such as density (which may possibly be represented by moisture content). Even then, characterizing the geometry of all the defects present in a pole is not likely to be possible, and models that define strength, instead of particular defects, would likely have to be pursued. By normalizing frequency in this way, and not considering any other potentially important factors, we see that some level of correlation does seem to emerge. The measured first modal frequency essentially has no correlation with either maximum break location stress or maximum ground line stress. However, when they are normalized with FEA predictions of first natural frequency using individual pole geometries and published properties, modest correlations take shape. However, the correlations are in fact quite modest, at 0.305 and 0.243 respectively. The slope of the linear model is also very shallow. This level of correlation is obviously not sufficient for strength predictions, and further work has to be done. Although, it is at least holds some promise for the eventual use of frequency in assessing the condition of full scale poles.

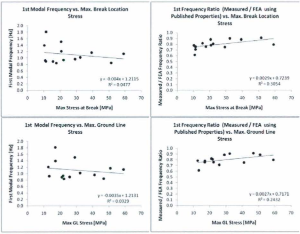

Figure 6.5 - Normalizing Modal Frequency using FEA Predictions

Even though measured modal frequencies will not be used here to develop models for predicting the strength of full scale poles, it can at least validate the results of our static tests to some degree. Referring back to Table 6-4, we can see that each measured modal frequency is much closer to its corresponding FEA predicted frequency when measured properties are used, than when published properties are used. This is consistently true for each pole tested. Note again that the measured properties were obtained from our static test data. This leads us to believe that the true material properties of each specimen, which affected modal frequencies, are much closer to our measured properties than they are to published average values. This provides one more level of certainty that our static tests were performed adequately. There are obviously some errors that will account for the difference between the measured frequency and the FEA predicted frequency using measured properties. These include, but are not limited to, the FEA model having an ideal fixed end condition, whereas the physical poles were secured by a clamp with some compliance. Also, the material properties of the physical poles were probably not evenly distributed throughout the pole, whereas properties were evenly distributed in the FEA models. For example, we measured an average density based on the poles geometry and mass. However, density is likely to change throughout the pole. In fact, moisture content, which is known to affect density, was noticed to be much higher near the center of the poles cross section compared to its surface. Other such variations in material properties are likely in the physical specimens.

6.2 Modal Damping Ratio as an Indicator of Pole Condition

Throughout most of the current study, modal frequency has been the parameter of primary concern. It was the only factor considered in the defect detection method presented in Chapter 4 and Chapter 5, partly because of the ease of determining undamped natural frequencies for ideal specimens using theory and finite element analysis. This allowed for simulation of a number of scenarios before laboratory experiments were undertaken. However, it was discussed in the previous section that frequency is not suited to assessing full-scale poles at this point. Therefore, we will shift our focus towards the use of modal damping.

Determining the modal behaviour of a specimen with a known level of damping is straightforward. If that were of interest, it would have been covered along with the other theoretical background in Chapter 3. However, attempting to deduce through theoretical means how modal damping changes with the introduction of defects is a more complex matter. Distinct geometric defects in an otherwise clear specimen (such as a lab specimen with an artificially machined defect) will possibly affect damping much differently than a specimen with a localized deterioration of material. With material that is deteriorating progressively, such as wood, there may be layers separated (or splintered) from the surface that are unstable during modal excitation. These fringe pieces may 'flap' around (for lack of a better word) as the specimen vibrates, continuously impacting the surface at various locations and dissipating energy; thus creating a higher level of damping in the specimen. For a wooden pole in transverse vibration, cracks or even separation along the rings of grain may allow for layers of material to rub against each other as well. Many sources of damping such as these could potentially be distributed throughout the specimen with varying degrees of severity. This type of deterioration is complex and essentially impossible to introduce in a controlled manner. It is also prohibitive with respect to simulation or traditional design of experiment techniques that require controlling parameters. As a result, the exclusive use of experimental testing of actual deteriorated specimens, with random levels of naturally developed deterioration, seems like the best approach for examining the way damping changes with damage in wooden poles.

Note that Appendix D contains supplementary material relating to this section including extra plots and figures that are not includes here.

6.2.1 Modifying the Regression Model Method to Accept Damping as its Response

Some of the various means by which damping could be developed in wooden poles were mentioned above. It stands to reason, by comparison to the behaviour of modal frequency, that if any of these sources of damping were located near a location of low curvature for a mode shape, then their effect on the modal damping ratio of that particular mode should be diminished. For example, if a longitudinal crack is located near a location of low curvature then there is little oscillation of strain to allow for surfaces within the crack to rub together. This type of behaviour (varying degree of effect depending on the proximity of damage to locations of low curvature) was the foundation for proposing the use of frequency as a damage identifier in previous chapters. It allowed for regression models of individual modal frequencies to be independent with respect to how they were affected by multiple defect parameters (such as defect size and location). That in turn allowed multiple modal frequencies to be used simultaneously for determining multiple defect parameters. Since it is logical that damping sources should behave in a similar manner, it may be possible for the method to be modified so that modal damping, instead of frequency, is used to indentify localized damage. However, applying this approach in practice would be a difficult task to accomplish.

In order to apply the approach suggested above, the nature of defect would have to be such that localized deterioration was naturally preferred over distributed deterioration. In some scenarios this could potentially occur. For example, if wooden poles were located in wet marshy soil one can imagine local rot being more common near the ground line. Other areas of poles, such as near holes that were drilled to mount cross members or hardware, could also be prone to localized rot due to the exposure of heartwood with potentially lower levels of preservative. Note that failure did actually occur at a drilled hole for at least one specimen in the current study. However, it is unclear whether this was due to local deterioration near the hole, the hole itself creating a stress concentration or simply due to the hole's effect on reducing the cross sectional second moment of area. Additional applications where localized deterioration may be favoured could exist in other fields as well, such as when dissimilar alloys are coupled resulting in localized galvanic corrosion. This type of approach could be pursued here if enough specimens with localized damage were analyzed, allowing regression models to be fit to an appropriately high order. However, as was the case with modal frequency, the low number of specimens involved in the current series of full-scale pole tests is very likely to be inadequate for developing regression models that capture the effect of every important factor. In addition, distributed deterioration and distributed properties (such as density, grain direction, diameter etc.) actually seem far more common than local deterioration for full-scale poles. These issues essentially render the regression model method unsuitable for the current application, at least at its current level of development. Therefore, the described method of adapting the regression model method to accept damping as its response, although noteworthy, will not be pursued here.

6.2.2 Damping Ratio as an Indicator of Maximum Fiber Stress at Break Location

Despite the low number of specimens, and the difficulties involved in fitting regression models, we can try an alternate approach here for the use of damping as an identifier of the condition of full-scale poles. Since for each pole deterioration is observed to be distributed over the entire specimen, it is likely that each mode's damping ratio is somewhat affected because of the likelihood that at least some deterioration occurs in areas of high curvature for each mode. In addition, deterioration should be proportional to reduction in maximum allowable fiber stress by definition.

6.2.2.1 The Use of Actual Measured Modal Damping Ratio

We can determine whether the above statements are valid simply by plotting modal damping ratio vs. fiber stress for each mode and observing whether a correlation exists. Note we are assuming here that maximum stress occurs at the surface furthest away from the neutral axis of the cross section for any given bending load. This may not strictly be true if material properties vary across the cross section. In general, properties probably would not be constant across any given cross section of a wooden pole. Heartwood and sapwood would vary in their properties. Preservative level gradients, that favour wood towards the surface, would also leave some areas more prone to deterioration than other areas. Nonetheless, for simplification purposes, we will assume that deterioration varies only along the poles length, and not across any given cross section.

For wooden poles in the current study there does indeed seem to be a distinct correlation between damping ratio and strength. In Figure 6.6 we can see the first six modal damping ratios (data from Table 6-3) plotted against the maximum fiber stress realized at the break location for each pole (date from Table 6-2). A second order polynomial is also fit to the data for each mode. Note that in the plots, SYP refers to southern yellow pine and WRC refers to western red cedar. The number of cedar poles included in this study was not adequate to allow for modelling each species separately. They were included in the plots for comparison with the behaviour of pine. However, they were not included in the data used to determine the goodness of fit. Also, note that data for the fifth and/or sixth modes was not obtained for some specimens.

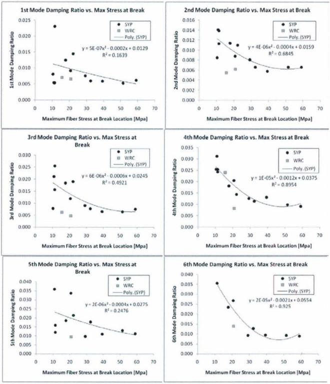

Figure 6.6 - Modal Damping Ratios vs. Maximum Break Location Stress

By inspecting Figure 6.6, we can see that the damping ratio is generally higher for poles with a lower maximum fiber stress at the location of failure. Using the second order polynomial fit, damping ratio also shows correlation, to some degree, with maximum fiber stress at the break location for each of the first six modes. However, the goodness of fit, represented here by the R^2

value, has a high degree of variability between modes. The R^2 value does not seem to favour higher or lower modes, and because of the high variability, we may not be convinced that the relative goodness of fit for each individual mode would be retained if we were to perform the same test on a separate set of poles.

At this point, there no clear explanation for the variability in goodness of fit between modes. Perhaps this variability is somehow related to the natural frequency of the corresponding modes, more so than the damping itself. The clamp is known to have some compliance, and perhaps a mode exists where the un-deflected pole rotates via flexure in the clamp. The frequency of this type of mode, if present, would depend on the stiffness of the clamp. However, it would also depend upon the location of the center of mass of the pole, which is actually somewhat variable between poles. This can be seen in Appendix C along with the rest of the measured full-scale pole data. If the frequency of this mode is near the frequency of a particular transverse mode, then interaction between them could affect how easily the transverse modes are excited and measured in practice. These issues could create higher variability in the accuracy of damping measurements for the particular modes affected. Torsion modes, or transverse modes in other planes, with frequency near the frequency of transverse modes we wish to measure, could also cause interference and affect damping measurements in a similar manner. Note that this is merely speculation at this point. Perhaps future work will shed light on the nature of the variation in goodness of fit between modes.

6.2.2.2 The Use of Average Modal Damping Ratios

There was shown to be a significant correlation between modal damping ratio and maximum stress at the location of failure for each the first six modes. However, as mentioned earlier the level of correlation varied between modes. Here we will investigate whether averaging the modal damping ratio for multiple modes is effective in diluting some of this variability.

As mentioned earlier, each specimen may contain a variable amount of deterioration, which is distributed along its length, and therefore each mode may be affected in a different manner depending on the proximity of that deterioration to areas of low curvature. By averaging the damping ratios of multiple modes, we can attempt to ensure that the deterioration condition of each pole is represented in a consistent way. Damping should be affected, for at least some of the modes considered, regardless of the specific distribution of deterioration. The average damping ratio across multiple modes is summarized in Table 6-5. These averages start with lower modes (initially only the first two) and progressively consider an increasing number of modes until all six measured modes are averaged. The averages then progressively consider a fewer number of modes by eliminating lower modes from the process. The initial set of averages that consider an increasing number of modes (up to modes one through four) is plotted against the maximum stress at each poles break location in Figure 6.7. Again, data for stress comes from Table 6-2, and a second order polynomial is fit to the data in each case. The other averages, that progressively eliminate lower modes, will be discussed later in this chapter.

Pole	Species	Average Modal Damping Ratio								
		Modes 1 to 2	Modes 1 to 3	Modes 1 to 4	Modes 1 to 5	Modes 1 to 6	Modes 2 to 6	Modes 3 to 6	Modes 4 to 6	Modes 5 to 6
BF1	(SYP)	0.007850	0.008233	0.009325	0.009400	0.009383	0.009740	0.010150	0.010533	0.009500
BF2	(SYP)	0.005850	0.006067	0.007825	0.008460	0.008633	0.009180	0.010025	0.011200	0.010250
BF3	(SYP)	0.006400	0.006767	0.007350	0.008120	0.008250	0.008660	0.009175	0.009733	0.010050
1st Old	(SYP)	0.011950	0.014100	0.015100	0.015780	0.017050	0.017960	0.019600	0.020000	0.020950
2nd Old	(SYP)	0.012750	0.014833	0.014725	0.016060	N/A	N/A	N/A	N/A	N/A
3rd Old	(WRC)	0.006250	0.006233	0.010675	N/A	N/A	N/A	N/A	N/A	N/A
4th Old	(WRC)	0.006400	0.005833	0.006425	0.007040	0.008200	0.008520	0.009100	0.010567	0.011750
5th Old	(SYP)	0.006300	0.006767	0.007925	0.009880	0.010367	0.011240	0.012400	0.013967	0.015250
6th Old	(SYP)	0.008300	0.008133	0.012450	N/A	N/A	N/A	N/A	N/A	N/A
7th Old	(SYP)	0.005950	0.006100	0.007025	0.008220	0.008400	0.009020	0.009625	0.010700	0.011150
8th Old	(SYP)	0.009750	0.013533	0.017950	0.021540	N/A	N/A	N/A	N/A	N/A
9th Old	(SYP)	0.009000	0.009967	0.012600	0.016820	0.018467	0.020320	0.023200	0.026967	0.030200
10th Old	(SYP)	0.009650	0.011633	0.015075	0.015240	N/A	N/A	N/A	N/A	N/A
11th Old	(SYP)	0.017200	0.019967	0.021050	0.019240	0.021950	0.021720	0.024325	0.023933	0.023750

Table 6-5 - Average Damping Ratio for Full Scale Poles

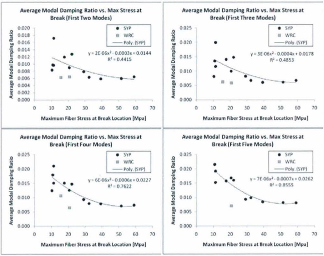

Figure 6.7 - Average Damping Ratios vs. Maximum Break Location Stress

It can be seen in Figure 6.7 that as the number of modes used in the averaging process increases so does the goodness of fit. Note again that only southern yellow pine specimens were included in the goodness of fit calculation. While the number of averaged modes increases from two to five the R^2 value progressively increases from 0.4415 to 0.8555. If we include all six measured modal damping ratios in the averaging process then the goodness of fit increases once again to 0.9387, as shown in Figure 6.8. This seems to be a significant and promising result in favor of using modal testing, and more specifically modal damping ratio, as an indicator of the condition of full scale poles.

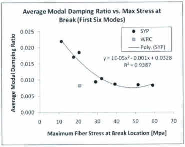

Figure 6.8 - Six-Mode Average Damping Ratio vs. Maximum Break Location Stress

It also becomes increasingly clear that, as the correlation improves with consideration of extra modes, the cedar specimen does not fit with the trend of the southern yellow pine. It clearly becomes an outlier as the southern yellow pine data progressively converges to fit the second order polynomial model. This suggests that separate models should ultimately be developed for each individual species used in the field. Also note again that fewer points are included on each plot that uses the fifth and sixth modes, since data for those modes was not obtained for all specimens.

6.2.2.3 The Use of Average Normalized Modal Damping Ratios

If we look back at Figure 6.6 we can see that the magnitude of damping is not necessarily the same for each mode. Notably, damping ratio for mode two does not reach 0.015 for any of the specimens, whereas for modes five and six some specimens reach levels of damping above 0.035. This difference in amplitude between modes is difficult to explain with any certainty. However one possible explanation could be that each pole's cross section is not constant along its length. Each pole has a certain degree of taper and therefore areas with a smaller cross section could be more susceptible to larger deflections during vibration. Larger deflections in some cases could potentially increase the relative effect of damping sources in those areas. Therefore depending on the shape of each mode, and the location of high levels of curvature, these areas of increased damping effect could affect each mode differently. If this is feasible, then variation in taper between individual poles could result in some of the lack of fit in the damping vs. maximum stress curves as well. Therefore, normalizing data for each pole with respect to the pole's relative taper could potentially improve the fit of the above models. This possibility is noted, but will not be investigated in the current work.

Regardless of the root cause of the variability in relative amplitude of damping ratio between modes, it is of interest to try and alleviate the weighted preference of any individual mode during our averaging process. The averaging process used earlier was one attempt to consider the cumulative effect of damage on damping ratio evenly across all modes. However, modes with higher average damping ratio, and larger ranges in damping ratio, would indeed have been more heavily weighted. This is simply because a certain percentage change over a large range for one mode has a larger effect on the average than an equal percentage change over a small range for another mode. Therefore, a further attempt to bring all modes into equal consideration would be to employ a simple normalizing process. Here we will consider the normalized damping ratio of each specimen as the relative magnitude of individual damping ratios with respect to the range in damping ratios for the entire set of specimens. This will be done on an individual mode basis and is perhaps better explained in equation form:

$$\zeta_{n,i_{Norm}} = \frac{\zeta_{n,i}}{\zeta_{n_{Max}} - \zeta_{n_{Min}}}$$

Where:

$$i = Index\ Number\ Identifying\ Individual\ Specimens$$

$$n = Mode\ Number$$

Pole	Species	Normalized Damping Ratio					
		Mode 1	Mode 2	Mode 3	Mode 4	Mode 5	Mode 6
BF1	(SYP)	0.1292	0.2771	0.1361	0.1584	0.0000	0.0150
BF2	(SYP)	0.0337	0.0000	0.0052	0.1810	0.0496	0.0226
BF3	(SYP)	0.0506	0.0964	0.0576	0.0000	0.0573	0.0000
1st Old	(SYP)	0.4045	0.6747	0.6283	0.4072	0.3359	0.5451
2nd Old	(SYP)	0.5169	0.6265	0.6597	0.2398	0.4466	N/A
3rd Old	(WRC)	N/A	N/A	N/A	N/A	N/A	N/A
4th Old	(WRC)	N/A	N/A	N/A	N/A	N/A	N/A
5th Old	(SYP)	0.0393	0.0964	0.0681	0.1041	0.3053	0.1466
6th Old	(SYP)	0.1573	0.3253	0.0733	0.7376	N/A	N/A
7th Old	(SYP)	0.0000	0.0964	0.0000	0.0317	0.1260	0.0150
8th Old	(SYP)	0.0056	1.0000	0.7696	1.0000	1.0000	N/A
9th Old	(SYP)	0.2191	0.3614	0.2880	0.5158	0.9160	0.6692
10th Old	(SYP)	0.0056	0.9759	0.4817	0.7376	0.2366	N/A
11th Old	(SYP)	1.0000	0.6627	1.0000	0.6878	0.0878	1.0000

Table 6-6 - Normalized Damping Ratios for Full Scale Poles

After normalizing the modal damping ratio data for each pole according to this equation, we get the data shown in Table 6-6. We can also plot this normalized data vs. maximum stress at the break location for each pole (as shown in Figure 6.9) in order to observe any potential differences in behavior between the normalized damping ratio and the actual damping ratio (which was used in Figure 6.6).

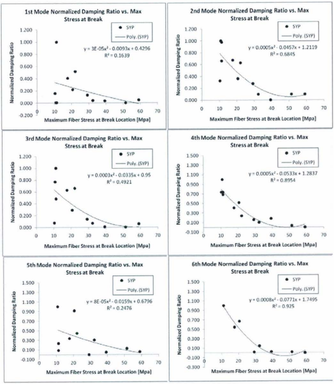

Figure 6.9 - Normalized Damping Ratios vs. Maximum Break Location Stress

We can see that the general appearance of each plot in Figure 6.9 for normalized damping ratio is roughly the same as its corresponding plot in Figure 6.6 for actual measured damping ratio. The

R^2 values are also identical between the two figures. This is expected since the normalizing process served only to rescale each individual mode so that the damping ratios were measured on a scale of zero to one. This was done so an averaging process would not favour any individual mode. It does not affect the relative damping ratio between specimens for any given mode. Note that western red cedar specimens will no longer be included in our analysis, since they were recognized earlier as outliers that did not fit with the trend of the southern yellow pine data. In addition, too few cedar specimens were tested to allow for independent normalization of the cedar specimens. Since a maximum of two exist for any mode, then we would have one with a normalized damping value of zero and one with a normalized value of one, no matter what their original damping values were. This is of little interest even if plotting in parallel with southern yellow pine specimens for comparative purposes.

We will now perform the averaging process that was first employed in section 6.2.2.2, using normalized damping ratio instead of absolute damping ratio. The corresponding data for average normalized modal damping ratio is shown in Table 6-7 for various combinations of modes. Figure 6.10 shows average normalized modal damping ratio plotted against maximum stress at the break location for an incrementally increasing number of modes, up to and including the first five modes. Again the data shown in Table 6-7 for averages that progressivly eliminate lower modes will be discussed later in this chapter.

Pole	Species	Average Normalized Damping Ratio								
		Modes 1 to 2	Modes 1 to 3	Modes 1 to 4	Modes 1 to 5	Modes 1 to 6	Modes 2 to 6	Modes 3 to 6	Modes 4 to 6	Modes 5 to 6
BF1	(SYP)	0.2032	0.1808	0.1752	0.1402	0.1193	0.1173	0.0774	0.0578	0.0075
BF2	(SYP)	0.0169	0.0130	0.0550	0.0539	0.0487	0.0517	0.0646	0.0844	0.0361
BF3	(SYP)	0.0735	0.0682	0.0511	0.0524	0.0436	0.0422	0.0287	0.0191	0.0286
1st Old	(SYP)	0.5396	0.5692	0.5287	0.4901	0.4993	0.5182	0.4791	0.4294	0.4405
2nd Old	(SYP)	0.5717	0.6010	0.5107	0.4979	N/A	N/A	N/A	N/A	N/A
3rd Old	(WRC)	N/A	N/A	N/A	N/A	N/A	N/A	N/A	N/A	N/A
4th Old	(WRC)	N/A	N/A	N/A	N/A	N/A	N/A	N/A	N/A	N/A
5th Old	(SYP)	0.0679	0.0679	0.0770	0.1226	0.1266	0.1441	0.1560	0.1853	0.2260
6th Old	(SYP)	0.2413	0.1853	0.3234	N/A	N/A	N/A	N/A	N/A	N/A
7th Old	(SYP)	0.0482	0.0321	0.0320	0.0508	0.0448	0.0538	0.0432	0.0576	0.0705
8th Old	(SYP)	0.5028	0.5918	0.6938	0.7551	N/A	N/A	N/A	N/A	N/A
9th Old	(SYP)	0.2903	0.2895	0.3461	0.4601	0.4949	0.5501	0.5972	0.7003	0.7926
10th Old	(SYP)	0.4908	0.4877	0.5502	0.4875	N/A	N/A	N/A	N/A	N/A
11th Old	(SYP)	0.8313	0.8876	0.8376	0.6876	0.7397	0.6876	0.6939	0.5919	0.5439

Table 6-7 - Average Normalized Damping Ratio for Full Scale Poles

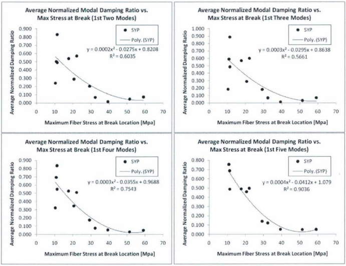

Figure 6.10 - Average Normalized Damping Ratios vs. Maximum Break Location Stress

Figure 6.10 shows that by incrementally considering a greater number of modes in the averaging process, we again see a progressively improving goodness of fit. By changing the number of modes from two to five, the R^2 value improves from 0.6035 to 0.9036. These results, for normalized damping ratio, are somewhat better than when absolute damping ratios were used. We see an even further level of improvement when the sixth mode is added. Inclusion of sixth mode results in a very respectable R^2 value of 0.9722, as shown in Figure 6.11.

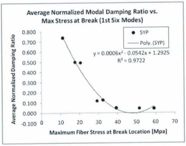

Figure 6.11 - Six Mode Avg. Normalized Damping Ratio vs. Max. Break Location Stress

6.2.2.4 The Use of Average Percentile Rank of Damping Ratios

Here we will basically follow the same process as previous sections and consider the average of an increasing number of modes. However, this time we will examine one last factor, percentile rank of damping ratio, instead of absolute or normalized damping ratio. Using the percentile rank is one last attempt to evenly weight each mode when employing the previously explained averaging process. We will determine whether this factor is any better suited to indentifying the maximum stress at the break location of full scale poles. Obtaining the percentile rank (represented by 'PR' here) is a standard statistics technique, and is performed here for all individual damping ratios according to the following formula:

$$PR_{n,i} = \frac{c_{n,i} + 0.5f_{n,i}}{N}$$

Where:

$$i = Index\ Number\ Identifying\ Individual\ Specimens$$

$$n = Mode\ Number$$

$$c = The\ Number\ of\ Specimens\ with\ a\ Lower\ Value\ than\ Specimen\ i$$

$$f = The\ Number\ of\ Instances\ of\ the\ Value\ of\ Specimen\ i$$

$$N = Total\ number\ of\ Specimens$$

After applying the above equation to each measured modal damping ratio, we get the damping ratio percentile ranks shown in Table 6-8.

Pole	Species	Percentile Rank of Damping Ratio					
		Mode 1	Mode 2	Mode 3	Mode 4	Mode 5	Mode 6
BF1	(SYP)	0.5450	0.3630	0.4540	0.2720	0.0000	0.1420
BF2	(SYP)	0.2720	0.0000	0.0900	0.3630	0.1000	0.4280
BF3	(SYP)	0.4540	0.0900	0.1810	0.0000	0.2000	0.0000
1st Old	(SYP)	0.8180	0.8180	0.7270	0.5450	0.7000	0.7140
2nd Old	(SYP)	0.9090	0.6360	0.8180	0.4540	0.8000	N/A
3rd Old	(WRC)	N/A	N/A	N/A	N/A	N/A	N/A
4th Old	(WRC)	N/A	N/A	N/A	N/A	N/A	N/A
5th Old	(SYP)	0.3630	0.0900	0.2720	0.1810	0.6000	0.5710
6th Old	(SYP)	0.6360	0.4540	0.3630	0.8180	N/A	N/A
7th Old	(SYP)	0.0000	0.0900	0.0000	0.0900	0.4000	0.1420
8th Old	(SYP)	0.0900	1.0000	0.9090	1.0000	1.0000	N/A
9th Old	(SYP)	0.7270	0.5450	0.5450	0.6360	0.9000	0.8570
10th Old	(SYP)	0.0900	0.9090	0.6360	0.8180	0.5000	N/A
11th Old	(SYP)	1.0000	0.7270	1.0000	0.7270	0.3000	1.0000

Table 6-8 - Percentile Rank of Damping Ratios for Full Scale Poles

We also determine the average percentile rank of various combinations of modes for each specimen. This data is shown in Table 6-9.

Pole	Species	Average Percentile Rank of Damping Ratio								
		Avg 1st 2	Avg 1st 3	Avg 1st 4	Avg 1st 5	Avg all 6	Avg Last 5	Avg Last 4	Avg Last 3	Avg Last 2
BF1	(SYP)	0.4540	0.4540	0.4085	0.3268	0.2960	0.2462	0.2170	0.1380	0.0710
BF2	(SYP)	0.1360	0.1207	0.1813	0.1650	0.2088	0.1962	0.2453	0.2970	0.2640
BF3	(SYP)	0.2720	0.2417	0.1813	0.1850	0.1542	0.0942	0.0953	0.0667	0.1000
1st Old	(SYP)	0.8180	0.7877	0.7270	0.7216	0.7203	0.7008	0.6715	0.6530	0.7070
2nd Old	(SYP)	0.7725	0.7877	0.7043	0.7234	N/A	N/A	N/A	N/A	N/A
3rd Old	(WRC)	N/A	N/A	N/A	N/A	N/A	N/A	N/A	N/A	N/A
4th Old	(WRC)	N/A	N/A	N/A	N/A	N/A	N/A	N/A	N/A	N/A
5th Old	(SYP)	0.2265	0.2417	0.2265	0.3012	0.3462	0.3428	0.4060	0.4507	0.5855
6th Old	(SYP)	0.5450	0.4843	0.5678	N/A	N/A	N/A	N/A	N/A	N/A
7th Old	(SYP)	0.0450	0.0300	0.0450	0.1160	0.1203	0.1444	0.1580	0.2107	0.2710
8th Old	(SYP)	0.5450	0.6663	0.7498	0.7998	N/A	N/A	N/A	N/A	N/A
9th Old	(SYP)	0.6360	0.6057	0.6133	0.6706	0.7017	0.6966	0.7345	0.7977	0.8785
10th Old	(SYP)	0.4995	0.5450	0.6133	0.5906	N/A	N/A	N/A	N/A	N/A
11th Old	(SYP)	0.8635	0.9090	0.8635	0.7508	0.7923	0.7508	0.7568	0.6757	0.6500

Table 6-9 - Average Percentile Rank of Damping Ratio for Full Scale Poles

We again plot the data for individual modes, as well averaged data considering an increasing number of modes, against maximum stress at the break location for each pole. This time we use percentile rank of damping ratio as our dependant variable. These plots behave in a manner similar to the plots for absolute and normalized damping ratios. In Appendix D the interested reader can find a comprehensive set of plots. There is again variation in goodness of fit among individual modes, but considering the average value of an increasing number of modes progressively improves the R^2 value. This time the R^2 value increases from 0.5794 (for the first two modes) to 0.9419 (for the first six modes). The goodness of fit of average percentile rank for the first six modes is essentially on par with using averaged absolute damping ratios. Figure 6.12 shows the average of the percentile ranks of the first six modes for each pole, plotted against maximum stress at the poles break location.

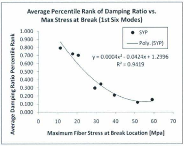

Figure 6.12 - Six-Mode Avg. Percentile Rank of Damping vs. Max. Break Location Stress

6.2.2.5 Comparing Damping Ratio, Normalized Damping Ratio and Percentile Rank

Here we will compare how measured damping ratio, normalized damping ratio and percentile rank of damping ratio compare in their correlation to maximum stress and the location of failure for full scale poles.

Shown in Table 6-10 are the R^2 values of the three parameters of interest when plotted against maximum stress at the break location of full scale poles. The table shows data for the first six transverse modes. These results are presented in a bar graph in Figure 6.13 to allow for visual comparison between modes and between the three parameters.

R^2 Values Using 2nd Order Polynomial Fit For Individual Modal Damping Parameters vs. Max Stress at Break Location			
Mode	Actual Damping Ratio	Normalized Damping Ratio	Percentile Rank of Damping Ratio
1	0.1639	0.1639	0.1358
2	0.6845	0.6845	0.7620
3	0.4921	0.4921	0.6402
4	0.8954	0.8954	0.9027
5	0.2476	0.2476	0.2755
6	0.9250	0.9250	0.7926

Table 6-10 - Fit Summary for Damping Parameters vs. Max. Break Location Stress

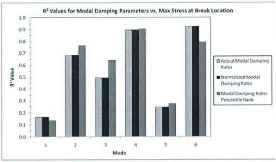

Figure 6.13 - Comparing Fit for Damping Parameters vs. Max. Break Location Stress

As mentioned earlier, there is variability in the goodness of fit between modes. The variability is also difficult to explain at this point. This was discussed in 6.2.2.1. However, the ratio in goodness of fit between modes seems to be maintained for each of the three parameters studied.

Next, Table 6-11 summarizes the R^2 values when averaging each of the three damping parameters over a number of modes. A bar graph is again presented for this data in Figure 6.14.

R^2 Values Using 2nd Order Polynomial Fit For Average Modal Damping Parameters vs. Max Stress at Break Location			
Modes	Average Actual Modal Damping Ratio	Average Normailized Damping Ratio	Average Percentile Rank of Damping Ratio
1 to 2	0.4415	0.6035	0.5794
1 to 3	0.4853	0.5661	0.6316
1 to 4	0.7622	0.7543	0.8019
1 to 5	0.8555	0.9036	0.8389
1 to 6	0.9387	0.9722	0.9419
2 to 6	0.8933	0.9406	0.9145
3 to 6	0.8709	0.9004	0.8721
4 to 6	0.7446	0.756	0.714
5 to 6	0.6371	0.6334	0.5514

Table 6-11 - Fit Summary for Average Damping Parameters vs. Max. Break Location Stress

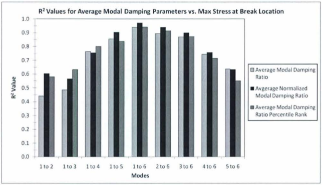

Figure 6.14 - Comparing Fit for Avg. Damping Parameters vs. Max. Break Location Stress

We can see that the goodness of fit increases progressively for each of the three parameters when considering an increasing number of modes in the averaging process. Using average normalized damping ratio here generally seems to result in the best fitting model. Also, note that when lower modes are incrementally removed from the averaging process the R^2 values seem to drop. This suggests that in practice, if attempting to predict the maximum stress in a pole at its break location, then as many modes as possible should be measured. The curve that fits the data for the maximum number of modes measurable in the specimen of interest should be considered when trying to predict the stress. For example, if only the first five modes are able to be measured in practice for a certain test specimen, then the polynomial curve that was found earlier by averaging the first five modes should be used as a model to predict maximum stress from the measured data of the test specimen. Figure 6.14 also shows that when using a fixed number of modes in the averaging process, higher modes seem to produce models with slightly better R^2 values. For example, if generating a model using three modes, modes three through six seem to produce a better model than modes one through 3. This seems to be true regardless of the parameter being considered (absolute, normalized or percentile rank). However, no data should be left out when choosing a model since more modes generally result in a better model. Note that if in practice an intermediate mode cannot be measured for some reason (such as environmental noise at the corresponding natural frequency or interference with other mode types at nearby frequencies), then models can be developed from our original data set to be used for prediction by averaging only the modes that were able to be measured for the test specimen. For example, if in the field we were able to obtain damping ratios of a test specimen for modes one, two, three and five, but not mode four. Then we could use a model that was developed from our database by averaging modes one, two, three and five for predicting the maximum stress of the test specimen. Note that due to the variation in fit between models developed using different modes, we should refrain from making predictions of stress using models developed from any set of modes other than the set we were able to obtain from the test specimen of interest.

In all the above models that were developed using either of the fifth or sixth modes (average of the first through fifth or the average of third through sixth for example), there were less specimens included in the models due to the fifth and/or sixth modes not being measureable for some specimens. Some of the specimens, where all six modes were not measurable, seemed to have had more severe levels of deterioration as well. Therefore, it is not definitive whether the entire extent of the increase in R^2 value when the fifth, and subsequently the sixth, mode were added to the averaging process was actually due to the consideration of more modes, as suggested, or the exclusion of some of the more deteriorated and potentially unpredictable specimens from the models. However, if we look at the rightmost portion of Figure 6.14, the same trend holds true when we progressively remove lower order modes from the averaging process. The R^2 value generally decreases as those lower order modes are removed. This leads us to believe that the averaging method is sound. Since all the rightmost models consider the sixth mode, they must all consider the specimens where the sixth mode was measurable. Therefore, the trend of degrading correlation with fewer averaged modes, at least on the right portion of the plot, was obtained using the same set of specimens. Thus the trend was solely due to the number of modes considered, and not the inclusion or exclusion of particular specimens.

6.2.3 Damping Ratio as an Indicator of Maximum Fiber Stress at Ground Line

While the above results are promising, determining the maximum stress at the break location during failure does not allow us to definitively solve for the maximum load carrying capacity of a pole. This is because failure does not always occur at the same location, and we have no way to determine the location of the failure beforehand. For this reason, we will pursue a model here that allows us to predict the maximum stress that occurs at the ground line during failure. If we can predict the maximum stress that occurs at ground line, then we can calculate the applied load that would be needed to produce that stress, simply based on the geometry of the pole. Note that the maximum stress that occurs at the ground line during failure (which we will be using here) is not necessarily the same as the ultimate fiber stress at ground line. It is possible, and likely in most cases, that failure will occur at some location away from the ground line. We will still use the stress that occurs at the ground line at the instant of failure, but that stress will likely be less than the ultimate stress at the ground line.

To develop models for damping parameters, as they relate to maximum stress at ground line, we will follow the same general procedure used in section 6.2.2. We will plot each individual damping ratio, normalized damping ratio and percentile rank of damping ratio against the maximum stress at ground line. We will also plot the average of these parameters when considering an increasingly large number of modes, to determine whether the models improve when a greater number of modes are considered, as they did earlier when plotting against the maximum stress at the break location. Because these calculations are essentially the same as section 6.2.2, they will not be presented here in detail. We will instead progress directly to the results. For the interested reader, Appendix D contains all relevant tables and plots.

R^2 Values Using 2nd Order Polynomial Fit For Individual Modal Damping Parameters vs. Max Stress at Ground Line			
Mode	Actual Damping Ratio	Normalized Damping Ratio	Percentile Rank of Damping Ratio
1	0.1900	0.1900	0.1684
2	0.7328	0.7328	0.7559
3	0.4279	0.4279	0.5723
4	0.7679	0.7679	0.7923
5	0.4044	0.4044	0.5468
6	0.7182	0.7182	0.7440

Table 6-12 – Fit Summary for Damping Parameters vs. Max. Ground Line Stress

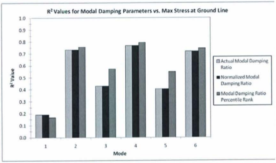

Figure 6.15 - Comparing Fit for Damping Parameters vs. Max. Ground Line Stress

Table 6-12 and Figure 6.15 show the variability in goodness of fit between modes for each of the three damping parameters considered (damping ratio, normalized damping ratio and percentile rank of damping ratio), when plotting against maximum stress at ground line. The ratio of fit between modes here, despite being slightly less extreme, is very similar to Figure 6.13 where maximum stress at the break location was used. Percentile rank seems to show a slight improvement in results here over damping ratio and normalized damping ratio, at least while we are comparing them on an individual mode basis.

R^2 Values Using 2nd Order Polynomial Fit For Average Modal Damping Parameters vs. Max Stress at Ground Line			
Modes	Average Actual Modal Damping Ratio	Average Normailized Damping Ratio	Average Percentile Rank of Damping Ratio
1 to 2	0.3486	0.4996	0.4891
1 to 3	0.3932	0.4767	0.5425
1 to 4	0.608	0.626	0.6808
1 to 5	0.7844	0.8083	0.8036
1 to 6	0.7673	0.7785	0.8834
2 to 6	0.7804	0.8097	0.8977
3 to 6	0.7595	0.7681	0.8694
4 to 6	0.691	0.6929	0.7886
5 to 6	0.6569	0.6549	0.743

Table 6-13 – Fit Summary for Average Damping Parameters vs. Max. Ground Line Stress

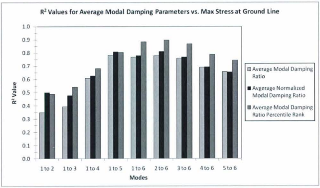

Figure 6.16 - Comparing Fit of Average Damping Parameters vs. Max. Ground Line Stress

When we consider the average of an increasing number of modes we again see goodness of fit progressively improve for each parameter. However, this time average percentile rank seems to offer the best fit of any of the three parameters. When using percentile rank averaged over six modes here, we obtain a model with an R^2 value of 0.8834. This fit is not quite as good as was seen for the average normalized damping ratio plotted against maximum stress at break location in sections 6.2.2.3 and 6.2.2.5. However, it is still quite respectable. Also, since the goodness of fit improves with the consideration of a greater number of modes, there is promise of improving this fit if we focused on measuring higher modes in practice.

In this case, when considering a fixed number of modes, higher modes did seem to produce better models than lower modes. However, as was the case with maximum stress at break location, the goodness of fit decreases as we remove lower modes from the averages. This suggests that no data should be omitted, and using the maximum number of measurable modes is desirable in any case. When attempting to use models for assessing the condition of a test specimen however, we should again use models that were developed from only the specific modes measureable in the test specimen of interest. Repeating the previous example, if we can only measure modes one, two, three and five in a test specimen, then we should predict its condition using a model developed from averages of modes one two three and five (not all possible modes that are available in our database for developing models).

While the models here show adequate fit, the most important thing is that they show promise of improvement by considering further modes in the averaging process. Since we now know that models are available to predict the maximum strength that occurs at a specific location, the ground line, we can directly estimate the load carrying capacity of any pole by using measured modal damping ratios, these models and the poles geometry. This is a significantly useful result in favor of assessing the condition of in service wooden poles using modal impact testing.

6.2.4 Maximum Stress Prediction Using Modal Damping Ratios

Based on laboratory trials, section 6.2.3 developed models relating modal damping ratios to the ground line stress at which failure will occur in full-scale poles. We will now evaluate the ability of these models to predict failure in the lab specimens that were tested in the current study. Note that due to the limited number of full-scale specimens available, we will not used these models to assess the condition of an independent set of specimens at this time. We will compare the predictions made using modal damping ratio with predictions made on the same specimens using commercial ultrasonic NDT equipment. The ultrasonic equipment used here has the commercial name of 'POLETEST' and is manufactured by EDM. This equipment is widely used in line management programs for strength assessment of wooden utility poles.

6.2.4.1 Predictions Using Second Order Polynomial Models

Pole	Species	Actual Max Stress at GL	Prediction from Modal Damping	Prediction from Ultrasonic NDT
BF1	SYP	41.0962	39.86	44.75
BF2	SYP	50.9205	45.35	50.33
BF3	SYP	59.0780	51.70	54.68
1st Old	SYP	22.3465	24.92	34.40
2nd Old	SYP	21.8630	18.52	51.02
3rd Old	WRC	21.0537	N/A	23.24
4th Old	WRC	12.6479	N/A	14.41
5th Old	SYP	32.2951	37.44	31.78
6th Old	SYP	17.0699	26.09	26.13
7th Old	SYP	46.7950	55.55	42.33
8th Old	SYP	13.3008	14.69	N/A
9th Old	SYP	29.0190	25.42	45.85
10th Old	SYP	16.9925	25.56	31.78
11th Old	SYP	25.8385	23.05	N/A

Table 6-14 - Max. GL Stress Predictions Made Using Modal Impact and Ultrasonic Tests

Table 6-14 summarizes the predictions of maximum ground line stress made using modal impact and ultrasonic tests. The predictions for modal impact testing were based on models in Figure 6.17 for average percentile rank of multiple damping ratio combinations. These models were developed based on a second-order polynomial regression model in section 6.2.3, and presented in Appendix D (along with other supplementary results from that section).

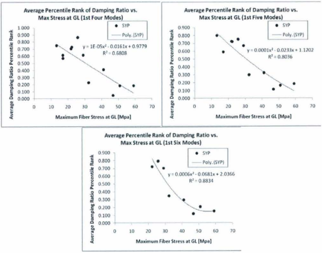

Figure 6.17 - Avg. Damping Ratio Percentile Rank Models for Predicting Max. GL Stress

Predictions were made for each pole using one of the three models presented in Figure 6.17. The maximum number of modal damping ratios measured for each specimen determined which of the models was used. Since second order models were used, two numeric solutions resulted in each case. The lower of these two numeric values was always chosen as the stress prediction, since the higher value corresponds to an ascending portion of the parabola, which extends to the right and outside of the range of values used to develop the models. Note that no predictions were made using modal impact testing for the western red cedar specimens. This is because the number of cedar specimens tested in this study was insufficient for developing models to relate damping ratio and maximum stress. Also, note there were two southern yellow pine specimens that could not be tested by the ultrasonic equipment. Upwards of twenty attempts were made to test those particular specimens without obtaining a measurement. The data in Table 6-14, once rearranged in order of descending values of actual maximum stress at ground line, is plotted in Figure 6.18 and Figure 6.19.

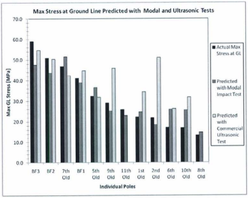

Figure 6.18 - Comparing Max Stress Predictions Made Using Modal and Ultrasonic Tests

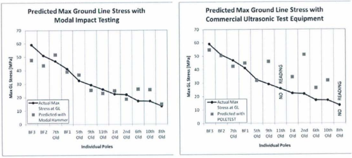

Figure 6.19 - Individual Max Stress Predictions Made Using Modal and Ultrasonic Tests

Inspection of Figure 6.18 and Figure 6.19 reveal that, despite the low number of specimens available for developing models of modal damping ratios in the current study, the predictions made using modal damping ratio measurement are generally better than predictions made using the commercial ultrasonic device. This is especially true for specimens that are in intermediate or advanced stages of deterioration and have lower values of maximum ground line stress. In addition, very good predictions were made using modal impact testing for the two specimens that could not be assessed using the ultrasonic device. Note that maximum stress at ground line was the parameter of interest in this case. However, if maximum load carrying capacity was desired for any given specimen, it could easily be determined based on the geometry of the specimen of interest. The applied load that results in the appropriate ground line stress would simply have to be solved for using straightforward mechanics of solids techniques.

6.2.4.2 Regression Model Considerations

All models used so far, including the ones used for the predictions in the previous section, were second order polynomials. However, this poses the previously mentioned problem that two solutions are returned in each prediction. In order to avoid this we have a number of options.

One option is to simply consider only the leftmost portion of the curve. This was the method used in the last section. However, if we take the six-mode model from Figure 6.17, determine its derivative and solve for the fiber stress at which the derivative of this curve is equal to zero, we get the location of the minimum point on the curve. This minimum point turns out to have an average maximum stress at ground line value of 55.55 and an average percentile rank of damping ratio as 0.145057. Note that this stress value is below the actual max stress value of the BF3 specimen and therefore the model, if used in this manner, could not have made an accurate prediction of the maximum stress for BF3 no matter what the damping values were for BF3. Also, note that the minimum percentile rank of damping value for the second order model was also slightly above the average percentile rank value for the '7th Old' specimen. Therefore, the model returned no solution when attempting to make a prediction for the seventh old pole, and the minimum of the curve was assumed as the predicted value. The algebraic issues of limited range, and occasional specimens not having solutions, can easily be solved by inverting the axes of the appropriate stress-damping graphs and performing an alternate polynomial regression, which will naturally result in an equation with inverted causality. However, the alternate equation would be prone to the same algebraic issues for specimens with high damping ratios. Either the original or the inverted equation would be chosen for use in prediction depending on the damping ratios obtained. Note that an inverted model was actually obtained and employed for comparison, and resulted in prediction values very similar to the original model.

Putting the above discussion aside, numeric issues seem more likely to have been imposed by the model choice than the physical system. The only reason for choosing a second order polynomial fit in previous sections is that it resulted in slightly better R^2 values. However, damping values generally decrease for poles that are in better condition, at least for poles that fall within the range of maximum stress values of our current population of specimens. And, if we think of damping as having been introduced by defects and material decay, then we would not expect real world damping to increase in a parabolic manner for poles with maximum stress values above the range of our current population. For these reasons, it seems appropriate for an exponential decay or power regression model to be considered, rather than the second order polynomial, which we have previously entertained.

For the reasons presented above, we will duplicate the predictions made in section 6.2.4.1 using a power and an exponential regression fit. The scenario here is the same as section 6.2.4.1 except for the modeling choice. Note that the six mode models for the power and exponential fits maintain respectable R^2 values of 0.8514 and 0.8254 respectively. Again, the corresponding plots can be found in Appendix D for this case.

Pole	Species	Max Stress at GL	Prediction from Power Model	Prediction from Exponential Model
BF3	SYP	59.0780	54.36	53.51
BF2	SYP	50.9205	46.51	47.56
7th Old	SYP	46.7950	61.74	58.37
BF1	SYP	41.0962	38.88	40.72
5th Old	SYP	32.2951	35.87	37.65
9th Old	SYP	29.0190	24.95	23.80
11th Old	SYP	25.8385	23.44	21.42
1st Old	SYP	22.3465	24.62	23.28
2nd Old	SYP	21.8630	18.77	18.62
3rd Old	WRC	21.0537	N/A	N/A
6th Old	SYP	17.0699	21.19	22.77
10th Old	SYP	16.9925	21.97	23.34
8th Old	SYP	13.3008	17.37	16.29
4th Old	WRC	12.6479	N/A	N/A

Table 6-15 - Max. GL Stress Predictions using Power an Exponential Regression Models

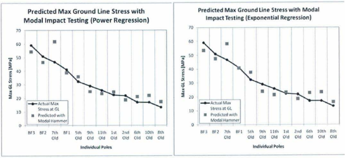

Figure 6.20 - Max Stress Predictions Made Using Power and Exponential Models

By inspecting Figure 6.20, the predictions made using power and exponential models appear slightly better than predictions made using the second order polynomial model, with the exception of specimen '7th Old'. The slightly lower R^2 values for these two regression models (as opposed to the second order polynomial) may have been largely due to that one outlier. Upon reviewing details of the seventh old pole, two potential reasons for its somewhat poor predicted value were found. The first reason is that even though six modes were obtained in the modal impact test, only the first three had very distinct solutions. The frequency response function (FRF) was somewhat noisy in the band containing modes four through six. Multiple stable solutions appeared near each of the noisy peaks of the FRF corresponding to the fourth through sixth modes. The solution candidate that seemed to be nearest to the center of the peak, with the most appropriate phase (+-90deg for each of the three accelerometers) and the most stable poles was chosen in each case. At the time of testing, the current method of using damping ratio was not foreseen as an option. Frequency was the parameter of primary concern at that time, and frequency was very close between the potential solutions. However, damping varied significantly between the potential solutions and the wrong potential solution could have been chosen for either of modes four through six, resulting in poor prediction based on damping ratio measurements for that specimen. This prediction may have been improved if the modal test was repeated with an increased number of runs and a higher sampling rate. If a poor measurement of damping is indeed the root cause of the somewhat poor prediction of maximum ground line stress for the seventh old specimen, then that is not of great concern with regard to the overall feasibility of the method.

One other possible cause of the poor maximum stress prediction of the seventh old pole could be that it failed at a drilled hole. That particular pole was not a mono-pole, it came from a structure and the drilled hole was used for mounting a cross member. This failure is shown in Figure 6.21.

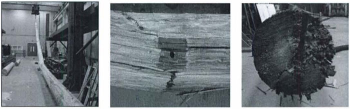

Figure 6.21 - 7th Old Pole Breaking at a Drilled Cross Member Hole

The drilled hole could have resulted in a local strength reduction that was not detected by the damping ratio method. The possibility that very localized defects, such as a drilled hole, may not be detected using the damping ratio method raises some concerns about its potential. However, note that a number of other poles did break at knots, which would have presumably caused a similar localized strength reduction, and the predictions do not seem to be unreasonable for any of the other poles. This could lead us to believe that an artificially imposed defect, such as a notch or hole, may not impart a localized damping effect on a pole in the same way a naturally developed defect would. This seems feasible if the artificial defect is 'open', such as the drilled hole is in the current case. Here an 'open' defect can be thought of as a defect that does not completely close as the specimen is stressed under vibration imposed by an impact from the modal hammer. For a 'closed' defect, such as a crack or a knot, the two separated surfaces of the defect could continuously open and close during oscillatory motion, thus impacting one another and releasing energy which damps that motion. The defect could also remain closed during vibration while the two surfaces rub against one another, resulting in friction losses that damp the specimen's motion. It's easy to imagine that an artificial defect may not impose significant damping on the system in this way. If this is indeed the case here, it still allows the use of damping ratio for assessment of poles which have not been purposefully compromised. Wooden mono-poles would still be an ideal candidate; since they would not be compromised by cross member holes to as great an extent. The holes in monopoles would not be positioned as far down the pole towards the ground line, where moments are higher for given applied loads (as the hole was in the '7th old' pole). Further works has to be done to study the effects of 'open' and 'closed' defects in this way. However, if naturally occurring defects do impart damping more consistently than imposed defects, then validating the suggested method of using damping to predict pole condition would likely have to be done solely based on experimental means. Theoretical and finite element models would become very complex and impractical if they were required to model grain interactions at the local level. As a side note, at least if drilled holes exist in a specimen, they would be known to exist, and if we knew they were not readily accounted for through modal impact tests then they could be manually accounted for to some degree, subsequent to modal testing. In addition, frequency has been shown to be a very useful parameter for locating and quantifying geometric defects such as a hole (in Chapter 4 and Chapter 5), and thus a method where both frequency and damping are jointly considered is conceivable, through further development and study.

6.2.4.3 Further Discussion on Predictions

What has been referred to in previous sections as 'maximum stress at ground line', is more specifically 'the ground line stress at which failure occurs'. Since failure does not always occur at the ground line, this parameter is not equivalent to the ultimate strength at ground line. With that being said, one additional point should be made concerning the inaccuracy of the ultrasonic predictions. This device measures the fiber strength at the location of the test, and the tests were always performed at the ground line. Therefore, it is expressing the ultimate strength at ground line, and not the ground line stress at which failure occurs. Even though the maximum bending moment occurs at the ground line for poles under an applied load, failure will not necessarily occur at the ground line. This likely accounts for some of the ultrasonic device's inaccuracy when only testing at the ground line location. Note that the two specimens that actually did fail near the ground line, labelled 'BF3' and '5th Old', were two of the specimens that were adequately predicted using the ultrasonic device.

If a pole is somewhat deteriorated, the fiber stress may not necessarily be consistent along the pole's entire length. In addition, poles generally have some degree of taper, which results in the second moment of area of the pole's cross section being a function of the location along the pole's length. Therefore, failure may result at a location away from the ground line if fiber stress at that location is higher (based on a lower second moment of area due to the pole taper), or if the ultimate fiber stress at that location is lower (based on localized deterioration). This topic will be discussed further in section 6.2.6 and it is depicted in Figure 6.29. Essentially, if ultrasonic tests were performed at many locations along a specimen's length, predictions of the maximum stress at ground line may be more accurately determined. First, the location where failure should occur could be determined based on localized ultimate stress measurements (in a manner similar to Figure 6.29), then the load required to obtain that particular local stress could be calculated, and finally the ground line stress resulting from that particular load could be determined. This process is somewhat indirect and, in addition, multiple ultrasonic measurements along the pole's entire length would be time consuming and impractical for upright in-service poles. Modal impact tests, however, can excite the entire pole from one impact location. The state of deterioration over the entire poles length is then directly reflected in the results of a single modal impact test, as long as enough damping ratios are obtained during the test. The more useful 'ground line stress at which failure occurs' is then directly obtained, for a specimen subjected to modal impact testing, from regression models as we have developed earlier. Note that in order to obtain the maximum stress at ground line using a modal impact test, the impact does not actually have to be at the ground line. It can essentially be performed at any practical location along the pole's length, except exactly at the actual ground line. However, some locations are more favourable than other locations for adequately exciting the vibration modes of interest, due to the presence of modal nodes.

The results presented in this chapter are promising and suggest that further work should be done in order to expand and better understand the modal damping models. Looking into the issues involved in assessing the condition of in-service poles using this method should also be a priority. The models we have obtained in the current study would not likely be directly applicable to assessing in-service poles. This is because factors such as attached transmission lines and different soil conditions may affect modal damping ratios. For example, soft soil could introduce external damping more so than firm soil. Therefore, soil conditions would have to be considered when developing models. Fully separate models may have to be developed in order to account for different categoric variables, such as structure configuration and wood species. Multi-factor regression models could possibly be pursued as well, taking into account factors that can be expressed as continuous numeric values, such as added mass of attachments or moisture content. Including extra factors in this way could serve to enhance the accuracy of predictions. These models would resemble, in some ways, the multi-factor regression models covered in Chapter 4 and Chapter 5. Additional concerns, such as how modal impact test results are affected by vibration disturbance due to varying wind conditions, ultimately have to be addressed before the method can be widely used.

6.2.5 Damping as an Indicator of Ground Line Stress for Old Poles

Previous sections were concerned with relating damping ratio to maximum stress by considering all southern yellow pine species in regression models. However, the question was raised of whether the method is applicable when considering only the old deteriorated poles, since assessing the condition of old poles is of primary concern in the field. The issue will be briefly addressed here of whether including the three new southern yellow pine specimens simply provided enough high strength samples to allow the range of values to be expanded, and regression models to show an adequate goodness of fit. We will investigate here whether the correlations break down if only old poles are considered.

In the interest of brevity, we will only consider the most important case for field assessment; predicting maximum ground line stress. Also, since percentile rank of damping ratio was most useful for predicting maximum stress at ground line when all pine specimens were considered, it will be the only parameter considered here. We wish to again prove that averaging more modes progressively improve goodness of fit, despite the fit of models that consider individual modes. A simple liner regression model will be considered in this case, since it will allow easier prediction, and show that complex models may increase the goodness of fit, but may not actually be necessary. Using second order models may have only improved the fit when old and new poles were considered simultaneously, because near the high strength end of the spectrum new poles were actually falling above the natural trend of the old poles. These more complex models would have adjusted to accommodate those high strength specimens. Further data is needed to adequately investigate these issues and to determine which regression model format is more closely related to the theoretical underpinnings of the method. Simply proving the approach of averaging modes for old poles alone will be the primary focus of this section.

Considering only old southern yellow pine specimens, we get the damping ratio percentile ranks shown in Figure 6.22 and the average percentile ranks in Figure 6.23 for various combinations of modes. These were obtained in a manner similar to previous sections.

Pole	Percentile Rank of Damping Ratio for Old SYP Poles					
	Mode 1	Mode 2	Mode 3	Mode 4	Mode 5	Mode 6
1st Old	0.750	0.750	0.625	0.375	0.571	0.500
2nd Old	0.875	0.500	0.750	0.250	0.714	N/A
5th Old	0.375	0.000	0.125	0.125	0.428	0.250
6th Old	0.500	0.250	0.250	0.750	N/A	N/A
7th Old	0.000	0.000	0.000	0.000	0.142	0.000
8th Old	0.125	1.000	0.875	1.000	1.000	N/A
9th Old	0.625	0.375	0.375	0.500	0.857	0.750
10th Old	0.125	0.875	0.500	0.750	0.285	N/A
11th Old	1.000	0.625	1.000	0.625	0.000	1.000

Figure 6.22 - Percentile Rank of Damping Ratios for Old SYP Poles

Pole	Average Percentile Rank of Damping Ratio for Old SYP Poles								
	Avg 1st 2	Avg 1st 3	Avg 1st 4	Avg 1st 5	Avg all 6	Avg Last 5	Avg Last 4	Avg Last 3	Avg Last 2
1st Old	0.750	0.708	0.625	0.614	0.595	0.564	0.518	0.482	0.536
2nd Old	0.688	0.708	0.594	0.618	N/A	N/A	N/A	N/A	N/A
5th Old	0.188	0.167	0.156	0.211	0.217	0.186	0.232	0.268	0.339
6th Old	0.375	0.333	0.438	N/A	N/A	N/A	N/A	N/A	N/A
7th Old	0.000	0.000	0.000	0.028	0.024	0.028	0.036	0.047	0.071
8th Old	0.563	0.667	0.750	0.800	N/A	N/A	N/A	N/A	N/A
9th Old	0.500	0.458	0.469	0.546	0.580	0.571	0.621	0.702	0.804
10th Old	0.500	0.500	0.563	0.507	N/A	N/A	N/A	N/A	N/A
11th Old	0.813	0.875	0.813	0.650	0.708	0.650	0.656	0.542	0.500

Figure 6.23 - Average Percentile Rank of Damping Ratios for Old SYP Poles

Individual plots that accompany the data in Figure 6.22 and Figure 6.23 can be found in Appendix D along with other supplementary material related to this topic. When the R^2 values are determined from each of these plots in a manner similar to previous sections, we get the data found in Table 6-16 through Figure 6.25 below.

R^2 Values for Percentile Rank of Damping Ratio vs. Max Sress at GL for Old SYP Poles	
Mode	R^2 Value
1	0.0339
2	0.5849
3	0.3838
4	0.6983
5	0.2338
6	0.5732

Table 6-16 - R Values for Damping Percentile Rank vs. Max GL Stress (Old SYP)

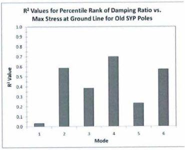

Figure 6.24 - R Values for Damping Percentile Rank vs. Max GL Stress (Old SYP)

R^2 Values for Average Percentile Rank of Damping Ratio vs. Max Sress at GL for Old SYP Poles	
Mode	R^2 Value
1 to 2	0.4172
1 to 3	0.4230
1 to 4	0.6111
1 to 5	0.7860
1 to 6	0.8067
2 to 6	0.7840
3 to 6	0.7483
4 to 6	0.6561
5 to 6	0.5916

Table 6-17 - R Values for Avg. Damping Percentile Rank vs. Max GL Stress (Old SYP)

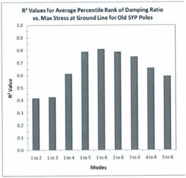

Figure 6.25 - R Values for Avg. Damping Percentile Rank vs. Max GL Stress (Old SYP)

By inspection of Figure 6.24 and Figure 6.25 we can see that in this case averaging the damping ratios of an increasing number of modes again increases the goodness of fit of the model. This is shown to be true here even when old poles alone are considered. Note that the data here is very limited, and further work with an increased database should be done. However, these results are indeed promising if the goal is to assess the condition of old in-service poles.

With the above results in mind, we can again take the average percentile rank of damping ratio of each pole and input it into the appropriate average multi-mode regression model in order to obtain predictions of maximum stress at ground line. This procedure is similar to what was done in section 6.2.4. Here we will use one of the models from Figure 6.26. The model used again depends upon the maximum number of modes able to be measured for each individual specimen. The resulting predictions are found in Table 6-18 and the predictions are compared graphically to the predictions made using the commercial ultrasonic device in Figure 6.27.

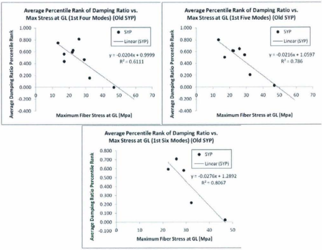

Figure 6.26 - Models for Predicting Old SYP Max GL Stress

Pole	Species	Max Stress at GL	Prediction from Damping Model	Prediction from POLETEST
7th Old	SYP	46.7950	45.85	42.33
5th Old	SYP	32.2951	38.84	31.78
9th Old	SYP	29.0190	25.68	45.85
11th Old	SYP	25.8385	21.05	N/A
1st Old	SYP	22.3465	25.15	34.40
2nd Old	SYP	21.8630	20.46	51.02
6th Old	SYP	17.0699	27.52	26.13
10th Old	SYP	16.9925	25.59	31.78
8th Old	SYP	13.3008	4.21	N/A

Table 6-18 - Predictions of Old SYP GL Stress

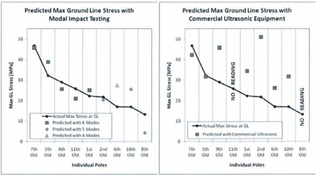

Figure 6.27 - Predictions of Old SYP GL Stress

We can see in Figure 6.27 that the predictions are still quite good when only old poles are considered in the models. Note that the particular model used for each prediction is indicated for each specimen. Each specimen that was predicted using all six modes was predicted quite well. This is expected since they all used the 'six mode' regression model, which had a decent goodness of fit to its data. We can see that the four poles in the worst condition were also the poles where all six attempted modes could not be obtained. This suggests that higher modes may have been harder to measure because of the condition of the poles. Those four poles also accounted for three of the four worst predictions of maximum ground line stress. For these reasons, once further data becomes available, it might be worth creating separate models for poles depending upon the number of measurable modes. Here the 'four mode' mode model, for example, was still developed using all poles, and even the poles where more than four modes were able to be measured were included in the model. The higher modes for those other poles were simply omitted when developing the 'four mode' model. However, if sufficient data becomes available with further testing, then dedicated 'four-mode' models could be developed using only poles with exactly four measurable modes. The range of this model would probably be in the low stress portion of the overall range, and therefore may give better predictions within that low stress range. In the current study, there was only one pole available with four as its maximum number of measurable modes. This one specimen is obviously insufficient for creating a 'four mode' regression model.

As a good practice, separate models should have been developed for each prediction which omitted the specimen desired to be predicted. However, due to the limited data set here, and the fact that percentile rank was used for modeling, it was simply not feasible. Percentile rank is only able to be calculated for a specific modal damping ratio of a specific specimen if that damping ratio falls within the range of damping ratio values used for calculating its rank. Therefore, if the specimen for which percentile rank is desired to be calculated cannot be included in the data set used to calculate rank, then for each mode there would be two specimens with indeterminate percentile rank. Those two specimens would correspond to the maximum and minimum values of damping for each mode. In addition, if we are using average percentile rank of all available modes of each specimen when developing prediction models, then it becomes very likely that at least one of the modes included in the average has a maximum or minimum damping ratio value, and therefore it becomes very likely that at least one of the modes included in the average has an indeterminate percentile rank. Due to these constraints, if specimens desired to be predicted are required to be omitted from their corresponding prediction models, then number of specimens able to be predicted from our already limited database becomes very low. The number of specimens able to be predicted in the current case, if using the ideal method, would actually be about half of the already limited set of old southern yellow pine specimens. Since using that method also results in the added complexity of creating multiple prediction modes, it will not be pursued in the current study. However, it should be kept in mind for future work.

6.2.6 Further Discussion on the Use of Damping Ratio

While the results of previous sections are promising, and suggest that we can use modal impact testing to predict the load carrying capacity of in service wooden poles, the underlying reasons why the results are so favorable seem somewhat mysterious. These results are simply based on experimental finding and no theory has been developed yet for why they should occur. In this section we will speculate on some possible reasons for why they occur, and also make suggestions for how a better understanding of the results could be achieved with further study. In addition, the results thus far only allow for estimation of the load carrying capacity of a pole. While that is a significant finding in its own right, it does not allow us to determine the specific location at which failure will occur. Failure location is a factor of interest since it could allow for appropriate bracing to be attached to deteriorated poles. The bracing could be designed to best support the weakest areas. A possible method for estimating the specific break location, and other weak areas, in addition to the failure load of a pole will be developed and suggested here based on the various speculations that will be made. Note again that this section does not contain any hard evidence to support its claims. It is merely to provide inspiration for potential future work.

The progressive increase of R^2 value with the increase in modes considered in the averaging process employed in previous sections could possibly be attributed to additional modes removing bias between different locations, in terms of the effect of damage on damping ratio. It can be imagined that if an increasing number of modes were considered, then damage located near a less sensitive area of any one mode becomes less significant and we should be able to detect it regardless of its location. Conversely, since we are assuming that the effect of damping is determined by its relativity to areas of low modal curvature, then localized damage is more likely to be far away from any of those areas for at least some modes if we increase the number of modes considered. In Figure 6.28, we can see that the area above the cumulative set of mode shapes diminishes as more modes are considered. This demonstrates that damage is more likely to be adequately far from any nodes (which often correspond to areas of low curvature) if we consider a greater number of modes. Note that considering the absolute value of each mode shape, or the shape that would result if all points were in phase, would have been more appropriate in Figure 6.28 (since modes obviously vibrate between two extremes). However, the figure would have become untidy, and modes might have become difficult for the reader to identify. Also, note that for any given loading, the stress distribution along the length of the specimen is better represented by the second derivative of these displacement mode shapes. As mentioned in Chapter 2 the second derivative is also referred to as the curvature mode shape. The various sources mentioned in that chapter develop the idea of stress being related to curvature mode shapes. A filling of space similar to Figure 6.28 also occurs when considering curvature mode shapes instead of displacement mode shapes.

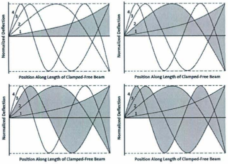

Figure 6.28 - Increasing the Number of Considered Modes Improves Damage Derection

By this logic, and considering the behaviour of the full-scale poles, if we consider an increasing number of modes, up to an infinite number, then the cumulative average normalized damping ratio should become solely dependent upon the extent of damage, and tend to become independent of location. Referring again to Figure 6.28, the space would become completely full for all area under the maximum normalized deflection.

We have shown that more modes continuously improved the fit of models when we attempted to relate damping ratio to stress at the break location in previous sections. Some of the lack of fit when a limited number of modes were considered could have been due to the break location not always occurring at the same location. Thinking of Figure 6.28, deflections are generally different at different locations and for low numbers of modes the averaging process gives different results depending on where the damage occurs. If this is true it makes sense that any deterioration of fixed magnitude should result in the average normalized damping ratio converging to one single value, independent of where it is located, if an infinite number of modes are considered. This means that in practice if we consider an adequately large number of modes, we should be able to estimate the maximum stress at the break location fairly accurately, regardless of the location of the break. This should occur if the data for our test specimens converge and perfectly fit our regression model when an infinite number of modes are considered, as our current data does indeed suggest. However, the most appropriate type of regression model (second order polynomial, power, exponential, linear etc.) is currently unknown by the author, as are the physical reasons behind which model is actually most appropriate.

Although, even if we do know the maximum stress at the break location, based on this method (or even based on some finite number of modes in practice), it is of little use if we do not know the location of the break. Since stress varies along the length of the specimen because of the variation in bending moment with applied load, and possibly the variation in moment of inertia for specimens with non-constant cross sections such as wooden poles, knowing the stress at the break alone is not sufficient. There are likely multiple location and applied load combinations that give the predicted stress at more than one unique location. Essentially, knowing the maximum stress, without knowing the location of failure, does not allow us to definitively solve for the maximum load carrying capacity of the specimen. Using this procedure to isolate the maximum stress at a specific location, such as at the ground line (as in section 6.2.3), would be of more use since then we can find the applied load based on the length of the specimen. We only first need to determine the bending moment required to get the appropriate ground line stress, based on cross sectional geometry.

Continuing on this thought, if we know that damping is dependent upon the relativity of damage to a areas of low modal curvature, we should be able to develop some means for locating damage based on its variation between modes. Again, consider an increasing number of modes, approaching an infinite number. If the amplitude of each modes curvature shape is weighted by the relative increase in damping of its corresponding mode, then mode shapes with high curvature near the location of damage should become more heavily weighted and therefore exhibit higher amplitude. Therefore, if we superimpose an increasing number of these weighted shapes the resultant should be a shape with high amplitudes in the regions of high damage. We would essentially approach a continuous damage profile, plotting the relative deterioration of each point along the length of the specimen. This damage profile should consider the cumulative effect of all damage, regardless of location, as long as enough modes were considered in the superposition process. If we normalize this resulting damage profile with the maximum stress at ground line (or any other specific location) from our method of averaging multiple modal damping ratios, we should get a curve that defines the maximum fiber stress (or local ultimate strength) at any point along the specimen's length. From this curve, we could determine the exact location of failure as well as the corresponding failure load.

In addition to maximum fiber stress, the local bending moment is not generally constant along the length of a beam (or pole) for any given applied load at the free end. For the case of tapered utility poles, the cross sectional geometry is non-constant with respect to location. Therefore, the fiber stress realized under any given applied load is also generally non-constant along the specimen's length, since it is related to the bending moment and cross sectional geometry, which are generally variable with length.

Despite both applied stress and maximum stress being generally non-constant along the length of any specimen, we should still be able to predict failure load and failure location using a graphical approach. We would essentially have to overlay plots of ultimate failure stress vs. location and applied stress vs. location. Applied stress vs. location would be a series of curves for varying applied loads. The minimum applied load that resulted in the two curves intersecting would be the maximum allowable applied load of the specimen. The location along the length of the specimen where that intersection takes place would be the failure location. This is demonstrated in Figure 6.29 for a hypothetical case.

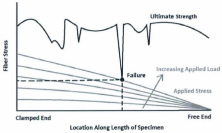

Figure 6.29 - Determining the Failure Load and Break Location of Full Scale Poles

The main difficulty with attempting to use this method for evaluating full-scale poles could be that the true ultimate stress vs. location may have significant spikes or discontinuities. It can be imagined as the superposition of at least two curves. One curve is a smooth and gradually changing; varying as rot or general fiber deterioration gradually changes along the specimen's length in a continuous manner. The other curve is a series of Dirac delta or step functions, with many discontinuities corresponding to knots, drilled holes and other abrupt changes in damage condition. This type of complex function would require a large number of measured modes to model accurately using regression, or the superposition method suggested above There is also a limit to the number of modes that can actually be measured in practice. In the current work, six modes were measured easily for most specimens. The maximum practical number of modes measurable with the equipment used in this study was not determined.

One potential way to validate this method would be to actually try it in the suggested manner, by measuring as many modes as possible for a single specimen in order to obtain the ultimate stress profile through the superposition method described above. The applied stress profiles are straightforward to obtain for a constant cross section specimen. For a tapered pole, the cross section would simply have to be considered at a number of locations along its length, in order to piece together the applied stress profiles. The predictions could then be validated once the static test to destruction is done.

One other way to see if the graphical technique is sound would be to employ a currently used NDT method. An ultrasonic device is already part of the standard arsenal of utility pole testing equipment. It can essentially estimate the maximum fiber stress at any specific location. Its downfall as a stand-alone method is that maximum fiber stress may be adequate at the location where the test is performed but may be dangerously low in other locations along the pole. Testing many locations is time consuming and impractical to do on a large scale, especially if the poles are standing upright in service. However, here we could validate the graphical method by measuring local ultimate strength at incremental locations along a poles length using ultrasonic tests. These measurements could then be pieced together in order to obtain a maximum strength profile of that specific pole. Predicting failure load and location would then be done graphically in the suggested manner, and validated using destructive static test results.

Figure 6.29, while hypothetical, portrays some of the difficulties involved in using any modal testing technique to assess structural integrity. Modal testing has been shown in earlier chapters to be well suited to characterizing ideal defects in controlled conditions, and even though modal vibration shows some promise of assessing entire structures by testing at one location, real world structures are often complex and nonlinear; therefore somewhat removed from any ideal representation. In addition to material-specific difficulties, there are usually environmental and equipment related issues to consider as well. When performing modal tests in the field, wind could disturb vibration response, ice could affect the structures mass and stiffness, and rain could affect the sensitive measurement equipment. Problems such as these could severely restrict the method to be used only on limited occasions. In addition, the equipment is somewhat specialized, and any linesperson would require training on its use. Perhaps the most realistic short-term goal is that modal testing be used as a final check on poles that have already been targeted as problem specimens using other, more practical, inspection methods. Further work is required in order to determine the effectiveness, robustness, and ultimately the role of modal impact testing in assessing the condition of in-service utility poles.

Chapter 7

Closing Remarks

To conclude this study, we will discuss what has been accomplished and then make recommendations for potential future work that could further develop the methods applied in the current study.

7.1 Conclusions

In this study, we ultimately pursued some non-destructive technique that would allow us to assess the condition of in service wooden utility poles. However, a more general goal was simply to validate that modal impact testing is indeed a feasible method for detecting damage under ideal circumstances.

Based on reviewing literature from a number of previous studies, there seemed to be some promise in using modal testing for the purpose of damage detection. Since modal frequency is tied to a specimen's geometry and material properties, such as stiffness and density, any damage that affects those parameters will result in a change in frequency. The magnitude of this change can be used to assess the extent of damage. Damping ratio has also been shown to change with the addition of defects in specimens. However, when frequency or damping from a single mode is considered alone, effects of damage may be diminished if it occurs near an area of low curvature for that particular mode. Mode shapes, particularly the second derivative of modes shapes (or curvature mode shapes), have also been proven useful for detecting localized damage, since they depart from a smooth function when localized damage exists. However if deterioration is evenly distributed throughout a specimen, these abrupt changes in mode shapes would not occur, even though the strength of the specimen would be compromised. While no existing method for assessing damage using modal parameters seemed perfect, there was definitely enough evidence gathered to warrant further study on the topic.

In this study, a somewhat novel approach was suggested first for making predictions of various defect parameters, such as defect location and depth. The method involves developing regression models of multiple modal frequencies using a design of experiments approach. The regression models express each modal frequency as a function of the defect parameters that are desired to be predicted using modal testing. Other factors that are variable and that have some effect on frequency should also be included in the models in order to improve their accuracy. Once the regression models are obtained, they can be inverted and used in the field to predict defect parameters in other specimens of similar type. The appropriate modal frequencies would simply have to be measured using modal testing and fed into the set of regression equations so that they could be solved for the desired defect parameters. A graphical method has also been suggested for solving the series of regression equations. The graphical method involves overlaying contour lines for a set of response surface models at the frequencies of the test specimen. The defect parameters are then taken as the point where these contour lines intersect.

In order to validate the proposed method, regression models were developed for various scenarios and then successfully used to predict defects in other specimens. The method was applied to theoretical, finite element and physical beam models, and was proven useful in each case. Scenarios where investigated that involved two and three defect parameters. The chosen defect parameters related to defect severity and location. Using the proposed method, accurate predictions of each defect parameter were made in each case. The graphical approach also proved to be useful for making predictions. In addition, it aided in visualizing the solution and determining how much confidence should be placed in each prediction.

One of the downfalls of the proposed regression approach is that it is so far only useful for idealized defects that can be defined by a modest number of numeric factors. For distributed and irregular damage, such as we find in wooden utility poles, the method is not as useful without further development. However, an alternate method of applying modal testing to assess the condition of utility poles was found to be promising.

In order to investigate how modal testing could be used to predict the strength of full-scale utility poles, a series of destructive pole tests was performed. During each test, poles were stressed in bending until failure occurred. Load and deflection measurements from the tests were used to calculate elastic modulus as well as maximum ground line stress and break location stress at failure. Prior to each destructive test, modal impact tests were performed to measure modal frequencies and damping ratios. Strength predictions were also made using non-destructive ultrasonic equipment that is currently used for monitoring utility poles in the field.

It was found that individual modal damping ratios correlated with maximum stress at the break location as well as with maximum stress at the ground line to varying degrees for full-scale poles. In addition, it was found that the average of multiple modal damping ratios correlated better with maximum stress than either individual modal damping ratio. Moreover, the level of correlation increased with the inclusion of a greater number of modes in the averaging process.

This was found to be true for absolute damping ratio, normalized damping ratio and percentile rank of damping ratio. Correlation was slightly better for maximum stress at the break location than maximum stress at ground line. However, the break location of a pole is not generally known in advance of failure. Therefore predicting maximum stress at ground line is of greater interest since it allows us to estimate the load carrying capacity of a pole based on its geometry. We assessed the accuracy of a regression model that was developed to relate average percentile rank of damping ratio to maximum stress at ground line by using it to make predictions of maximum ground line stress for the poles tested in our study. The model was found to predict maximum stress better than the ultrasonic equipment. A model was developed using only low strength specimens as well, in order to investigate the merit of applying the technique specifically to highly deteriorated poles, and predictions were again better than the ultrasonic predictions. Further work is required to expand the models and use them make predictions of maximum stress for poles outside the current series of tests. However, the results seem promising for eventually using modal impact testing to assess to condition of in-service wooden utility poles.

In any event, current and previous work relating to damage detection through modal testing indicate that it can be a useful technique. Most methods to date, including the methods suggested in the current study, have focused on using only one of the three main modal parameters at any given instance; the three main parameters being modal frequency, modal damping ratio and mode shape. However, an effort has been made in this study to at least consider multiple modes simultaneously, even if only one modal parameter from each of those modes is considered at a time. The 'frequency regression modelling' and 'damping ratio averaging' approaches, which were suggested in this study, have indeed seemed to substantially expand and improve damage detection results simply because they do consider multiple modes simultaneously.

The approach suggested in section 6.2.6 that involved superimposing curvature mode shapes that are weighted by each modes corresponding damping ratio, might be one possible way to assess the condition of specimens by using two modal parameters simultaneously. This suggested method is by no means substantiated, and is only speculation at this point. However, we can imagine that some similar type of unified method, which makes use of all three modal parameters simultaneously, is plausible. Each of the three parameters has already been independently proven useful to some extent. Each of the three therefore holds information that can be related back to the structure from which it was measured.

It is a fundamental law of physics that information is never lost though any physical process, although, it is often true that information becomes so disorganized that it cannot be deciphered. However, based on the results of this study and literature reviewed from previous studies, it is the belief of the author that the ability to decipher enough modal response information so that the medium through which an initial excitation travels can be adequately characterised based on its modal response to that excitation, is not out of reach. To do this, enough factors that significantly affect the measured modal response simply need to be accounted for in the proper manner. This may in fact include factors that are external to the specimen in many practical cases. Further work, combined with some creative thinking, could likely lead to a unified method that allows damage assessment to be performed quite adequately using modal analysis.

7.2 Recommendations for Future Work

Future work relating to the current study generally falls into two categories: work relating to the regression model technique and work relating to full scale pole testing. Some suggestions will be made here for what that work could involve.

7.2.1 Further Development of Defect Detection Technique

A method was proposed and applied in Chapter 4 and Chapter 5 where regression models, initially developed to relate multiple modal frequencies to defect parameters, are later used in conjunction with experimental modal frequency measurements to make predictions about the nature of defects in test specimens. This method has been proven useful for localizing and quantifying idealized defects in controlled specimens, and with further development, it could potentially be applied to a variety of more practical applications.

In section 3.2, we presented the derivation for a single stepped clamped free beam and then in section 5.1.3 we used that theoretical model to calculate modal frequencies of a defected beam, where the defect was a hole drilled lengthwise from one end. We then used those frequency calculations to develop regression models and validate the proposed defect detection technique through validation runs. A similar type of exercise could be performed by deriving a two-step beam. This type of theoretical beam could represent the 'two-factor rod' scenario that we investigated in section 5.2, and be used to gain a further understanding of that scenario.

Added mass and curvature mode shapes were discussed in the literature review, and continue to hold a fair amount of promise for detecting damage, but were largely neglected in the current study. However, if we observe the shape of the regression models that we obtained in some of our validating scenarios, we notice that they closely resemble the absolute value of curvature modes shapes as well as plots of frequency reduction as added masses are traversed along beams. This hints towards the possibly of eventually developing regression models much more efficiently. Scaling measured curvature mode shapes could be one possibility. In addition, if adding a mass has the effect of reducing frequency, and behaves in a manner similar to adding a defect, then there is promise of developing regression models that could be used for predicting defects by simply taking frequency measurements with masses added at various locations. The regression models taken from these measurements would behave similarly to the models developed using many specimens with locally imposed defects. These response surfaces would have to be scaled somehow to allow for actual prediction of defect parameters. However, if models could be obtained in this way, we would considerably reduce the effort, time, cost and materials required for model development. These savings would make the method much more feasible for a wide range of applications. Note that if models were eventually developed in this way, they would likely require inversion, since added mass has a larger effect when added to the free end of a cantilever, whereas a defect has a larger effect when added near the clamped end.

In general, scaling response surfaces that were obtained by indirect methods so that they can fit the desired application is very enticing, since it would allow regression models to be obtained much more easily and with great cost savings. We could attempt to scale response surfaces that were developed from finite element runs. Since the finite element and experimental response surfaces were shown to behave very similarly in our study of the 'two factor rod' scenario in section 5.2, it can be imagined that there may be a way to transform the finite element response surface in order to allow it to make predictions on physical specimens. A simple case would be if the frequency of all physical specimens were simply a consistent fraction lower (or even at a consistent offset lower) than the frequency of the FEA specimens over the entire design space. If we expected that to be the case, then simply testing one physical specimen would allow us to scale the entire FEA derived models. In general, even if this ratio between FEA and physical specimens did change throughout the design space, as long as the behaviour of that change could be characterized by fitting a transformation model which required less design points to derive than would be required to derive the complete regression model using physical specimens, then we would accomplish some savings in required design runs. An alternate method could involve developing regression models using FEA runs in order to determine which terms are significant, and thus required in the regression equations. If we then assume that the same terms should show up in the models developed from physical specimens, then we could use a number of physical runs to solve for a set of regression equation coefficients that would characterize the physical system. If each term found to be significant in the FEA regression equations were assigned a coefficient representing the effect of that term on the physical specimens, then we would only have to test the number of physical specimens required to set up a matrix of equations, which could subsequently be solved for the regression equation coefficients. This would allow models to be developed from many closely spaced FEA runs, so that we can accurately determine the significant regression model terms, and then scale that fine tuned model to fit the behaviour of any similar set of physical specimens. This method would be worthwhile as long the number of specimens that would be required to develop regression models from physical specimens in the regular way is moderately greater than as the number of terms in the highest order FEA derived regression equation for which we wish to determine coefficients. This is likely to be true in most cases.

Since we wish to expand the defect detection method to fit situations that are more practical, we need to confirm that including supplementary factors can maintain regression model accuracy under varying practical conditions. We have deemed supplementary factors to be necessary in Chapter 4, but have mostly studied scenarios with controlled conditions thus far. We should also attempt to detect multiple localized defects simultaneously using the method. Investigating a 'four-factor beam' seems like a logical first step in accomplishing this. The four factors could be the location and depth of two separate localized defects.

If we realize savings in design points required for fitting regression models by using more efficient design structures, or though one of the scaling methods described above, then we may be able to develop regression models that make use of a large number of defect parameters. In this case, using a larger number of defect parameters could mean that we are able to predict the superposition of a number of individual defects. This superposition, if enough individual defects are able to be included, could begin to resemble continuously variable distributed damage. Modelling distributed damage is an ultimate goal since it would mean that the method could be applied in essentially any situation, likely including the assessment of full-scale poles. Of course, including more defect parameters also means that we would be required to measure more modal frequencies in order to solve our regression models. There are an infinite number of modal frequencies to use for these predictions, however, there are obviously physical limits to the number of modes that can be practically be measured using our modal testing equipment, and thus there is some limit to how detailed our predictions can ultimately be.

One other, perhaps farfetched, potential method for detecting variable distributed damage would be to model the damage profile (or alternately the strength profile) of a specimen as some function of the location along the specimens length. Suppose that this function were generally considered as a polynomial. We could develop regression models that could be used to predict the coefficients of the polynomial terms instead of predicting actual physical dimensions of defects. For example, if we represented the change in strength along a beam by third order polynomial, then we would need to measure four modal frequencies to predict the four constants in that polynomial equation. Obviously, we would still be required to develop the appropriate regression models beforehand to be used for prediction. If this was proven to work, it could potentially be useful for predicting complex damage using a small number of measured frequencies. However, if we have a superposition of smoothly varying distributed damage and abrupt step changes in condition (which is anticipated to be the case for wooden poles as we have varying degrees of rot interspersed with knots and holes), then the function required to represent the change in condition along the specimens length would become prohibitively complex.

As we mentioned earlier, the proposed method of defect detection has so far been proven useful for prediction of idealized defects under controlled conditions, and with future work, it could be applied in situations that are more practical. Some of the work presented above could be pursued to help extend the scope of the method.

7.2.2 Future Development of Methods Relating to Full Scale Pole Testing

The method of averaging modal damping ratios, which we have so far found to be promising for assessing condition of wooden poles, should definitely be the initial focus of future efforts. More poles should be tested in the lab in order to expand the database that is being used to develop models. In addition, models should be developed and used to predict the condition of specimens that were not used in the model's initial development. Because of the limited number of specimens in this study, and the fact that were using percentile rank instead of actual damping ratio, removing the predicted specimens from the models was not feasible.

Modally testing poles in the field is another target area for future work. Since modal testing is desired to be used in the field for assessment of in-service poles, then models for damping should be developed from data collected from in-service poles. This would allow damping effects from sources such as soil and attached hardware to be included in the models. It would also allow the practicality of performing modal tests on in-service poles to be assessed. It was found that modal impact tests could be performed adequately in the lab by impacting at heights between five and ten feet from the ground line. It seems reasonable that someone standing on the ground with a large hammer could impart a suitable force at least five to seven feet from the pole's ground line. However, field trials are required to validate this assumption. In addition, field trials would determine whether modal impact tests are practical in the presence of varying environmental challenges such as wind, rain and ice.

For in-lab full-scale tests, some minor issues relating to the test bed were discussed in section 6.1.2 and should be addressed. For other in-lab work, attempting to use the average damping ratio method to predict the strength of small-scale beams could be an option. Many more tests could be done with much less effort that way. We could easily get enough data to develop accurate prediction models if the method works. The beams could be subjected to crude techniques of imparting damage, so that damage better represents the random, naturally developed damage that occurs in in-service poles. Techniques such as chipping the surface with tools could be applied to achieve that effect. Precise machined defects that cleanly remove material may not have the same effect on damping, as we discussed in Chapter 6.

Since we have only employed modal damping for assessment of full-scale poles thus far, further investigation into the use of modal frequency is warranted, based on the success that we have had using modal frequency in other applications. Model frequency will likely be a little more difficult to incorporate into our assessment methods, simply because it is affected by so many factors. Pole length, diameter, taper, density and stiffness all affect frequency and would have to be accounted for somehow. In addition, many of these factors would not be evenly distributed. Perhaps some averaging technique, similar to what we used for damping ratio, could be employed for frequency. In this case, frequency may first require normalization in order to moderate the effect of factors such as variable geometry. Normalizing with respect to finite element predictions of frequency, using constant properties (such as published average properties) and specimen specific geometry, could help alleviate the effect of geometry on frequency. Determining whether moisture content is closely correlated with stiffness or density should also be a priority. If it is, and if we later wish to use natural frequency as an indicator of damage, then we can account for variation in stiffness or density between specimens simply by measuring moisture content.

Determining which factors impose the need for completely separate regression models is also of importance. We have seen that the western red cedar specimens were outliers relative to regression models that related damping to maximum stress. Therefore, separate regression models would likely need to be developed for individual wood species. Other factors likely demand the use of separate models as well. For example, it may be best to create separate models for poles falling within certain age groups. Since old poles likely have lower strength, regression models developed specifically from old poles may better reflect the behaviour of lower strength specimens, and thus may be more accurate in the lower strength regions of the spectrum. Other factors, such as structure arrangement (monopole vs. double pole structures) will likely mean even further model creation. However, with the creation of different models, comes the need for larger quantities of test data. More test data would be required in order to accurately develop each regression model.

If the modal test method does indeed turn out to be useful for accurately testing the strength of poles in the field, then other challenges will likely arise, such as how the data will be kept organized and accessible. Models will continuously need updating with the collection of new data, and predictions of condition will have to be readily available each time a decision is to be made about the remaining service life of a particular pole. Developing in house software for these organizational challenges seems like a logical choice, once the modelling and prediction method has been well developed. Software would allow moderate levels of automation to be incorporated as well. If results prove to be very good, then developing commercial products could potentially be an option, based on the idea that investments have already been made to collect data and develop accurate models. Despite the fact that the method used for assessing condition could be widely known, it would only be widely known in a general way. Having put forward the significant initial investment required to obtain pole test data would be enough to secure a commercial advantage.

Modal testing has already been proven useful in idealized specimens, and now assessing the condition of more complex structures such as wooden utility poles seems promising. No matter what avenues are pursued for future study in this field, work completed in the current study at least provides motivation for doing future work of some kind.

Bibliography

Ackers, S., Evans, R., Johnson, T., Kess, H., White, J., Adams, D. E., et al. (2006). Crack Detection in a Wheel End Spindle Using Wave Propagation Via Modal Impacts and Piezo Actuation. *Health Monitoring and Smart Nondestructive Evaluation of Structural and Biological Systems V*, (pp. 61770B-1 - 61770B-13).

Al-Said, M. S. (2008). Crack Detection in Stepped Beam Carrying Slowly Moving Mass. *Journal of Vibration and Control*, 14(12): 1903-1920.

Al-Said, S. A., & Al-Qaisia, A. A. (2008). Influence of Crack Depth and Attached Masses on Beam Natural Frequencies. *International Journal of Modelling and Simulation*, Vol. 28, No. 3, 239-247.

ASTM. (1999). *Annual Book of Standards, Section 4 - Construction, Volume 04.10 - Wood.* West Conshohocken, PA: American Society for Testing and Materials.

Budipriyanto, A., Swamidas, A. S., Adluri, S. M., & Haldar, A. (2007). Nondestructive Assesment of Wood Beams Using Vibration Response. *Nondestructive Testing and Evaluation*, Vol. 23, No. 3, 175-193.

Caracoglia, L., & Velazquez, A. (2008). Experimental comparison of the dynamic performance for steel, aluminum and glass-fiber-reinforced-polymer light poles. *Engineering Structures*, Vol. 30, 1113-1123.

Chapra, S. C. (2005). *Applied Numerical Methods with Matlab: for Engineers and Scientists.* New York, NY: McGraw-Hill.

Chui, Y. H., Barclay, D. W., & Cooper, P. A. (1999). Evaluation of Wood Poles Using a Free Vibration Technique. *Journal of Testing and Evaluation* , vol:27 no:3, 191-195.

Fung, E. H., & Yau, D. T. (2001). Vibration Frequencies of A Rotating Flexible Arm Carrying A Moving Mass. *Journal of Sound and Vibration* , 241(5), 857-878.

Gibson, R. F. (2000). Modal vibration response measurements for characterization of composite materials and structures. *Composites Science and Technology* , Vol. 60, 2769-2780.

Green, D., Winandy, J. E., & Kretschmann, D. E. (1999). Mechanical Properties of Wood. In F. P. Labratory, *Wood Handbook - Wood as an Engineering Material* (pp. 4.1 - 4.45). Madison, WI: U.S. Department of Agriculture, Forest Service.

Haldar, A. (2003). *Wood Pole Line Management Using RCM Primciples.* St. John's: Newfoundlan and Labrador Hydro.

Haldar, A., & Tucker, K. (2006). Condition Based Management of Wood Pole Transmission Lines Using Structural Reliability Analysis. *2006 Electrical Transmission Conference* (pp. v218, 304-316). Birmingham, AL, United states: American Society of Civil Engineers.

Inman, D. J. (2001). *Engineering Vibration: Second Edition.* Upper Saddle River, New Jersey: Prentice Hall Inc.

Jang, S. K., & Bert, C. W. (1989). Free Vibration of Stepped Beams: Exact and Numerical Solutions. *Journal of Sound and Vibration* , 130 (2), 342-346.

Koplow, M. A., Bhattacharyya, A., & Mann, B. P. (2006). Closed form solutions for the dynamic response of Euler–Bernoulli beams with step changes in cross section. *Journal of Sound and Vibration* , Vol. 295, 214-225.

Lestari, W., Qiao, P., & Hanagud, S. (2007). Curvature Mode Shape-based Damage Assessment of Carbon/Epoxy Composite Beams. *Journal of Intelligent Material Systems and Structures* , Vol. 18, 189-208.

LMS International. (2009). LMS Test.LAB Revision 9A. Leuven, Belgium.

Montgomery, D. C. (2009). *Design and Analysis of Experiments (7th Ed.).* Hoboken, NJ: John Wiley & Sons Inc.

Ouis, D. (2003). Effect of structural defects on the strength and damping properties of a solid material. *European Journal of Mechanics A/Solids* , Vol. 22, 47-54.

Ouis, D., & Zerizer, A. (2006). Modeling rot in wood by replacement of wood with sand: an experimental study. *Journal of Wood Science* , Vol. 52, No. 3, 208-212.

Pandey, A. K., Biswas, M., & Samman, M. M. (1991). Damage Detection From Changes in Curvature Mode Shapes. *Journal of Sound and Vibration* , 145(2), 321-332.

Salawu, O. S. (1997). Detection of structural damage through changes in frequency: a review. *Engineering Structures* , Vol. 19, No. 9, 718-723.

SAS Instituite, Inc. (2009). JMP Version 8.0.2. Cary, NC.

SAS IP, Inc. (2009). ANSYS Workbench 2.0 Framework Version 12.0.1. Canonsburg, PA.

Stat-ease, Inc. (2010). Design Expert Version 8.0.1. Minneapolis, MN.

Wareing, B. (2005). *Wood Pole Overhead Lines.* London: Institution of Electrical Engineers.

Zhong, S., & Oyadiji, S. O. (2008). Analytical Predictions of Natural Frequencies of Cracked Simply Supported Beams with a Stationary Roving Mass. *Journal of Sound and Vibration* , 311, 328-352.

Appendix A - Solving a Stepped Beam in Maple

The following Maple worksheet was used for solving for the roots and the natural frequencies of stepped beams according to the theory presented in section 3.2. Note that the roots are actually solved for here by zooming in on the plot of the characteristic equation at points where it crosses the x-axis.

---------------------------- *Solving for Roots of Clamped-Free Beam with two Different Cross Sections According to Paper by Jang* -- ------------------------------------

restart;

$dia := 0.04064;$

$L1 := 0.4064;$

$E1 := 8470000000;$

$\rho 1 := 320;$

$b1 := 0.0889;$

$h1 := 0.0889;$

$$A1 := (b1 \cdot h1) - \left(\pi \cdot \left(\frac{dia}{2}\right)^2\right);$$

$$I1 := \left(\frac{1}{12} \cdot b1 \cdot h1^3\right) - \left(\frac{1}{4} \cdot \pi \cdot \left(\frac{dia}{2}\right)^4\right);$$

$L := 1.0668;$

$L2 := L - L1;$

$E2 := E1;$

$\rho 2 := \rho 1;$

$b2 := b1;$

$h2 := h1;$

$A2 := b2 \cdot h2;$

$I2 := \frac{1}{12} \cdot b2 \cdot h2^3;$

$K2 := K1 \cdot \left(\frac{E1 \cdot I1 \cdot \rho 2 \cdot A2}{\rho 1 \cdot A1 \cdot E2 \cdot I2} \right)^{0.25};$

$K := \frac{K1}{K2};$

$I21 := \frac{I2}{I1};$

$S1 := \sin(K1 \cdot L1);$

$S2 := \sin(K2 \cdot L2);$

$C1 := \cos(K1 \cdot L1);$

$C2 := \cos(K2 \cdot L2);$

$SH1 := \sinh(K1 \cdot L1);$

$SH2 := \sinh(K2 \cdot L2);$

$CH1 := \cosh(K1 \cdot L1);$

$CH2 := \cosh(K2 \cdot L2);$

$with(LinearAlgebra); Mat := [[(S1 - SH1), (C1 - CH1), (-S2 - SH2), (-C2 - CH2)],$
$[(C1 - CH1), (-S1 - SH1), (K \cdot (C2 + CH2)), (K \cdot (-S2 + SH2))],$
$[(-S1 - SH1), (-C1 - CH1), (K^2 \cdot I21 \cdot (S2 - SH2)), (K^2 \cdot I21 \cdot (C2 - CH2))],$
$[(-C1 - CH1), (S1 - SH1), (-K^3 \cdot I21 \cdot (C2 - CH2)), (K^3 \cdot I21 \cdot (S2 + CH2))]];$

$CharEqtn := Determinant(Mat);$

$plot(CharEqtn, K1 = 0..5);$

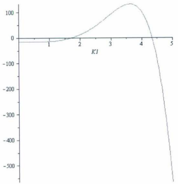

$K1plot := 4.3367;$

4.3367

$$\varpi rad := evalf\left(K1plot^2 \cdot \left(\frac{E1 \cdot I1}{\rho 1 \cdot A1}\right)^{0.5}\right);$$

2680.825502

$$\varpi Hz := evalf\left(\frac{\varpi rad}{2 \cdot \pi}\right);$$

426.666630

Appendix B - Three Factor Beam FEA Model Development Data

Run	FEA 3-Factor Rod Data [mm]			Transverse Modal Frequency [Hz]			
	Location	Dia.	Length	Mode 1	Mode 2	Mode 3	Mode 4
1	5	4	1	13.34	317.99	1010.92	2063.10
2	5	6	1	25.56	325.89	1021.42	2081.32
3	5	8	1	36.42	338.14	1036.28	2098.70
4	5	10	1	46.49	355.07	1057.67	2121.71
5	5	12	1	55.97	379.55	1093.63	2163.18
6	5	14	1	61.15	395.81	1121.71	2198.65
7	5	16	1	64.82	410.34	1149.70	2236.80
8	5	18	1	67.47	422.60	1175.34	2274.30
9	5	20	1	69.23	431.59	1196.45	2307.64
10	5	22	1	70.28	437.19	1209.80	2330.16
11	5	24	1	70.85	440.43	1217.87	2343.85
12	5	4	25	4.86	297.06	811.22	1513.08
13	5	6	25	10.89	316.76	972.91	1870.57
14	5	8	25	18.74	323.68	1009.57	2008.13
15	5	10	25	28.07	332.25	1031.24	2076.67
16	5	12	25	37.75	344.05	1048.85	2111.77
17	5	14	25	46.71	359.42	1071.63	2143.46
18	5	16	25	54.38	377.25	1097.21	2174.99
19	5	18	25	60.45	395.75	1126.76	2212.64
20	5	20	25	64.97	412.63	1158.40	2253.19
21	5	22	25	67.97	425.89	1185.36	2292.35
22	5	24	25	70.13	436.60	1208.64	2328.77
23	5	4	50	3.79	211.03	583.14	1409.70
24	5	6	50	8.50	298.99	804.54	1553.59
25	5	8	50	14.99	324.63	982.63	1881.08
26	5	10	50	22.76	332.99	1024.08	2014.80
27	5	12	50	31.58	342.40	1049.86	2094.70
28	5	14	50	40.37	354.32	1070.89	2142.16
29	5	16	50	48.69	369.16	1094.25	2178.77
30	5	18	50	55.95	386.29	1119.76	2213.70
31	5	20	50	61.89	404.03	1149.42	2251.03
32	5	22	50	66.37	420.67	1178.10	2288.05
33	5	24	50	69.65	434.75	1205.62	2326.01
34	5	4	75	3.25	146.51	563.53	1465.71
35	5	6	75	7.29	255.71	671.80	1517.75
36	5	8	75	12.85	308.10	841.12	1643.85
37	5	10	75	19.91	335.40	1011.45	1953.86
38	5	12	75	28.10	345.17	1055.65	2084.47
39	5	14	75	36.38	355.17	1079.70	2146.25
40	5	16	75	44.69	367.53	1098.41	2182.17
41	5	18	75	52.47	382.78	1123.30	2224.43
42	5	20	75	59.37	400.08	1149.47	2260.33
43	5	22	75	64.80	416.87	1175.72	2290.65
44	5	24	75	69.23	433.70	1205.49	2329.35
45	5	4	100	2.92	107.60	578.59	1542.43
46	5	6	100	6.55	210.13	635.28	1562.92
47	5	8	100	11.59	286.39	760.92	1635.11
48	5	10	100	17.84	320.91	892.17	1748.65
49	5	12	100	25.29	340.96	998.71	1916.49
50	5	14	100	33.27	354.14	1057.84	2057.29
51	5	16	100	41.93	369.42	1108.49	2200.76
52	5	18	100	49.85	382.94	1131.99	2242.48
53	5	20	100	57.40	399.25	1159.03	2285.66
54	5	22	100	63.55	415.44	1180.15	2303.32
55	5	24	100	68.83	432.98	1205.80	2330.95

Run	FEA 3-Factor Rod Data [mm]			Transverse Modal Frequency [Hz]			
	Location	Dia.	Length	Mode 1	Mode 2	Mode 3	Mode 4
56	20	4	1	13.32	337.20	1070.09	2175.29
57	20	6	1	25.31	344.46	1079.57	2193.66
58	20	8	1	36.78	356.07	1092.88	2210.24
59	20	10	1	46.48	370.90	1110.79	2228.11
60	20	12	1	56.04	390.70	1136.33	2253.47
61	20	14	1	60.79	403.58	1154.78	2272.02
62	20	16	1	64.62	415.84	1174.01	2293.02
63	20	18	1	67.42	426.25	1191.87	2313.64
64	20	20	1	69.25	433.75	1205.93	2331.46
65	20	22	1	70.28	438.05	1213.37	2339.44
66	20	24	1	70.87	440.76	1218.80	2345.87
67	20	4	25	4.14	243.93	627.83	1443.39
68	20	6	25	9.23	315.73	888.71	1660.62
69	20	8	25	16.25	332.87	1019.55	1973.25
70	20	10	25	24.21	340.03	1048.46	2069.87
71	20	12	25	33.15	349.69	1072.33	2143.40
72	20	14	25	41.87	361.34	1091.89	2181.41
73	20	16	25	50.03	375.99	1112.09	2213.33
74	20	18	25	57.06	392.41	1135.73	2243.60
75	20	20	25	62.65	409.02	1163.23	2278.46
76	20	22	25	66.79	423.67	1188.81	2306.82
77	20	24	25	69.81	436.03	1209.70	2335.03
78	20	4	50	3.18	137.13	565.01	1479.19
79	20	6	50	7.12	246.73	660.30	1525.17
80	20	8	50	12.57	305.06	823.83	1638.83
81	20	10	50	19.39	335.90	1007.42	1941.35
82	20	12	50	27.35	345.14	1048.94	2057.15
83	20	14	50	35.78	355.74	1081.81	2149.58
84	20	16	50	44.03	367.53	1099.40	2182.17
85	20	18	50	51.91	382.77	1127.86	2237.84
86	20	20	50	58.96	399.54	1150.67	2263.77
87	20	22	50	64.53	416.45	1175.47	2291.46
88	20	24	50	69.14	433.48	1205.28	2329.44
89	20	4	75	2.87	101.87	583.04	1556.23
90	20	6	75	6.43	201.74	633.58	1575.01
91	20	8	75	11.37	278.91	744.95	1631.93
92	20	10	75	17.56	319.82	885.04	1749.00
93	20	12	75	24.91	341.23	996.00	1916.58
94	20	14	75	32.82	354.13	1053.26	2042.81
95	20	16	75	41.47	370.14	1113.01	2205.59
96	20	18	75	49.40	383.30	1135.29	2249.32
97	20	20	75	57.04	399.24	1159.25	2288.40
98	20	22	75	63.37	415.47	1179.29	2301.96
99	20	24	75	68.75	432.85	1205.50	2330.66
100	20	4	100	2.65	80.01	610.51	1638.36
101	20	6	100	5.96	166.33	640.05	1649.64
102	20	8	100	10.54	250.07	714.58	1682.27
103	20	10	100	16.31	302.88	822.73	1744.99
104	20	12	100	23.20	335.33	945.23	1864.97
105	20	14	100	30.83	353.42	1029.37	1998.02
106	20	16	100	39.01	368.51	1088.45	2121.82
107	20	18	100	47.18	384.00	1137.91	2244.90
108	20	20	100	55.26	399.88	1167.59	2304.34
109	20	22	100	62.19	414.62	1179.89	2299.31
110	20	24	100	68.32	432.23	1205.30	2329.63

Run	FEA 3-Factor Rod Data [mm]			Transverse Modal Frequency [Hz]			
	Location	Dia.	Length	Mode 1	Mode 2	Mode 3	Mode 4
111	40	4	1	14.12	365.18	1148.60	2296.07
112	40	6	1	26.86	372.00	1156.97	2315.07
113	40	8	1	38.44	381.58	1165.88	2324.32
114	40	10	1	48.01	393.61	1175.93	2331.36
115	40	12	1	57.68	409.49	1190.76	2342.01
116	40	14	1	61.84	418.25	1198.40	2343.02
117	40	16	1	65.34	425.98	1204.95	2343.62
118	40	18	1	67.86	432.72	1211.90	2347.65
119	40	20	1	69.63	437.80	1218.09	2352.40
120	40	22	1	70.47	439.94	1219.30	2349.82
121	40	24	1	70.99	441.55	1221.29	2350.94
122	40	4	25	4.42	254.98	668.48	1566.33
123	40	6	25	9.83	338.28	930.47	1757.70
124	40	8	25	17.19	359.20	1084.07	2063.77
125	40	10	25	25.60	367.16	1121.01	2182.59
126	40	12	25	34.80	375.87	1144.99	2258.77
127	40	14	25	43.62	386.25	1161.99	2295.30
128	40	16	25	51.66	397.92	1174.76	2318.05
129	40	18	25	58.21	409.80	1187.18	2331.00
130	40	20	25	63.58	421.71	1204.58	2347.88
131	40	22	25	67.32	431.02	1212.70	2349.66
132	40	24	25	69.96	438.20	1216.67	2347.28
133	40	4	50	3.16	121.36	607.67	1609.60
134	40	6	50	7.06	231.31	675.20	1640.06
135	40	8	50	12.41	305.56	810.12	1713.86
136	40	10	50	19.07	342.28	964.29	1864.92
137	40	12	50	26.74	360.50	1065.68	2048.89
138	40	14	50	34.92	371.63	1111.27	2162.34
139	40	16	50	43.45	384.43	1150.59	2268.23
140	40	18	50	51.23	395.79	1165.49	2293.58
141	40	20	50	58.48	409.77	1185.88	2327.42
142	40	22	50	64.25	422.74	1200.99	2340.03
143	40	24	50	69.00	435.16	1212.28	2342.32
144	40	4	75	2.59	73.28	630.19	1692.65
145	40	6	75	5.82	153.76	653.68	1700.30
146	40	8	75	10.29	236.30	713.88	1726.59
147	40	10	75	15.92	295.59	810.97	1774.08
148	40	12	75	22.60	330.94	919.06	1861.29
149	40	14	75	30.13	352.30	1008.65	1968.28
150	40	16	75	38.16	368.37	1073.24	2083.09
151	40	18	75	46.37	383.05	1118.76	2175.46
152	40	20	75	54.44	401.70	1174.60	2316.13
153	40	22	75	61.68	415.27	1183.81	2306.95
154	40	24	75	68.11	432.22	1206.81	2333.15
155	40	4	100	2.42	59.21	652.71	1781.43
156	40	6	100	5.43	127.04	678.51	1785.71
157	40	8	100	9.62	204.27	716.57	1793.20
158	40	10	100	14.94	271.13	787.39	1825.75
159	40	12	100	21.30	316.38	879.37	1876.59
160	40	14	100	28.50	345.93	974.01	1961.52
161	40	16	100	36.39	365.06	1045.74	2046.99
162	40	18	100	44.61	382.05	1104.97	2147.09
163	40	20	100	52.98	400.11	1160.96	2267.66
164	40	22	100	60.66	414.60	1180.16	2292.01
165	40	24	100	67.81	432.41	1208.03	2333.92

Run	FEA 3-Factor Rod Data [mm]			Transverse Modal Frequency [Hz]			
	Location	Dia.	Length	Mode 1	Mode 2	Mode 3	Mode 4
166	60	4	1	15.17	394.09	1205.84	2241.48
167	60	6	1	28.17	399.37	1211.15	2268.13
168	60	8	1	40.21	406.54	1214.20	2288.92
169	60	10	1	49.91	414.92	1216.61	2308.13
170	60	12	1	58.65	424.86	1219.87	2329.77
171	60	14	1	62.68	429.19	1219.65	2334.21
172	60	16	1	65.99	433.76	1219.91	2339.63
173	60	18	1	68.21	437.32	1221.43	2347.90
174	60	20	1	69.71	439.61	1221.31	2348.63
175	60	22	1	70.53	440.83	1221.27	2350.18
176	60	24	1	70.97	441.55	1221.15	2350.45
177	60	4	25	4.72	266.04	715.56	1703.53
178	60	6	25	10.50	362.12	972.40	1869.77
179	60	8	25	18.23	386.85	1138.57	2126.64
180	60	10	25	27.17	394.44	1176.50	2224.43
181	60	12	25	36.66	401.95	1200.11	2295.52
182	60	14	25	45.48	409.46	1210.49	2325.54
183	60	16	25	53.37	417.80	1220.15	2349.85
184	60	18	25	59.57	425.38	1222.04	2358.95
185	60	20	25	64.45	432.05	1224.81	2365.32
186	60	22	25	67.82	437.07	1226.35	2366.79
187	60	24	25	70.17	440.33	1221.72	2352.83
188	60	4	50	3.37	124.94	664.60	1767.21
189	60	6	50	7.54	240.81	729.01	1793.69
190	60	8	50	13.23	323.18	858.50	1857.60
191	60	10	50	20.27	365.87	1013.94	1989.78
192	60	12	50	28.29	385.20	1110.66	2131.10
193	60	14	50	36.77	396.99	1167.18	2243.83
194	60	16	50	45.20	406.91	1198.35	2317.10
195	60	18	50	52.85	415.63	1210.41	2340.21
196	60	20	50	59.69	424.60	1219.75	2362.94
197	60	22	50	65.09	432.46	1224.67	2369.25
198	60	24	50	69.26	438.30	1219.68	2349.84
199	60	4	75	2.77	75.25	692.61	1863.55
200	60	6	75	6.19	158.42	714.49	1861.48
201	60	8	75	10.93	245.44	770.60	1891.69
202	60	10	75	16.83	310.07	862.06	1928.96
203	60	12	75	23.83	350.62	969.14	2015.48
204	60	14	75	31.62	374.74	1060.34	2108.37
205	60	16	75	39.75	390.47	1123.12	2185.57
206	60	18	75	47.87	403.42	1164.93	2254.17
207	60	20	75	55.81	418.77	1213.47	2357.32
208	60	22	75	62.62	427.01	1214.00	2351.34
209	60	24	75	68.43	436.64	1217.59	2347.86
210	60	4	100	2.39	52.74	630.96	1732.12
211	60	6	100	5.37	114.02	739.39	1949.19
212	60	8	100	9.50	186.90	765.03	1951.40
213	60	10	100	14.72	255.91	815.31	1957.56
214	60	12	100	20.96	308.97	888.08	1985.35
215	60	14	100	28.10	346.09	972.70	2044.20
216	60	16	100	35.90	371.24	1052.48	2113.89
217	60	18	100	44.08	389.73	1111.88	2178.45
218	60	20	100	52.41	405.45	1158.24	2246.42
219	60	22	100	60.33	419.92	1190.45	2305.48
220	60	24	100	67.62	434.03	1211.15	2334.30

Run	FEA 3-Factor Rod Data [mm]			Transverse Modal Frequency [Hz]			
	Location	Dia.	Length	Mode 1	Mode 2	Mode 3	Mode 4
221	80	4	1	16.14	420.49	1181.38	1967.30
222	80	6	1	30.15	423.74	1192.67	2017.08
223	80	8	1	41.98	427.34	1198.75	2076.86
224	80	10	1	51.54	431.30	1207.04	2150.54
225	80	12	1	59.84	435.26	1212.85	2226.25
226	80	14	1	63.58	437.51	1217.79	2271.75
227	80	16	1	66.55	439.06	1218.84	2301.58
228	80	18	1	68.53	440.23	1219.64	2322.44
229	80	20	1	69.86	441.08	1221.14	2339.10
230	80	22	1	70.59	441.44	1221.20	2346.93
231	80	24	1	70.99	441.62	1220.70	2348.75
232	80	4	25	5.06	276.18	769.10	1864.29
233	80	6	25	11.25	383.69	998.74	1983.15
234	80	8	25	19.49	412.45	1152.21	2119.83
235	80	10	25	28.84	419.47	1191.53	2175.69
236	80	12	25	38.55	424.74	1211.69	2216.74
237	80	14	25	47.31	429.27	1222.39	2260.63
238	80	16	25	54.97	433.91	1230.96	2300.49
239	80	18	25	60.80	437.06	1232.52	2328.35
240	80	20	25	65.21	439.39	1230.83	2345.48
241	80	22	25	68.32	441.97	1234.63	2374.29
242	80	24	25	70.26	441.26	1222.29	2348.71
243	80	4	50	3.62	128.91	730.41	1938.90
244	80	6	50	8.09	250.57	791.35	1983.65
245	80	8	50	14.16	339.76	910.49	2031.20
246	80	10	50	21.63	388.35	1052.37	2115.40
247	80	12	50	30.07	409.00	1147.79	2227.56
248	80	14	50	38.72	419.45	1193.31	2264.65
249	80	16	50	47.10	427.14	1221.84	2312.25
250	80	18	50	54.43	431.48	1226.44	2322.75
251	80	20	50	61.00	436.77	1234.25	2353.75
252	80	22	50	65.88	439.82	1233.59	2365.80
253	80	24	50	69.51	440.64	1222.44	2347.25
254	80	4	75	2.96	77.68	724.60	2065.26
255	80	6	75	6.64	164.01	785.65	2055.25
256	80	8	75	11.69	255.15	838.14	2071.73
257	80	10	75	17.98	325.84	923.24	2108.96
258	80	12	75	25.35	370.24	1020.99	2152.98
259	80	14	75	33.40	395.95	1104.21	2224.04
260	80	16	75	41.71	411.57	1161.57	2270.23
261	80	18	75	49.71	421.97	1196.46	2321.91
262	80	20	75	57.27	433.45	1234.78	2363.41
263	80	22	75	63.55	436.09	1224.36	2348.78
264	80	24	75	68.81	440.00	1222.46	2347.50
265	80	4	100	2.57	54.69	646.53	1743.85
266	80	6	100	5.76	118.39	817.43	2126.92
267	80	8	100	10.17	194.60	841.04	2140.50
268	80	10	100	15.73	267.80	887.48	2149.07
269	80	12	100	22.34	325.11	955.06	2171.56
270	80	14	100	29.80	365.56	1031.66	2197.64
271	80	16	100	37.80	391.53	1101.06	2234.25
272	80	18	100	46.00	409.10	1154.23	2280.13
273	80	20	100	54.07	421.66	1189.70	2304.53
274	80	22	100	61.49	431.15	1210.30	2331.68
275	80	24	100	68.05	438.19	1218.52	2343.40

Run	FEA 3-Factor Rod Data [mm]			Transverse Modal Frequency [Hz]			
	Location	Dia.	Length	Mode 1	Mode 2	Mode 3	Mode 4
276	100	4	1	17.51	438.03	1053.24	1886.15
277	100	6	1	32.05	439.16	1079.62	1924.63
278	100	8	1	43.93	439.78	1111.72	1985.09
279	100	10	1	53.12	440.38	1144.69	2064.39
280	100	12	1	61.02	440.91	1176.90	2163.15
281	100	14	1	64.42	441.14	1191.18	2217.73
282	100	16	1	67.08	441.45	1203.29	2267.09
283	100	18	1	68.83	441.57	1211.67	2304.36
284	100	20	1	69.99	441.66	1217.05	2329.93
285	100	22	1	70.63	441.63	1219.03	2340.68
286	100	24	1	70.99	441.81	1221.37	2350.74
287	100	4	25	5.44	283.40	828.99	2039.15
288	100	6	25	12.09	398.93	1003.81	2066.13
289	100	8	25	20.89	430.41	1106.43	2083.62
290	100	10	25	30.58	436.23	1135.82	2095.15
291	100	12	25	40.52	440.01	1162.27	2126.39
292	100	14	25	49.24	442.09	1184.00	2180.90
293	100	16	25	56.33	442.53	1198.30	2218.97
294	100	18	25	61.88	442.73	1208.03	2260.96
295	100	20	25	65.88	442.86	1217.30	2304.10
296	100	22	25	68.54	442.73	1222.20	2335.86
297	100	24	25	70.35	441.77	1220.69	2343.92
298	100	4	50	3.89	132.98	806.92	2146.73
299	100	6	50	8.68	257.81	862.02	2163.89
300	100	8	50	15.20	352.69	963.65	2193.57
301	100	10	50	23.10	404.70	1075.02	2221.94
302	100	12	50	31.85	426.35	1144.95	2240.28
303	100	14	50	40.68	436.07	1186.18	2270.07
304	100	16	50	49.07	441.56	1208.41	2276.53
305	100	18	50	56.11	443.34	1220.69	2300.75
306	100	20	50	62.10	444.73	1229.74	2332.37
307	100	22	50	66.51	444.25	1230.19	2350.16
308	100	24	50	69.70	441.77	1220.61	2340.48
309	100	4	75	3.19	80.41	742.87	2279.39
310	100	6	75	7.13	169.68	868.46	2270.71
311	100	8	75	12.56	264.76	916.09	2294.99
312	100	10	75	19.26	339.28	989.59	2298.58
313	100	12	75	27.02	386.17	1070.40	2309.00
314	100	14	75	35.33	413.04	1134.72	2318.91
315	100	16	75	43.71	427.32	1176.64	2315.65
316	100	18	75	51.51	435.03	1199.43	2311.50
317	100	20	75	58.84	444.69	1235.20	2341.51
318	100	22	75	64.52	442.90	1227.20	2347.36
319	100	24	75	69.08	441.76	1221.42	2342.74
320	100	4	100	2.76	56.81	663.75	1746.40
321	100	6	100	6.19	122.98	908.87	2315.16
322	100	8	100	10.92	202.36	929.30	2360.50
323	100	10	100	16.87	278.98	970.51	2355.89
324	100	12	100	23.87	339.51	1027.12	2351.35
325	100	14	100	31.65	381.22	1089.15	2345.78
326	100	16	100	39.83	407.83	1141.80	2342.28
327	100	18	100	47.96	423.96	1179.91	2336.34
328	100	20	100	55.74	433.94	1205.60	2333.92
329	100	22	100	62.62	438.88	1216.60	2338.76
330	100	24	100	68.49	441.16	1220.40	2344.05

Run	FEA 3-Factor Rod Data [mm]			Transverse Modal Frequency [Hz]			
	Location	Dia.	Length	Mode 1	Mode 2	Mode 3	Mode 4
331	120	4	1	18.49	436.50	934.63	1961.62
332	120	6	1	34.23	438.00	974.12	1992.10
333	120	8	1	46.06	439.12	1024.88	2037.84
334	120	10	1	54.98	439.91	1080.13	2098.65
335	120	12	1	62.26	440.52	1135.64	2177.04
336	120	14	1	65.23	440.86	1162.89	2224.81
337	120	16	1	67.62	441.27	1186.08	2269.85
338	120	18	1	69.14	441.56	1202.52	2307.01
339	120	20	1	70.13	441.62	1212.11	2328.59
340	120	22	1	70.68	441.53	1217.28	2341.17
341	120	24	1	70.96	441.45	1219.88	2347.95
342	120	4	25	5.87	288.05	895.76	1695.93
343	120	6	25	12.97	399.49	986.10	1984.00
344	120	8	25	22.33	433.11	1030.57	2068.30
345	120	10	25	32.43	438.88	1054.76	2094.22
346	120	12	25	42.55	442.34	1085.22	2127.89
347	120	14	25	51.12	443.66	1119.69	2165.50
348	120	16	25	57.92	443.97	1151.71	2206.48
349	120	18	25	62.94	444.77	1183.87	2265.89
350	120	20	25	66.56	444.28	1203.60	2303.11
351	120	22	25	68.85	442.98	1212.96	2326.82
352	120	24	25	70.44	441.96	1219.08	2343.94
353	120	4	50	4.20	136.79	891.79	1949.59
354	120	6	50	9.37	263.55	942.86	2016.15
355	120	8	50	16.32	357.21	1012.78	2121.29
356	120	10	50	24.71	409.88	1074.18	2180.22
357	120	12	50	33.84	431.46	1111.65	2200.61
358	120	14	50	42.75	440.58	1136.98	2216.93
359	120	16	50	50.94	445.10	1161.20	2245.10
360	120	18	50	57.64	446.32	1186.08	2274.99
361	120	20	50	63.17	446.32	1203.27	2303.95
362	120	22	50	67.01	444.20	1211.41	2319.89
363	120	24	50	69.90	442.29	1217.96	2339.55
364	120	4	75	3.44	83.28	762.40	2468.19
365	120	6	75	7.69	175.47	965.75	2461.16
366	120	8	75	13.51	272.04	1005.14	2411.69
367	120	10	75	20.68	347.67	1059.98	2377.76
368	120	12	75	28.84	396.21	1114.36	2367.07
369	120	14	75	37.45	422.88	1152.96	2342.60
370	120	16	75	45.77	434.66	1170.55	2306.14
371	120	18	75	53.44	441.59	1193.32	2310.89
372	120	20	75	60.10	447.47	1209.74	2320.70
373	120	22	75	65.28	444.14	1211.56	2325.19
374	120	24	75	69.38	442.61	1218.30	2339.54
375	120	4	100	2.98	59.16	682.56	1744.24
376	120	6	100	6.68	127.75	992.66	2383.52
377	120	8	100	11.77	209.98	1032.62	2529.18
378	120	10	100	18.13	288.37	1064.60	2507.75
379	120	12	100	25.52	349.80	1104.70	2452.56
380	120	14	100	33.62	392.20	1143.47	2405.96
381	120	16	100	41.98	418.54	1174.30	2373.47
382	120	18	100	49.97	432.73	1191.82	2351.60
383	120	20	100	57.40	440.88	1208.05	2341.35
384	120	22	100	63.73	443.59	1217.77	2349.51
385	120	24	100	68.84	442.28	1217.79	2343.28

Run	FEA 3-Factor Rod Data [mm]			Transverse Modal Frequency [Hz]			
	Location	Dia.	Length	Mode 1	Mode 2	Mode 3	Mode 4
386	140	4	1	20.12	409.55	889.82	2100.94
387	140	6	1	36.37	416.41	929.47	2124.85
388	140	8	1	48.31	423.34	985.51	2154.11
389	140	10	1	56.73	429.48	1045.82	2193.69
390	140	12	1	63.35	434.73	1111.53	2241.96
391	140	14	1	66.01	437.03	1144.53	2270.98
392	140	16	1	68.12	439.05	1174.93	2300.15
393	140	18	1	69.42	440.17	1194.64	2320.83
394	140	20	1	70.31	441.31	1209.51	2338.47
395	140	22	1	70.73	441.29	1215.76	2343.28
396	140	24	1	70.97	441.41	1219.63	2347.70
397	140	4	25	6.36	286.80	955.18	1303.82
398	140	6	25	14.06	387.82	968.86	1830.35
399	140	8	25	24.00	415.94	981.55	2090.83
400	140	10	25	34.62	423.66	1003.41	2145.45
401	140	12	25	44.81	431.39	1041.08	2196.33
402	140	14	25	53.13	435.83	1082.97	2235.32
403	140	16	25	59.47	438.76	1123.26	2274.57
404	140	18	25	64.01	441.26	1161.74	2296.57
405	140	20	25	67.19	442.86	1191.73	2320.04
406	140	22	25	69.23	442.84	1209.07	2337.67
407	140	24	25	70.52	441.74	1217.14	2344.63
408	140	4	50	4.55	140.86	915.30	1360.46
409	140	6	50	10.15	267.08	1030.15	1475.52
410	140	8	50	17.62	355.70	1054.27	1720.87
411	140	10	50	26.51	403.83	1068.28	1998.62
412	140	12	50	35.97	423.95	1081.81	2149.49
413	140	14	50	44.95	434.27	1101.97	2224.44
414	140	16	50	52.93	440.22	1128.09	2266.83
415	140	18	50	59.19	442.04	1155.42	2284.60
416	140	20	50	64.23	444.56	1187.64	2326.01
417	140	22	50	67.58	443.43	1202.88	2333.57
418	140	24	50	70.05	442.00	1215.37	2343.88
419	140	4	75	3.73	86.41	783.87	1659.97
420	140	6	75	8.33	180.83	1079.47	1674.94
421	140	8	75	14.61	277.42	1103.00	1744.37
422	140	10	75	22.23	349.94	1123.89	1883.59
423	140	12	75	30.78	394.23	1134.80	2036.55
424	140	14	75	39.57	418.68	1142.07	2152.19
425	140	16	75	47.93	432.12	1151.88	2226.17
426	140	18	75	55.25	439.30	1168.80	2279.38
427	140	20	75	61.46	446.33	1193.60	2339.64
428	140	22	75	66.09	443.50	1201.22	2325.96
429	140	24	75	69.62	442.41	1215.07	2343.50
430	140	4	100	3.23	61.72	702.76	1711.74
431	140	6	100	7.23	133.13	1020.55	1982.23
432	140	8	100	12.73	217.03	1152.54	1988.56
433	140	10	100	19.53	295.60	1166.53	2013.25
434	140	12	100	27.38	356.07	1178.97	2095.59
435	140	14	100	35.77	396.51	1184.10	2169.03
436	140	16	100	44.11	419.76	1183.70	2223.33
437	140	18	100	51.99	432.97	1185.28	2263.12
438	140	20	100	58.95	439.83	1193.24	2301.76
439	140	22	100	64.64	442.18	1203.27	2320.46
440	140	24	100	69.13	441.97	1213.98	2339.49

Run	FEA 3-Factor Rod Data [mm]			Transverse Modal Frequency [Hz]			
	Location	Dia.	Length	Mode 1	Mode 2	Mode 3	Mode 4
441	160	4	1	21.48	367.54	906.51	2252.31
442	160	6	1	38.43	381.74	940.46	2268.34
443	160	8	1	50.59	398.43	991.67	2285.50
444	160	10	1	58.52	412.71	1048.52	2300.36
445	160	12	1	64.30	425.25	1110.92	2315.50
446	160	14	1	66.79	430.79	1143.75	2327.88
447	160	16	1	68.58	435.27	1173.36	2334.97
448	160	18	1	69.67	438.12	1193.71	2341.38
449	160	20	1	70.44	440.36	1209.09	2347.56
450	160	22	1	70.78	441.05	1215.76	2347.94
451	160	24	1	70.97	441.39	1219.83	2349.32
452	160	4	25	6.93	280.62	928.45	1195.22
453	160	6	25	15.24	360.64	964.48	1735.33
454	160	8	25	25.83	384.62	979.56	2126.18
455	160	10	25	36.94	395.38	1001.08	2215.53
456	160	12	25	47.16	407.35	1033.26	2262.90
457	160	14	25	55.04	417.94	1072.74	2290.17
458	160	16	25	60.91	427.19	1115.00	2314.13
459	160	18	25	65.04	435.51	1159.43	2357.63
460	160	20	25	67.78	438.58	1184.95	2344.75
461	160	22	25	69.49	440.71	1204.68	2345.83
462	160	24	25	70.61	441.41	1216.49	2348.63
463	160	4	50	4.96	144.78	941.56	1133.93
464	160	6	50	11.02	266.56	1035.10	1250.72
465	160	8	50	19.10	345.54	1048.89	1533.34
466	160	10	50	28.55	386.04	1056.56	1878.00
467	160	12	50	38.32	404.17	1067.85	2092.82
468	160	14	50	47.32	416.24	1088.15	2217.45
469	160	16	50	54.93	426.93	1118.02	2295.28
470	160	18	50	60.77	433.81	1149.63	2327.62
471	160	20	50	65.22	439.09	1177.70	2350.22
472	160	22	50	68.17	441.25	1200.56	2355.26
473	160	24	50	70.22	441.42	1214.35	2345.81
474	160	4	75	4.06	89.87	807.60	1214.59
475	160	6	75	9.06	186.15	1156.31	1266.21
476	160	8	75	15.85	280.59	1153.29	1401.79
477	160	10	75	24.04	347.11	1140.73	1612.78
478	160	12	75	32.97	385.43	1130.20	1833.84
479	160	14	75	41.99	407.73	1130.93	2029.25
480	160	16	75	50.17	422.95	1140.70	2185.33
481	160	18	75	57.13	430.99	1158.23	2258.92
482	160	20	75	62.86	440.50	1183.50	2358.29
483	160	22	75	66.87	441.35	1201.32	2344.75
484	160	24	75	69.84	441.34	1212.61	2343.68
485	160	4	100	3.51	64.64	725.39	1436.30
486	160	6	100	7.87	138.75	1051.25	1446.53
487	160	8	100	13.82	224.15	1266.75	1496.53
488	160	10	100	21.13	300.64	1237.95	1606.10
489	160	12	100	29.41	356.12	1204.50	1745.22
490	160	14	100	38.10	392.08	1185.10	1919.75
491	160	16	100	46.47	413.48	1175.25	2068.96
492	160	18	100	54.05	427.09	1179.17	2197.63
493	160	20	100	60.50	434.62	1183.14	2263.79
494	160	22	100	65.62	439.59	1198.95	2313.89
495	160	24	100	69.47	441.19	1212.63	2340.02

Run	FEA 3-Factor Rod Data [mm]			Transverse Modal Frequency [Hz]			
	Location	Dia.	Length	Mode 1	Mode 2	Mode 3	Mode 4
496	180	4	1	23.83	324.24	963.18	2320.40
497	180	6	1	41.02	345.32	990.85	2334.34
498	180	8	1	52.79	370.11	1030.96	2340.21
499	180	10	1	60.14	393.45	1077.61	2344.22
500	180	12	1	65.44	414.32	1129.86	2345.04
501	180	14	1	67.48	423.42	1156.97	2345.69
502	180	16	1	69.00	430.95	1181.57	2348.37
503	180	18	1	69.90	435.53	1197.79	2348.54
504	180	20	1	70.52	438.85	1209.92	2348.79
505	180	22	1	70.82	440.56	1216.46	2348.84
506	180	24	1	70.98	441.33	1219.73	2350.14
507	180	4	25	7.57	269.50	820.92	1277.78
508	180	6	25	16.63	328.48	975.89	1729.79
509	180	8	25	28.02	348.19	1013.21	2127.42
510	180	10	25	39.51	362.55	1034.13	2232.87
511	180	12	25	49.60	380.07	1062.24	2288.18
512	180	14	25	57.07	397.62	1095.32	2311.43
513	180	16	25	62.47	414.21	1132.79	2334.04
514	180	18	25	66.01	425.76	1164.28	2358.67
515	180	20	25	68.40	434.78	1192.96	2359.29
516	180	22	25	69.81	439.18	1208.70	2363.56
517	180	24	25	70.69	440.90	1217.21	2349.13
518	180	4	50	5.43	148.83	769.22	1283.14
519	180	6	50	12.03	263.20	874.35	1348.99
520	180	8	50	20.75	327.87	991.03	1545.23
521	180	10	50	30.76	359.20	1049.72	1849.08
522	180	12	50	40.78	377.41	1076.73	2077.18
523	180	14	50	49.70	393.71	1101.31	2216.56
524	180	16	50	56.97	409.01	1129.76	2297.68
525	180	18	50	62.29	421.69	1157.46	2336.97
526	180	20	50	66.15	431.01	1180.80	2342.03
527	180	22	50	68.68	437.29	1201.05	2349.44
528	180	24	50	70.38	440.45	1214.69	2346.85
529	180	4	75	4.44	93.70	834.19	1381.43
530	180	6	75	9.90	191.10	906.78	1397.27
531	180	8	75	17.26	279.70	979.72	1459.72
532	180	10	75	26.02	336.81	1051.40	1603.24
533	180	12	75	35.42	369.04	1093.72	1801.73
534	180	14	75	44.52	389.66	1117.06	1991.02
535	180	16	75	52.54	406.96	1141.98	2166.98
536	180	18	75	59.02	418.16	1157.07	2233.22
537	180	20	75	64.11	430.30	1182.15	2350.65
538	180	22	75	67.60	436.03	1198.45	2333.29
539	180	24	75	70.07	440.06	1213.08	2343.78
540	180	4	100	3.85	67.95	750.51	1483.54
541	180	6	100	8.60	144.75	1029.00	1491.46
542	180	8	100	15.07	230.52	1051.80	1513.74
543	180	10	100	22.93	302.15	1089.29	1582.57
544	180	12	100	31.69	351.08	1121.83	1707.40
545	180	14	100	40.61	381.74	1141.17	1868.07
546	180	16	100	48.97	401.67	1154.88	2026.58
547	180	18	100	56.18	416.09	1169.66	2162.46
548	180	20	100	62.12	427.44	1184.08	2262.12
549	180	22	100	66.54	434.75	1198.14	2308.07
550	180	24	100	69.75	439.71	1212.97	2339.65

Appendix C - Full Scale Pole Test Data and Measurements

Pole Statistics (BF1)					
Identification	BF1		Class	2	
Species	SYP		Treatment Type (Year)	Penta (2005)	
Property / Measurement	**Value (Metric Units)**		**Property / Measurement**	**Value (Imperial Units)**	
Length [mm]	16725.9		Length [ft]	55' Nominal (54' 10.5" Actual)	
GL to POL [mm]	13830.30		GL to POL [in]	544.50	
Butt to GL [mm]	2286		Butt to GL [in]	90.00	
POL to Tip [mm]	609.6		POL to Tip [in]	24.00	
GL to Break [mm]	6390		GL to Break [in]	251.57	
Circ. at Break [mm]	1018.4		Circ. at Break [in]	40.09	
Butt Circumference [mm]	1287		Butt Circumference [in]	50.67	
GL Circumference [mm]	1130		GL Circumference [in]	44.49	
5' from GL Circumference [mm]	1115		5' from GL Circumference [in]	43.90	
10' from GL Circumference [mm]	1080		10' from GL Circumference [in]	42.52	
15' from GL Circumference [mm]	1045		15' from GL Circumference [in]	41.14	
20' from GL Circumference [mm]	1023		20' from GL Circumference [in]	40.28	
25' from GL Circumference [mm]	1000		25' from GL Circumference [in]	39.37	
30' from GL Circumference [mm]	989		30' from GL Circumference [in]	38.94	
35' from GL Circumference [mm]	946		35' from GL Circumference [in]	37.24	
40' from GL Circumference [mm]	883		40' from GL Circumference [in]	34.76	
45' from GL Circumference [mm]	802		45' from GL Circumference [in]	31.57	
POL Circumference [mm]	795		POL Circumference [in]	31.30	
Tip Circumference [mm]	780		Tip Circumference [in]	30.71	
Volume (m^3)	1.41		Volume (ft^3)	49.80	
CM from Butt (mm)	7352.95		CM from Butt (in)	289.49	
LVDT Spacing (mm)	2200		LVDT Spacing (in)	86.61	
Mass [kg]	866.36		Mass [lb]	1910	
Density [kg/m^3]	614.41		Density [lb/ft^3]	38.36	
POLETEST: 1' from GL (inline, 90 deg) [Mpa]	44.75	47.30	POLETEST: 1' from GL (inline, 90 deg) [psi]	6490	6860
POLETEST: 10' from GL (inline, 90 deg) [Mpa]	40.40	38.54	POLETEST: 10' from GL (inline, 90 deg) [psi]	5860	5590
POLETEST: 20' from GL (inline, 90 deg) [Mpa]	38.47	38.96	POLETEST: 20' from GL (inline, 90 deg) [psi]	5580	5650

Static Test (BF1)			
Property (Metric Units)	**Measured Value**	**Property (Imperial Units)**	**Measured Value**
Max Load [N]	14244.98	Max Load [lb]	3200.00
Yield Load [N]	9348.27	Load at Yield [lb]	2100.00
POL Deflection at Max Load (corrected) [mm]	2886.89	POL Deflection at Max Load (corrected) [in]	113.66
POL Deflection at Yield Load (corrected) [mm]	1365.13	POL Deflection at Yield Load (corrected) [in]	53.75
POL Displacement Along Pole at Max Load [mm]	650.00	POL Displacement Along Pole at Max Load [in]	25.59
POL Displacement Along Pole at Yield Load [mm]	225.00	POL Displacement Along Pole at Yield Load [in]	8.86
Max Stress at GL [Mpa]	41.10	Max Stress at GL [psi]	5960.50
GL Stress at Yield [Mpa]	27.84	GL Stress at Yield [psi]	4037.71
Max Stress at Break Location [Mpa]	29.20	Max Stress at Break Location [psi]	4234.55
Break Location Stress at Yield [Mpa]	20.23	Break Location Stress at Yield [psi]	2934.23
Modulus of Elasticity [Mpa]	10446.19	Modulus of Elasticity [psi*10^6]	1.52
Density [kg/m^3]	614.41	Density [lb/ft^3]	38.36

Modal Test (BF1)				
Transverse Mode	Measured Frequency [Hz]	Measured Damping ratio	FEA Undamped Frequency (Measured Properties)	FEA Undamped Frequency (Published Properties)
1st	0.963	0.0076	1.153	1.283
2nd	4.681	0.0081	6.110	6.790
3rd	11.908	0.0090	15.975	17.736
4th	22.558	0.0126	30.330	33.642
5th	35.799	0.0097	49.442	54.788
6th	51.680	0.0093	72.938	80.809

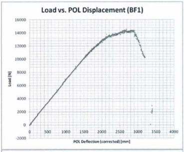

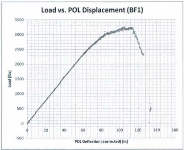

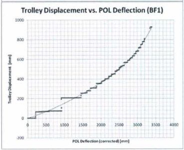

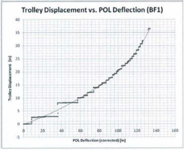

Pole Statistics (BF2)			
Identification	BF2	Class	2
Species	SYP	Treatment Type (Year)	Penta (2005)
Property / Measurement	**Value (Metric Units)**	**Property / Measurement**	**Value (Imperial Units)**
Length [mm]	16675.1	Length [ft]	55' Nominal (54' 8.5" Actual)
GL to POL [mm]	13779.50	GL to POL [in]	542.50
Butt to GL [mm]	2286	Butt to GL [in]	90.00
POL to Tip [mm]	609.6	POL to Tip [in]	24.00
GL to Break [mm]	3759.2	GL to Break [in]	148.00
Circ. at Break [mm]	1066.8	Circ. at Break [in]	42.00
Butt Circumference [mm]	1234	Butt Circumference [in]	48.58
GL Circumference [mm]	1092	GL Circumference [in]	42.99
5' from GL Circumference [mm]	1052	5' from GL Circumference [in]	41.42
10' from GL Circumference [mm]	1067	10' from GL Circumference [in]	42.01
15' from GL Circumference [mm]	1011	15' from GL Circumference [in]	39.80
20' from GL Circumference [mm]	991	20' from GL Circumference [in]	39.02
25' from GL Circumference [mm]	929	25' from GL Circumference [in]	36.57
30' from GL Circumference [mm]	895	30' from GL Circumference [in]	35.24
35' from GL Circumference [mm]	867	35' from GL Circumference [in]	34.13
40' from GL Circumference [mm]	814	40' from GL Circumference [in]	32.05
45' from GL Circumference [mm]	805	45' from GL Circumference [in]	31.69
POL Circumference [mm]	799	POL Circumference [in]	31.46
Tip Circumference [mm]	777	Tip Circumference [in]	30.59
Volume (m^3)	1.41	Volume (ft^3)	49.80
CM from Butt (mm)	7352.95	CM from Butt (in)	289.49
LVDT Spacing (mm)	2200	LVDT Spacing (in)	86.61
Mass [kg]	842.06	Mass [lb]	1856.416
Density [kg/m^3]	597.17	Density [lb/ft^3]	37.28
POLETEST: 1' from GL (inline, 90 deg) [Mpa]	50.33 48.47	POLETEST: 1' from GL (inline, 90 deg) [psi]	7300 7030
POLETEST: 10' from GL (inline, 90 deg) [Mpa]	39.92 45.23	POLETEST: 10' from GL (inline, 90 deg) [psi]	5790 6560
POLETEST: 20' from GL (inline, 90 deg) [Mpa]	37.99 37.37	POLETEST: 20' from GL (inline, 90 deg) [psi]	5510 5420

Static Test (BF2)			
Property (Metric Units)	**Measured Value**	**Property (Imperial Units)**	**Measured Value**
Max Load [N]	15691.73	Max Load [lb]	3525.00
Yield Load [N]	6677.33	Load at Yield [lb]	1500.00
POL Deflection at Max Load (corrected) [mm]	2801.09	POL Deflection at Max Load (corrected) [in]	110.28
POL Deflection at Yield Load (corrected) [mm]	946.54	POL Deflection at Yield Load (corrected) [in]	37.27
POL Displacement Along Pole at Max Load [mm]	400.00	POL Displacement Along Pole at Max Load [in]	15.75
POL Displacement Along Pole at Yield Load [mm]	0.92	POL Displacement Along Pole at Yield Load [in]	0.04
Max Stress at GL [Mpa]	50.92	Max Stress at GL [psi]	7385.39
GL Stress at Yield [Mpa]	22.31	GL Stress at Yield [psi]	3236.46
Max Stress at Break Location [Mpa]	39.30	Max Stress at Break Location [psi]	5700.43
Break Location Stress at Yield [Mpa]	17.40	Break Location Stress at Yield [psi]	2524.22
Modulus of Elasticity [Mpa]	11734.28	Modulus of Elasticity [psi*10^6]	1.70
Density [kg/m^3]	597.17	Density [lb/ft^3]	37.28

Modal Test (BF2)				
Transverse Mode	Measured Frequency [Hz]	Measured Damping ratio	FEA Undamped Frequency (Measured Properties)	FEA Undamped Frequency (Published Properties)
1st	1.168	0.0059	1.205	1.319
2nd	5.609	0.0058	6.044	6.616
3rd	14.336	0.0065	16.053	17.572
4th	27.475	0.0131	30.981	33.914
5th	44.243	0.0110	51.075	55.909
6th	63.495	0.0095	75.797	82.971

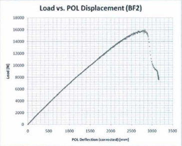

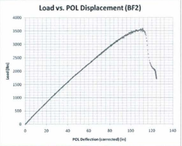

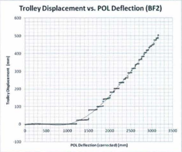

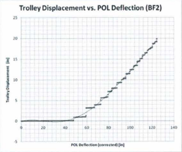

Pole Statistics (BF3)					
Identification	BF3		Class	2	
Species	SYP		Treatment Type (Year)	Penta (2005)	
Property / Measurement	**Value (Metric Units)**		**Property / Measurement**	**Value (Imperial Units)**	
Length [mm]	16700.5		Length [ft]	55' Nominal (54' 9.5" Actual)	
GL to POL [mm]	13804.90		GL to POL [in]	543.50	
Butt to GL [mm]	2286		Butt to GL [in]	90.00	
POL to Tip [mm]	609.6		POL to Tip [in]	24.00	
GL to Break [mm]	0		GL to Break [in]	0.00	
Circ. at Break [mm]	1148		Circ. at Break [in]	45.20	
Butt Circumference [mm]	1180		Butt Circumference [in]	46.46	
GL Circumference [mm]	1148		GL Circumference [in]	45.20	
5' from GL Circumference [mm]	1119		5' from GL Circumference [in]	44.06	
10' from GL Circumference [mm]	1112		10' from GL Circumference [in]	43.78	
15' from GL Circumference [mm]	1074		15' from GL Circumference [in]	42.28	
20' from GL Circumference [mm]	1040		20' from GL Circumference [in]	40.94	
25' from GL Circumference [mm]	1014		25' from GL Circumference [in]	39.92	
30' from GL Circumference [mm]	979		30' from GL Circumference [in]	38.54	
35' from GL Circumference [mm]	922		35' from GL Circumference [in]	36.30	
40' from GL Circumference [mm]	867		40' from GL Circumference [in]	34.13	
45' from GL Circumference [mm]	812		45' from GL Circumference [in]	31.97	
POL Circumference [mm]	813		POL Circumference [in]	32.01	
Tip Circumference [mm]	767		Tip Circumference [in]	30.20	
Volume (m^3)	1.41		Volume (ft^3)	49.65	
CM from Butt (mm)	7352.95		CM from Butt (in)	289.49	
LVDT Spacing (mm)	2200		LVDT Spacing (in)	86.61	
Mass [kg]	962.23		Mass [lb]	2121.36	
Density [kg/m^3]	684.45		Density [lb/ft^3]	42.73	
POLETEST: 1' from GL (inline, 90deg) [Mpa]	54.68	47.71	POLETEST: 1' from GL (inline, 90deg) [psi]	7930	6920
POLETEST: 10' from GL (inline, 90deg) [Mpa]	39.58	43.30	POLETEST: 10' from GL (inline, 90deg) [psi]	5740	6280
POLETEST: 20' from GL (inline, 90deg) [Mpa]	34.20	37.58	POLETEST: 20' from GL (inline, 90deg) [psi]	4960	5450

Static Test (BF3)			
Property (Metric Units)	**Measured Values**	**Property (Imperial Units)**	**Measured Values**
Max Load [N]	21367.47	Max Load [lb]	4800.00
Yield Load [N]	14000.14	Load at Yield [lb]	3145.00
POL Deflection at Max Load (corrected) [mm]	3150.00	POL Deflection at Max Load (corrected) [in]	124.02
POL Deflection at Yield Load (corrected) [mm]	1800.00	POL Deflection at Yield Load (corrected) [in]	70.87
POL Displacement Along Pole at Max Load [mm]	560.00	POL Displacement Along Pole at Max Load [in]	22.05
POL Displacement Along Pole at Yield Load [mm]	150.00	POL Displacement Along Pole at Yield Load [in]	5.91
Max Stress at GL [Mpa]	59.08	Max Stress at GL [psi]	8568.54
GL Stress at Yield [Mpa]	39.91	GL Stress at Yield [psi]	5787.97
Max Stress at Break Location [Mpa]	59.08	Max Stress at Break Location [psi]	8568.54
Break Location Stress at Yield [Mpa]	39.91	Break Location Stress at Yield [psi]	5787.97
Modulus of Elasticity [Mpa]	11004.03	Modulus of Elasticity [psi*10^6]	1.60
Density [kg/m^3]	684.45	Density [lb/ft^3]	42.73

Modal Test (BF3)				
Transverse Mode	Measured Frequency [Hz]	Measured Damping ratio	FEA Undamped Frequency (Measured Properties)	FEA Undamped Frequency (Published Properties)
1st	1.129	0.0062	1.173	1.420
2nd	5.500	0.0066	5.975	7.230
3rd	14.085	0.0075	15.541	18.808
4th	26.930	0.0091	29.793	36.055
5th	43.006	0.0112	48.621	58.840
6th	63.133	0.0089	71.868	86.972

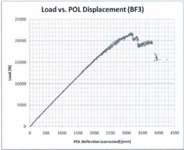

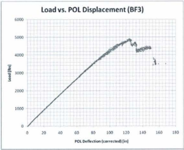

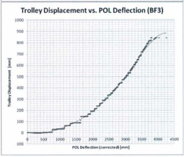

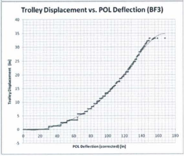

Pole Statistics (TL-222 108 SYP A) (1st Old Pole)			
Identification	TL-222 108 SYP A	Class	N/A
Species	SYP	Treatment Type (Year)	N/A
Property / Measurement	**Value (Metric Units)**	**Property / Measurement**	**Value (Imperial Units)**
Length [mm]	18199.1	Length [ft]	60' Nominal (59' 8.5" Actual)
GL to POL [mm]	15151.10	GL to POL [in]	596.50
Butt to GL [mm]	2438.4	Butt to GL [in]	96.00
POL to Tip [mm]	609.6	POL to Tip [in]	24.00
GL to Break [mm]	5230	GL to Break [in]	205.91
Circ. at Break [mm]	968	Circ. at Break [in]	38.11
Butt Circumference [mm]	1058	Butt Circumference [in]	41.65
GL Circumference [mm]	1034	GL Circumference [in]	40.71
5' from GL Circumference [mm]	996	5' from GL Circumference [in]	39.21
10' from GL Circumference [mm]	1005	10' from GL Circumference [in]	39.57
15' from GL Circumference [mm]	996	15' from GL Circumference [in]	39.21
20' from GL Circumference [mm]	932	20' from GL Circumference [in]	36.69
25' from GL Circumference [mm]	899	25' from GL Circumference [in]	35.39
30' from GL Circumference [mm]	897	30' from GL Circumference [in]	35.31
35' from GL Circumference [mm]	832	35' from GL Circumference [in]	32.76
40' from GL Circumference [mm]	783	40' from GL Circumference [in]	30.83
45' from GL Circumference [mm]	725	45' from GL Circumference [in]	28.54
50' from GL Circumference [mm]	650	50' from GL Circumference [in]	25.59
POL Circumference [mm]	660	POL Circumference [in]	25.98
Tip Circumference [mm]	566	Tip Circumference [in]	22.28
Volume (m^3)	1.20	Volume (ft^3)	42.39
CM from Butt (mm)	7809.7	CM from Butt (in)	307.47
LVDT Spacing (mm)	2200	LVDT Spacing (in)	86.61
Mass [kg]	858.97	Mass [lb]	1893.7
Density [kg/m^3)	715.52	Density [lb/ft^3)	44.67
POLETEST: 1' from GL (inline, 90 deg) [Mpa]	34.40 25.23	POLETEST: 1' from GL (inline, 90 deg) [psi]	4990 3660
POLETEST: 10' from GL (inline, 90 deg) [Mpa]	27.72 15.58	POLETEST: 10' from GL (inline, 90 deg) [psi]	4020 2260
POLETEST: 20' from GL (inline, 90 deg) [Mpa]	3.45 N/A	POLETEST: 20' from GL (inline, 90 deg) [psi]	500 N/A

Static Test (TL-222 108 SYP A) (1st Old Pole)			
Property (Metric Units)	**Measured Values**	**Property (Imperial Units)**	**Measured Values**
Max Load [N]	5252.84	Max Load [lb]	1180.00
Yield Load [N]	3205.12	Load at Yield [lb]	720.00
POL Deflection at Max Load (corrected) [mm]	2650.00	POL Deflection at Max Load (corrected) [in]	104.33
POL Deflection at Yield Load (corrected) [mm]	1075.00	POL Deflection at Yield Load (corrected) [in]	42.32
POL Displacement Along Pole at Max Load [mm]	260.00	POL Displacement Along Pole at Max Load [in]	10.24
POL Displacement Along Pole at Yield Load [mm]	0.00	POL Displacement Along Pole at Yield Load [in]	0.00
Max Stress at GL [Mpa]	22.35	Max Stress at GL [psi]	3241.08
GL Stress at Yield [Mpa]	13.87	GL Stress at Yield [psi]	2012.14
Max Stress at Break Location [Mpa]	17.69	Max Stress at Break Location [psi]	2565.70
Break Location Stress at Yield [Mpa]	11.07	Break Location Stress at Yield [psi]	1605.86
Modulus of Elasticity [Mpa]	9400.94	Modulus of Elasticity [psi*10^6]	1.36
Density [kg/m^3]	715.52	Density [lb/ft^3]	44.67

Modal Test (TL-222 108 SYP A) (1st Old Pole)				
Transverse Mode	Measured Frequency [Hz]	Measured Damping ratio	FEA Undamped Frequency (Measured Properties)	FEA Undamped Frequency (Published Properties)
1st	0.840	0.0125	0.827	1.107
2nd	3.945	0.0114	4.092	5.478
3rd	9.848	0.0184	10.486	14.038
4th	18.008	0.0181	20.098	26.905
5th	29.962	0.0185	32.726	43.810
6th	44.097	0.0234	48.392	64.782

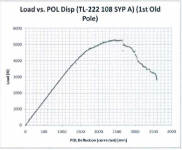

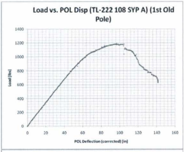

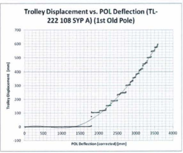

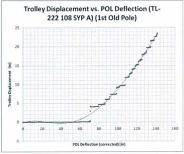

Pole Statistics (TL-222 108 SYP B) (2nd Old Pole)			
Identification	TL-222 108 SYP B	Class	N/A
Species	SYP	Treatment Type (Year)	N/A
Property / Measurement	**Value (Metric Units)**	**Property / Measurement**	**Value (Imperial Units)**
Length [mm]	16605.6	Length [ft]	65' Nominal (Brkn to 54' 6')
GL to POL [mm]	13710.00	GL to POL [in]	539.76
Butt to GL [mm]	2286	Butt to GL [in]	90.00
POL to Tip [mm]	609.6	POL to Tip [in]	24.00
GL to Break [mm]	1420	GL to Break [in]	55.91
Circ. at Break [mm]	972	Circ. at Break [in]	38.27
Butt Circumference [mm]	1072	Butt Circumference [in]	42.20
GL Circumference [mm]	1013	GL Circumference [in]	39.88
5' from GL Circumference [mm]	969	5' from GL Circumference [in]	38.15
10' from GL Circumference [mm]	932	10' from GL Circumference [in]	36.69
15' from GL Circumference [mm]	917	15' from GL Circumference [in]	36.10
20' from GL Circumference [mm]	871.5	20' from GL Circumference [in]	34.31
25' from GL Circumference [mm]	865	25' from GL Circumference [in]	34.06
30' from GL Circumference [mm]	860	30' from GL Circumference [in]	33.86
35' from GL Circumference [mm]	806	35' from GL Circumference [in]	31.73
40' from GL Circumference [mm]	830	40' from GL Circumference [in]	32.68
45' from GL Circumference [mm]	746	45' from GL Circumference [in]	29.37
POL Circumference [mm]	746	POL Circumference [in]	29.37
Tip Circumference [mm]	671	Tip Circumference [in]	26.42
Volume (m^3)	1.08	Volume (ft^3)	37.98
CM from Butt (mm)	7403.88	CM from Butt (in)	291.49
LVDT Spacing (mm)	2200	LVDT Spacing (in)	86.61
Mass [kg]	750.24	Mass [lb]	1654
Density [kg/m^3]	697.61	Density [lb/ft^3]	43.55
POLETEST: 1' from GL (inline, 90 deg) [Mpa]	51.02 49.23	POLETEST: 1' from GL (inline, 90 deg) [psi]	7400 7140
POLETEST: 10' from GL (inline, 90 deg) [Mpa]	46.75 32.20	POLETEST: 10' from GL (inline, 90 deg) [psi]	6780 4670
POLETEST: 20' from GL (inline, 90 deg) [Mpa]	42.06 40.33	POLETEST: 20' from GL (inline, 90 deg) [psi]	6100 5850

Static Test (TL-222 108 SYP B) (2nd Old Pole)			
Property (Metric Units)	**Measured Value**	**Property (Imperial Units)**	**Measured Value**
Max Load [N]	5430.90	Max Load [lb]	1220.00
Yield Load [N]	3605.76	Load at Yield [lb]	810.00
POL Deflection at Max Load (corrected) [mm]	2350.00	POL Deflection at Max Load (corrected) [in]	92.52
POL Deflection at Yield Load (corrected) [mm]	1050.00	POL Deflection at Yield Load (corrected) [in]	41.34
POL Displacement Along Pole at Max Load [mm]	460.00	POL Displacement Along Pole at Max Load [in]	18.11
POL Displacement Along Pole at Yield Load [mm]	220.00	POL Displacement Along Pole at Yield Load [in]	8.66
Max Stress at GL [Mpa]	21.86	Max Stress at GL [psi]	3170.95
GL Stress at Yield [Mpa]	14.78	GL Stress at Yield [psi]	2143.44
Max Stress at Break Location [Mpa]	22.10	Max Stress at Break Location [psi]	3204.85
Break Location Stress at Yield [Mpa]	14.97	Break Location Stress at Yield [psi]	2170.93
Modulus of Elasticity [Mpa]	7548.51	Modulus of Elasticity [psi*10^6]	1.09
Density [kg/m^3]	697.61	Density [lb/ft^3]	43.55

Modal Test (TL-222 108 SYP B) (2nd Old Pole)				
Transverse Mode	Measured Frequency [Hz]	Measured Damping ratio	FEA Undamped Frequency (Measured Properties)	FEA Undamped Frequency (Published Properties)
1st	0.939	0.0145	0.787	1.161
2nd	4.818	0.0110	4.263	6.288
3rd	12.046	0.0190	11.385	16.795
4th	23.050	0.0144	21.972	32.412
5th	36.154	0.0214	36.057	53.188
6th	N/A	N/A	53.258	78.562

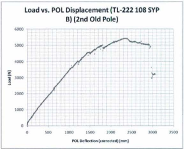

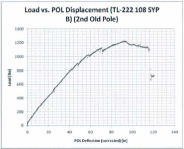

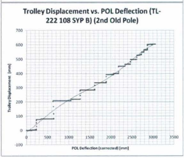

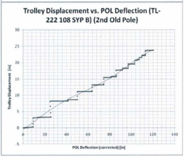

Pole Statistics (TL-222 142 WRC A) (3rd Old Pole)					
Identification	TL-222 142 WRC A		Class	N/A	
Species	WRC		Treatment Type (Year)	N/A	
Property / Measurement	**Value (Metric Units)**		**Property / Measurement**	**Value (Imperial Units)**	
Length [mm]	19830		Length [ft]	65' Nominal (65' 6" Actual)	
GL to POL [mm]	16616.90		GL to POL [in]	654.21	
Butt to GL [mm]	2603.5		Butt to GL [in]	102.50	
POL to Tip [mm]	609.6		POL to Tip [in]	24.00	
GL to Break [mm]	14020.8		GL to Break [in]	552.00	
Circ. at Break [mm]	666.6		Circ. at Break [in]	26.24	
Butt Circumference [mm]	1253		Butt Circumference [in]	49.33	
GL Circumference [mm]	1140		GL Circumference [in]	44.88	
5' from GL Circumference [mm]	1073		5' from GL Circumference [in]	42.24	
10' from GL Circumference [mm]	1015		10' from GL Circumference [in]	39.96	
15' from GL Circumference [mm]	974		15' from GL Circumference [in]	38.35	
20' from GL Circumference [mm]	927		20' from GL Circumference [in]	36.50	
25' from GL Circumference [mm]	886		25' from GL Circumference [in]	34.88	
30' from GL Circumference [mm]	833		30' from GL Circumference [in]	32.80	
35' from GL Circumference [mm]	776		35' from GL Circumference [in]	30.55	
40' from GL Circumference [mm]	723		40' from GL Circumference [in]	28.46	
45' from GL Circumference [mm]	673		45' from GL Circumference [in]	26.50	
50' from GL Circumference [mm]	641		50' from GL Circumference [in]	25.24	
55' from GL Circumference [mm]	557		55' from GL Circumference [in]	21.93	
POL Circumference [mm]	567		POL Circumference [in]	22.32	
Tip Circumference [mm]	518		Tip Circumference [in]	20.39	
Volume (m^3)	1.31		Volume (ft^3)	46.22	
CM from Butt (mm)	7522.86		CM from Butt (in)	296.18	
LVDT Spacing (mm)	2200		LVDT Spacing (in)	86.61	
Mass [kg]	548.39		Mass [lb]	1209	
Density [kg/m^3]	419.04		Density [lb/ft^3]	26.16	
POLETEST: 1' from GL (inline, 90 deg) [Mpa]	23.24	17.37	POLETEST: 1' from GL (inline, 90 deg) [psi]	3370	2520
POLETEST: 10' from GL (inline, 90 deg) [Mpa]	27.30	23.79	POLETEST: 10' from GL (inline, 90 deg) [psi]	3960	3450
POLETEST: 20' from GL (inline, 90 deg) [Mpa]	27.10	27.51	POLETEST: 20' from GL (inline, 90 deg) [psi]	3930	3990

Static Test (TL-222 142 WRC A) (3rd Old Pole)			
Property (Metric Units)	**Measured Values**	**Property (Imperial Units)**	**Measured Values**
Max Load [N]	6143.15	Max Load [lb]	1380.00
Yield Load [N]	4496.07	Load at Yield [lb]	1010.00
POL Deflection at Max Load (corrected) [mm]	4100.00	POL Deflection at Max Load (corrected) [in]	161.42
POL Deflection at Yield Load (corrected) [mm]	2750.00	POL Deflection at Yield Load (corrected) [in]	108.27
POL Displacement Along Pole at Max Load [mm]	540.00	POL Displacement Along Pole at Max Load [in]	21.26
POL Displacement Along Pole at Yield Load [mm]	140.00	POL Displacement Along Pole at Yield Load [in]	5.51
Max Stress at GL [Mpa]	21.05	Max Stress at GL [psi]	3053.58
GL Stress at Yield [Mpa]	15.79	GL Stress at Yield [psi]	2290.47
Max Stress at Break Location [Mpa]	15.59	Max Stress at Break Location [psi]	2261.47
Break Location Stress at Yield [Mpa]	12.18	Break Location Stress at Yield [psi]	1766.18
Modulus of Elasticity [Mpa]	5906.92	Modulus of Elasticity [psi*10^6]	0.86
Density [kg/m^3]	419.04	Density [lb/ft^3]	26.16

Modal Test (TL-222 142 WRC A) (3rd Old Pole)				
Transverse Mode	Measured Frequency [Hz]	Measured Damping ratio	FEA Undamped Frequency (Measured Properties)	FEA Undamped Frequency (Published Properties)
1st	0.893	0.0070	0.835	1.090
2nd	3.755	0.0055	3.534	4.618
3rd	9.235	0.0062	8.812	11.513
4th	16.738	0.0240	16.632	21.730
5th	N/A	N/A	27.064	35.359
6th	N/A	N/A	39.867	52.088

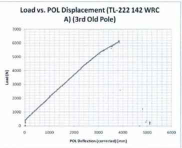

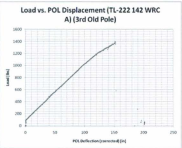

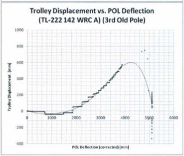

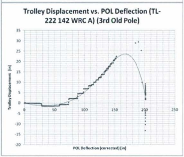

Pole Statistics (TL-222 142 WRC B) (4th Old Pole)			
Identification	TL-222 142 WRC B	Class	N/A
Species	WRC	Treatment Type (Year)	N/A
Property / Measurement	**Value (Metric Units)**	**Property / Measurement**	**Value (Imperial Units)**
Length [mm]	19812	Length [ft]	65' Nominal (65' Actual)
GL to POL [mm]	16611.60	GL to POL [in]	654.00
Butt to GL [mm]	2590.8	Butt to GL [in]	102.00
POL to Tip [mm]	609.6	POL to Tip [in]	24.00
GL to Break [mm]	10668	GL to Break [in]	420.00
Circ. at Break [mm]	837	Circ. at Break [in]	32.95
Butt Circumference [mm]	1666	Butt Circumference [in]	65.59
GL Circumference [mm]	1398	GL Circumference [in]	55.04
5' from GL Circumference [mm]	1296	5' from GL Circumference [in]	51.02
10' from GL Circumference [mm]	1248	10' from GL Circumference [in]	49.13
15' from GL Circumference [mm]	1191	15' from GL Circumference [in]	46.89
20' from GL Circumference [mm]	1097	20' from GL Circumference [in]	43.19
25' from GL Circumference [mm]	1033	25' from GL Circumference [in]	40.67
30' from GL Circumference [mm]	944	30' from GL Circumference [in]	37.17
35' from GL Circumference [mm]	837	35' from GL Circumference [in]	32.95
40' from GL Circumference [mm]	760	40' from GL Circumference [in]	29.92
45' from GL Circumference [mm]	668	45' from GL Circumference [in]	26.30
50' from GL Circumference [mm]	609	50' from GL Circumference [in]	23.98
55' from GL Circumference [mm]	516	55' from GL Circumference [in]	20.31
POL Circumference [mm]	522	POL Circumference [in]	23.98
Tip Circumference [mm]	496	Tip Circumference [in]	20.31
Volume (m^3)	1.82	Volume (ft^3)	64.40
CM from Butt (mm)	6713.92	CM from Butt (in)	264.33
LVDT Spacing (mm)	2200	LVDT Spacing (in)	86.61
Mass [kg]	792.43	Mass [lb]	1747
Density [kg/m^3)	434.55	Density [lb/ft^3)	27.13
POLETEST: 1' from GL (inline, 90 deg) [Mpa]	14.41 24.27	POLETEST: 1' from GL (inline, 90 deg) [psi]	2090 3520
POLETEST: 10' from GL (inline, 90 deg) [Mpa]	24.20 27.44	POLETEST: 10' from GL (inline, 90 deg) [psi]	3510 3980
POLETEST: 20' from GL (inline, 90 deg) [Mpa]	13.86 N/A	POLETEST: 20' from GL (inline, 90 deg) [psi]	2010 N/A

Static Test (TL-222 142 WRC B) (4th Old Pole)			
Property (Metric Units)	**Measured Values**	**Property (Imperial Units)**	**Measured Values**
Max Load [N]	6677.33	Max Load [lb]	1500.00
Yield Load [N]	6677.33	Load at Yield [lb]	1500.00
POL Deflection at Max Load (corrected) [mm]	2530.00	POL Deflection at Max Load (corrected) [in]	99.61
POL Deflection at Yield Load (corrected) [mm]	2530.00	POL Deflection at Yield Load (corrected) [in]	99.61
POL Displacement Along Pole at Max Load [mm]	225.00	POL Displacement Along Pole at Max Load [in]	8.86
POL Displacement Along Pole at Yield Load [mm]	225.00	POL Displacement Along Pole at Yield Load [in]	8.86
Max Stress at GL [Mpa]	12.65	Max Stress at GL [psi]	1834.43
GL Stress at Yield [Mpa]	12.65	GL Stress at Yield [psi]	1834.43
Max Stress at Break Location [Mpa]	20.78	Max Stress at Break Location [psi]	3014.04
Break Location Stress at Yield [Mpa]	20.78	Break Location Stress at Yield [psi]	3014.04
Modulus of Elasticity [Mpa]	4809.35	Modulus of Elasticity [psi*10^6]	0.70
Density [kg/m^3]	434.55	Density [lb/ft^3]	27.13

Modal Test (TL-222 142 WRC B) (4th Old Pole)				
Transverse Mode	Measured Frequency [Hz]	Measured Damping ratio	FEA Undamped Frequency (Measured Properties)	FEA Undamped Frequency (Published Properties)
1st	1.207	0.0066	1.043	1.539
2nd	4.371	0.0062	3.684	5.432
3rd	10.395	0.0047	8.756	12.910
4th	19.209	0.0082	16.248	23.957
5th	31.155	0.0095	26.375	38.890
6th	45.246	0.0140	38.558	56.854

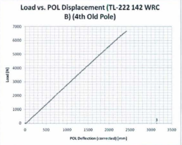

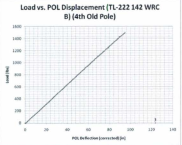

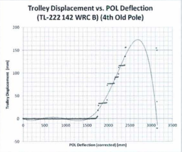

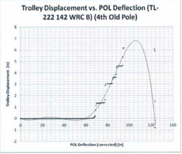

Pole Statistics (TL-201 SYP A) (5th Old Pole)			
Identification	TL-201 SYP A	Class	N/A
Species	SYP	Treatment Type (Year)	N/A
Property / Measurement	**Value (Metric Units)**	**Property / Measurement**	**Value (Imperial Units)**
Length [mm]	18288	Length [ft]	60' Nominal (60' Actual)
GL to POL [mm]	15240.00	GL to POL [in]	600.00
Butt to GL [mm]	2438.4	Butt to GL [in]	96.00
POL to Tip [mm]	609.6	POL to Tip [in]	24.00
GL to Break [mm]	381	GL to Break [in]	15.00
Circ. at Break [mm]	999.25	Circ. at Break [in]	39.34
Butt Circumference [mm]	1205	Butt Circumference [in]	47.44
GL Circumference [mm]	1008	GL Circumference [in]	39.69
5' from GL Circumference [mm]	973	5' from GL Circumference [in]	38.31
10' from GL Circumference [mm]	965	10' from GL Circumference [in]	37.99
15' from GL Circumference [mm]	913	15' from GL Circumference [in]	35.94
20' from GL Circumference [mm]	900	20' from GL Circumference [in]	35.43
25' from GL Circumference [mm]	845	25' from GL Circumference [in]	33.27
30' from GL Circumference [mm]	812	30' from GL Circumference [in]	31.97
35' from GL Circumference [mm]	778	35' from GL Circumference [in]	30.63
40' from GL Circumference [mm]	706	40' from GL Circumference [in]	27.80
45' from GL Circumference [mm]	647	45' from GL Circumference [in]	25.47
50' from GL Circumference [mm]	557	50' from GL Circumference [in]	21.93
POL Circumference [mm]	557	POL Circumference [in]	21.93
Tip Circumference [mm]	563	Tip Circumference [in]	22.17
Volume (m^3)	1.11	Volume (ft^3)	39.04
CM from Butt (mm)	7333	CM from Butt (in)	288.70
LVDT Spacing (mm)	2200	LVDT Spacing (in)	86.61
Mass [kg]	718.49	Mass [lb]	1584
Density [kg/m^3]	649.91	Density [lb/ft^3]	40.57
POLETEST: 1' from GL (inline, 90 deg) [Mpa]	31.78 38.13	POLETEST: 1' from GL (inline, 90 deg) [psi]	4610 5530
POLETEST: 10' from GL (inline, 90 deg) [Mpa]	46.61 43.30	POLETEST: 10' from GL (inline, 90 deg) [psi]	6760 6280
POLETEST: 20' from GL (inline, 90 deg) [Mpa]	42.75 42.40	POLETEST: 20' from GL (inline, 90 deg) [psi]	6200 6150

Static Test (TL-201 SYP A) (5th Old Pole)			
Property (Metric Units)	**Measured Values**	**Property (Imperial Units)**	**Measured Values**
Max Load [N]	6988.94	Max Load [lb]	1570.00
Yield Load [N]	4006.40	Load at Yield [lb]	900.00
POL Deflection at Max Load (corrected) [mm]	2550.00	POL Deflection at Max Load (corrected) [in]	100.39
POL Deflection at Yield Load (corrected) [mm]	1260.00	POL Deflection at Yield Load (corrected) [in]	49.61
POL Displacement Along Pole at Max Load [mm]	255.00	POL Displacement Along Pole at Max Load [in]	10.04
POL Displacement Along Pole at Yield Load [mm]	30.00	POL Displacement Along Pole at Yield Load [in]	1.18
Max Stress at GL [Mpa]	32.30	Max Stress at GL [psi]	4684.00
GL Stress at Yield [Mpa]	18.79	GL Stress at Yield [psi]	2725.42
Max Stress at Break Location [Mpa]	32.31	Max Stress at Break Location [psi]	4685.89
Break Location Stress at Yield [Mpa]	18.81	Break Location Stress at Yield [psi]	2727.56
Modulus of Elasticity [Mpa]	13049.99	Modulus of Elasticity [psi*10^6]	1.89
Density [kg/m^3]	649.91	Density [lb/ft^3]	40.57

Modal Test (TL-201 SYP A) (5th Old Pole)				
Transverse Mode	Measured Frequency [Hz]	Measured Damping ratio	FEA Undamped Frequency (Measured Properties)	FEA Undamped Frequency (Published Properties)
1st	1.022	0.0060	1.043	1.129
2nd	4.358	0.0066	4.823	5.223
3rd	10.579	0.0077	12.092	13.094
4th	19.712	0.0114	22.700	24.581
5th	31.529	0.0177	36.927	39.987
6th	45.877	0.0128	54.361	58.865

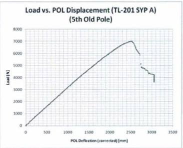

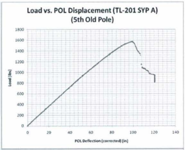

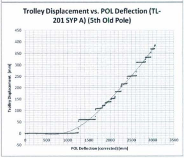

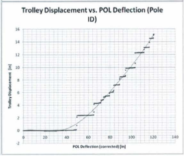

Pole Statistics (TL-201 244 SYP) (6th Old Pole)

Identification	TL-201 244 SYP	Class	N/A
Species	SYP	Treatment Type (Year)	N/A
Property / Measurement	**Value (Metric Units)**	**Property / Measurement**	**Value (Imperial Units)**
Length [mm]	16611.6	Length [ft]	55' Nominal (54' 6" Actual)
GL to POL [mm]	13731.24	GL to POL [in]	540.60
Butt to GL [mm]	2270.76	Butt to GL [in]	89.40
POL to Tip [mm]	609.6	POL to Tip [in]	24.00
GL to Break [mm]	11887.2	GL to Break [in]	468.00
Circ. at Break [mm]	808.6	Circ. at Break [in]	31.83
Butt Circumference [mm]	1421	Butt Circumference [in]	55.94
GL Circumference [mm]	1345	GL Circumference [in]	52.95
5' from GL Circumference [mm]	1250	5' from GL Circumference [in]	49.21
10' from GL Circumference [mm]	1182	10' from GL Circumference [in]	46.54
15' from GL Circumference [mm]	1104	15' from GL Circumference [in]	43.46
20' from GL Circumference [mm]	1043	20' from GL Circumference [in]	41.06
25' from GL Circumference [mm]	989	25' from GL Circumference [in]	38.94
30' from GL Circumference [mm]	930	30' from GL Circumference [in]	36.61
35' from GL Circumference [mm]	851	35' from GL Circumference [in]	33.50
40' from GL Circumference [mm]	798	40' from GL Circumference [in]	31.42
45' from GL Circumference [mm]	706	45' from GL Circumference [in]	27.80
POL Circumference [mm]	703	POL Circumference [in]	27.68
Tip Circumference [mm]	646	Tip Circumference [in]	25.43
Volume (m^3)	1.54	Volume (ft^3)	54.30
CM from Butt (mm)	6434.59	CM from Butt (in)	253.33
LVDT Spacing (mm)	2200	LVDT Spacing (in)	86.61
Mass [kg]	661.79	Mass [lb]	1459
Density [kg/m^3)	430.37	Density [lb/ft^3)	26.87
POLETEST: 1' from GL (inline, 90 deg) [Mpa]	26.13 26.89	POLETEST: 1' from GL (inline, 90 deg) [psi]	3790 3900
POLETEST: 10' from GL (inline, 90 deg) [Mpa]	39.99 27.79	POLETEST: 10' from GL (inline, 90 deg) [psi]	5800 4030
POLETEST: 20' from GL (inline, 90 deg) [Mpa]	33.09 31.78	POLETEST: 20' from GL (inline, 90 deg) [psi]	4800 4610

Static Test (TL-201 244 SYP) (6th Old Pole)

Property (Metric Units)	Measured Values	Property (Imperial Units)	Measured Values
Max Load [N]	9704.39	Max Load [lb]	2180.00
Yield Load [N]	5608.96	Load at Yield [lb]	1260.00
POL Deflection at Max Load (corrected) [mm]	2220.00	POL Deflection at Max Load (corrected) [in]	87.40
POL Deflection at Yield Load (corrected) [mm]	1050.00	POL Deflection at Yield Load (corrected) [in]	41.34
POL Displacement Along Pole at Max Load [mm]	180.00	POL Displacement Along Pole at Max Load [in]	7.09
POL Displacement Along Pole at Yield Load [mm]	30.00	POL Displacement Along Pole at Yield Load [in]	1.18
Max Stress at GL [Mpa]	17.07	Max Stress at GL [psi]	2475.78
GL Stress at Yield [Mpa]	9.98	GL Stress at Yield [psi]	1446.79
Max Stress at Break Location [Mpa]	10.32	Max Stress at Break Location [psi]	1497.33
Break Location Stress at Yield [Mpa]	6.14	Break Location Stress at Yield [psi]	891.03
Modulus of Elasticity [Mpa]	5348.21	Modulus of Elasticity [psi*10^6]	0.78
Density [kg/m^3]	430.37	Density [lb/ft^3]	26.87

Modal Test (TL-201 244 SYP) (6th Old Pole)				
Transverse Mode	Measured Frequency [Hz]	Measured Damping ratio	FEA Undamped Frequency (Measured Properties)	FEA Undamped Frequency (Published Properties)
1st	1.394	0.0081	1.298	1.786
2nd	6.354	0.0085	5.711	7.861
3rd	15.421	0.0078	14.205	19.553
4th	29.300	0.0254	26.869	36.985
5th	N/A	N/A	43.479	59.849
6th	N/A	N/A	63.867	87.911

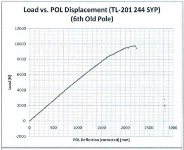

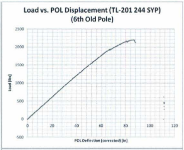

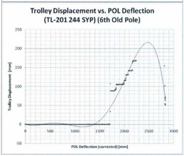

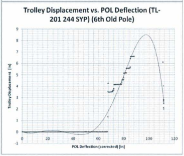

Pole Statistics (TL-201 242 SYP) (7th Old Pole)			
Identification	TL-201 242 SYP	Class	N/A
Species	SYP	Treatment Type (Year)	N/A
Property / Measurement	**Value (Metric Units)**	**Property / Measurement**	**Value (Imperial Units)**
Length [mm]	19558	Length [ft]	65' Nominal (64' 2" Actual)
GL to POL [mm]	16383.00	GL to POL [in]	645.00
Butt to GL [mm]	2565.4	Butt to GL [in]	101.00
POL to Tip [mm]	609.6	POL to Tip [in]	24.00
GL to Break [mm]	5486.4	GL to Break [in]	216.00
Circ. at Break [mm]	878	Circ. at Break [in]	34.57
Butt Circumference [mm]	1298	Butt Circumference [in]	51.10
GL Circumference [mm]	1045	GL Circumference [in]	41.14
5' from GL Circumference [mm]	1003	5' from GL Circumference [in]	39.49
10' from GL Circumference [mm]	966	10' from GL Circumference [in]	38.03
15' from GL Circumference [mm]	929	15' from GL Circumference [in]	36.57
20' from GL Circumference [mm]	844	20' from GL Circumference [in]	33.23
25' from GL Circumference [mm]	868	25' from GL Circumference [in]	34.17
30' from GL Circumference [mm]	833	30' from GL Circumference [in]	32.80
35' from GL Circumference [mm]	788	35' from GL Circumference [in]	31.02
40' from GL Circumference [mm]	760	40' from GL Circumference [in]	29.92
45' from GL Circumference [mm]	710	45' from GL Circumference [in]	27.95
50' from GL Circumference [mm]	675	50' from GL Circumference [in]	26.57
55' from GL Circumference [mm]	638	55' from GL Circumference [in]	25.12
POL Circumference [mm]	620	POL Circumference [in]	24.41
Tip Circumference [mm]	594	Tip Circumference [in]	23.39
Volume (m^3)	1.24	Volume (ft^3)	43.71
CM from Butt (mm)	7869.8	CM from Butt (in)	309.83
LVDT Spacing (mm)	2200	LVDT Spacing (in)	86.61
Mass [kg]	928.50	Mass [lb]	2047
Density [kg/m^3]	750.14	Density [lb/ft^3]	46.83
POLETEST: 1' from GL (inline, 90 deg) [Mpa]	42.33 36.13	POLETEST: 1' from GL (inline, 90 deg) [psi]	6140 5240
POLETEST: 10' from GL (inline, 90 deg) [Mpa]	45.85 47.64	POLETEST: 10' from GL (inline, 90 deg) [psi]	6650 6910
POLETEST: 20' from GL (inline, 90 deg) [Mpa]	38.89 39.44	POLETEST: 20' from GL (inline, 90 deg) [psi]	5640 5720

Static Test (TL-201 242 SYP) (7th Old Pole)			
Property (Metric Units)	**Measured Values**	**Property (Imperial Units)**	**Measured Values**
Max Load [N]	10795.02	Max Load [lb]	2425.00
Yield Load [N]	7612.16	Load at Yield [lb]	1710.00
POL Deflection at Max Load (corrected) [mm]	3700.00	POL Deflection at Max Load (corrected) [in]	145.67
POL Deflection at Yield Load (corrected) [mm]	2400.00	POL Deflection at Yield Load (corrected) [in]	94.49
POL Displacement Along Pole at Max Load [mm]	720.00	POL Displacement Along Pole at Max Load [in]	28.35
POL Displacement Along Pole at Yield Load [mm]	310.00	POL Displacement Along Pole at Yield Load [in]	12.20
Max Stress at GL [Mpa]	46.79	Max Stress at GL [psi]	6787.04
GL Stress at Yield [Mpa]	33.86	GL Stress at Yield [psi]	4911.19
Max Stress at Break Location [Mpa]	51.40	Max Stress at Break Location [psi]	7454.63
Break Location Stress at Yield [Mpa]	37.65	Break Location Stress at Yield [psi]	5459.95
Modulus of Elasticity [Mpa]	13039.01	Modulus of Elasticity [psi*10^6]	1.89
Density [kg/m^3]	750.14	Density [lb/ft^3]	46.83

Modal Test (TL-201 242 SYP) (7th Old Pole)				
Transverse Mode	Measured Frequency [Hz]	Measured Damping ratio	FEA Undamped Frequency (Measured Properties)	FEA Undamped Frequency (Published Properties)
1st	0.846	0.0053	0.796	0.927
2nd	3.693	0.0066	3.817	4.442
3rd	9.068	0.0064	9.683	11.270
4th	16.474	0.0098	18.576	21.620
5th	27.499	0.0130	30.343	35.315
6th	39.131	0.0093	45.025	52.403

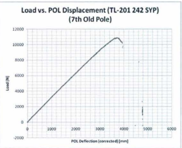

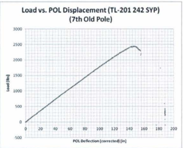

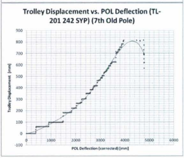

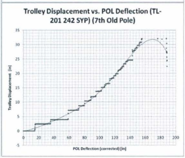

Pole Statistics (TL-201 241 SYP) (8th Old Pole)					
Identification	TL-201 241 SYP		Class	N/A	
Species	SYP		Treatment Type (Year)	N/A	
Property / Measurement	**Value (Metric Units)**		**Property / Measurement**	**Value (Imperial Units)**	
Length [mm]	17538.4		Length [ft]	60' Nomial (57' 6.5" Actual)	
GL to POL [mm]	14490.40		GL to POL [in]	570.49	
Butt to GL [mm]	2438.4		Butt to GL [in]	96.00	
POL to Tip [mm]	609.6		POL to Tip [in]	24.00	
GL to Break [mm]	9855.2		GL to Break [in]	388.00	
Circ. at Break [mm]	939		Circ. at Break [in]	36.97	
Butt Circumference [mm]	1348		Butt Circumference [in]	53.07	
GL Circumference [mm]	1285		GL Circumference [in]	50.59	
5' from GL Circumference [mm]	1220		5' from GL Circumference [in]	48.03	
10' from GL Circumference [mm]	1185		10' from GL Circumference [in]	46.65	
15' from GL Circumference [mm]	1126		15' from GL Circumference [in]	44.33	
20' from GL Circumference [mm]	1075		20' from GL Circumference [in]	42.32	
25' from GL Circumference [mm]	1018		25' from GL Circumference [in]	40.08	
30' from GL Circumference [mm]	967		30' from GL Circumference [in]	38.07	
35' from GL Circumference [mm]	907		35' from GL Circumference [in]	35.71	
40' from GL Circumference [mm]	841		40' from GL Circumference [in]	33.11	
45' from GL Circumference [mm]	808		45' from GL Circumference [in]	31.81	
POL Circumference [mm]	823		POL Circumference [in]	32.40	
Tip Circumference [mm]	780		Tip Circumference [in]	30.71	
Volume (m^3)	1.61		Volume (ft^3)	57.02	
CM from Butt (mm)	7136.38		CM from Butt (in)	280.96	
LVDT Spacing (mm)	2200		LVDT Spacing (in)	86.61	
Mass [kg]	847.76		Mass [lb]	1869	
Density [kg/m^3]	525.07		Density [lb/ft^3]	32.78	
POLETEST: 1' from GL (inline, 90 deg) [Mpa]	N/A	30.34	POLETEST: 1' from GL (inline, 90 deg) [psi]	N/A	4400
POLETEST: 10' from GL (inline, 90 deg) [Mpa]	N/A	N/A	POLETEST: 10' from GL (inline, 90 deg) [psi]	N/A	N/A
POLETEST: 20' from GL (inline, 90 deg) [Mpa]	N/A	N/A	POLETEST: 20' from GL (inline, 90 deg) [psi]	N/A	N/A

Static Test (TL-201 241 SYP) (8th Old Pole)			
Property (Metric Units)	**Measured Values**	**Property (Imperial Units)**	**Measured Values**
Max Load [N]	6201.02	Max Load [lb]	1393.00
Yield Load [N]	6201.02	Load at Yield [lb]	1393.00
POL Deflection at Max Load (corrected) [mm]	1930.00	POL Deflection at Max Load (corrected) [in]	75.98
POL Deflection at Yield Load (corrected) [mm]	1930.00	POL Deflection at Yield Load (corrected) [in]	75.98
POL Displacement Along Pole at Max Load [mm]	80.00	POL Displacement Along Pole at Max Load [in]	3.15
POL Displacement Along Pole at Yield Load [mm]	80.00	POL Displacement Along Pole at Yield Load [in]	3.15
Max Stress at GL [Mpa]	13.30	Max Stress at GL [psi]	1929.12
GL Stress at Yield [Mpa]	13.30	GL Stress at Yield [psi]	1929.12
Max Stress at Break Location [Mpa]	10.83	Max Stress at Break Location [psi]	1571.44
Break Location Stress at Yield [Mpa]	10.83	Break Location Stress at Yield [psi]	1571.44
Modulus of Elasticity [Mpa]	3702.93	Modulus of Elasticity [psi*10^6]	0.54
Density [kg/m^3]	525.07	Density [lb/ft^3]	32.78

Modal Test (TL-201 241 SYP) (8th Old Pole)				
Transverse Mode	Measured Frequency [Hz]	Measured Damping ratio	FEA Undamped Frequency (Measured Properties)	FEA Undamped Frequency (Published Properties)
1st	0.924	0.0054	0.823	1.504
2nd	3.796	0.0141	3.733	6.820
3rd	9.249	0.0211	9.485	17.332
4th	16.664	0.0312	18.106	33.084
5th	24.403	0.0359	29.517	53.934
6th	N/A	N/A	43.712	79.871

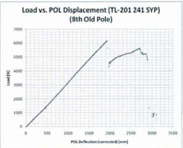

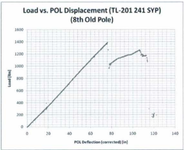

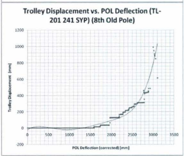

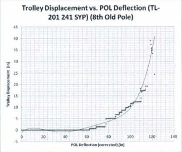

Pole Statistics (TL-222 140 SYP A) (9th Old Pole)					
Identification	TL-222 140 SYP A		Class	N/A	
Species	SYP		Treatment Type (Year)	N/A	
Property / Measurement	**Value (Metric Units)**		**Property / Measurement**	**Value (Imperial Units)**	
Length [mm]	13716		Length [ft]	45' Nominal (45' Actual)	
GL to POL [mm]	11125.20		GL to POL [in]	438.00	
Butt to GL [mm]	1981.2		Butt to GL [in]	78.00	
POL to Tip [mm]	609.6		POL to Tip [in]	24.00	
GL to Break [mm]	5486.4		GL to Break [in]	216.00	
Circ. at Break [mm]	806		Circ. at Break [in]	31.73	
Butt Circumference [mm]	1035		Butt Circumference [in]	40.75	
GL Circumference [mm]	906		GL Circumference [in]	35.67	
5' from GL Circumference [mm]	896		5' from GL Circumference [in]	35.28	
10' from GL Circumference [mm]	862		10' from GL Circumference [in]	33.94	
15' from GL Circumference [mm]	821		15' from GL Circumference [in]	32.32	
20' from GL Circumference [mm]	796		20' from GL Circumference [in]	31.34	
25' from GL Circumference [mm]	766		25' from GL Circumference [in]	30.16	
30' from GL Circumference [mm]	695		30' from GL Circumference [in]	27.36	
35' from GL Circumference [mm]	637		35' from GL Circumference [in]	25.08	
POL Circumference [mm]	613		POL Circumference [in]	24.13	
Tip Circumference [mm]	587		Tip Circumference [in]	23.11	
Volume (m^3)	0.73		Volume (ft^3)	25.67	
CM from Butt (mm)	5860.82		CM from Butt (in)	230.74	
LVDT Spacing (mm)	2200		LVDT Spacing (in)	86.61	
Mass [kg]	449.06		Mass [lb]	990	
Density [kg/m^3]	617.71		Density [lb/ft^3]	38.56	
POLETEST: 1' from GL (inline, 90 deg) [Mpa]	45.85	30.61	POLETEST: 1' from GL (inline, 90 deg) [psi]	6650	4440
POLETEST: 10' from GL (inline, 90 deg) [Mpa]	45.71	47.44	POLETEST: 10' from GL (inline, 90 deg) [psi]	6630	6880
POLETEST: 20' from GL (inline, 90 deg) [Mpa]	40.20	41.85	POLETEST: 20' from GL (inline, 90 deg) [psi]	5830	6070

Static Test (TL-222 140 SYP A) (9th Old Pole)			
Property (Metric Units)	**Measured Values**	**Property (Imperial Units)**	**Measured Values**
Max Load [N]	6254.44	Max Load [lb]	1405.00
Yield Load [N]	4206.72	Load at Yield [lb]	945.00
POL Deflection at Max Load (corrected) [mm]	1830.00	POL Deflection at Max Load (corrected) [in]	72.05
POL Deflection at Yield Load (corrected) [mm]	900.00	POL Deflection at Yield Load (corrected) [in]	35.43
POL Displacement Along Pole at Max Load [mm]	200.00	POL Displacement Along Pole at Max Load [in]	7.87
POL Displacement Along Pole at Yield Load [mm]	15.00	POL Displacement Along Pole at Yield Load [in]	0.59
Max Stress at GL [Mpa]	29.02	Max Stress at GL [psi]	4208.85
GL Stress at Yield [Mpa]	19.85	GL Stress at Yield [psi]	2878.80
Max Stress at Break Location [Mpa]	20.61	Max Stress at Break Location [psi]	2989.01
Break Location Stress at Yield [Mpa]	14.27	Break Location Stress at Yield [psi]	2070.32
Modulus of Elasticity [Mpa]	9338.73	Modulus of Elasticity [psi*10^6]	1.35
Density [kg/m^3]	617.71	Density [lb/ft^3]	38.56

Modal Test (TL-222 140 SYP A) (9th Old Pole)				
Transverse Mode	Measured Frequency [Hz]	Measured Damping ratio	FEA Undamped Frequency (Measured Properties)	FEA Undamped Frequency (Published Properties)
1st	1.504	0.0092	1.362	1.700
2nd	6.571	0.0088	6.805	8.493
3rd	15.182	0.0119	17.432	21.754
4th	28.954	0.0205	33.219	41.456
5th	45.508	0.0337	54.253	67.706
6th	66.503	0.0267	80.309	100.220

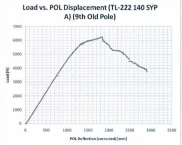

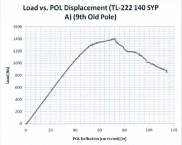

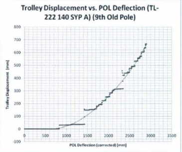

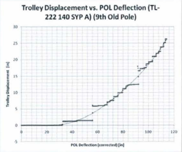

Pole Statistics (TL-222 140 SYP B) (Old Pole 10)			
Identification	TL-222 140 SYP B	Class	N/A
Species	SYP	Treatment Type (Year)	N/A
Property / Measurement	**Value (Metric Units)**	**Property / Measurement**	**Value (Imperial Units)**
Length [mm]	12192	Length [ft]	40' Nominal (40' Actual)
GL to POL [mm]	9753.60	GL to POL [in]	384.00
Butt to GL [mm]	1828.8	Butt to GL [in]	72.00
POL to Tip [mm]	609.6	POL to Tip [in]	24.00
GL to Break [mm]	6375.4	GL to Break [in]	251.00
Circ. at Break [mm]	738.3	Circ. at Break [in]	29.07
Butt Circumference [mm]	1012	Butt Circumference [in]	39.84
GL Circumference [mm]	919	GL Circumference [in]	36.18
5' from GL Circumference [mm]	898	5' from GL Circumference [in]	35.35
10' from GL Circumference [mm]	830	10' from GL Circumference [in]	32.68
15' from GL Circumference [mm]	780	15' from GL Circumference [in]	30.71
20' from GL Circumference [mm]	757	20' from GL Circumference [in]	29.80
25' from GL Circumference [mm]	655	25' from GL Circumference [in]	25.79
30' from GL Circumference [mm]	583	30' from GL Circumference [in]	22.95
POL Circumference [mm]	579	POL Circumference [in]	22.80
Tip Circumference [mm]	548	Tip Circumference [in]	21.57
Volume (m^3)	0.61	Volume (ft^3)	21.61
CM from Butt (mm)	4980.88	CM from Butt (in)	196.10
LVDT Spacing (mm)	2200	LVDT Spacing (in)	86.61
Mass [kg]	435.90	Mass [lb]	961
Density [kg/m^3]	712.26	Density [lb/ft^3]	44.47
POLETEST: 1' from GL (inline, 90 deg) [Mpa]	31.78 31.72	POLETEST: 1' from GL (inline, 90 deg) [psi]	4610 4600
POLETEST: 10' from GL (inline, 90 deg) [Mpa]	43.23 32.61	POLETEST: 10' from GL (inline, 90 deg) [psi]	6270 4730
POLETEST: 20' from GL (inline, 90 deg) [Mpa]	23.30 25.44	POLETEST: 20' from GL (inline, 90 deg) [psi]	3380 3690

Static Test (TL-222 140 SYP B) (Old Pole 10)			
Property (Metric Units)	**Measured Values**	**Property (Imperial Units)**	**Measured Values**
Max Load [N]	4295.75	Max Load [lb]	965.00
Yield Load [N]	3098.28	Load at Yield [lb]	696.00
POL Deflection at Max Load (corrected) [mm]	1200.00	POL Deflection at Max Load (corrected) [in]	47.24
POL Deflection at Yield Load (corrected) [mm]	680.00	POL Deflection at Yield Load (corrected) [in]	26.77
POL Displacement Along Pole at Max Load [mm]	32.50	POL Displacement Along Pole at Max Load [in]	1.28
POL Displacement Along Pole at Yield Load [mm]	0.00	POL Displacement Along Pole at Yield Load [in]	0.00
Max Stress at GL [Mpa]	16.99	Max Stress at GL [psi]	2464.56
GL Stress at Yield [Mpa]	12.30	GL Stress at Yield [psi]	1783.49
Max Stress at Break Location [Mpa]	11.31	Max Stress at Break Location [psi]	1640.34
Break Location Stress at Yield [Mpa]	8.21	Break Location Stress at Yield [psi]	1191.35
Modulus of Elasticity [Mpa]	6222.86	Modulus of Elasticity [psi*10^6]	0.90
Density [kg/m^3]	712.26	Density [lb/ft^3]	44.47

Modal Test (TL-222 140 SYP B) (Old Pole 10)				
Transverse Mode	Measured Frequency [Hz]	Measured Damping ratio	FEA Undamped Frequency (Measured Properties)	FEA Undamped Frequency (Published Properties)
1st	1.810	0.0054	1.458	2.393
2nd	6.829	0.0139	6.716	11.026
3rd	17.154	0.0156	16.574	27.208
4th	32.077	0.0254	31.688	52.020
5th	48.897	0.0159	51.434	84.436
6th	N/A	N/A	75.924	124.640

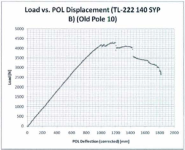

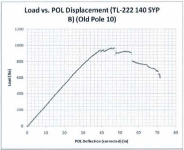

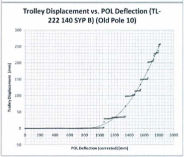

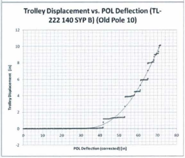

Pole Statistics (TL-222 97 SYP) (11th Old Pole)			
Identification	TL-222 97 SYP	Class	N/A
Species	SYP	Treatment Type (Year)	N/A
Property / Measurement	**Value (Metric Units)**	**Property / Measurement**	**Value (Imperial Units)**
Length [mm]	15925.8	Length [ft]	52'3" Actual
GL to POL [mm]	13131.80	GL to POL [in]	517.00
Butt to GL [mm]	2184.4	Butt to GL [in]	86.00
POL to Tip [mm]	609.6	POL to Tip [in]	24.00
GL to Break [mm]	9906	GL to Break [in]	390.00
Circ. at Break [mm]	748	Circ. at Break [in]	29.45
Butt Circumference [mm]	953	Butt Circumference [in]	37.52
GL Circumference [mm]	925	GL Circumference [in]	36.42
5' from GL Circumference [mm]	905	5' from GL Circumference [in]	35.63
10' from GL Circumference [mm]	934	10' from GL Circumference [in]	36.77
15' from GL Circumference [mm]	872	15' from GL Circumference [in]	34.33
20' from GL Circumference [mm]	855	20' from GL Circumference [in]	33.66
25' from GL Circumference [mm]	814	25' from GL Circumference [in]	32.05
30' from GL Circumference [mm]	759	30' from GL Circumference [in]	29.88
35' from GL Circumference [mm]	737	35' from GL Circumference [in]	29.02
40' from GL Circumference [mm]	739	40' from GL Circumference [in]	29.09
POL Circumference [mm]	626	POL Circumference [in]	24.65
Tip Circumference [mm]	578	Tip Circumference [in]	22.76
Volume (m^3)	0.90	Volume (ft^3)	31.65
CM from Butt (mm)	7041.58	CM from Butt (in)	277.23
LVDT Spacing (mm)	2200	LVDT Spacing (in)	86.61
Mass [kg]	687.65	Mass [lb]	1516
Density [kg/m^3]	767.26	Density [lb/ft^3]	47.90
POLETEST: 1' from GL (inline, 90 deg) [Mpa]	N/A N/A	POLETEST: 1' from GL (inline, 90 deg) [psi]	N/A N/A
POLETEST: 10' from GL (inline, 90 deg) [Mpa]	N/A N/A	POLETEST: 10' from GL (inline, 90 deg) [psi]	N/A N/A
POLETEST: 20' from GL (inline, 90 deg) [Mpa]	N/A N/A	POLETEST: 20' from GL (inline, 90 deg) [psi]	N/A N/A

Static Test (TL-222 97 SYP) (11th Old Pole)			
Property (Metric Units)	**Measured Values**	**Property (Imperial Units)**	**Measured Values**
Max Load [N]	5150.45	Max Load [lb]	1157.00
Yield Load [N]	3405.44	Load at Yield [lb]	765.00
POL Deflection at Max Load (corrected) [mm]	2750.00	POL Deflection at Max Load (corrected) [in]	108.27
POL Deflection at Yield Load (corrected) [mm]	1300.00	POL Deflection at Yield Load (corrected) [in]	51.18
POL Displacement Along Pole at Max Load [mm]	560.00	POL Displacement Along Pole at Max Load [in]	22.05
POL Displacement Along Pole at Yield Load [mm]	210.00	POL Displacement Along Pole at Yield Load [in]	8.27
Max Stress at GL [Mpa]	25.84	Max Stress at GL [psi]	3747.56
GL Stress at Yield [Mpa]	17.56	GL Stress at Yield [psi]	2546.84
Max Stress at Break Location [Mpa]	11.30	Max Stress at Break Location [psi]	1638.30
Break Location Stress at Yield [Mpa]	7.98	Break Location Stress at Yield [psi]	1157.69
Modulus of Elasticity [Mpa]	7919.75	Modulus of Elasticity [psi*10^6]	1.15
Density [kg/m^3]	767.26	Density [lb/ft^3]	47.90

Modal Test (TL-222 97 SYP) (11th Old Pole)				
Transverse Mode	Measured Frequency [Hz]	Measured Damping ratio	FEA Undamped Frequency (Measured Properties)	FEA Undamped Frequency (Published Properties)
1st	0.898	0.0231	0.837	1.264
2nd	3.943	0.0113	4.205	6.351
3rd	9.559	0.0255	11.160	16.855
4th	17.666	0.0243	21.868	33.027
5th	27.220	0.0120	35.785	54.046
6th	39.462	0.0355	52.751	79.670

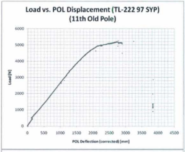

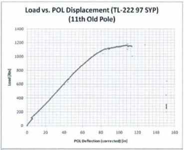

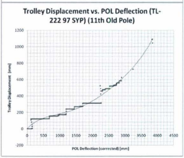

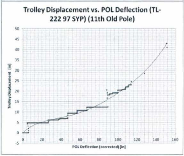

Appendix D - Supplementary Results Using Damping Ratio of Full Scale Poles

Damping ratio, normalized damping ratio and percentile rank of damping ratio data:

Run	Pole	Species	Damping Ratio					
			Mode 1	Mode 2	Mode 3	Mode 4	Mode 5	Mode 6
1	BF1	SYP	0.0076	0.0081	0.0090	0.0126	0.0097	0.0093
2	BF2	SYP	0.0059	0.0058	0.0065	0.0131	0.0110	0.0095
3	BF3	SYP	0.0062	0.0066	0.0075	0.0091	0.0112	0.0089
4	1st Old	SYP	0.0125	0.0114	0.0184	0.0181	0.0185	0.0234
5	2nd Old	SYP	0.0145	0.0110	0.0190	0.0144	0.0214	N/A
6	3rd Old	WRC	0.0070	0.0055	0.0062	0.0240	N/A	N/A
7	4th Old	WRC	0.0066	0.0062	0.0047	0.0082	0.0095	0.0140
8	5th Old	SYP	0.0060	0.0066	0.0077	0.0114	0.0177	0.0128
9	6th Old	SYP	0.0081	0.0085	0.0078	0.0254	N/A	N/A
10	7th Old	SYP	0.0053	0.0066	0.0064	0.0098	0.0130	0.0093
11	8th Old	SYP	0.0054	0.0141	0.0211	0.0312	0.0359	N/A
12	9th Old	SYP	0.0092	0.0088	0.0119	0.0205	0.0337	0.0267
13	10th Old	SYP	0.0054	0.0139	0.0156	0.0254	0.0159	N/A
14	11th Old	SYP	0.0231	0.0113	0.0255	0.0243	0.0120	0.0355

Pole	Species	Average Modal Damping Ratio								
		Modes 1 to 2	Modes 1 to 3	Modes 1 to 4	Modes 1 to 5	Modes 1 to 6	Modes 2 to 6	Modes 3 to 6	Modes 4 to 6	Modes 5 to 6
BF1	(SYP)	0.007850	0.008233	0.009325	0.009400	0.009383	0.009740	0.010150	0.010533	0.009500
BF2	(SYP)	0.005850	0.006067	0.007825	0.008460	0.008633	0.009180	0.010025	0.011200	0.010250
BF3	(SYP)	0.006400	0.006767	0.007350	0.008120	0.008250	0.008660	0.009175	0.009733	0.010050
1st Old	(SYP)	0.011950	0.014100	0.015100	0.015780	0.017050	0.017960	0.019600	0.020000	0.020950
2nd Old	(SYP)	0.012750	0.014833	0.014725	0.016060	N/A	N/A	N/A	N/A	N/A
3rd Old	(WRC)	0.006250	0.006233	0.010675	N/A	N/A	N/A	N/A	N/A	N/A
4th Old	(WRC)	0.006400	0.005833	0.006425	0.007040	0.008200	0.008520	0.009100	0.010567	0.011750
5th Old	(SYP)	0.006300	0.006767	0.007925	0.009880	0.010367	0.011240	0.012400	0.013967	0.015250
6th Old	(SYP)	0.008300	0.008133	0.012450	N/A	N/A	N/A	N/A	N/A	N/A
7th Old	(SYP)	0.005950	0.006100	0.007025	0.008220	0.008400	0.009020	0.009625	0.010700	0.011150
8th Old	(SYP)	0.009750	0.013533	0.017950	0.021540	N/A	N/A	N/A	N/A	N/A
9th Old	(SYP)	0.009000	0.009967	0.012600	0.016820	0.018467	0.020320	0.023200	0.026967	0.030200
10th Old	(SYP)	0.009650	0.011633	0.015075	0.015240	N/A	N/A	N/A	N/A	N/A
11th Old	(SYP)	0.017200	0.019967	0.021050	0.019240	0.021950	0.021720	0.024325	0.023933	0.023750

Pole	Species	Normalized Damping Ratio					
		Mode 1	Mode 2	Mode 3	Mode 4	Mode 5	Mode 6
BF1	(SYP)	0.1292	0.2771	0.1361	0.1584	0.0000	0.0150
BF2	(SYP)	0.0337	0.0000	0.0052	0.1810	0.0496	0.0226
BF3	(SYP)	0.0506	0.0964	0.0576	0.0000	0.0573	0.0000
1st Old	(SYP)	0.4045	0.6747	0.6283	0.4072	0.3359	0.5451
2nd Old	(SYP)	0.5169	0.6265	0.6597	0.2398	0.4466	N/A
3rd Old	(WRC)	N/A	N/A	N/A	N/A	N/A	N/A
4th Old	(WRC)	N/A	N/A	N/A	N/A	N/A	N/A
5th Old	(SYP)	0.0393	0.0964	0.0681	0.1041	0.3053	0.1466
6th Old	(SYP)	0.1573	0.3253	0.0733	0.7376	N/A	N/A
7th Old	(SYP)	0.0000	0.0964	0.0000	0.0317	0.1260	0.0150
8th Old	(SYP)	0.0056	1.0000	0.7696	1.0000	1.0000	N/A
9th Old	(SYP)	0.2191	0.3614	0.2880	0.5158	0.9160	0.6692
10th Old	(SYP)	0.0056	0.9759	0.4817	0.7376	0.2366	N/A
11th Old	(SYP)	1.0000	0.6627	1.0000	0.6878	0.0878	1.0000

Pole	Species	Average Normalized Damping Ratio								
		Modes 1 to 2	Modes 1 to 3	Modes 1 to 4	Modes 1 to 5	Modes 1 to 6	Modes 2 to 6	Modes 3 to 6	Modes 4 to 6	Modes 5 to 6
BF1	(SYP)	0.2032	0.1808	0.1752	0.1402	0.1193	0.1173	0.0774	0.0578	0.0075
BF2	(SYP)	0.0169	0.0130	0.0550	0.0539	0.0487	0.0517	0.0646	0.0844	0.0361
BF3	(SYP)	0.0735	0.0682	0.0511	0.0524	0.0436	0.0422	0.0287	0.0191	0.0286
1st Old	(SYP)	0.5396	0.5692	0.5287	0.4901	0.4993	0.5182	0.4791	0.4294	0.4405
2nd Old	(SYP)	0.5717	0.6010	0.5107	0.4979	N/A	N/A	N/A	N/A	N/A
3rd Old	(WRC)	N/A	N/A	N/A	N/A	N/A	N/A	N/A	N/A	N/A
4th Old	(WRC)	N/A	N/A	N/A	N/A	N/A	N/A	N/A	N/A	N/A
5th Old	(SYP)	0.0679	0.0679	0.0770	0.1226	0.1266	0.1441	0.1560	0.1853	0.2260
6th Old	(SYP)	0.2413	0.1853	0.3234	N/A	N/A	N/A	N/A	N/A	N/A
7th Old	(SYP)	0.0482	0.0321	0.0320	0.0508	0.0448	0.0538	0.0432	0.0576	0.0705
8th Old	(SYP)	0.5028	0.5918	0.6938	0.7551	N/A	N/A	N/A	N/A	N/A
9th Old	(SYP)	0.2903	0.2895	0.3461	0.4601	0.4949	0.5501	0.5972	0.7003	0.7926
10th Old	(SYP)	0.4908	0.4877	0.5502	0.4875	N/A	N/A	N/A	N/A	N/A
11th Old	(SYP)	0.8313	0.8876	0.8376	0.6876	0.7397	0.6876	0.6939	0.5919	0.5439

Pole	Species	Percentile Rank of Damping Ratio					
		Mode 1	Mode 2	Mode 3	Mode 4	Mode 5	Mode 6
BF1	(SYP)	0.5450	0.3630	0.4540	0.2720	0.0000	0.1420
BF2	(SYP)	0.2720	0.0000	0.0900	0.3630	0.1000	0.4280
BF3	(SYP)	0.4540	0.0900	0.1810	0.0000	0.2000	0.0000
1st Old	(SYP)	0.8180	0.8180	0.7270	0.5450	0.7000	0.7140
2nd Old	(SYP)	0.9090	0.6360	0.8180	0.4540	0.8000	N/A
3rd Old	(WRC)	N/A	N/A	N/A	N/A	N/A	N/A
4th Old	(WRC)	N/A	N/A	N/A	N/A	N/A	N/A
5th Old	(SYP)	0.3630	0.0900	0.2720	0.1810	0.6000	0.5710
6th Old	(SYP)	0.6360	0.4540	0.3630	0.8180	N/A	N/A
7th Old	(SYP)	0.0000	0.0900	0.0000	0.0900	0.4000	0.1420
8th Old	(SYP)	0.0900	1.0000	0.9090	1.0000	1.0000	N/A
9th Old	(SYP)	0.7270	0.5450	0.5450	0.6360	0.9000	0.8570
10th Old	(SYP)	0.0900	0.9090	0.6360	0.8180	0.5000	N/A
11th Old	(SYP)	1.0000	0.7270	1.0000	0.7270	0.3000	1.0000

Pole	Species	Average Percentile Rank of Damping Ratio								
		Avg 1st 2	Avg 1st 3	Avg 1st 4	Avg 1st 5	Avg all 6	Avg Last 5	Avg Last 4	Avg Last 3	Avg Last 2
BF1	(SYP)	0.4540	0.4540	0.4085	0.3268	0.2960	0.2462	0.2170	0.1380	0.0710
BF2	(SYP)	0.1360	0.1207	0.1813	0.1650	0.2088	0.1962	0.2453	0.2970	0.2640
BF3	(SYP)	0.2720	0.2417	0.1813	0.1850	0.1542	0.0942	0.0953	0.0667	0.1000
1st Old	(SYP)	0.8180	0.7877	0.7270	0.7216	0.7203	0.7008	0.6715	0.6530	0.7070
2nd Old	(SYP)	0.7725	0.7877	0.7043	0.7234	N/A	N/A	N/A	N/A	N/A
3rd Old	(WRC)	N/A	N/A	N/A	N/A	N/A	N/A	N/A	N/A	N/A
4th Old	(WRC)	N/A	N/A	N/A	N/A	N/A	N/A	N/A	N/A	N/A
5th Old	(SYP)	0.2265	0.2417	0.2265	0.3012	0.3462	0.3428	0.4060	0.4507	0.5855
6th Old	(SYP)	0.5450	0.4843	0.5678	N/A	N/A	N/A	N/A	N/A	N/A
7th Old	(SYP)	0.0450	0.0300	0.0450	0.1160	0.1203	0.1444	0.1580	0.2107	0.2710
8th Old	(SYP)	0.5450	0.6663	0.7498	0.7998	N/A	N/A	N/A	N/A	N/A
9th Old	(SYP)	0.6360	0.6057	0.6133	0.6706	0.7017	0.6966	0.7345	0.7977	0.8785
10th Old	(SYP)	0.4995	0.5450	0.6133	0.5906	N/A	N/A	N/A	N/A	N/A
11th Old	(SYP)	0.8635	0.9090	0.8635	0.7508	0.7923	0.7508	0.7568	0.6757	0.6500

Damping ratio and average damping ratio plotted against maximum break location stress:

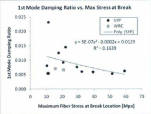

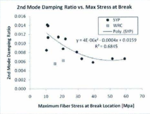

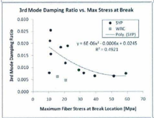

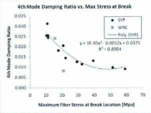

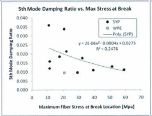

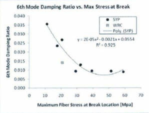

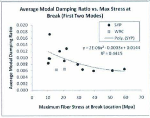

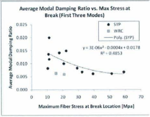

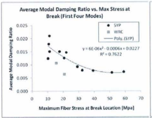
Average Modal Damping Ratio vs. Max Stress at Break (First Four Modes)
SYP
WRC
Poly. (SYP)
y = 6E-06x² - 0.0006x + 0.0227
R² = 0.7622
Average Modal Damping Ratio
Maximum Fiber Stress at Break Location [Mpa]

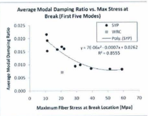
Average Modal Damping Ratio vs. Max Stress at Break (First Five Modes)
SYP
WRC
Poly. (SYP)
y = 7E-06x² - 0.0007x + 0.0262
R² = 0.8555
Average Modal Damping Ratio
Maximum Fiber Stress at Break Location [Mpa]

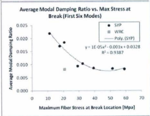
Average Modal Damping Ratio vs. Max Stress at Break (First Six Modes)
SYP
WRC
Poly. (SYP)
y = 1E-05x² - 0.001x + 0.0328
R² = 0.9387
Average Modal Damping Ratio
Maximum Fiber Stress at Break Location [Mpa]

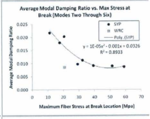
Average Modal Damping Ratio vs. Max Stress at Break (Modes Two Through Six)
SYP
WRC
Poly. (SYP)
y = 1E-05x² - 0.001x + 0.0326
R² = 0.8933
Average Modal Damping Ratio
Maximum Fiber Stress at Break Location [Mpa]

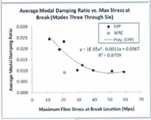
Average Modal Damping Ratio vs. Max Stress at Break (Modes Three Through Six)
SYP
WRC
Poly. (SYP)
y = 1E-05x² - 0.0011x + 0.0367
R² = 0.8709
Average Modal Damping Ratio
Maximum Fiber Stress at Break Location [Mpa]

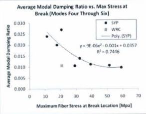
Average Modal Damping Ratio vs. Max Stress at Break (Modes Four Through Six)
SYP
WRC
Poly. (SYP)
y = 9E-06x² - 0.001x + 0.0357
R² = 0.7446
Average Modal Damping Ratio
Maximum Fiber Stress at Break Location [Mpa]

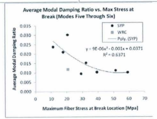
Average Modal Damping Ratio vs. Max Stress at Break (Modes Five Through Six)
SYP
WRC
Poly. (SYP)
y = 9E-06x² - 0.001x + 0.0371
R² = 0.6371
Average Modal Damping Ratio
Maximum Fiber Stress at Break Location [Mpa]

Normalized and average normalized damping ratios plotted against max. break location stress:

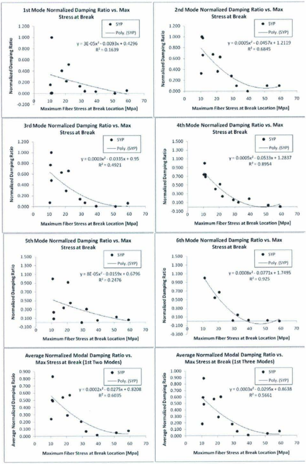

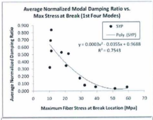
Average Normalized Modal Damping Ratio vs. Max Stress at Break (1st Four Modes)
SYP
Poly. (SYP)
y = 0.0003x² - 0.0355x + 0.9688
R² = 0.7543
Average Normalized Damping Ratio
Maximum Fiber Stress at Break Location [Mpa]

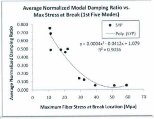
Average Normalized Modal Damping Ratio vs. Max Stress at Break (1st Five Modes)
SYP
Poly. (SYP)
y = 0.0004x² - 0.0412x + 1.079
R² = 0.9036
Average Normalized Damping Ratio
Maximum Fiber Stress at Break Location [Mpa]

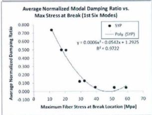
Average Normalized Modal Damping Ratio vs. Max Stress at Break (1st Six Modes)
SYP
Poly. (SYP)
y = 0.0006x² - 0.0542x + 1.2925
R² = 0.9722
Average Normalized Damping Ratio
Maximum Fiber Stress at Break Location [Mpa]

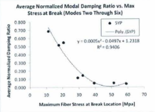
Average Normalized Modal Damping Ratio vs. Max Stress at Break (Modes Two Through Six)
SYP
Poly. (SYP)
y = 0.0005x² - 0.0497x + 1.2318
R² = 0.9406
Average Normalized Damping Ratio
Maximum Fiber Stress at Break Location [Mpa]

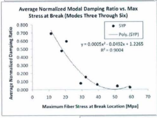
Average Normalized Modal Damping Ratio vs. Max Stress at Break (Modes Three Through Six)
SYP
Poly. (SYP)
y = 0.0005x² - 0.0492x + 1.2265
R² = 0.9004
Average Normalized Damping Ratio
Maximum Fiber Stress at Break Location [Mpa]

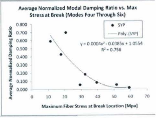
Average Normalized Modal Damping Ratio vs. Max Stress at Break (Modes Four Through Six)
SYP
Poly. (SYP)
y = 0.0004x² - 0.0385x + 1.0554
R² = 0.756
Average Normalized Damping Ratio
Maximum Fiber Stress at Break Location [Mpa]

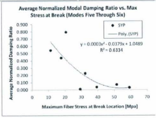
Average Normalized Modal Damping Ratio vs. Max Stress at Break (Modes Five Through Six)
SYP
Poly. (SYP)
y = 0.0003x² - 0.0379x + 1.0489
R² = 0.6334
Average Normalized Damping Ratio
Maximum Fiber Stress at Break Location [Mpa]

Actual and averaged percentile rank of damping ratios plotted against max. break location stress:

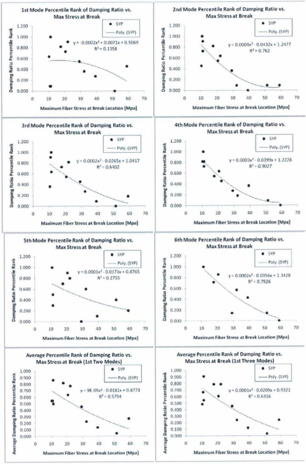

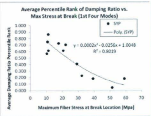
Average Percentile Rank of Damping Ratio vs.
Max Stress at Break (1st Four Modes)
SYP
Poly. (SYP)
y = 0.0002x² - 0.0256x + 1.0048
R² = 0.8019
Average Damping Ratio Percentile Rank
Maximum Fiber Stress at Break Location [Mpa]

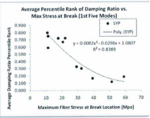
Average Percentile Rank of Damping Ratio vs.
Max Stress at Break (1st Five Modes)
SYP
Poly. (SYP)
y = 0.0002x² - 0.0298x + 1.0807
R² = 0.8389
Average Damping Ratio Percentile Rank
Maximum Fiber Stress at Break Location [Mpa]

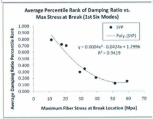
Average Percentile Rank of Damping Ratio vs.
Max Stress at Break (1st Six Modes)
SYP
Poly. (SYP)
y = 0.0004x² - 0.0424x + 1.2996
R² = 0.9419
Average Damping Ratio Percentile Rank
Maximum Fiber Stress at Break Location [Mpa]

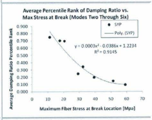
Average Percentile Rank of Damping Ratio vs.
Max Stress at Break (Modes Two Through Six)
SYP
Poly. (SYP)
y = 0.0003x² - 0.0386x + 1.2234
R² = 0.9145
Average Damping Ratio Percentile Rank
Maximum Fiber Stress at Break Location [Mpa]

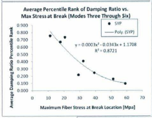
Average Percentile Rank of Damping Ratio vs.
Max Stress at Break (Modes Three Through Six)
SYP
Poly. (SYP)
y = 0.0003x² - 0.0343x + 1.1708
R² = 0.8721
Average Damping Ratio Percentile Rank
Maximum Fiber Stress at Break Location [Mpa]

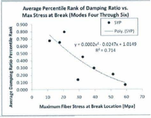
Average Percentile Rank of Damping Ratio vs.
Max Stress at Break (Modes Four Through Six)
SYP
Poly. (SYP)
y = 0.0002x² - 0.0247x + 1.0149
R² = 0.714
Average Damping Ratio Percentile Rank
Maximum Fiber Stress at Break Location [Mpa]

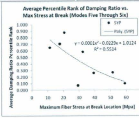
Average Percentile Rank of Damping Ratio vs.
Max Stress at Break (Modes Five Through Six)
SYP
Poly. (SYP)
y = 0.0001x² - 0.0229x + 1.0124
R² = 0.5514
Average Damping Ratio Percentile Rank
Maximum Fiber Stress at Break Location [Mpa]

Summary of results for damping ratio parameters plotted against maximum break location stress:

R^2 Values Using 2nd Order Polynomial Fit For Individual Modal Damping Parameters vs. Max Stress at Break Location			
Mode	Actual Damping Ratio	Normalized Damping Ratio	Percentile Rank of Damping Ratio
1	0.1639	0.1639	0.1358
2	0.6845	0.6845	0.7620
3	0.4921	0.4921	0.6402
4	0.8954	0.8954	0.9027
5	0.2476	0.2476	0.2755
6	0.9250	0.9250	0.7926

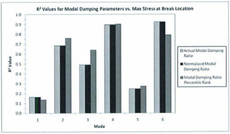

R^2 Values Using 2nd Order Polynomial Fit For Average Modal Damping Parameters vs. Max Stress at Break Location			
Modes	Average Actual Modal Damping Ratio	Average Normalized Damping Ratio	Average Percentile Rank of Damping Ratio
1 to 2	0.4415	0.6035	0.5794
1 to 3	0.4853	0.5661	0.6316
1 to 4	0.7622	0.7543	0.8019
1 to 5	0.8555	0.9036	0.8389
1 to 6	0.9387	0.9722	0.9419
2 to 6	0.8933	0.9406	0.9145
3 to 6	0.8709	0.9004	0.8721
4 to 6	0.7446	0.756	0.714
5 to 6	0.6371	0.6334	0.5514

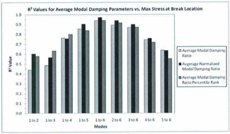

Damping ratio and average damping ratio plotted against maximum Ground line stress:

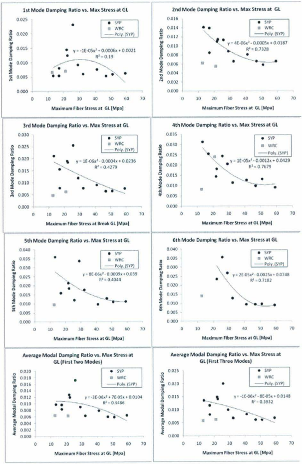

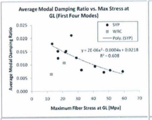
Average Modal Damping Ratio vs. Max Stress at GL (First Four Modes)
SYP
WRC
Poly. (SYP)
y = 2E-06x² - 0.0004x + 0.0218
R² = 0.608
Average Modal Damping Ratio
0.025 0.020 0.015 0.010 0.005 0.000
0 10 20 30 40 50 60 70
Maximum Fiber Stress at GL [Mpa]

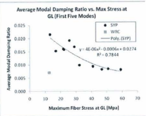
Average Modal Damping Ratio vs. Max Stress at GL (First Five Modes)
SYP
WRC
Poly. (SYP)
y = 4E-06x² - 0.0006x + 0.0274
R² = 0.7844
Average Modal Damping Ratio
0.025 0.020 0.015 0.010 0.005 0.000
0 10 20 30 40 50 60 70
Maximum Fiber Stress at GL [Mpa]

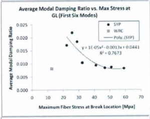
Average Modal Damping Ratio vs. Max Stress at GL (First Six Modes)
SYP
WRC
Poly. (SYP)
y = 1E-05x² - 0.0013x + 0.0441
R² = 0.7673
Average Modal Damping Ratio
0.025 0.020 0.015 0.010 0.005 0.000
0 10 20 30 40 50 60 70
Maximum Fiber Stress at Break Location [Mpa]

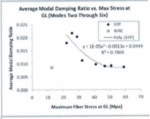
Average Modal Damping Ratio vs. Max Stress at GL (Modes Two Through Six)
SYP
WRC
Poly. (SYP)
y = 1E-05x² - 0.0013x + 0.0444
R² = 0.7804
Average Modal Damping Ratio
0.025 0.020 0.015 0.010 0.005 0.000
0 10 20 30 40 50 60 70
Maximum Fiber Stress at GL [Mpa]

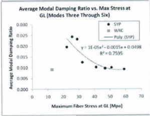
Average Modal Damping Ratio vs. Max Stress at GL (Modes Three Through Six)
SYP
WRC
Poly. (SYP)
y = 1E-05x² - 0.0015x + 0.0498
R² = 0.7595
Average Modal Damping Ratio
0.030 0.025 0.020 0.015 0.010 0.005 0.000
0 10 20 30 40 50 60 70
Maximum Fiber Stress at GL [Mpa]

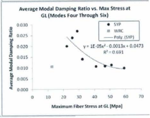
Average Modal Damping Ratio vs. Max Stress at GL (Modes Four Through Six)
SYP
WRC
Poly. (SYP)
y = 1E-05x² - 0.0013x + 0.0473
R² = 0.691
Average Modal Damping Ratio
0.030 0.025 0.020 0.015 0.010 0.005 0.000
0 10 20 30 40 50 60 70
Maximum Fiber Stress at GL [Mpa]

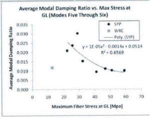
Average Modal Damping Ratio vs. Max Stress at GL (Modes Five Through Six)
SYP
WRC
Poly. (SYP)
y = 1E-05x² - 0.0014x + 0.0514
R² = 0.6569
Average Modal Damping Ratio
0.035 0.030 0.025 0.020 0.015 0.010 0.005 0.000
0 10 20 30 40 50 60 70
Maximum Fiber Stress at GL [Mpa]

Normalized and average normalized damping ratios plotted against maximum ground line stress:

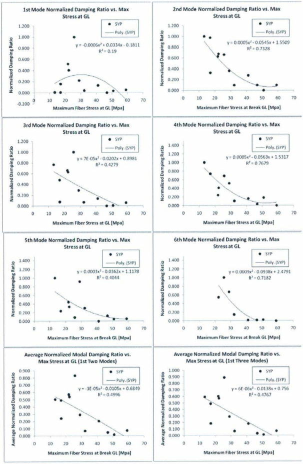

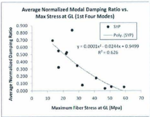
Average Normalized Modal Damping Ratio vs. Max Stress at GL (1st Four Modes)
SYP
Poly. (SYP)
y = 0.0001x² - 0.0244x + 0.9499
R² = 0.626
Average Normalized Damping Ratio
Maximum Fiber Stress at GL [Mpa]

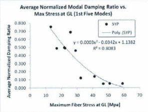
Average Normalized Modal Damping Ratio vs. Max Stress at GL (1st Five Modes)
SYP
Poly. (SYP)
y = 0.0003x² - 0.0342x + 1.1382
R² = 0.8083
Average Normalized Damping Ratio
Maximum Fiber Stress at GL [Mpa]

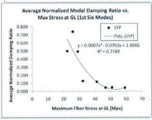
Average Normalized Modal Damping Ratio vs. Max Stress at GL (1st Six Modes)
SYP
Poly. (SYP)
y = 0.0007x² - 0.0703x + 1.8886
R² = 0.7785
Average Normalized Damping Ratio
Maximum Fiber Stress at GL [Mpa]

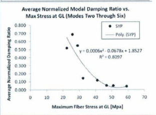
Average Normalized Modal Damping Ratio vs. Max Stress at GL (Modes Two Through Six)
SYP
Poly. (SYP)
y = 0.0006x² - 0.0678x + 1.8527
R² = 0.8097
Average Normalized Damping Ratio
Maximum Fiber Stress at GL [Mpa]

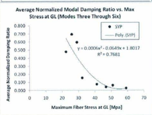
Average Normalized Modal Damping Ratio vs. Max Stress at GL (Modes Three Through Six)
SYP
Poly. (SYP)
y = 0.0006x² - 0.0649x + 1.8017
R² = 0.7681
Average Normalized Damping Ratio
Maximum Fiber Stress at GL [Mpa]

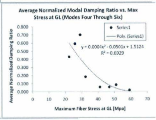
Average Normalized Modal Damping Ratio vs. Max Stress at GL (Modes Four Through Six)
Series1
Poly. (Series1)
y = 0.0004x² - 0.0501x + 1.5124
R² = 0.6929
Average Normalized Damping Ratio
Maximum Fiber Stress at GL [Mpa]

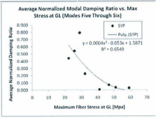
Average Normalized Modal Damping Ratio vs. Max Stress at GL (Modes Five Through Six)
SYP
Poly. (SYP)
y = 0.0004x² - 0.053x + 1.5871
R² = 0.6549
Average Normalized Damping Ratio
Maximum Fiber Stress at GL [Mpa]

Actual and averaged percentile rank of damping ratios plotted against max. ground line stress:

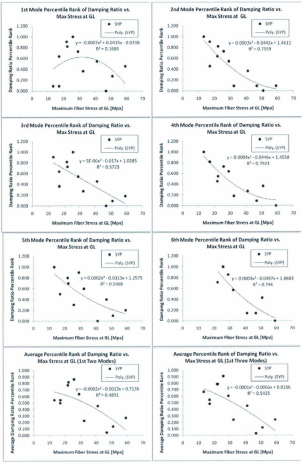

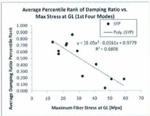
Average Percentile Rank of Damping Ratio vs.
Max Stress at GL (1st Four Modes)
SYP
Poly. (SYP)
y = 1E-05x² - 0.0161x + 0.9779
R² = 0.6808
Average Damping Ratio Percentile Rank
Maximum Fiber Stress at GL [Mpa]

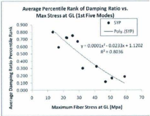
Average Percentile Rank of Damping Ratio vs.
Max Stress at GL (1st Five Modes)
SYP
Poly. (SYP)
y = 0.0001x² - 0.0233x + 1.1202
R² = 0.8036
Average Damping Ratio Percentile Rank
Maximum Fiber Stress at GL [Mpa]

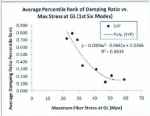
Average Percentile Rank of Damping Ratio vs.
Max Stress at GL (1st Six Modes)
SYP
Poly. (SYP)
y = 0.0006x² - 0.0681x + 2.0366
R² = 0.8834
Average Damping Ratio Percentile Rank
Maximum Fiber Stress at GL [Mpa]

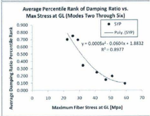
Average Percentile Rank of Damping Ratio vs.
Max Stress at GL (Modes Two Through Six)
SYP
Poly. (SYP)
y = 0.0005x² - 0.0604x + 1.8832
R² = 0.8977
Average Damping Ratio Percentile Rank
Maximum Fiber Stress at GL [Mpa]

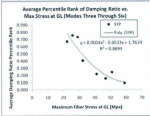
Average Percentile Rank of Damping Ratio vs.
Max Stress at GL (Modes Three Through Six)
SYP
Poly. (SYP)
y = 0.0004x² - 0.0533x + 1.7619
R² = 0.8694
Average Damping Ratio Percentile Rank
Maximum Fiber Stress at GL [Mpa]

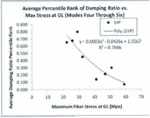
Average Percentile Rank of Damping Ratio vs.
Max Stress at GL (Modes Four Through Six)
SYP
Poly. (SYP)
y = 0.0003x² - 0.0426x + 1.5567
R² = 0.7886
Average Damping Ratio Percentile Rank
Maximum Fiber Stress at GL [Mpa]

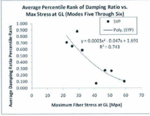
Average Percentile Rank of Damping Ratio vs.
Max Stress at GL (Modes Five Through Six)
SYP
Poly. (SYP)
y = 0.0003x² - 0.047x + 1.691
R² = 0.743
Average Damping Ratio Percentile Rank
Maximum Fiber Stress at GL [Mpa]

Summary of results for damping ratio parameters plotted against maximum ground line stress:

R^2 Values Using 2nd Order Polynomial Fit For Individual Modal Damping Parameters vs. Max Stress at Ground Line			
Mode	Actual Damping Ratio	Normalized Damping Ratio	Percentile Rank of Damping Ratio
1	0.1900	0.1900	0.1684
2	0.7328	0.7328	0.7559
3	0.4279	0.4279	0.5723
4	0.7679	0.7679	0.7923
5	0.4044	0.4044	0.5468
6	0.7182	0.7182	0.7440

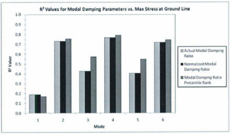

R^2 Values Using 2nd Order Polynomial Fit For Average Modal Damping Parameters vs. Max Stress at Ground Line			
Modes	Average Actual Modal Damping Ratio	Average Normalized Damping Ratio	Average Percentile Rank of Damping Ratio
1 to 2	0.3486	0.4996	0.4891
1 to 3	0.3932	0.4767	0.5425
1 to 4	0.608	0.626	0.6808
1 to 5	0.7844	0.8083	0.8036
1 to 6	0.7673	0.7785	0.8834
2 to 6	0.7804	0.8097	0.8977
3 to 6	0.7595	0.7681	0.8694
4 to 6	0.691	0.6929	0.7886
5 to 6	0.6569	0.6549	0.743

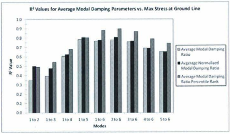

Power and exponential regression models that were used for predicting max. stress at GL:

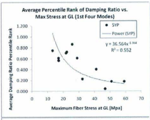

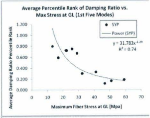

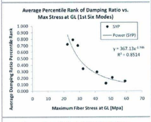

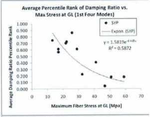

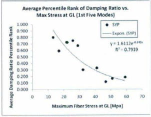

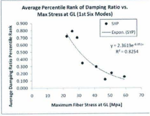

Linear models of actual and average percentile rank vs. max GL stress using only old SYP:

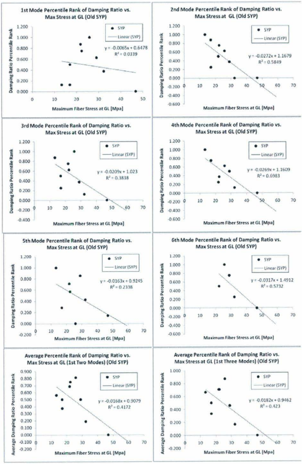

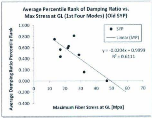
Average Percentile Rank of Damping Ratio vs.
Max Stress at GL (1st Four Modes) (Old SYP)
SYP
Linear (SYP)
y = -0.0204x + 0.9999
R² = 0.6111
Average Damping Ratio Percentile Rank
Maximum Fiber Stress at GL [Mpa]

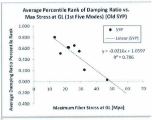
Average Percentile Rank of Damping Ratio vs.
Max Stress at GL (1st Five Modes) (Old SYP)
SYP
Linear (SYP)
y = -0.0216x + 1.0597
R² = 0.786
Average Damping Ratio Percentile Rank
Maximum Fiber Stress at GL [Mpa]

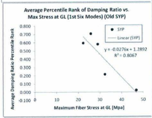
Average Percentile Rank of Damping Ratio vs.
Max Stress at GL (1st Six Modes) (Old SYP)
SYP
Linear (SYP)
y = -0.0276x + 1.2892
R² = 0.8067
Average Damping Ratio Percentile Rank
Maximum Fiber Stress at GL [Mpa]

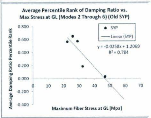
Average Percentile Rank of Damping Ratio vs.
Max Stress at GL (Modes 2 Through 6) (Old SYP)
SYP
Linear (SYP)
y = -0.0258x + 1.2069
R² = 0.784
Average Damping Ratio Percentile Rank
Maximum Fiber Stress at GL [Mpa]

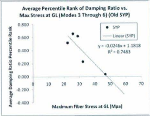
Average Percentile Rank of Damping Ratio vs.
Max Stress at GL (Modes 3 Through 6) (Old SYP)
SYP
Linear (SYP)
y = -0.0246x + 1.1818
R² = 0.7483
Average Damping Ratio Percentile Rank
Maximum Fiber Stress at GL [Mpa]

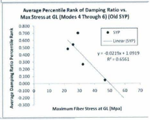
Average Percentile Rank of Damping Ratio vs.
Max Stress at GL (Modes 4 Through 6) (Old SYP)
SYP
Linear (SYP)
y = -0.0219x + 1.0919
R² = 0.6561
Average Damping Ratio Percentile Rank
Maximum Fiber Stress at GL [Mpa]

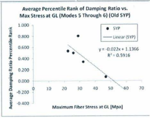
Average Percentile Rank of Damping Ratio vs.
Max Stress at GL (Modes 5 Through 6) (Old SYP)
SYP
Linear (SYP)
y = -0.022x + 1.1366
R² = 0.5916
Average Damping Ratio Percentile Rank
Maximum Fiber Stress at GL [Mpa]